

Alma Mater Studiorum – Università di Bologna

DOTTORATO DI RICERCA IN

CHIMICA

Ciclo XXVIII

Settore Concorsuale di afferenza: 03/A1 – Chimica Analitica

Settore Scientifico disciplinare: CHIM/01 – Chimica Analitica

**MODIFIED ELECTRODES FOR ENERGY
AND SENSING APPLICATIONS**

Presentata da: Dott.ssa Ylea Vlamidis

Coordinatore Dottorato

Prof. Aldo Roda

Relatore

Prof.ssa Domenica Tonelli

Esame finale anno 2016

Dr Ylea Vlamidis, Curriculum: Analytical Chemistry, Supervisor: Professor Domenica Tonelli

Dissertation thesis: *Modified electrodes for energy and sensing applications*

During the three years of her PhD, Ylea Vlamidis focused her research activity on the study of different electrode supports modified with layered double hydroxides (LDHs) or conductive polymers for energy applications (energy conversion and storage processes). The scientific work carried during the first year mainly concerned the electrochemical synthesis of poly(3,4-ethylenedioxythiophene) (PEDOT) on Indium Tin Oxide (ITO) in order to estimate the possibility of an alternative route to fabricate bulk heterojunction solar cells with similar performances but less expensive than those obtained from casting of a commercial polymer having polystyrene sulfonate as the counter ion. Furthermore, the electrochemical approach was also tentatively applied to the photoactive layer deposition by trying the synthesis of a polythiophene copolymer functionalized with a porphyrin derivative, previously synthesized by chemical route. Later, LDHs modified electrodes were studied as catalysts for the oxygen evolution reaction (OER) and as pseudocapacitor materials for which capacitance derives from the redox reactions occurring at the electrode. Again, the electrochemical approach was used for the deposition of thin films of LDHs on Pt and glassy carbon (GC). Due to the slow kinetics of electrochemical oxidation of water it is necessary to find efficient catalysts, preferably cheaper than the ones employed nowadays (IrO_2 e RuO_2). Four LDHs, based on Ni/Al, Ni/Fe, Co/Al and Co/Fe, were taken into account and the role of Fe instead of Al was deeply investigated. The best performances were displayed by the Co/Fe LDH for both applications demonstrating the positive effect played by the presence of iron.

The electrochemical behaviour of the LDHs modified electrodes was studied by cyclic voltammetry and electrochemical impedance spectroscopy. The morphologies and composition of the coatings were investigated by FEG-SEM and EDS, and atomic force microscopy, the structure was confirmed by recording X-ray diffraction spectra and the mass deposited on the electrode surface was estimated by Electrochemical Quartz Crystal Microbalance.

In the second part of her PhD, the LDHs modified electrodes were employed also for sensing, taking into account the electrocatalytic oxidation of sugars. Glucose determination is fundamental in food industry and in clinical applications; consequently, there is a considerable interest in the development of new methodologies for its simple, rapid and selective determination. Ni/Al or Ni/Fe LDHs were studied with the aim to investigate again the effect of Fe on the electrocatalysis. In this research LDHs prepared both by chemical and electrochemical syntheses were employed, obtaining film with good adhesion to the support. The reason why different syntheses were tried was to study the effect of the order degree on the LDHs performance since this parameter is crucial to improve the “sensing” properties. Finally, the glucose determination was investigated with GC electrodes modified with carbon-based nanomaterials (reduced graphene oxide and/or multi wall carbon nanotubes).

During the PhD period, Ylea Vlamidis acquired an excellent expertise in conventional and unconventional electroanalytical techniques. In addition, she achieved several skills in the use of analytical surface techniques, XRD, in manuscripts writing, and in the organization of the results. She is collaborative with the other researchers and students of the Lab. The candidate has been the co-supervisor of five first level degree theses in Industrial Chemistry and also tutor for the Course Analytical Chemistry Laboratory for two years demonstrating a great ability in coordinating the students activities. The main results achieved in the three years of PhD research have been documented by four scientific papers published on important peer-review international journals. Furthermore, two more papers are at present under review.

The candidate took an active part in two national and two international congresses and attended the “**Scuola Divisionale di Elettrochimica - Energetica e Sensori**” in 2013, and the “**Scuola Nazionale di Chimica Analitica**” in 2014, and several scientific seminars.

As supervisor of his thesis, my overall evaluation of the candidate is excellent.

*"The important thing is not to stop questioning.
Curiosity has its own reason for existing.
One cannot help but be in awe
when he contemplates the mysteries
of eternity, of life, of the marvelous structure of reality.
It is enough if one tries merely
to comprehend a little of this mystery every day."
Albert Einstein*

TABLE OF CONTENTS

<i>LIST OF ACRONYMS AND ABBREVIATIONS</i>	<i>i</i>
1. PREFACE AND AIM OF THE RESEARCH WORK	1
REFERENCES	7
INTRODUCTION	9
2. CHEMICALLY MODIFIED ELECTRODES	9
2.1 Main methods for electrodes modification	10
2.2 Modified electrodes characterizations	11
2.2.1 X-rays diffraction	12
2.2.2 X-ray absorption spectroscopy	13
2.2.3 Scanning electron microscopy	18
2.2.4 Energy dispersive X-rays analysis	19
2.2.5 Atomic force microscopy	19
2.2.6 Electrochemical methods of analysis	21
2.2.6.1 Cyclic voltammetry	21
2.2.6.2 Capacitance and charge	22
2.2.6.3 Galvanostatic charge-discharge experiments	23
2.2.6.4 Polarization curves	24
2.2.6.5 Rotating disk electrode	26
2.2.6.6 Electrochemical quartz crystal microbalance	27
REFERENCES	29
3. LAYERED DOUBLE HYDROXIDES (LDHs)	31
3.1 Structure	31
3.2 Synthesis methods	32
3.2.1 Coprecipitation at a constant pH	33
3.2.2 Urea hydrolysis method	33
3.2.3 Hydrothermal method	34
3.2.4 Glycine assisted hydrothermal synthesis	35
3.2.5 Topochemical oxidation	35
3.2.6 Reconstruction method	36
3.2.7 Microemulsion method	36
3.2.8 Electrochemical synthesis	36
3.3 LDH modified electrodes applications	37

3.3.1	Biochemical and medical applications	38
3.3.2	Environmental applications	39
3.3.3	Detection	40
3.3.3.1	Electrocatalysis and sensors	41
3.3.3.2	Biocatalysis and biosensors	41
3.3.4	Energy	42
3.3.4.1	Production: fuel cells and metal-air batteries	42
3.3.4.2	Storage: supercapacitors	45
REFERENCES		47
4.	<i>ENERGY STORAGE AND CONVERSION</i>	51
4.1	Oxygen Evolution Reaction	52
4.1.1	Catalytic activity and kinetic parameters for OER	53
4.1.2	Requirements for oxygen evolution catalysts	54
4.1.3	Trend of the catalysts activity for OER	55
4.1.3.1	Noble metal oxides	56
4.1.3.2	Non-noble metals for alkaline water electrolysis	57
4.2	Electrochemical capacitors	58
4.2.1	Electrical double layer supercapacitors and pseudocapacitors	58
4.2.1.1	Faradaic supercapacitors	59
	• Electrode materials	60
4.2.2	Electrochemical studies of the EC materials	63
4.2.3	Properties and applications of EC	64
4.3	Solar cells and organic solar cells	65
4.3.1	Organic cells mechanism	66
4.3.2	Devices architecture	68
4.3.2.1	Single layer heterojunction	68
4.3.2.2	Bilayer heterojunction	69
4.3.2.3	Bulk heteriojunction	69
4.3.3	Common OPV devices materials	70
4.3.4	Structure of the OPV cells and role of the “hole extracting layer”	71
4.3.4.1	Annealing treatments	72
4.3.5	Parameters and performances	72
REFERENCES		75
5.	<i>ELECTROCHEMICAL SENSORS</i>	83
5.1	Electrocatalytic process at a CME	83
5.2	Carbohydrates electrochemical determination	85

5.3	Mechanism involved in LDHs electrocatalysis	86
	REFERENCES	88
6.	EXPERIMENTAL SECTION	91
6.1	Chemicals	91
6.2	Chemical equipments	92
6.3	Modification of the electrodes with LDHs	93
6.3.1	Electrodes modification procedures	94
6.3.1.1	Pt pre-treatment and electrode modification	94
6.3.1.2	GC pre-treatment and electrode modification	95
6.4	LDHs modified electrode characterizations	95
6.4.1	Electrochemical characterization	95
6.4.1.1	Cyclic Voltammetry	95
6.4.1.2	Electrodeposition monitored by Electrochemical Quartz Chrystal Microbalance	96
6.4.2	Structural characterization	96
6.4.2.1	X-ray diffraction	96
6.4.2.2	X-ray Photoelectron Spectroscopy	96
6.4.2.3	X-ray Absorption Spectroscopy	97
6.4.3	Morphological characterization	97
6.5	Evaluation of the performances of LDH modified electrodes	98
6.5.1	OER catalytic activity and modified electrode durability	98
6.5.2	Pseudocapacitors performances	98
6.6	Bulk heterojunction solar cells fabrication	99
6.6.1	Electrochemical measurements and characterizations	99
6.6.2	ITO electrode preparation	101
6.6.3	Fabrication of the OPV devices	101
6.6.4	Synthesis of PEDOT:ClO ₄	103
6.7	Amperometric sensors based on LDH modified electrodes	103
6.7.1	Sensors based on chemically and electrochemically synthesized Ni-based LDH for the detection of glucose	103
6.7.1.1	Equipments	103
6.7.1.2	Pt surface modification	104
6.7.1.3	CV characterizations and amperometric detection of glucose	104
6.7.2	Co/Al LDH coated Pt for in flow amperometric detection of sugars	106
6.7.2.1	Pt surface modification	107
6.8	Data elaboration	107

REFERENCES	108
RESULTS AND DISCUSSION	109
7. LDHs AND CONDUCTING POLYMERS AS ELECTRODES MODIFIERS: ENERGY APPLICATIONS	111
7.1 LDHs characterizations and performances	111
7.1.1 LDHs electrochemical characterizations	111
7.1.1.1 Ni/Al-LDH	111
7.1.1.2 Co/Al LDH	113
7.1.1.3 Ni/Fe LDH	116
7.1.1.4 Co/Fe LDH	117
7.1.1.5 Electrode support and pH influence	118
7.1.2 Structural characterization	121
7.1.2.1 X-ray diffraction	121
7.1.2.2 X-ray photoelectron spectroscopy	122
7.1.2.3 X-ray absorption spectroscopy	125
7.1.3 Morphological characterizations	128
7.1.4 OER catalytic activity and modified electrode durability	130
7.1.4.1 OER onset potential determined by linear sweep voltammetry	130
7.1.4.2 Durability tests	134
7.1.4.3 Tafel slopes and OER proposed mechanism	135
7.1.5 Pseudocapacitors performances	137
7.1.5.1 Performances of the LDHs coatings on Pt	137
7.1.5.2 Specific capacitance and cycling life-time	140
7.1.5.3 Performances of the LDHs on GC	144
7.2 Conducting polymers electrodeposition: bulk heterojunction solar cells	146
7.2.1 Electrochemical synthesis of PEDOT:ClO ₄	147
7.2.2 Annealing treatments	148
7.2.3 Electrochemical characterization of the polymeric films and the blend	148
7.2.3.1 Electrochemical characterization of PEDOT:PSS and PEDOT:ClO ₄ films	148
7.2.3.2 Electrochemical characterization of rr-P(T6Br-co-T6TPP), PCBM and blend	149
7.2.4 Optical properties of the OPV cells components	151
7.2.4.1 Cells components absorption spectra	151
7.2.4.2 Emission spectra of the photoactive layer components	153
7.2.5 Photovoltaic performances of the BHJ cells	154
7.2.6 AFM morphological characterizations	156
REFERENCES	160

8. AMPEROMETRIC SENSORS BASED ON LDH MODIFIED ELECTRODES	163
8.1 Sensors based on chemically and electrochemically synthesized Ni-based LDH for glucose detection	163
8.1.1 LDHs composition	163
8.1.2 Structural characterizations	164
8.1.3 Electrochemical characterizations	165
8.1.4 Morphological characterization of the chemical Ni-based LDHs	169
8.1.5 Glucose detection	171
8.2 Co/Al LDH coated Pt for in flow amperometric detection of sugars	177
8.1.1 Co/Al LDH morphology and effect of deposition time	177
8.1.2 Amperometric sensors performances	178
8.1.3 Mechanical stability of the Co/Al LDH coating	181
8.1.4 Flow injection analysis (FIA) of sugars	182
8.1.5 HPLC determination of sugars	184
REFERENCES	187
9. CONCLUSIONS	189
SCIENTIFIC PUBLICATIONS	193
ACKNOWLEDGEMENTS	195

LIST OF ACRONYMS AND ABBREVIATIONS

In the following table the most frequent acronyms and abbreviations are summarized in alphabetic order to facilitate the reading.

<i>Acronym or abbreviation</i>	<i>Extended word</i>
AFM	Atomic Force Microscopy
AM	Air Mass
BHJ	Bulk Heterojunction
CA	Chronoamperometry
CME	Chemically Modified Electrode
C_s	Specific Capacitance
CV	Cyclic Voltammetry
EC	Electrochemical Capacitor
EDLS	Electrical double-layer supercapacitor
EDOT	3,4-Ethylenedioxythiophene
EDX	Energy Dispersive X-rays
EE	Electrocatalytic Efficiency
E_g	Energy gap
EIS	Electrochemical Impedance Spectroscopy
EQCM	Electrochemical Quartz Crystal Microbalance
EXAFS	Extended X-ray Absorption Fine-Structure
FE-SEM	Field Emission Scanning Electron Microscopy
FF	Fill Factor
FIA	Flow Injection Analysis
FS	Faradaic Supercapacitor
FWHM	Full Width at Half Maximum
GC	Glassy Carbon
HPLC	High Performance Liquid Chromatography

I_{dark}	Dark current
I_{sc}	Short circuit current
ITO	Indium Tin Oxide
LDH	Layered Double Hydroxide
LOD	Limit of Detection
LOL	Limit of Linearity
LSV	Linear Sweep Voltammetry
OER	Oxygen Evolution Reaction
OPV	Organic Photovoltaic
P3HT	Poly(3-hexylthiophene)
PCBM	[6,6]-Phenyl C61 butyric acid methyl ester
PCE	Power Conversion Efficiency
PEDOT:PSS	Poly(3,4-ethylenedioxythiophene-poly(styrene sulfonate))
P_i	Incident light power density
PL	Photoluminescence
P_{max}	Maximum power point
RDE	Rotating Disk Electrode
RHE	Reversible Hydrogen Electrode
rr-P(T6Br-co-T6TPP)	Regioregular Poly [(3-(6-bromohexyl)] thiophene)-co-(3-[5-(4-phenoxy)-10,15,20-triphenylporphyrinyl] hexylthiophene)
SCE	Saturated Calomel Electrode
TOF	Turnover Frequency
V_{oc}	Open circuit potential
XANES	X-ray Absorption Near-Edge Spectroscopy
XAS	X-ray Absorption Spectroscopy
XPS	X-ray Photoelectron Spectroscopy
XRD	X-ray Diffraction

1. PREFACE AND AIM OF THE RESEARCH WORK

The climate change, the environmental pollution and the depletion of fossil fuels have greatly affected the global economy and ecology [1]. With a growing market for electronic devices and the development of hybrid electric vehicles, there has been an increasing and urgent demand of environmentally friendly high-power energy resources. Nowadays it is particularly important to exploit alternative power resources, and from this point of view the challenge is to develop new technologies and materials to obtain more efficient devices for water splitting and to improve renewable energy systems and components.

Electrochemistry can offer solutions to energy challenges in several ways. Energy conversion in electrochemical processes is often limited by high overpotentials, which means high activation barrier [2]. For example, in the case of water splitting, electrocatalysts are often applied as electrodes modifiers, in order to lower activation energy and increase the conversion rate [3]. Due to the expensive and scarcely available raw materials which constitute the most commonly used catalysts for oxygen evolution reaction (OER) [4,5], in the last decade many efforts have been made to develop new materials displaying high efficiency, low cost and environmental friendliness [3,6].

Sustainable and renewable resources such as hydrogen and energy production from sun, wind, hydro and geothermal heat, unfortunately cannot provide the energetic autonomy required for new systems such as portable electronics, hybrid electric vehicles and so on [7]. For this reason the development of efficient systems, allowing to storage the surplus energy when electricity supply is higher than demand and to release it when necessary, is becoming more and more important [8]. In this regard, electrochemical devices with desired energy and power output characteristics, long cycle life, high efficiency and low cost are under study and the new generation of supercapacitors seems to offer a promising alternative to batteries and fuel cells due to many advantages such as higher power density and longer lifecycle [9,10].

Among the electrochemical capacitors, the so called pseudocapacitors, containing electrochemically active materials such as metal oxides and hydroxides, are attracting particular attention [11,12]. In this kind of devices the capacitance derives from a redox reaction occurring at the electrode which is responsible for much higher specific

capacitance (C_s) and energy density than electrochemical double layer capacitors [13]. Even for these applications precious metal-based compounds are the most employed, thus the research for new suitable low-cost materials able to enhance the performances is still going on [14].

Chemically modified electrodes (CMEs) [15] are conducting or semiconducting materials, coated with a selected film of a chemical modifier which, by means of Faradaic reactions or interfacial potential differences, confers them peculiar chemical, electrochemical, and/or optical properties. CMEs allow fabricating electrochemical devices and systems for applications in chemical sensing, energy conversion and storage, corrosion protection, biosensors, electrocatalysts, etc [16].

The first part of the research activity carried out during my PhD program was focused on the study of different electrode supports modified with layered double hydroxides (LDHs) or conducting polymers for energy applications. In particular, LDH modified electrodes were studied as oxygen evolution reaction catalysts and as pseudocapacitor materials. Moreover, an electrochemical synthesis of poly(3,4-ethylenedioxythiophene) (PEDOT) on indium tin oxide (ITO) was investigated in order to estimate the possibility of an alternative route to fabricate bulk heterojunction solar cells [17] with similar performances but less expensive than those obtained by casting.

The following researches were carried out and are presented below:

- LDHs based on Co or Ni as M(II) and Al or Fe as M(III) were electrosynthesized in potentiostatic conditions and characterized.

LDHs consist in a class of lamellar compounds with positively charged brucite-like layers and charge balancing anions located in the interlayer region. LDHs are commonly represented by the formula $[M(II)_{1-x}M(III)_x(OH)_2]^{q+}(X^{n-})_{q/n} \cdot yH_2O$, where M(II) and M(III) are the divalent and the trivalent cations, respectively [18].

The experiments were carried out employing as electrode support highly conductive materials, *i.e.*, Pt electrodes, but also glassy carbon (GC) electrodes in order to study the LDHs synthesis conditions on a cheaper electrode material which could represent an alternative to Pt. The electrochemical behaviour of the LDHs modified electrodes was studied by cyclic voltammetry (CV) and electrochemical impedance spectroscopy (EIS). The morphologies and composition of the coatings on both supports were investigated by field emission scanning electron microscopy (FE-SEM) and energy dispersive spectroscopy

(EDX), and the structure was confirmed by recording X-ray diffraction spectra (XRD). X-ray photoelectron spectroscopy (XPS) experiments were performed in order to study the oxidization states of the metal cations in the four LDHs just synthesized and after oxidation. Furthermore, X-ray absorption spectroscopy (XAS) was applied to pristine and oxidized Ni/Fe LDHs in order to gain information about the structural and electronic changes in the local environment around the selected metallic site.

- LDHs modified electrodes were tested as OER catalysts using a rotating disk electrode in alkaline solutions. The onset potential was determined by recording polarization curves, and the catalysts stability was checked by chronopotentiometry. The performances in terms of onset potential, Tafel slope and current density of the LDH coatings on GC as OER catalysts were compared to those obtained for Pt.
- The specific capacitance and long-term stability of the LDHs modified electrodes were investigated in alkaline solutions (0.1 and 1.0 M NaOH). The former was calculated using the data obtained from three techniques, *i.e.*, CVs, EIS and charge-discharge galvanostatic curves at different current densities. The latter was tested by calculating the C_s before and after performing 1000 charge-discharge cycles at 5.0 mA g^{-1} .
- Concerning the modified electrodes for energy applications, organic solar cells were fabricated employing different PEDOT buffers [19]: one deposited by electrochemical potentiostatic synthesis (PEDOT:ClO₄) and the other by casting a commercial polymer having polystyrene sulfonate (PSS) as the counterion (PEDOT:PSS) on ITO electrodes. As reported in the literature, the best properties of PEDOT are obtained in the presence of LiClO₄ as the supporting electrolyte since this salt leads to an increase of electroactivity and crystallinity of the polymer [20]. To exploit the potentialities of the electrochemical approach a detailed study to find the best experimental conditions for PEDOT:ClO₄ electrosynthesis was carried out.

The advantages of the electrochemical synthesis are the rapid obtainment of PEDOT films directly on the electrode surface with tunable electroactivity and thickness, the consuming of very low amount of monomer and the interesting possibility to introduce different counterions to compensate the polymer positive charge in dependence on the employed electrolyte [21]. PEDOT:PSS and

PEDOT:ClO₄ were characterized using electrochemical techniques and recording UV/Vis spectra, with the aim of studying the oxidation degree of the two materials and the performances of the cells containing electrosynthesized PEDOT:ClO₄ were compared to the ones displayed by cells where the hole extracting layer was obtained by casting the commercially available PEDOT:PSS. The photoactive layer was composed by [6,6]-phenyl-C61 butyric acid methyl ester (PCBM) as electron acceptor in the blend, while as donor polymer it was employed either the most commonly employed regioregular poly(3-hexylthiophene) (P3HT) [22] or a polythiophene copolymer, functionalized with a porphyrin derivative. The regioregular thiophenic copolymer (poly[3-(6-bromohexyl) thiophene - *o*- (3 -[5- (4- phenoxy)- 10,15,20- triphenylporphyrinyl] hexylthiophene)] (rr-P(T6Br-*co*-T6TTP)), *ad hoc* synthesized by the Polymers group of the Department of Industrial Chemistry “Toso Montanari” at the University of Bologna, was employed in order to improve the absorption in the UV/Vis region in terms of both wideness and intensity [23]. The HOMO and LUMO energy level of rr-P(T6Br-*co*-T6TTP) were calculated from CV data and taking into account the optical energy gap estimated from the UV/Vis spectra. Emission spectra of the photoactive layer containing rr-P(T6Br-*co*-T6TTP) and PCBM were carried out in order to confirm the possibility of charge transfer between the donor and the acceptor molecules in the photoactive layer. Moreover, the morphologies of the PEDOT and the photoactive layers were extensively investigated by atomic force microscopy (AFM) in order to correlate the particles size and film compactness with the cells performances, and the performances of all the devices will be reported in this thesis.

Another topic of my research concerned the application of the CMEs as electrochemical sensors. These devices operate by reacting with the analyte of interest, producing an electrical signal which is proportional to the concentration [24]. Since 1999, when Ni/Al LDH modified electrodes were employed for the first time for the electrocatalytic oxidation of methanol and ethanol in strongly basic solution by the research group of Analytical Chemistry at the Department of Industrial Chemistry “Toso Montanari” (University of Bologna) [25], many kind of amperometric sensors based on LDHs containing redox active metals (such as Co and Ni) have been proposed as sensors for oxidizable analytes [26].

In this work the LDHs modified electrodes were employed for the electrocatalytic oxidation of sugars. In nature carbohydrates are involved in very important properties related to fruits, honey and other natural matrices, such as flavor, maturity, quality and storage conditions [27]. Thus, the knowledge of the qualitative and quantitative distribution of sugars is essential and their determination is highly relevant in food industry [28]. Besides industrial applications, glucose plays a central role also in clinical applications because its concentration is a crucial indicator for many diseases, such as diabetes and endocrine metabolic disorders [29]; consequently, there is a considerable interest in the development of new methodologies for its simple, rapid and selective determination.

Concerning sugar determination the following studies will be presented in this thesis:

- the behaviour toward glucose oxidation of Pt electrodes coated by Ni/Al or Ni/Fe LDHs with the aim to investigate the effect of Fe on the electrocatalysis. LDHs prepared by electrochemical and chemical syntheses were employed, obtaining films with good adhesion to the support. The reason why different synthesis approaches were tried was to investigate the effect of the order degree on the LDHs performance since this parameter is crucial to improve the “sensing” properties. CV and chronoamperometric curves were recorded in order to determine the main parameters, such as the sensitivity and limit of linearity, of glucose analytical determination. Furthermore, the catalytic process was deeply investigated determining its efficiency and the catalytic constant. The percentage of electroactive Ni centers was calculated for the four LDHs and EIS measurements were conducted in order to study the materials conductivity. Furthermore, the particle size and the crystallinity degree were estimated by XRD analysis, and the morphology of the chemically and electrochemically synthesized LDHs was investigated by AFM and SEM.
- A sensor for the amperometric detection of sugars in flow systems, based on Co/Al LDH electrosynthesized on Pt electrodes, was developed. The best deposition time in order to obtain a film with the desired mechanical properties and sensing performances was investigated. The former were checked performing bending tests and acquiring SEM images of films obtained for different deposition times. The sensing responses were evaluated from the calibration curves. The efficiency of the catalytic Co centres was studied in solutions with different pHs considering the most important mono- and di-saccharides. A mixture of sugars was submitted to high

PREFACE AND AIM OF THE RESEARCH WORK

performance anion chromatography with amperometric detection, using the CME as the working electrode. Moreover, to assess the applicability of the device glucose, fructose, and sucrose contents in real samples were successfully determined.

REFERENCES

- [1] N. Heidari, J.M. Pearce. *Renew. Sust. Energ. Rev.* 55 (2016) 899.
- [2] Y. Liang, Y. Li, H. Wang, H. Dai. *J. Am. Chem. Soc.* 135 (2013) 2013.
- [3] J. Lee, B. Jeong, J.D. Ocon. *Curr. Appl. Phys.* 13 (2013) 309.
- [4] V.D. Patake, C.D. Lokhande, O.S. Joo, *Appl. Surf. Sci.* 255 (2009) 4192.
- [5] E. Fabbri, A. Habereeder, K. Waltar, R. Kötz, T.J. Schmidt. *Catal. Sci. Technol.* 4 (2014) 3800.
- [6] I. Katsounaros, S. Cherevko, A.R. Zeradjanin, K.J.J. Mayrhofer. *Angew. Chem. Int. Ed.* 53 (2014) 102.
- [7] P. Simon, Y. Gogotsi. *Nat. Mater.* 7 (2008) 845.
- [8] H. Wang, H. Dai. *Chem. Soc. Rev.* 42 (2013) 3088.
- [9] J.R. Miller, A.F. Burke, *Electrochem. Soc. Interface* 17 (2008) 53.
- [10] S. Kandalkar, D. Dhawale, C. Kim, C. Lokhande. *Synth. Met.* 160 (2010) 1299.
- [11] H. Che, A. Liu. *J. Mater. Sci: Mater. Electron.* 26 (2015) 4097.
- [12] W. Sun, L. Chen, S. Meng, Y. Wang, H. Li, Y. Han, N. Wei. *Mater. Sci. Semicond. Process.* 17 (2014) 129.
- [13] T. Stimpfling, F. Leroux. *Chem. Mater.* 22 (2010) 974.
- [14] G. Wang, L. Zhang, J. Zhang. *Chem. Soc. Rev.* 41 (2012) 797.
- [15] J.-M. Zen, A.S. Kumar, D.-M. Tsai, *Electroanalysis* 15 (2003) 1073.
- [16] J. Cox, R. Jaworski, P.J. Kulesza, *Electroanalysis* 3 (1991) 869.
- [17] P.W. M. Blom, V.D. Mihailetschi, L.J.A. Koster, D.E. Markov. *Adv. Mater.* 19 (2007) 1551.
- [18] D. Tonelli, E. Scavetta, M. Giorgetti. *Anal. Bioanal. Chem.* 405 (2013) 603.
- [19] H.-Y. Wei, J.-H. Huang, K.-C. Ho, C.-W. Chu. *ACS Appl. Mater. Interfaces* 2 (2010) 1281.
- [20] A.I. Melato, M.H. Mendonça, L.M. Abrantes. *J. Solid State Electrochem.* 13 (2009) 417.
- [21] L. Groenendaal, G. Zotti, P.H. Aubert, S.M. Waybright, J.R. Reynolds. *Adv Mater.* 15 (2003) 855.
- [22] M.T. Dang, L. Hirsch, G. Wantz. *Adv. Mater.* 23 (2011) 3597.
- [23] L. Angiolini, V. Cocchi, M. Lanzi, E. Salatelli, D. Tonelli, Y. Vlamidis. *Mater. Chem. Phys.* 146 (2014) 464.

[24] J. Wang, Analytical electrochemistry, John Wiley & Sons, Inc., Hoboken, New Jersey, 2006.

[25] B. Ballarin, R. Seeber, D. Tonelli, A. Vaccari. *J. Electroanal. Chem.* 463 (1999) 123.

[26] E. Scavetta, B. Ballarin, M. Berrettoni, I. Carpani, M. Giorgetti, D. Tonelli. *Electrochim. Acta* 51 (2006) 2129.

[27] F. Jiménez-Márquez, J. Vázquez, J. Úbeda, J.L. Sánchez-Rojas. *Sens. Actuators B* 225 (2016) 121.

[28] C. Martinez Montero, M.C. Rodriguez Doderó, D.A. Guillén Sánchez, C.G. Barroso. *Cromatographia* 59 (2004) 15.

[29] R. Yin, D. Zhang, Y. Song, B. Zhu, H. Wang. *Sci. Rep.* 3 (2013) 1787.

INTRODUCTION

In the following chapters the state of art of the research concerning the modified electrodes for energy and sensors applications will be discussed.

First of all the concept of the chemically modified electrodes (CMEs) will be discussed pointing out the main ways of preparation and characterization. As to the modifiers a particular attention will be dedicated to layered double hydroxides.

Later the topic will concern energy storage and conversion. In particular, the studies on the oxygen evolution reaction, the electrochemical pseudocapacitors and the organic solar cells will be discussed in details. The mechanisms, the materials and the main fields of application will be also described.

Eventually, an application of the CMEs as electrochemical sensors will be presented exploiting their property to act as redox mediators.

2. CHEMICALLY MODIFIED ELECTRODES

Chemically modified electrodes represent a relatively modern approach to electrode systems that is useful for a wide range of electrochemical investigations, such as electrostatic phenomena at electrode surfaces, electron and ionic transport phenomena in polymers and design of electrochemical devices and systems for applications in chemical sensing, energy conversion and storage, molecular electronics, electrochromic displays, corrosion protection, and electro-organic syntheses.

A chemically modified electrode is a conductive material whose surface has been modified in order to enhance the electrochemical performances in different applications [1]. Generally, in a CME a quite thin film (from a molecular monolayer to a few micrometers-thick multilayer) of a selected chemical is bonded to or coated on the electrode surface to change properties of the conductor according to its targeted function, since the modifier endows the electrode with the desired chemical, electrochemical, optical, electrical features and other useful properties.

The modification of electrodes is performed to improve or facilitate the following processes in analytical chemistry [2]:

- enhance the selectivity of the electrodes;
- avoid the fouling;
- concentrate species;
- improve electrocatalytic properties;
- improve selectivity in complex samples.

For these reasons the electrodes modification allows for applications in many fields. CMEs are commonly employed in electroanalysis because of their own electrocatalytic properties or their ability to immobilize reagents that improve the sensitivity and selectivity of the detection step. Furthermore, CMEs are particular useful in performing trace analysis, since it is possible to preconcentrate the analyte confining it in a small volume near the electrode surface, thus allowing lower concentrations to be measured [3].

Most frequently, the layer coating on the electrode surface is electroactive, so it can exchange electrons with the underlying substrate material being oxidized or reduced.

2.1 Main methods for electrodes modification

Modified electrodes can be prepared according to several different techniques [4]; the main routes to modify the electrode surface are described below.

- **Chemisorption.** Some species attach spontaneously to the surface of the electrode due to their higher affinity with the conductive material than with the bulk solution. A chemical reaction between the surface and the species occurs, due to the strong interaction, leading to new electronic bonds. For example, organic species, such as those containing double bonds, are often hydrophobic and strongly adsorb from aqueous solutions on carbon, graphite or platinum. In these cases the amount adsorbed on the electrode surface is almost a monolayer. Self-assembled monolayers (SAM) of organic molecules are molecular assemblies formed spontaneously on surfaces by adsorption and are organized into more or less large ordered domains [5]. SAMs are created by the chemisorption of a molecular head group onto a substrate due to the strong affinity with it. Commonly head groups are thiols, silanes, phosphonates, etc [6].
- **Physical adsorption.** Organic or organometallic complexes can be physically adsorbed (by van der Waals forces) on porous carbon-based electrodes like glassy

carbon, graphite and pyrolytic graphite by simple coating with non-aqueous solution followed by droplet evaporation. For example, it is possible to obtain a thin film of a polymer on the electrode surfaces by dipping the electrode into a solution containing a dissolved polymer and allowing the solvent to evaporate [7]. In order to produce more uniform films a better method than "dip-coating" is "spin-coating", a technique that consists in the deposition of a drop of coating material on the center of the substrate, which is then rotated at high speed in order to spread the material by centrifugal force.

- **Covalent bonding.** Chemical reactions can be carried out to create bonds between the substrate and a molecule of interest. Electrode materials such as Pt and glassy carbon can be oxidized in order to form hydroxyl groups on the surface [8]. This technique could give rise to a monolayer, but often, when organic molecules are employed, the reaction causes the polymerization and thicker layers are formed.
- **Electrosynthesis.** The electrode modification can be performed also by synthesizing chemical compounds using electrochemical techniques. The main advantages of the electrosynthesis are the selectivity, since it is possible to precisely control the applied potentials, the short deposition times and the possibility to carry out reactions also at low temperature, since the application of a potential can cause the decrease in activation energy.

2.2 Modified electrodes characterizations

A wide range of analytical techniques are frequently used to characterize the modifying materials, among them the most common are X-ray diffraction (XRD), Fourier transform infrared spectroscopy (FTIR), and Raman spectroscopy. The thermal properties of the electrode coatings are commonly studied using thermogravimetry (TG), differential scanning calorimetry (DSC), differential thermal analysis (DTA), while the morphologies are usually observed through scanning electron microscopy (SEM), transmission electron microscopy (TEM) and atomic force microscopy (AFM). Using these techniques it is possible to obtain the direct evidence of the dimension of the particles and of the layer thickness. Among the specific techniques there are electron spin resonance (ESR), nuclear magnetic resonance (NMR), X-ray absorption spectroscopy

(XAS), Mössbauer spectroscopy, UV/VIS spectroscopy, wide and low angle X-rays photoelectron spectroscopy (XPS), energy dispersive spectroscopy (EDX), etc.

The most employed characterization techniques will be described in the next sections.

2.2.1 X-rays diffraction

This technique is probably the most widely used method for solid characterization. The diffraction pattern allows the crystal structure analysis as well as the determination of the crystallite size and distribution. The method is based on the Bragg's law of diffraction which expresses the condition of constructive reflection. Since the energy of a photon is related to its wavelength ($\varepsilon = h \cdot \nu = h \cdot c/\lambda$), photon with energy of 10 to 50 keV are required for the study of crystals. The X-rays are usually emitted during the friction of accelerated electrons or by inelastic excitation of the inner electrons of the target (see scheme in Figure 2.1). From the latter process thin lines are normally obtained, superimposed to a broad emission band, which are used as analytical beam (the most commonly used are the $K\alpha_1$ and $K\alpha_2$ lines of copper). Considering the crystalline material as an infinite recurrence of parallel atoms planes (with interplanar distance d), reflected beams interact constructively only if the Bragg condition ($2d \sin\theta = n\lambda$) is respected (θ is the incident angle, and n must be an integer number). The copper $K\alpha_1$ line corresponds to 1.541 Å. The intensity of a single peak of the pattern expresses the probability of a single diffraction order.

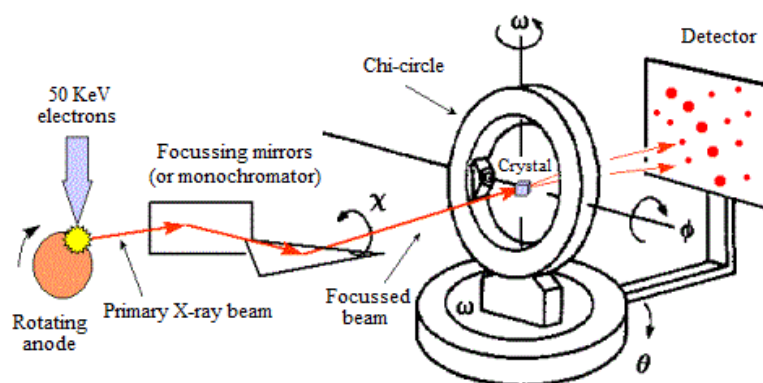


Figure 2.1 – Schematic representation of a XRD apparatus.

The powders method is usually applied for the analysis of a huge number of monocrystals randomly oriented, in a polycrystalline sample. Powder samples show

diffraction patterns with peaks given by the Bragg relationship for each crystal orientation, and, therefore, XRD provides a method to identify crystallographic phases in a sample.

XRD only provides information on the bulk crystals present in the sample. Furthermore, the shapes of the peaks give additional information, and the width is a measure of the amplitude of thermal oscillations of the atoms at their regular lattice sites [9]. The crystallite size is related to the peak broadening, and Scherrer equation explains the phenomena in terms of incident beam divergence which makes it possible to satisfy the Bragg condition for non-adjacent diffraction planes:

$$L = K \lambda / \beta_{1/2} \cos \theta \quad (2.1)$$

where L is the nanocrystallite size, calculated by XRD radiation of wavelength λ (nm) from measuring the full width at half maximum of peaks ($\beta_{1/2}$) in radian located at any 2θ in the pattern [10].

Unfortunately, there are other sources of signal broadening, in addition to instrumental distortion (already taken in account in the Scherrer equation), such as lattice microstrain effects. To overcome these aspects is possible to apply the Warren and Averbach's method which takes into account not only the peak width, but also the shape of the peak. This method is based on a Fourier deconvolution of the recorded peaks and the instrument broadening to obtain the true diffraction profile. Using this approach it is possible to obtain both the average crystallite size and the lattice microstrain using the characteristic averages of any distribution.

As an example, the layered double hydroxides phase can be confirmed by XRD measurement using Ni-filtered Cu-K α radiation with a graphite diffracted beam monochromator. This technique gives information also about the interlayer distance and, hence, about the nature of the interlayer anion originally present or coming from a possible ion-exchange reaction. For example, the interlayer distance when NO $_3^-$ is the charge-balancing anion is about 8.7 Å.

2.2.2 *X-ray absorption spectroscopy*

X-rays have a wavelength ranging from 0.01 to 10 nanometers, corresponding to energies in the range 100 keV to 100 eV. This range of wavelengths values is of the same order of magnitude as atom-atom separation in molecular structures, so XAS is a useful tool to

deduce local structure of atoms. Furthermore, the method leads to a direct determination of the absolute valence of the metal atoms.

X-rays are absorbed by matter giving the photo-electric effect (Figure 2.2). In particular, an X-ray is absorbed by an atom when the energy of the X-ray is transferred to a core-level electron (K, L, or M shell) which is ejected from the atom. The atom is left in an excited state with an empty electronic level (a core hole).

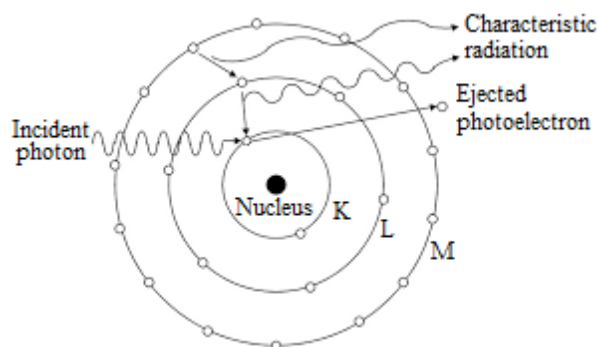


Figure 2.2 – Scheme of X-ray photoelectric effect.

Any excess energy from the X-ray is given to the ejected photo-electron. After the occurrence of the photoelectric effect, the excited core-hole will relax back to a “ground state” of the atom. A higher level core electron drops into the core hole, and a fluorescent X-ray or Auger electron is emitted. X-ray fluorescence and Auger emission occur at discrete energies that are characteristic of the absorbing atom, and can be used to its identification (EDX techniques).

We refer to X-ray fluorescence when an X-ray with energy equal to the difference of the core-levels is emitted and Auger effect when an electron is promoted to the continuum from another core-level.

The principle of XAS measurements is how the absorption coefficient varies with the X-ray energy. The absorption coefficient (μ) depends on the atomic number Z , density ρ , atomic mass A and energy E ($\mu = \rho Z^4/AE^3$). It gives the probability of the absorption of X-rays and is related to the X-ray intensity by Beer’s Law:

$$I_t = I_0 e^{-\mu x} \quad (2.2)$$

where I_0 is the incoming X-ray intensity to the sample, I_t is the intensity transmitted through the sample and x is the sample thickness.

If x is expressed in cm, μ results in cm^{-1} . In this case the equation can be expressed as follows:

$$I = I_0 e^{-\mu_m \rho x} \quad (2.3)$$

where ρ is the atom density expressed in g/cm^3 and $\mu_m = (\mu/\rho)$ is the mass absorption coefficient. It is more convenient to use μ_m since this quantity is not dependent on the physical or chemical state of the element as X-ray absorption is primarily an atomic property.

The absorption coefficient has a characteristic value depending on both the atomic number of the element and on the wavelength of the incident X-ray radiation. The typical trend is shown in Figure 2.3.

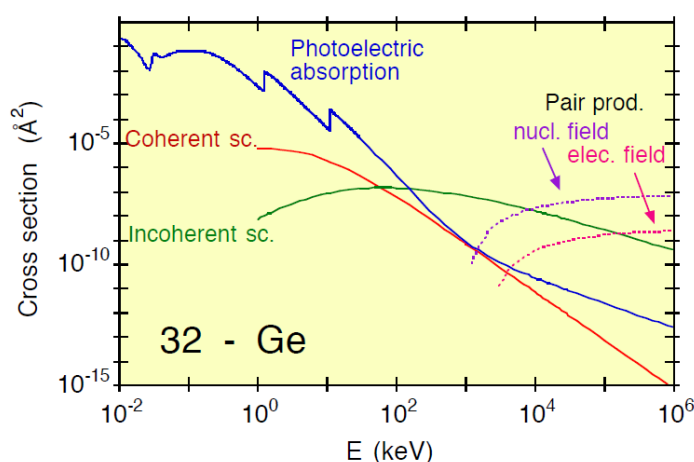


Figure 2.3 – Characteristic trend of mass absorption coefficient (absorption cross section) vs X-ray radiation energy.

The discontinuity of photoelectric absorption values is due to absorption edge. The values of mass attenuation coefficients are dependent upon the absorption and scattering of the incident radiation caused by several different mechanisms such as Rayleigh scattering (coherent scattering), Compton scattering (incoherent scattering), photoelectric absorption, pair production, electron-positron production in the fields of the nucleus and atomic electrons. The photoelectric absorption is dominant for photon energy between a few electronvolts to over 1 MeV in elements with a high atomic number.

The X absorption is expressed in electronvolt (eV). One electronvolt is the amount of energy gained (or lost) by the charge of a single electron moving across an electric potential difference of one volt ($1\text{eV}=1.602 \cdot 10^{-19} \text{ J}$).

XAS is the modulation of the X-ray absorption coefficient at energies near and above an X-ray absorption edge. The explored energy range is divided into two regimes: X-ray Absorption Near-Edge Spectroscopy (XANES), and Extended X-ray Absorption Fine-Structure (EXAFS) which contain related, but slightly different information about a local atomic coordination and oxidation state. In Figure 2.4 is reported as an example, the typical absorption spectrum K edge transitions) of iron.

XANES concerns the features in the XAS of condensed matter due to the photoabsorption cross section for electronic transitions from an atomic core level to final states, in the energy region of 50–100 eV above the selected atomic core level ionization energy, where the wavelength of the photoelectron is larger than the interatomic distance between the absorbing atom and its first neighbor atoms [11].

The EXAFS oscillations result from the interference between the outgoing photoelectron wave and components of backscattered wave from neighboring atoms in the molecule, which starts immediately past an absorption edge and extends to about 1 keV above the edge.

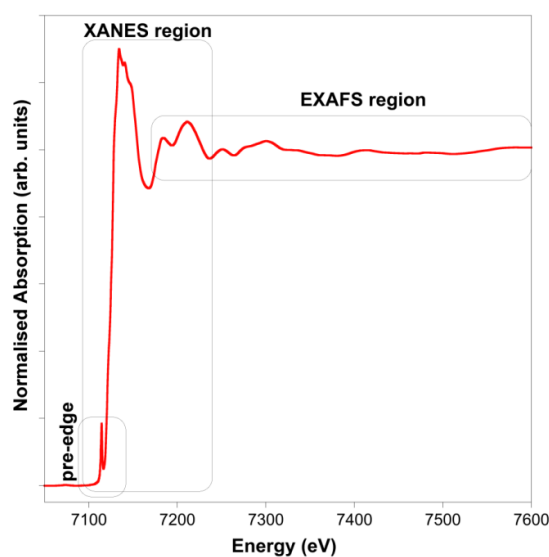


Figure 2.4 – XAS spectrum near-edge of iron. The main regions of the spectra are evidenced.

The general definition for the EXAFS phenomenon, which is the oscillatory portion of the absorption coefficient, is the difference between the observed absorption coefficient μ and the free-atom absorption coefficient μ_0 , normalized by the free-atom contribution.

The XANES spectra describe electronic structure and symmetry of the metal site (numbers, types, and distances to ligands and neighboring atoms from the absorbing element), while EXAFS studies the fine structure in the absorption at energies greater

than the threshold for electron release. These two methods give complementary structural information.

The experimental setup and data acquisition required to perform XAS experiments involve X-rays sources with high energy and with very collimated beams (synchrotron radiations). Synchrotron radiation is the name given to the radiation which occurs when charged particles are accelerated in a curved path or orbit. In Figure 2.5 a schematic image of a synchrotron is shown. The main elements which constitute the apparatus are the bending magnets, which are placed at a number of locations on the ring to guide the beam along the reference path, the wiggler and the undulators magnets, that deflect the electron beam in alternate directions, producing an angular excursion of the beam.

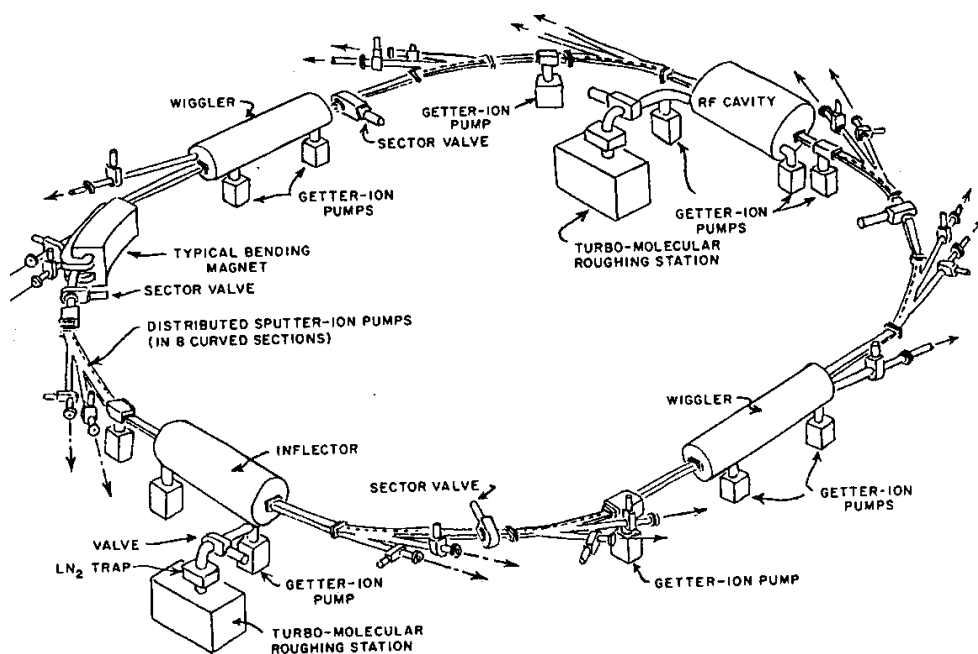


Figure 2.5 – Schematic image of a synchrotron.

Synchrotron radiation emitted by electrons in particle accelerators is extremely intense and extends over a broad energy range from the infrared through the visible and ultraviolet, into the soft and hard X-ray regions of the electromagnetic spectrum.

Due to these and other characteristics, nowadays synchrotron radiation is used to study many aspects of the structure of matter at the atomic and molecular scale, from surface properties of solids to the structure of protein molecules [12].

2.2.3 Scanning electron microscopy

The scanning electron microscopy is an advanced technique derived from the older optical microscopy. Regarding the dualistic nature of wave-particle, electrons possess the optimum wavelength to probe conductive surfaces with a high magnification. The capability of resolving between two points is called ‘resolution’ and it is expressed by the Abbe’s equation (Eq. 2.4) [13].

$$r = \frac{\lambda}{2n \sin \alpha} \quad (2.4)$$

where r is the minimum resolved distance, λ is the illumination wavelength, α is the aperture angle, and n is the refractive index of the considered medium.

According to the De Broglie’s equation:

$$\lambda = \frac{h}{mv} \quad (2.5)$$

where h is Planck’s constant, m is the mass of the electron, and v its velocity of propagation. If the accelerating voltage (V) is equal to 100 keV the electrons possess a wavelength of 0.004 nm. So if the resolution is around 240 μm for an optical microscope, it is 0.002 μm for an electron microscope. In a transmission electron microscope the accelerating voltages are of the MeV order and the resolution is even lower than 0.2 nm, for this reason the SEM images provide surface information. The SEM apparatus is shown in Figure 2.6.

In SEM, a primary electron beam is produced, usually from a cold Field-Emission gun, and focused on a sample and either the secondary or backscattered electrons emitted from the sample, are measured. Other sources of deactivation can also be cathode luminescence, Auger electrons, and characteristic X-rays. Secondary electrons are due to non-elastic collisions between the primary electron beam and the outer electrons of the sample. These electrons are ejected and usually recovered by the objective lens (detectors).

The apparatus is completely under vacuum (10⁻¹¹ torr) and a complex system of electron lens permit both magnification and movement for the topographical analysis.

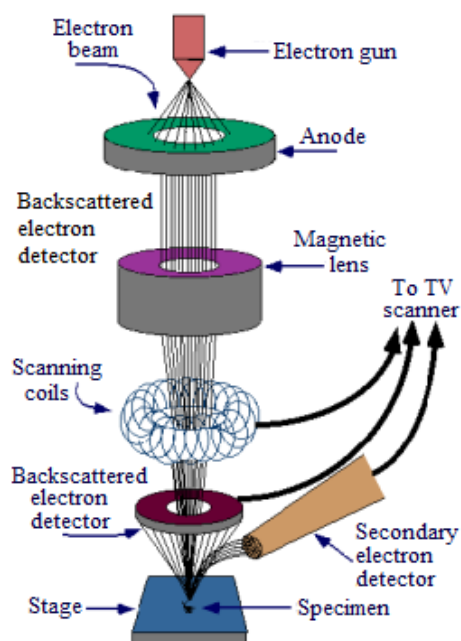


Figure 2.6 – Schematic image of SEM

The backscattered electrons are primary electrons which, conserving the 80 % of the initial energy, through elastic interactions are re-emitted. Because this elastic effect is proportional to the square of the atomic number, usually this information can be used to clarify doubts from the secondary electrons map.

2.2.4 Energy dispersive X-rays analysis

EDX is a semi-quantitative analytical technique useful for the elemental analysis or chemical characterization of a sample, and it is generally coupled with SEM. The analysis is based on the interaction of a source of X-ray excitation and the sample. The number and energy of the X-rays emitted after the collision of the electron beam with the sample can be measured by an energy-dispersive detector. With an internal standard it is possible to obtain the relative abundances of several elements, especially the heaviest ones. This is a powerful method of analysis especially because of its fast data collection.

2.2.5 Atomic force microscopy

The Atomic Force Microscope is more versatile than SEM because it is not necessary any conductivity property from the sample. By using AFM it is possible not only to

obtain an image of the surface with an atomic resolution but also to measure the force at nano-newton scale.

The AFM principles are very simple, the general setup is shown in Figure 2.7. A tip is scanned over a surface with feedback mechanisms that enable the piezoelectric scanners to maintain the tip at a constant force (to obtain height information), or height (to obtain force information) above the sample surface. Tips are typically made from Si_3N_4 or Si, and extended down from the end of a cantilever. Generally the force between the tip and the sample surface is very small, usually less than 10^{-9} N. The detection system does not measure force directly but it records the deflection of the microcantilever. There are many categories of detecting systems for monitoring such a deflection. In the beam-bounce method a diode laser is focused onto the back of a reflective cantilever. As the tip scans the surface of the sample, moving up and down with the contour of the surface, the laser beam is deflected off the attached cantilever into a dual element photodiode. In this arrangement a small deflection of the cantilever will tilt the reflected beam and change its position on the photodetector [14].

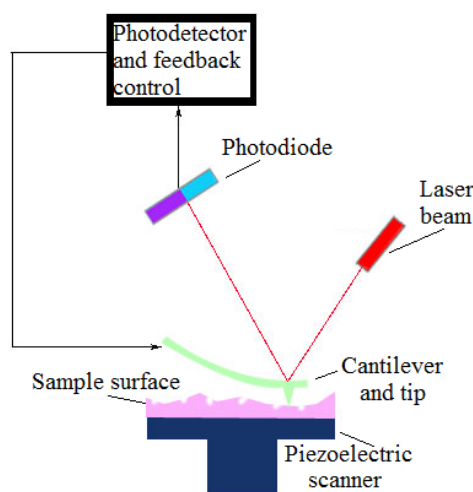


Figure 2.7 – Schematic setup of atomic force microscopy.

The photodetector measures the difference in light intensities between the upper and lower elements, and then converts the difference to voltage. Feedback from the photodiode difference signal, through software controlled by the computer, enables the tip to maintain either a constant force or a constant height above the sample. In the constant force mode the piezo-electric transducer monitors real time height deviation. In the constant height mode the deflection force on the sample is recorded. According to the

interaction of the tip and the sample surface, the AFM can be classified as repulsive or contact mode and attractive or non-contact mode.

The primary information that can be obtained by this instrument is the quantitative measure of the samples surface roughness and also the determination of the coatings thickness.

2.2.6 Electrochemical methods of analysis

The electrochemical measurements on chemical systems involve transport of charge across interfaces between chemical phases. Measuring and controlling the cell potential it is possible to accelerate reactions, according to thermodynamics, or reverse them. Two types of processes occur at those electrodes: one kind involves the movement of charges across the interface causing oxidation or reduction (governed by the Faraday's law); the other one is connected to the structural changes coupled with the change of potential or solution composition. These two phenomena are called Faradaic processes and non-Faradaic processes, respectively.

Electrochemical methods are often used for the assessment of batteries, capacitors and their components. Cyclic voltammetry is useful for a rapid determination of the domain of electroactivity, the redox peak systems, the reversibility and the capacity. In order to study the performances of electrochemical capacitors materials, besides CV, galvanostatic measurements and electrochemical impedance spectroscopy (EIS) are especially useful for the determination of the capacity, cyclability, cell resistance and kinetic parameters. Linear sweep voltammetry using rotating disk electrodes is the most commonly employed technique to study the properties of OER and HOR (hydrogen oxidation reaction) catalysts. In the following sections the mentioned techniques will be briefly described.

2.2.6.1 Cyclic voltammetry

Performing cyclic voltammetry it is possible to study the electrochemical behaviour of a chemical system or a modified electrode. CV is the most widely used technique to gain qualitative information about electrochemical reactions. Using this technique it is possible to rapidly provide considerable information on the thermodynamics of redox

processes and the kinetics of heterogeneous electron transfer reactions and on adsorption processes. In this potentiodynamic electrochemical experiment, as shown in Figure 2.8 A, the working electrode potential is ramped linearly versus time and after the set potential is reached, the working electrode's potential is ramped in the opposite direction to return to the initial value [15]. The current at the working electrode is plotted versus the applied voltage to give the cyclic voltammogram trace (Figure 2.8 B).

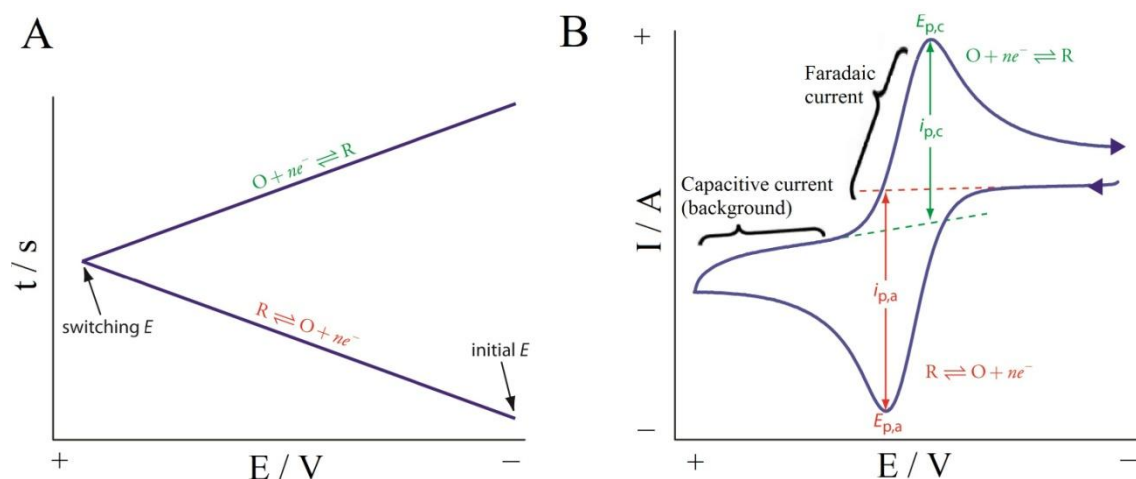


Figure 2.8 – A) Applied potential vs time, B) typical cyclic voltammogram recorded in the presence of electroactive species.

If a species is initially present in a reduced form (R), as the applied potential approaches the characteristic E° for the redox process, an increased anodic current is recorded until a peak is reached ($E_{p,a}$). After traversing the potential region in which the oxidation process takes place, the direction of the potential sweep is reversed. During the reverse scan, the oxidized molecules (generated in the forward half-cycle, and accumulated near the electrode surface) are reduced back to R, resulting in a cathodic peak ($E_{p,c}$).

Some applications will be reported in the results and discussion section.

2.2.6.2 Capacitance and charge

The electrodes for which no net charge transfer occurs across the solid-solution interface, are called ideally polarizable electrodes, but this is just an ideal behaviour. In a limited potential range, some electrodes can approach this ideal polarizability. Since no charge passes the electrode-solution interface, it is analogous to a capacitor. For an ideal capacitor, the charge (q) is directly proportional to the potential difference:

$$C = q/E \quad (2.6)$$

where C is the capacitance (in Farads, F), specifically, the ratio of the charge stored to the applied potential.

During this process a charging current will flow. In the case of solutions the charge carried by an array of charged species and oriented dipoles, generates the so called electrical double layer, usually divided in an inner layer (the compact layer or Helmholtz layer) and an outer layer (called the outer Helmholtz layer).

The centres of specifically adsorbed ions constitute a compact layer which is called the inner Helmholtz plane, whereas the centres of nearest solvated ions (species which are not able to overcome the energetic barrier necessary to lose their solvation shell) generate the so called outer Helmholtz plane. The charge density involved in these two layers is equal and opposite to the local excess of charge density in the electrode. Of course the thickness and the structure of these layers depend on the solution characteristics and, once defined the reciprocity, depends even on the surface which has generated it. A solution can be approximated by the electrical circuit of a resistor, R_s , and a capacitor, C , representing the double layer, in series. According to physics the behaviour of the current, i , in the time, t , when applying a potential step of magnitude E is [16]:

$$i = \frac{dq}{dt} = \frac{E}{R_s} e^{-t/RC_{dl}} \quad (2.7)$$

By recording linear scan voltammograms at different scan rates, and plotting the charging current (at a given potential) versus the scan rate, one would obtain a straight line, with a slope corresponding to $C_{dl}A$. When Faradaic processes are permitted, reactions occur at the electrode so the current can flow beyond the simple charging process. The net resultant is the $i = f(E)$.

2.2.6.3 Galvanostatic charge-discharge experiments

Galvanostatic techniques are suitable for the characterization of supercapacitors. Charge-discharge measurements are critical for the analysis of the active materials performance under practical operating conditions. The working electrode is submitted to a constant current and voltage vs time is recorded between fixed potential values. The main parameters obtained from this experiment are the capacity of the electrode, the change of potential in function of the state of charge, the cyclability and the estimation of the ohmic

drop. A pure capacitive behaviour leads to the same charge-discharge times. Otherwise, an irreversible Faradaic reaction occurs. Galvanostatic curves are often recorded at current densities between 0.5 and 20 mA cm⁻².

Long term cycling is often employed to test the cycling stability and Faradaic efficiency over long periods of time. This kind of measurements is considered more reliable than CV for the determination of capacitance during charge and discharge because the current can be kept rigorously constant and the time can be evaluated with accuracy.

2.2.6.4 Polarization curves

The so-called polarization curves are a particular case of linear sweep voltammetry (LSV) [17]. These techniques record the current vs potential trend under steady state conditions, at very slow sweep rates and in a potential region very close to the equilibrium potential for the reaction of interest. In these conditions a reversible (Nernstian) system is at equilibrium and the interface is governed only by thermodynamic aspects. In these cases i-E curves are useful for obtaining thermodynamic properties such as standard potentials, free energies of reaction and equilibrium constants.

The Butler–Volmer equation can be written in terms of the exchange current [18]:

$$i = i_0 e^{-\alpha n F \eta / RT} - e^{(1-\alpha) n F \eta / RT} \quad (2.8)$$

where $\eta = E - E_{eq}$ is the overvoltage (*i.e.*, the extra potential beyond the equilibrium value leading to a net current i). The overvoltage is always defined with respect to a specific reaction, for which the equilibrium potential is known. Equation 2.8 can be used for extracting information on i_0 and α , which are important kinetic parameters.

When the equilibrium is reached, no net current flow is detected so we have to recall two kinds of approximation [18]: linearization at high overpotentials and linearization at small overpotentials.

a) Linearization at large overpotential (Tafel behaviour)

For sufficiently large overvoltages ($\eta > 118\text{mV}/n$), one of the exponential terms in Eq. 2.8 is negligible compared to the other. For example, at large negative overpotentials, $i_c \gg i_a$ and Eq. 2.8 becomes:

$$i = i_0 e^{\frac{-\alpha n F \eta}{RT}} \quad (2.9)$$

hence, we get:

$$\ln i = \ln i_0 - \alpha n F \eta / RT \quad (2.10)$$

This logarithmic current–potential dependence was derived by Tafel, and is known as the Tafel equation. By plotting $\log i$ against η it is possible to obtain the Tafel plots for the cathodic and anodic branches of the current–overvoltage curves. Such plots are linear only at high overpotential values; severe deviations from linearity are observed as η approaches zero. Extrapolation of the linear portions of these plots to the zero overvoltage gives an intercept, which corresponds to $\log i_0$; the slope can be used to obtain the value of the transfer coefficient α . Another form of the Tafel equation is obtained by rearrangement of Eq. 2.10:

$$\eta = a - b \log i \quad (2.11)$$

with b , the Tafel slope, having the value of $2.303RT/\alpha nF$. For $\alpha = 0.5$ and $n = 1$, this corresponds to 118 mV (at 25°C).

From the Tafel slope we can extract information about the mechanism of reaction (if the electrochemical step is before the rate determining step), and sometimes information about the involved chemical steps (*i.e.*, the adsorption/desorption, if there is any).

Equation 2.11 indicates that the application of small potentials (beyond the equilibrium potential) can increase the current by many orders of magnitude. In practice, however, the current could not rise to an infinite value because of the restrictions imposed by the rate at which the reactant reaches the surface.

b) Linearization at Small overpotential

For small departures from E° , the exponential term in Eq. 2.9 may be linearized:

$$i = i_0 n F \eta / RT \quad (2.12)$$

which shows that the net current is linearly related to overpotential in a narrow potential range near E_{eq} (the ratio η/i has the dimensions of a resistance and is often called the charge transfer resistance R_{ct} ; when the reaction has very high k^0 this resistance approaches zero). Hence, the net current is directly proportional to the overvoltage in a narrow potential range near E° .

2.2.6.5 Rotating disk electrode

Let's consider an overall electrode reaction $O + ne^- = R$ composed of a series of steps. It causes the conversion of the dissolved oxidized species to a reduced form. The current is governed by the rates of processes as:

- a) Mass transfer
- b) Electron transfer
- c) Chemical reactions preceding or following the electron transfer
- d) Other surface reaction, such as adsorption, desorption, velocity profiles as a function of rotation rates, solution viscosities, and densities.

It is possible to carry out electrochemical measurements under defined mass-transport conditions using a rotating disk electrode (RDE) which induces a forced convective mass-flow into the electrolyte.

The RDE consists of a smooth circular electrode embedded in an insulator. The electrode surface normal, z , denotes the rotation axis. While rotating the electrode acts like a pump, that draws the electrolyte solution from the bulk to its surface and propels it outwards radially, following the streamlines shown in Figure 2.9. The knowledge of the velocities in vertical and radial directions allows for the determination of the mass-transport rate to the disk surface through a diffusion layer with thickness, δ_{RDE} , calculated according to [19]:

$$\delta = 1.61D^{1/3}\omega^{-1/2}\nu^{1/6} \quad (2.13)$$

where ν , D and ω denote the kinematic viscosity of the electrolyte, the diffusion coefficient of the reactant in the electrolyte, and the angular velocity or rotation rate of the electrode (in rad/s), respectively. According to the previous equation the thickness of the RDE diffusion layer only depends on the rotation rate, in contrast to the diffusion layer thickness of a stationary electrode, which grows with time into the electrolyte until natural convection becomes the controlling one. Therefore, the thickness of the diffusion layer for a RDE is roughly one or two orders of magnitudes smaller than for a stationary electrode.

The limiting current (for a reversible system) is proportional to the square root of the angular velocity, as described by the Levich equation [14]:

$$i_l = 0.62nFAD^{2/3}\omega^{1/2}\nu^{-1/6}C \quad (2.14)$$

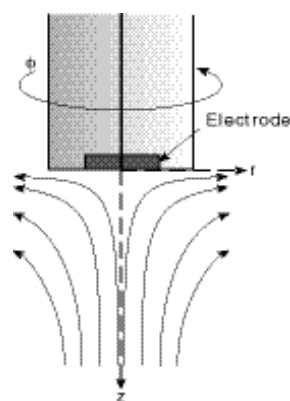


Figure 2.9 - Sketch of a rotating disk electrode with the schematic streamlines (side view) in the electrolyte. Z denotes the rotation axis.

When working with low reactant concentrations the time-independent small diffusion layer thickness for a RDE results in increased and constant current densities compared to stationary electrodes.

Overall, the RDE provides an efficient and reproducible mass transport and, hence, analytical measurements can be made with high sensitivity and precision. Such well-defined behaviour greatly simplifies interpretation of the measurement. The convection induced by the electrode results also in very short response times.

This kind of electrode was used for the experimental determination of the onset potential related to the layered double hydroxides modified electrodes when tested as OER catalysts.

2.2.6.6 Electrochemical quartz crystal microbalance

Electrochemical quartz crystal microbalance (EQCM) is a powerful tool for studying interfacial reactions based on the simultaneous measurement of electrochemical parameters and mass changes at the electrode surface. The principle is based on the piezoelectric properties of a slice of quartz crystal wafer which is sandwiched between two electrodes (Figure 2.10) that apply an oscillating electric field, resulting in a standing wave within the wafer and in mechanical oscillation at resonant frequencies (generally in the range from 2 MHz to 20 MHz). Such a field produces a mechanical oscillation in the bulk of the wafer. Surface reactions, involving minor mass changes, can cause perturbation of the resonant frequency of the crystal oscillator. The bare quartz crystal has a particular mechanical resonant mode depending upon its size and thickness, and it

oscillates at a frequency, f_0 , when a sinusoidal electrical signal of this frequency is applied to the gold contacts.

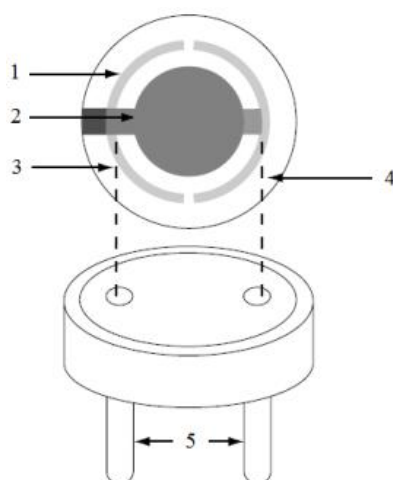


Figure 2.10 - Quartz crystal microbalance: (1) the quartz crystal, (2) the Au or Pt electrode, (3 and 4) connecting metal wires, (5) the base.

Typical quartz crystals used in EQCM experiments have a 1.37 cm^2 area and $f_0 = 5 \text{ MHz}$. At this frequency a mass change of 18 ng cm^{-2} of an electrode causes a frequency change of 1 Hz, a resolution attainable with good frequency counters. The frequency change (Δf) relates to the mass change (Δm) according to the Sauerbrey equation [17]:

$$\Delta f = -2\Delta m n f_0^2 / A \sqrt{\rho \mu} = -C_f m \quad (2.15)$$

where n is the harmonic number of the oscillation (*e.g.*, $n = 1$ for 5 MHz crystal), f_0 the base resonant frequency of the crystal (prior to the mass change), A is the area (cm^2), μ is the shear modulus of quartz ($2.95 \times 10^{11} \text{ g cm}^{-1} \text{ s}^{-1}$), and ρ is the density of quartz (2.65 g cm^{-3}). C_f is the sensitivity factor for the crystal used. As expected from the negative sign, decreases in mass correspond to increases in frequency and *vice versa*. The EQCM is very useful for probing processes that occur uniformly across the surface. Numerous surface reactions have been investigated, including deposition or dissolution of surface layers and various uptake processes (such as doping/de-doping of conducting polymers or ion exchange reactions). Such changes can be probed using various controlled-potential or controlled-current experiments. In these experiments, one of the electrodes is employed as working electrode in the electrochemical cell, to allow simultaneous frequency and current measurements.

REFERENCES

- [1] R.W. Murray, A.G. Ewing, R.A. Durst. *Anal. Chem.* 59 (1987) 380A.
- [2] R.W. Murray, J.B. Goodenough, W.J. Albery. *Phil. Trans. R. Soc. Lond. A* 302 (1981) 253.
- [3] S.V. Prabhu, R.P. Baldwin, L. Kryger. *Electroanalysis* 1 (1989) 13.
- [4] A.J. Bard. *J. Chem. Edu.* 60 (1983) 302.
- [5] D.K. Schwartz. *Annu. Rev. Phys. Chem.* 52 (2001) 107.
- [6] D. Mandler, I. Turyan. *Electroanalysis* 8 (1996) 207.
- [7] D. Dicu, L. Muresan, I. C. Popescu, C. Cristea, I. A. Silberg, P. Brouant. *Electrochim. Acta* 45 (2000) 3951.
- [8] A.J. Downard. *Electroanalysis* 12 (2000) 1085.
- [9] H.P. Klug, L.E. Alexander, *X-ray Diffraction Procedures for Polycrystalline and Amorphous Materials*, 1974, Wiley–Interscience, New York.
- [10] A. Monshi, M.R. Foroughi, M.R. Monshi. *World J. Nano Sci. Eng.* 2 (2012) 154.
- [11] D.C. Koeningsberger, R. Prins, *X-ray Absorption: principles, applications and techniques of EXAFS, SEXAFS and XANES*, 1988, Wiley.
- [12] D. Norman. *J. Synchrotron Rad.* 8 (2001) 72.
- [13] C.W. Oatley, W.C. Nixon, R.F.W. Pease. *Adv. Electronics. Electron. Phys.* 21 (1965) 181.
- [14] N. Yao, Z.L. Wang, *Handbook of microscopy for nanotechnology*, 2005, Springer Science & Business.
- [15] D.C. Harris, *Quantitative Chemical Analysis*, 2007, Seventh Edition, W.H. Freeman and Company, California.
- [16] C.G. Zoski, *Handbook of Electrochemistry*, 2007, Elsevier, First Edition, Amsterdam.
- [17] J. Wang, *Analytical Electrochemistry*, 2006, Third Edition, John Wiley & Sons, Inc., Hoboken, New Jersey.
- [18] P. Monk, *Fundamentals of Electroanalytical Chemistry*, 2001, Second Edition, John Wiley & Sons Ltd, England.
- [19] A.J. Bard and Larry R. Faulkner, *Electrochemical Methods - Fundamentals and Applications*, 2001, Second Edition, John Wiley & Sons, Phoenix.

3. LAYERED DOUBLE HYDROXIDES (LDHs)

The natural mineral hydrotalcite belongs to the class of materials of layered double hydroxides and for this reason LDHs are also known as hydrotalcite-like compounds (HTLCs). The natural hydrotalcite, which was discovered in Sweden around 1842, is a hydroxycarbonate of magnesium and aluminum and can be considered a prototype of this class of materials. The correct formula for hydrotalcite, $[\text{Mg}_6\text{Al}_2(\text{OH})_{16}\text{CO}_3 \times 4\text{H}_2\text{O}]$, was suggested by Manasse, who was the first who realized that carbonate ions were an essential feature of the mineral [1].

3.1 Structure

LDHs are a class of layered materials having a structure closely related to brucite ($\text{Mg}(\text{OH})_2$), which consists in Mg^{2+} ions octahedrally surrounded by six OH^- ions. The octahedral units share edges to form an infinite 2D layer and the layers stack on the top of one another forming the three-dimensional structure. An LDH can be obtained by the substitution of a fraction of the divalent cations in the brucite layer with trivalent cations. The resulting structure, shown schematically in Figure 3.1 consists of a positively charged brucite-like layers and the charge is balanced by the intercalation of anions in the interlayer region. The chemical composition of LDHs is generally expressed by the following formula $[\text{M}(\text{II})_{1-x}\text{M}(\text{III})_x(\text{OH})_2]^{x+}(\text{A}^{n-})_{x/n} \times y\text{H}_2\text{O}$, where, M(II) is a divalent cation, M(III) represents a trivalent one, A is the interlayer anion, n is the charge of the interlayer ion, x represents the molar ratio $[\text{M}(\text{III})/(\text{M}(\text{II})+\text{M}(\text{III}))]$ and y is the number of water molecules located in the interlayer region [2,3]. Both inorganic and organic anions can be introduced among brucitic layers by ion exchange or during the precipitation.

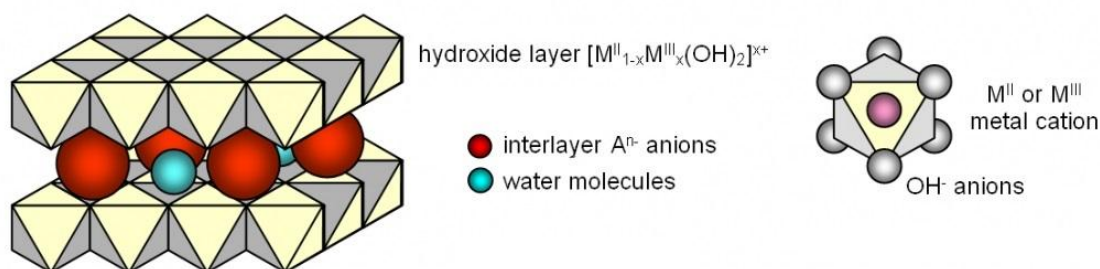


Figure 3.1 - Structure of a Layered Double Hydroxide.

LDHs may be synthesized with a wide range of compositions varying M(II) and M(III) cation combinations and also inserting different anions in the interlayer. By virtue of this opportunity materials with widely tunable properties can be obtained. Concerning the cations, the only restriction is the size of the radius since only M(II) and M(III) ions having ionic radii not too different from those of Mg^{2+} and Al^{3+} , respectively, may be accommodated in the octahedral sites of the brucite-like layers to form LDH compounds [4]. For this reason, the positively charged layers are constructed employing divalent cations such as Ni^{2+} , Mg^{2+} , Ca^{2+} , Mn^{2+} , Co^{2+} , Cu^{2+} or Zn^{2+} and as trivalent cations Al^{3+} , Co^{3+} , Fe^{3+} or Cr^{3+} . The cations which are too small or too large give rise to other types of compounds. Furthermore, the most reliable molar fraction $M(III)/(M(II)+M(III))$, in order to have a LDH structure, corresponds approximately to stoichiometric values between 0.2 and 0.4 [5]. The intercalated anions are typically carbonate (CO_3^{2-}), but other common anions are SO_4^{2-} , OH^- , F^- , Cl^- , Br^- and NO_3^- [6]. Therefore, the LDH structures are attractive for use in electrochemical processes since they are highly accessible to electrolytes by anion exchange (on the basis of this peculiarity they are also called anionic clays).

Due to the possibility to insert cations which can undergo a redox reaction within a certain range of potential and the peculiar property of fast and easy exchange of interlayer anions, LDHs are attracting for applications in many fields of research such as catalysis, photochemistry, polymer additives, drug carriers for many different pharmaceutically active compounds, and electrochemical applications (sensors based on chemically modified electrodes, biosensors, energy storage devices, etc). LDHs can be synthesized according to many different methods; the main synthesis strategies and the applications will be illustrated in the following paragraphs.

3.2 Synthesis methods

Several synthetic techniques have been developed and reported in literature for LDHs preparation. The most commonly employed are the simple coprecipitation and hydrothermal methods, but other methods include urea hydrolysis, glycine assisted hydrothermal synthesis, topochemical oxidation and reconstruction, which is based on the so-called “memory effect”. Furthermore, some other synthetic approaches such as

microemulsion method and electrochemical synthesis have been successfully employed. In the following the methods will be briefly described.

3.2.1 Coprecipitation at a constant pH

This synthesis is one of the most commonly employed and consists in the following procedure [7]: typically the solutions of two different metal salts (commonly nitrates or chlorides) are prepared with a total cationic concentration of 0.1 M in order to keep a constant M(II)/M(III) ratio of about 2-3. The solution is then added dropwise to an aqueous solution containing organic guest species. Throughout the addition, the pH is maintained constant at a value of ~9 by the simultaneous addition of a 0.2 M NaOH solution in order to induce the co-precipitation. The reaction is carried out under N₂ atmosphere to avoid carbonate contamination, with vigorous stirring. The addition of the salts solution is completed within about 3 hours and then the suspensions is immediately centrifuged at 4500 rpm without any ageing in order to quench the crystal growth and, therefore, obtain small platelets. The solids recovered by centrifugation are washed a few times with deionized water and dried in air at 30°C overnight.

Otherwise, in order to obtain bigger particles, the precipitate is aged at room temperature for 24 h, filtered, washed carefully with decarbonated water and finally dried under vacuum.

3.2.2 Urea hydrolysis method

Urea has a number of unique properties such as its very weak Brønsted base characteristic ($pK_b = 13.8$), high solubility in water, and a hydrolysis rate that can be easily controlled, making it an attractive agent to precipitate several metal ions as hydroxides or as insoluble salts in the presence of a appropriate anion. The hydrolysis of urea consists in two steps, the formation of ammonium cyanate (rate determining step) and the fast hydrolysis of the cyanate to ammonium carbonate:



The acid-base reactions of ammonium and carbonate to give ammonia and hydrogen carbonate lead to a pH of about 9, depending on the temperature. This pH is suitable for precipitating a large number of metal hydroxides. Costantino *et al.* [8] investigated the best conditions in terms of temperature, total metal cations concentration, molar fraction Al/Al+M(II) and molar fraction urea/M(II)+Al to prepare Mg, Zn or Ni/Al-carbonate LDHs by this method.

A well crystalline LDH phase can be prepared in a relatively short time using the homogeneous precipitation method based on urea hydrolysis, dissolving solid urea in an aqueous solution of the chosen metal chlorides to give the chosen urea to ion ratio [9]. The precipitation of the LDH is achieved by thermal hydrolysis of urea with formation of ammonium carbonate. The obtained solid is separated from the mother solution, washed with deionized water and 0.1 M sodium carbonate in order to exchange residual chloride ions incorporated during the synthetic procedure, with carbonate anions. Eventually, the solid is dried at room temperature overnight.

Alternatively, the so obtained precipitate can be submitted to a hydrothermal treatment, at 90 °C for 24-48 hours at pH 9.

The compounds prepared using this method display homogeneous sizes and platelet-like primary particles with well-defined hexagonal shapes, which may be very interesting from the viewpoint of nanotechnology since LDHs provide nano-size two-dimensional spaces for the creation of functional materials.

3.2.3 Hydrothermal method

The hydrothermal method is usually employed when organic guest species with low affinity for LDHs are required to be intercalated into the interlayers or when the anion-exchange reactions or the coprecipitation using soluble metal salts cannot be applied. This method is particularly interesting because only the desired organic anions can occupy the interlayer space under the hydrothermal condition since insoluble hydroxides are used as precursors and no other competing species are present [10].

The following is a typical synthetic procedure: the hydroxides precursors and the organic species are mixed and stirred in de-ionized water at room temperature. Then the suspension is transferred into an autoclave and heated at 100-150 °C for a few days. The

solid precipitate is collected by filtration using a membrane filter and subsequently washed with ethanol.

The hydrothermal synthesis is particularly useful when LDH-like materials are prepared using powders as starting materials and it has been found out that the temperature influences the crystal structure of the resulting material. Structures synthesized at different temperatures, despite having identical main layers, show a different arrangement of water molecules and carbonate groups forming the interlayer region.

3.2.4 Glycine assisted hydrothermal synthesis

LDHs are usually prepared by glycine assisted hydrothermal method, according to the following procedure [11]. In a typical experiment, glycine ($\text{NH}_2\text{CH}_2\text{COOH}$; $\text{pK}_{\text{a}1} = 2.3$, $\text{pK}_{\text{a}2} = 9.6$) and sodium sulfate are dissolved in a solution of $\text{Ni}(\text{NO}_3)_2$ and $\text{Al}(\text{NO}_3)_3$ in a fixed molar ratio. After a few minutes of stirring a clear green solution is obtained. Then 5 M NaOH is added under stirring, to induce a pH increase from ~ 3.5 to ~ 13.5 . Afterward, the solution is transferred into an autoclave and heated at $120\text{ }^\circ\text{C}$ for 24 h. After the hydrothermal treatment, the autoclave is allowed to cool to room temperature, the resulting precipitate is recovered by centrifugation, and the supernatant is removed. There is no change in the solution pH before and after the hydrothermal treatment. The precipitate is then washed a few times with de-ionized water and dried at room temperature.

Depending on the reactants ratio in this method (the metal salt and the glycine amounts) it is possible to obtain different shapes and sizes of the particles.

3.2.5 Topochemical oxidation

Taking the example of a Co-based LDH, through a topochemical oxidative reaction under air, a $\beta\text{-Co}(\text{OH})_2$ brucite-like structure can be converted into a monometallic Co(II)/Co(III)- CO_3 layered double hydroxide [12].

The synthesis of the LDH consists in the partial oxidation of $\beta\text{-Co}(\text{OH})_2$ and is carried out for 60 hours at $40\text{ }^\circ\text{C}$, in 0.5 M NaOH. The modification of the electrodes can be performed by casting the colloidal suspension and drying it at ambient temperature obtaining stable and homogeneous films.

3.2.6 Reconstruction method

Another common method to produce LDHs is rehydration/reconstruction using the structural “memory effect”. This method involves calcination of LDHs to remove the interlayer water, interlayer anions, and structural water, resulting in mixed metal oxides. It is interesting to note that the calcined LDHs are able to regenerate the layered structure when they are exposed to water and anions [13]. Again in addition, the included anions do not need to be the same species originally present in the interlayer of the uncalcined LDHs, and, therefore, this is an important method to synthesize LDHs with the desired inorganic or organic anions in order to accomplish specific application requirements [14]. Metal salts are calcined at 500°C for 4 h, under nitrogen, at a heating rate of 5 °C/min. The solid is then added to a solution containing decarbonated water with the guest molecule. The desired pH value (7-8) is adjusted by adding NaOH. Then, the precipitate is aged at room temperature, filtered, washed with decarbonated water thoroughly, and finally dried under vacuum.

3.2.7 Microemulsion method

Colloidal aqueous dispersions of LDHs can be prepared by the double-microemulsion method according to literature data [15]. This method utilizes two water-in-oil microemulsions containing cetyl trimethylammonium bromide as surfactant, n-butanol as cosurfactant and isooctane as oil phase, mixed together. One solution contains the reactants M(II) and M(III) salt precursors in aqueous phase and the other one a precipitating agent such as NH₃. In this case, the intermicellar exchange of solutes is essential to the formation and precipitation of the product.

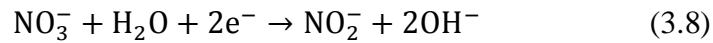
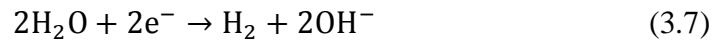
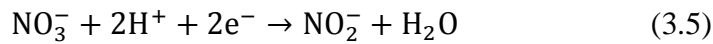
3.2.8 Electrochemical synthesis

The electrodeposition of LDHs is an appealing route of synthesis since it allows the simultaneous synthesis and modification of the electrode surface [16]. The electrochemical synthesis can be performed starting from a solution containing the nitrate salts of the metal M(II) and M(III) in a proper molar ratio and KNO₃ as supporting

electrolyte, then a cathodic potential is applied for a fixed time, usually between 30 and 90 seconds [17].

The method is based on the electrochemical production of hydroxide anions necessary to induce the LDH precipitation on the electrode surface by the cathodic reduction of nitrate ions [18].

During the cathodic reduction of nitrates the following reactions occur near and on the electrode surface, leading to the disappearance of H^+ and to the generation of OH^- , and contribute to the precipitation of the LDH.



Recently, it has been proved that a pre-treatment of the Pt electrodes can lead to a more adherent film and avoids the addition of KNO_3 as further nitrates source [19]. On the activated Pt surface the LDH films are electrodeposited by cathodic reduction of a freshly prepared 0.03 M solution containing M(II) and M(III) at a molar ratio of 3:1. After performing the modification, the electrode is immediately rinsed with bi-distilled water in order to avoid the dissolution of the LDH due to the local acidity.

3.3 LDH modified electrodes applications

LDHs have been studied for their potential use in a wide range of important areas, *i.e.* catalysis, biomedical science, and environmental applications [20-22]. For example, LDHs have been applied for the catalysis of acid–base processes, for the production of basic chemicals [23], and for the catalysis of redox processes [24]. Furthermore, LDHs have demonstrated to be suitable materials for applications in photochemistry and photocatalytic degradation of toxic compounds has been reported [25,26]. LDHs have

also been investigated for their use to prevent metal alloys corrosion [27] and as reinforcing materials in nanocomposite polymers [28]. In medical applications, LDHs have been studied as components in pharmaceutical formulations and in the development of new delivery systems [29]. Moreover, LDHs have been used as heat stabilizing and UV absorption additives in polymers [30,31], flame retardants [32,33] and precursors to magnetic materials [34].

In the next paragraphs the most important fields of LHDs application will be discussed.

3.3.1 Biochemical and medical applications

Many of the divalent and trivalent metal cations which can form LDHs have low toxicity. Mg/Al LDHs are most frequently used as a LDH-based drug carrier and further studies have also been carried out with Zn/Al LDHs. Novel biohybrids of LDHs and biomolecules are designed and organized on nanometer scale to provide opportunities for reservoir and delivery carriers of functional biomolecules in gene therapy [35] and drug delivery since LDHs can act as inorganic vectors. Negatively charged biomolecules intercalated in the gallery spaces would gain more stabilization energy due to the electrostatic interaction with the cationic brucite-like layers [36]. Such biomolecules incorporated between hydroxide layers can be intentionally dissolved in an acidic media, which offers a way of recovering encapsulated or intercalated biomolecules [37].

Hosting of biologically active molecules inside LDHs can protect host from degradation. The addition of LDHs to a solution of a chosen pharmaceutical in water at room temperature results in intercalation of these molecules between the layers. LDHs are able to swell up to 20 Å in order to accommodate new guest molecules. Additionally, hosting of a negatively charged species could provide improved ways of drugs and genetic material to be introduced into cells [29]. If ingested, biomolecules-LDH nanohybrid can move across mucous membrane of intestine into bloodstream. Neutral hybrids can then enter cells by moving across negatively charged membrane without repulsive electrostatic interactions that would be experienced by the guest anions alone. Once inside the cell, LDH is broken down by lysosomes resulting in the release of intercalated molecules. These features will allow LDHs to be applied as new drug or gene carriers if transfer efficiency of biohybrids to target organs or cells is proved. It has been

demonstrated that hybridization between cationic layers and anionic biomolecules greatly enhances transfer efficiency of biomolecules to mammalian cells or organs [38].

It will be possible to control the point of release and pharmacokinetic profile by selection of metal ions in host layers. Drugs like Ibuprofen, Naproxen, 2-Propylpentanoic acid have been reversibly intercalated into LDHs [39] and LDHs containing magnesium and aluminum have already been used as antacid and antipepsin agents due to their basic properties and biocompatibility [40]. Antacid performance and pH stability is controllable by choosing the metal inside the layers, which restricts molecular interactions and dynamics and should improve long-term stability. For example antacids products such as TalcidTM and AltacitetmTM contain $[\text{Mg}_6\text{Al}_2(\text{OH})_{16}]\text{CO}_3$.

Furthermore, layered double hydroxides show beneficial properties in the controlled release of different types of drugs [41]. It is generally observed that suspending a drug LDH-hybrid system in aqueous solutions, the release of the drug undergoes a two step process. First, a rapid release occurs, and secondly a slow one, usually related to the anionic exchange with anions of the medium. For this reason, a number of cardiovascular, anti-inflammatory agents, being either carboxylic acids or their derivatives, could be by ion exchange intercalated into a LDH, to have a controlled release [42]. In vitro studies show that the drug is released by a de-intercalation process due to its exchange with ions present in dissolution medium [43]. Kinetic analysis shows the importance of diffusion through particles in controlling drug release rate. Hence, reversible intercalation of a number of active cardiovascular and anti-inflammatory agents into LDHs can lead to novel tunable drug delivery systems. At the present time, it has been reported even anticancer drug therapy using LDHs [44].

3.3.2 Environmental applications

As in the recent decades the environmental pollution has emerged as an important issue, the application of LDHs to remove environmental contaminants has become more and more interesting. Thanks to the relatively weak interlayer bonding of LDHs, these materials exhibit excellent ability to capture organic and inorganic anions.

LDHs have been evaluated and successfully used to bind and remove, by the process of adsorption and ion exchange, inorganic contaminants such as oxyanions (phosphates [45], arsenates [46], arsenites, iodides [47], dichromates [48], selenites [49], selenates,

borates [50], nitrates [51], *etc.*) and monoatomic anions [52,53] (*e.g.* fluoride, chloride, bromide, and iodide) from aqueous solutions. In addition to these applications, calcined LDHs have been used to concentrate anions in aqueous solutions as a result of reconstruction [54].

However, because of their strongly hydrophilic surface, LDHs seem to be less effective in binding hydrophobic organic compounds, such as phenols or pesticides. To adsorb organic pollutants in aqueous environments is commonly employed activated carbon, but this process is very expensive. To enhance the application of LDHs for processing aqueous contaminants, intercalating anionic surfactants can induce a more hydrophobic character to their surface and increase their sorptive capacity for organic pollutants [55].

While extensive studies on the adsorption behaviour of anion pollutants onto LDHs have been conducted, only little information is available on the use of LDHs as adsorbents for heavy metals. Among the main conventional techniques used for heavy metals removal from aqueous solutions, adsorption is generally considered to be one of the most frequently used and promising techniques due to its low cost, easy operation, high efficiency, simplicity of the equipment and easy regeneration. The adsorbent species should have high surface areas and more binding sites are required. Using LDHs as adsorbent material, beside the chelation with the functional ligand in the interlayer, the adsorption mechanisms of metal cations include the precipitation of metal hydroxides or insoluble metal carbonates on the surface of the LDH, and the adsorption or surface complexation through bonding with surface hydroxyl groups of the LDH [56]. As an example, in literature a Mg/Al-CO₃ LDH was studied as adsorbent for easy Cd(II) removal and a Fe₃O₄/Mg/Al-CO₃ LDH was synthesized in order to introduce magnetic properties to the adsorbent, so enhancing the final separation of the powdered adsorbent from the suspension, using an external magnetic field [57].

3.3.3 *Detection*

Amperometric sensors and biosensors based on electrodes modified with LDHs represent one of the most interesting and relevant applications in the field of analytical chemistry.

3.3.3.1 Electrocatalysis and sensors

The use of LDHs containing electroactive transition bivalent metals (Co, Ni, Mn) in the field of amperometric sensors, arises from their conductive character and is based on the occurrence of a redox reaction involving the bivalent metal itself in a suitable potential window, in basic solution [58]. Such LDHs are able to enhance charge transport within the clay structure by using acceptor/donor sites in the lattice as relays to transfer electrons from the intercalated ions to the conductive substrate; this aspect makes the LDH capable of improved charge transfer properties. The LDH-based sensors show interesting enhancing performances in terms of sensitivity and detection limit, especially when the analyte is an anion, since the catalytic properties are favored by the capability of pre-concentrating the substrate inside the interlayer domains. Moreover, the transition metal can display electrocatalytic properties which allow the amperometric detection of a wide group of oxidizable analytes, such as alcohols, amines, polyhydric compounds and complex molecules, such as pesticides [59-62]. The sensitivity of the measurements depends both on the number of oxidizable sites and on the steric hindrance of the analyte and, thus, on the interlayer spacing.

Ni/Al LDHs show also good performance as amperometric sensors for the determination of alcohols, alditols, and sugars, through an electrocatalytic mechanism involving the Ni(III) centres. The substitution of Ni with Co as M(II) induces a selectivity in the electro-oxidation of molecules containing hydroxyl groups; indeed Co/Al LDH modified electrodes do not display electrocatalytic activity towards monohydric compounds due to the lower redox potential of the Co(III)/Co(II) couple. Therefore, the different behaviour of Co and Ni based LDHs has offered the interesting opportunity to develop an analytical method for the selective determination of alcohols in the presence of polyhydric compounds [59].

3.3.3.2 Biocatalysis and biosensors

Biosensors have been extensively studied for the determination of analytes of interest in many application fields such as food quality, medical diagnostics and environmental monitoring. Biosensors are chemical sensors in which the recognition system exploits a biological sensing element, *e.g.*, enzymes or proteins. The stable immobilization of an enzyme on an electrode surface, with the retention of its biological activity, and good

diffusion properties for substrates, are the major problems related to the development of biosensors. Various methods for enzyme immobilization have been reported, such as cross-linking of proteins by bifunctional reagent, covalent binding, and entrapment in a suitable matrix. Among all the inorganic and organic matrices reported in the literature, clays and in the last decade, LDHs in particular, have become attracting materials due to their hydrophilic, swelling, and porosity properties. The biosensor fabrication procedure consists of the adsorption of an enzyme/clay aqueous mixture onto the electrode surface and the addition of cross linking agents, such as glutaraldehyde and bovine serum albumin or polymethyl methacrylate (PMMA) on the coating film [63]. This method of deposition offers the possibility of entrapping an established amount of enzyme into the clay film and can be tailored for the conductive supports.

As an example, a very sensitive glucose amperometric biosensor was developed entrapping the enzyme glucose oxidase (GOx) within a Ni/Al-NO₃ LDH during the phase of electrosynthesis [64]. Amperometric detection of glucose is an important topic mainly due to the physiological importance of this analyte, the stability of glucose oxidase, and the variety of the relevant sensing methods. In the presence of oxygen the enzyme catalyzes the oxidation of glucose to gluconolactone with the concomitant production of hydrogen peroxide which is electrochemically oxidized and detected at a sufficient anodic potential.

Furthermore, biosensors were developed based on a wide selection of enzymes entrapped into LDHs such as on laccase [65], cholesterol oxidase [66], alkaline phosphatase [67], and also other biomolecules such as DNA or hemoglobin [68].

3.3.4 Energy

3.3.4.1 Production: fuel cells and metal-air batteries

Due to their high energy-conversion efficiency, low emission, and high energy and power density, fuel cells and metal-air batteries have drawn remarkable attention as potential efficient power sources for both electric vehicles and portable electronics [69,70]. The oxygen reduction reaction (ORR) occurring at fuel cells cathode and metal-air batteries plays a key role in controlling the performance of those devices, and efficient ORR electrocatalysts are essential for practical applications of fuel cells and

metal-air batteries [71]. Noble metal-based materials are the most effective electrocatalysts for both ORR and oxygen evolution reaction (OER) in fuel cells or metal-air batteries due to their excellent properties, but the prohibitive cost and the scarcity of the noble metals prevent the development of efficient and inexpensive electrocatalysts and this remains one of the main topics of the current research in the field of energy production devices.

LDHs and their nanocomposites can be employed as electrocatalysts [72,73]. They represent low cost materials with a high catalytic activity, and high chemical stability; for these reasons LDHs are becoming ideal materials in the fields of electrocatalysis. Up to now one of the main research topics concerns the improvement of the performances of LDH-based electrocatalysts by developing an easy and rapid preparation method to obtain nanomaterials with well defined morphology, dimension and microstructure. It has been demonstrated that Ni/Fe LDHs have an important effect on the OER which can be improved by tuning the Ni/Fe ratios in the structure. When Ni/Fe = 1.5, the Ni/Fe LDHs show a combination of paramagnetic and ferromagnetic interactions which enhances the catalytic activity on the electrochemical process in alkaline media, and the LDHs do not exhibit structural changes after the electrochemical processes [74]. The 2D porous architecture can offer several significant advantages, such as facilitating electron transportation, promoting electrolyte penetration, and increasing the electrochemically active surface area. For example, coatings of Ni/Fe LDH nanoplates on nickel foam exhibited significantly reduced onset potential, yielded high current density at small overpotentials, and showed excellent stability in OER [75]. The synthesis of a well-defined hierarchical architecture with high surface area and proper pore-size distribution is necessary for preventing the aggregation of LDHs and ensuring an efficient electron transfer and a fast mass transport of electrolytes, improving the Faradaic redox reaction [76].

Moreover, carbon nanomaterials have an excellent electrical conductivity and can provide a support for anchoring LDHs, enhancing the specific surface area and improving the conductivity of LDHs. Therefore, LDHs/carbon-based materials showed a very high activity as OER and hydrogen evolution reaction (HER) electrocatalysts. Dai *et al.* described the nucleation and growth of ultrathin Ni/Fe LDH nanoplates on mildly oxidized CNTs. The resulting Ni/Fe LDH/CNT composite formed interconnected electrically conducting networks and exhibited higher electrocatalytic activity and stability for OER than commercial Ir catalysts. The enhancement of the performance can

be ascribed to the high activity of Ni/Fe LDHs and the improved electron transport induced by CNT network [77].

Also LDHs-reduced graphene oxide (rGO) composites were studied; by electrostatic attraction, the GO nanosheets with multifunctional oxygen groups were intercalated into the Ni/Fe LDHs, forming charge balancing interlayers in the resulting hybrid sheets. The Ni/Fe LDH/rGO hybrids exhibited advanced electrocatalytic activity and stability on OER in alkaline solution. The high catalytic performance is mainly attributed to the intrinsic catalytic activity of the Ni/Fe LDHs and the strong interactions between LDHs and rGO, which assisted in exposing the catalytically active sites and improved the charge transport through the rGO layers [78]. Ni/Fe LDH/carbon quantum dot composites used for OER have also been reported to improve the electrocatalytic activity of Ni/Fe LDHs [79].

LDHs can also represent precursor materials for the synthesis of electrocatalysts since after a thermal treatment they lead to various mixed metal oxide nanocomposite materials consisting of interdispersed metal oxide and spinel-like phases [80,81]. Those oxides have been demonstrated to be efficient electrocatalysts since they give rise to a very high electrocatalytic activity and chemical stability if compared to similar materials prepared by traditional methods. The calcination method provides also an efficient synthesis strategy for the production of electrocatalysts on a large scale for industrial applications. Furthermore, as a result of the possibility to change the composition of the LDH precursors, the nanocomposite catalysts possess tunable catalytic activities for ORR and OER. Wang *et al.* reported a new class of $\text{Co}_3\text{O}_4/\text{Co}_2\text{MnO}_4$ nanocomposite bifunctional catalysts, which were synthesized by calcination of a Co/Mn LDH precursor [82]. They exhibited excellent activities both for ORR and OER in alkaline solution, which compare with those catalysts based on precious metals and better ORR durability than the one exhibited by the commercial Pt/C catalysts. The enhanced performance can be attributed to the high surface area and well-dispersed heterogeneous nanostructure of the nanocomposites.

LDHs can also be employed as modifier material for polyelectrolyte membranes. Methanol crossover occurring in the direct methanol fuel cell (DMFC) results in direct oxidation of methanol at the anode, and hence, leads to decreased fuel efficiency, anode voltage, fuel loss and CO corrosion. Commercial membranes, such as Nafion, are expensive, and more than 40 % of the methanol is often lost through crossover during fuel cell operation [83].

When LDH is incorporated into Nafion polymer chains, the negatively charged sulfonic groups in Nafion polymer chains intercalate into the positively charged LDH phase resulting in a well-dispersed composite structure. The composite gave rise to an increment of the maximum power density compared with the pristine Nafion membrane, meaning that the methanol crossover was highly suppressed by the incorporation of LDH [84], due to the modified diffusion rate of methanol crossover and the hindering effect of LDHs for the transport of methanol molecules. In addition, also other composites based on LDHs and new membrane materials, less expensive than Nafion, have been recently investigated. For example, low-cost membranes based on sulfonated poly(ether ether ketone) (SPEEK) and Mg/Al-LDHs displayed good chemical, thermal and mechanical stability and higher proton conductivity if compared to the pure SPEEK membrane due to the structural water inside the LDHs [85]. In the reported cases, well-dispersed LDH particles act as physical barriers and hinder methanol diffusion in the hybrid membrane further improving the properties of these materials.

3.3.4.2 Storage: supercapacitors

Transition metal (Mn, Fe, Co, Ni, etc.) oxides or hydroxides are common electrode materials for supercapacitors [86]. Active transition metal ions into LDH layers can improve the specific capacity of active materials, and enhance structural stability (cycle life) of electrode during the charge-discharge process. Thereby, LDHs are considered one of the most promising electrode materials for developing high-performance electrochemical capacitors.

The microstructure is a key factor for these applications since it is extremely important to obtain a high surface area and a mesoporous distribution. The main problem related to LDH materials in electrochemical capacitors is that they show a poor electrical conductivity which, consequently, results in lower energy output. The realization of LDH/carbon nanocomposites is a good way to put together the advantages of LDHs and carbon nanomaterials. Carbon nanomaterials have an excellent electrical conductivity and provide a support for anchoring well-dispersed LDHs with a higher active surface area. Graphene nanosheet/NiAl LDH composite [87], exhibited a specific capacitance of 781.5 F g^{-1} and more excellent cycle life compared with pure Ni/Al LDHs. The reason could be related to the presence of graphene that provides the high electrical conductivity of the overall electrode due to its peculiar characteristics.

Co-based LDHs also show a high activity due to the Faradaic redox reaction and have been used as component for Co/Al LDH/carbon nanocomposites, which have been prepared by several methods. As an example through a one-step method, Ni/Co LDH films was grown on nickel foam by hydrothermal co-deposition using cetyltrimethylammonium bromide as nanostructure growth assisting agent [88]. Ultrathin nanosheets and porous nanostructures were obtained, and the as-obtained modified electrodes displayed a high specific capacitance (2682 F g^{-1} at 3 A g^{-1}) and energy density (77.3 Wh kg^{-1} at 623 W kg^{-1}). Moreover, the asymmetric supercapacitor, realized using the Ni/Co LDH film as the positive electrode material and porous rGO as the negative one, exhibited a very high energy density (188 Wh kg^{-1}) at an average power density of 1499 W kg^{-1} .

REFERENCES

- [1] E. Manasse, *Rocce eritree e di aden della collezione issel*, 1915, Atti Soc Toscana Sc Nat Proc Verb 24, 92.
- [2] D. Tonelli, E. Scavetta, M. Giorgetti. *Anal. Bioanal. Chem.* 405 (2013) 603.
- [3] V.R.L. Constantino, T. Pinnavaia. *Inorg. Chem.* 34 (1995) 883.
- [4] F. Cavani, F. Trifirò, A. Vaccari. *Catal. Today* 11 (1991) 173.
- [5] A.I. Khan, D. O'Hare. *J. Mater. Chem.* 12 (2002) 3191.
- [6] S. Miyata. *Clays Clay Miner.* 31 (1983) 305.
- [7] P. Nalawade, B. Aware, V.K. Kadam, R.S. Hirlekar. *J. Sci. Ind. Res.* 68 (2009) 267.
- [8] U. Costantino, F. Marmottini, M. Nocchetti, R. Vivani. *Eur. J. Inorg. Chem.* 10 (1998) 1439.
- [9] M. Adachi-Pagano, C. Forano, J.B. Besse. *J. Mater. Chem.* 13 (2003) 1988.
- [10] M. Ogawa, S. Asai. *Chem. Mater.* 12 (2000) 3253.
- [11] V. Prevot, N. Caperaa, C. Taviot-Guého, C. Forano. *Cryst. Growth. Des.* 9 (2009) 3646.
- [12] P. Vialat, C. Mousty, C. Taviot-Gueho, G. Renaudin, H. Martinez, J.C. Dupin, E. Elkaim, F. Leroux. *Adv. Funct. Mater.* 24 (2014) 4831.
- [13] K.L. Erickson, T.E. Bostrom, R.L. Frost. *Mater. Lett.* 59 (2005) 226.
- [14] T. Hibino, Y. Yamashita, K. Kosuge, A. Tsunashima. *Clays Clay Miner.* 43 (1995) 427.
- [15] F. Bellezza, M. Nocchetti, T. Posati, S. Giovagnoli, A. Cipiciani. *J. Colloid. Interface Sci.* 376 (2013) 20.
- [16] E. Scavetta, B. Ballarin, M. Giorgetti, I. Carpani, F. Cogo, D. Tonelli. *J. New. Mat. Electrochem. Systems* 7 (2004) 43.
- [17] E. Scavetta, A. Mignani, D. Prandstraller, D. Tonelli. *Chem. Mater.* 19 (2007) 4523.
- [18] L. Indira, P.V. Kamath. *J. Mater. Chem.* 4 (1994) 1487.
- [19] I. Gualandi, A. G. Solito, E. Scavetta, D. Tonelli. *Electroanalysis* 24(4) (2012) 857.
- [20] A. Romero, M. Jobbàgy, M. Laborde, G. Baronetti, N. Amadeo. *Catal. Today* 149 (2010) 407.
- [21] K. Ladewig, M. Niebert, Z.P. Xu, P.P. Gray, G.Q. Lua. *Appl. Clay Sci.* 48 (2010) 280.
- [22] F. Bruna, R. Celis, I. Pavlovic, C. Barriga, J. Cornejo, M.A. Ulibarri. *J. Hazard. Mater.* 168 (2009) 1476.

- [23] Z. Xu, N. Wang, W. Chu, J. Deng, S. Luo. *Catal. Sci. Technol.* 5 (2015) 1588.
- [24] I. Gualandi, E. Scavetta, S. Zappoli, D. Tonelli. *Biosens. Bioelectron.* 26 (2011) 3200.
- [25] J.S. Valente, F. Tzompantzi, J. Prince, J.G.H. Cortez, R. Gomez. *Appl. Catal. B* 90 (2009) 330.
- [26] S.J. Xia, F.X. Liu, Z.-M. Ni, J.L. Xue, P.P. Qian. *J. Colloid. Interface Sci.* 405 (2013) 195.
- [27] T. Stimpfling, F. Leroux, H. Hintze-Bruening. *Colloids Surf. A* 458 (2014) 147.
- [28] M. Hajibeygia, M. Shabaniab, H.A. Khonakdarc. *Appl. Clay Sci.* 114 (2015) 256.
- [29] F. Barahuie, M.Z. Hussein, S. Fakurazi, Z. Zainal. *Int. J. Mol. Sci.* 15 (2014) 7750.
- [30] F.J.W.J. Labuschagne, D.M. Molefe, W.W. Focke, I. van der Westhuizen, H.C. Wright, M.D. Royeppen. *Polym. Degrad. Stabil.* 113 (2015) 46.
- [31] Q. Wang, J. Wu, Y. Gao, Z. Zhang, J. Wang, X. Zhang, X. Yan, A. Umar, Z. Guo, D. O'Hare. *RSC Adv.* 3 (2013) 26017.
- [32] S. Elbasuney. *Powder Technol.* 277 (2015) 63.
- [33] X. Wang, E.N. Kalaly, D.-Y. Wang. *ACS Sustainable Chem.* 3 (2015) 3281.
- [34] L. Wang, J. Liu, Y. Zhou, Y. Song, J. He, D.G. Evans. *Chem. Commun.* 46 (2010) 3911.
- [35] B. Balcomb, M. Singh, S. Singh. *Chem. Open* 4 (2015) 137.
- [36] A.I. Khan, L. Lei, A.J. Norquist, D. O'Hare. *Chem. Commun.* 22 (2001) 2342.
- [37] V. Rives, M. del Arco, C. Martín. *Appl. Clay Sci.* 88–89 (2014) 239.
- [38] J. H. Choy. *Solid State Phenom.* 111 (2006) 1.
- [39] C.R. Gordijo, C.A.S. Barbosa, A.M. da Costa Ferreira, V.R.L. Constantino, D. de Oliveira Silva. *J. Pharm. Sci.* 94 (2005) 1135.
- [40] P. Parashar, V. Sharma, D.D. Agarwal, N. Richhariya. *Mater. Lett.* 74 (2012) 93.
- [41] C. Viseras, P. Cerezo, R. Sanchez, I. Salcedo, C. Aguzzi. *Appl. Clay Sci.* 48 (2010) 291.
- [42] M. Trikeriotis, D.F. Ghanotakis. *Int. J. Pharm.* 332 (2007) 176-184.
- [43] V. Ambrogi, G. Fardella, G. Grandolini, L. Perioli. *Int. J. Pharm.* 220 (2001) 23.
- [44] D. Wang, N. Ge, J. Li, Y. Qiao, H. Zhu, X. Liu. *ACS Appl. Mater. Interfaces.* 7 (2015) 7843.
- [45] K. Kuzawa, Y. Jung, Y. Kiso, T. Yamada, M. Nagai, T. Lee. *Chemosphere* 62 (2006) 45.
- [46] N.K. Lazaridis, A. Hourzemanoglou, K.A. Matis. *Chemosphere* 47 (2002) 319.

- [47] T. Toraishi, S. Nagasaki, S. Tanaka, *Appl. Clay Sci.* 22 (2002) 17.
- [48] S. Kaneko a, M. Ogawa. *Appl. Clay Sci.* 75-76 (2013) 109.
- [49] S. Mandal, S. Mayadevi, B.D. Kulkarni. *Ind. Eng. Chem. Res.* 48 (2009) 7893.
- [50] X. Qiu, M. Yoshida, T. Hirajima, K. Sasaki. *Mater. Trans.* 56 (2015) 224.
- [51] S. Tezuka, R. Chitrakar, A. Sonoda, K. Ooi, T. Tomida. *Green Chem.* 6 (2004) 104.
- [52] F.L. Theiss, S.J. Couperthwaite, G.A. Ayoko, R.L. Frost. *J. Colloid. Interface Sci.* 417 (2014) 356.
- [53] M. Mohapatra, S. Anand, B.K. Mishra, D.E. Giles, P. Singh. *J. Environ. Manage.* 91 (2009) 67.
- [54] R.L. Goswamee, P. Sengupta, K.G. Bhattacharyya, D.K. Dutta. *Appl. Clay Sci.* 13 (1998) 21.
- [55] P. Zhao, X. Liu, W. Tian, D. Yan, X. Sun, X. Lei. *Chem. Eng. J.* 279 (2015) 597.
- [56] M. Park, C.L. Choi, Y.J. Seo, S.K. Yeo, J. Choi, S. Komarneni, J.H. Lee. *Appl. Clay Sci.* 37 (2007) 143.
- [57] R. Shan, L. Yan, K. Yang, Y. Hao, B. Du. *J. Hazard. Mater.* 299 (2015) 42.
- [58] E. Scavetta, B. Ballarin, M. Berrettoni, I. Carpani, M. Giorgetti, D. Tonelli. *Electrochim. Acta* 51 (2006) 2129.
- [59] E. Scavetta, D. Tonelli. *Electroanalysis* 17 (2005) 363.
- [60] A. Khenifi, Z. Derriche, C. Forano, V. Prevot, C. Mousty, E. Scavetta, B. Ballarin, L. Guadagnini, D. Tonelli. *Anal. Chim. Acta* 654 (2009) 97.
- [61] E. Scavetta, A. Casagrande, I. Gualandi, D. Tonelli. *J. Electroanal. Chem.* 722-723 (2014) 15.
- [62] I. Gualandi, E. Scavetta, Y. Vlamidis, A. Casagrande, D. Tonelli. *Electrochim. Acta* 173 (2015) 67.
- [63] C. Mousty, V. Prévot. *Anal. Bioanal. Chem.* 405 (2013) 3513.
- [64] E. Scavetta, L. Guadagnini, A. Mignani, D. Tonelli. *Electroanalysis* 20 (2008) 2199.
- [65] C. Mousty, L. Vieille, S. Cosnier. *Biosens. Bioelectron.* 22 (2007) 1733.
- [66] S.N. Ding, D. Shan, Tao Zhang, Y.-Z. Dou. *J. Electroanal. Chem.* 659 (2011) 1.
- [67] C. Mousty, O. Kaftan, V. Prevot, C. Forano. *Sensor. Actuat. B-Chem.* 133 (2008) 442.
- [68] T. Zhan, Q. Yang, Y. Zhang, X. Wang, J. Xu, W. Hou. *J. Colloid. Interface Sci.* 433 (2014) 49.
- [69] H.J. Hwang, J. Koo, M. Park, N. Park, Y. Kwon, H. Lee. *J. Phys. Chem. C* 2013, 117, 6919.

- [70] H.W. Park, D.U. Lee, L.F. Nazar, Z. Chen. *J. Electrochem. Soc.* 160 (2013) A344.
- [71] X. Zhang, Y. Wang, S. Dong, M. Li. *Electrochim. Acta* 170 (2015) 248.
- [72] H. Lin, Y. Zhang, G. Wang, J.-B. Li. *Mater. Sci.* 6 (2012) 142.
- [73] Y. Lee, J.H. Choi, H.J. Jeon, *et al.* *Energy Environ. Sci.* 4 (2011) 914.
- [74] M.A. Oliver-Tolentino, J. Vázquez-Samperio, A. Manzo-Robledo, R. de Guadalupe González-Huerta, J.L. Flores-Moreno, D. Ramírez-Rosales, A. Guzmán-Vargas. *J. Phys. Chem. C* 118 (2014) 22432.
- [75] Z. Lu, W. Xu, W. Zhu, Q. Yang, X. Lei, J. Liu, Y. Li, X. Sun, X. Duan. *Chem. Commun.* 50 (2014) 6479.
- [76] M. Shao, R. Zhang, Z. Li, M. Wei, D.G. Evans, X. Duan. *Chem. Commun.* 51 (2015) 15880.
- [77] M. Gong, Y. Li, H. Wang, Y. Liang, J.Z. Wu, J. Zhou, J. Wang, T. Regier, F. Wei, H. Dai. *J. Am. Chem. Soc.* 135 (2013) 8452.
- [78] D.H. Youna, Y.B. Parkb, J.Y. Kima, G. Magesha, Y.J. Jangb, J.S. Lee. *J. Power Sources* 294 (2015) 437.
- [79] D. Tang, J. Liu, X. Wu, R. Liu, X. Han, Y. Han, H. Huang, Y. Liu, Z. Kang. *ACS Appl. Mater. Interfaces* 6 (2014) 7918.
- [80] R. Zhang, L. Hua, L. Guo, B. Song, J. Chen, Z. Hou. *Chin. J. Chem.* 31 (2013) 381.
- [81] I. Pettiti, D. Gazzoli, P. Benito, G. Fornasari, A. Vaccari. *RSC Adv.* 5 (2015) 82282.
- [82] D. Wang, X. Chen, D.G. Evans, W. Yang. *Nanoscale* 5 (2013) 5312.
- [83] T. Wook Kim, M. Sahimi, T.T. Tsotsis. *Ind. Eng. Chem. Res.* 48 (2009) 9504.
- [84] I. Nicotera, K. Angjeli, L. Coppola, A. Enotiadis, R. Pedicini, A. Carbone, D. Gournis. *Solid State Ionics* 276 (2015) 40.
- [85] N.H. Kim, A.K. Mishra, D. Kim, J.H. Lee. *Chem. Eng. J.* 272 (2015) 119.
- [86] X.-M. Liu, Y.-H. Zhang, X.-G. Zhang, *et al.* *Electrochim. Acta* 49 (2004) 3137.
- [87] M. Shao, R. Zhang, Z. Li, M. Wei, D.G. Evans, X. Duan. *Chem. Commun.* 51 (2015) 15880.
- [88] H. Chen, L. Hu, M. Chen, Y. Yan, L. Wu. *Adv. Funct. Mater.* 24 (2014) 934.

4. ENERGY STORAGE AND CONVERSION

The increasing demand for energy and the decrement of natural energy resources have led to a lot of efforts aimed to discover earth-abundant energy alternatives and designing efficient energy-storage devices [1,2]. Energy storage and conversion with high efficiency and cleanliness have a great effect on the sustainable development of world economics and ecology. To replace the traditional fossil fuels, electrochemical energy storage and conversion systems, which include batteries such as rechargeable lithium-ion and magnesium-ion batteries, and fuel cells, offer promising alternatives [3].

The energy utilization efficiency and the renewable energy implementation represent a fundamental issue. Primary renewable energy sources, such as wind and solar power, having the advantages of being sustainable should be further improved and exploited. However, renewable energy sources have a significant disadvantage that is their intermittence on daily, seasonal and regional scales too, with considerable variability in supply. This problem can be overcome by connecting a local energy storage system to an electricity producing element [4]. Employing electrochemical energy storage devices would allow for the storage of the surplus energy when electricity supply is higher than demand and for its release when demand becomes higher than supply [5]. From this point of view, water electrolysis can play a fundamental role in the development of a sustainable energy system. Water electrolyzers are electrochemical energy conversion devices producing hydrogen. The hydrogen energy vector represents an alternative to electricity storage in batteries since its reconversion into electricity via fuel cells opens up independent scaling of power and energy due to the separation of the hydrogen storage from the conversion device [6].

In many application areas, beside fuel cells and batteries, one of the most employed electrical devices for energy conversion and storage are the electrochemical supercapacitors. In recent years, these devices have attracted considerable interest, mainly due to their high power density and long lifecycle. The performance of such devices depends intimately on the properties of the functional materials [7], for this reason, currently the challenge is to address the demand of new functional materials with higher and faster storage and conversion efficiency.

In the next paragraphs the attention will be focused sequentially on the mechanism, materials and state-of-the-art of oxygen evolution reaction, electrochemical capacitors and organic solar cells.

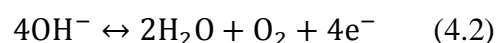
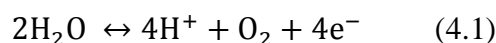
4.1 Oxygen Evolution Reaction

Hydrogen is a promising energy source and a good candidate to substitute fossil fuels due to its high energy density/mass-specific ratio [8]. At present H₂ production still mostly depends on the fossil fuel industry from which it is obtained with low purity and high cost [9]. One of the most efficient ways to obtain high purity and inexpensive H₂ is water splitting into hydrogen and oxygen by electricity or sunlight [10,11].

The oxygen evolution reaction has been deeply investigated for decades [12,13] since it is one of the half-reactions involved in water splitting. Oxygen evolution reaction is a complex reaction that includes four proton-coupled electron transfers and oxygen–oxygen bond formation, it is kinetically not favored so requiring an efficient catalyst to expedite the reaction [14]. Iridium and ruthenium dioxides (IrO₂ and RuO₂) have been proposed as anodes for this application since they display the best OER electrocatalytic efficiencies in terms of overpotential and Tafel slope [15].

However, due to their scarcity and high cost, they cannot find industrial applications to obtain economic H₂ energy resources.

Water oxidation is a reaction generating molecular oxygen through several proton/electron-coupled processes [16]. In acidic conditions, the reaction operates through oxidation of two water molecules to give four protons and one oxygen molecule by losing a total of four electrons (Eq. 4.1) [17]. In basic solutions the oxidation of hydroxyl groups takes place, and they are converted into H₂O and O₂ with the same number of involved electrons (Eq. 4.2).



Since OER is a redox reaction, electricity is usually used to drive it. The standard potential for OER at pH 0 is 1.23 V vs the normal hydrogen electrode (NHE) [18]. In Figure 4.1 the Pourbaix diagram for water is shown.

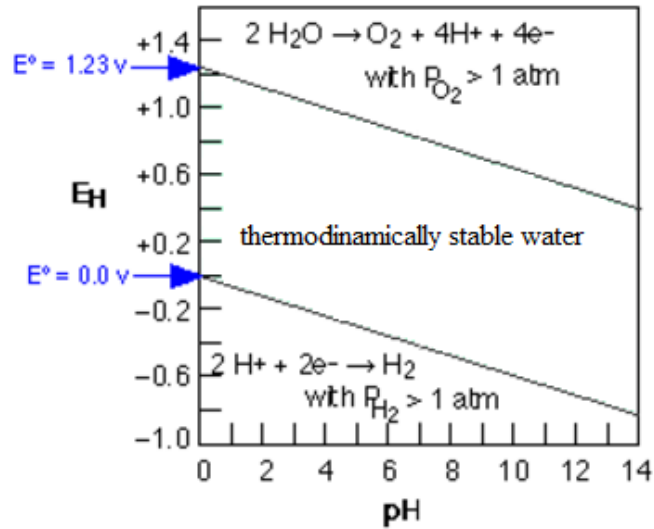


Figure 4.1 – Pourbaix diagram of water.

The reaction involves H^+ or OH^- , so the potential is pH-dependent by shifting of 59 mV for each pH unit increase ($T = 298.15 \text{ K}$) according to the Nernst equation (4.3), where E is the half cell potential, E° is the cell potential in standard conditions, R is the ideal gas constant, T is the temperature in Kelvin, n is the number of moles of electrons involved for each mole of reaction, F is the Faraday constant, a_{Red} is the activity of the reduced molecules and a_{Ox} is the activity of the oxidized ones, respectively.

$$E = E^\circ - \frac{RT}{nF} \ln \frac{a_{\text{red}}}{a_{\text{ox}}} \quad (4.3)$$

To avoid the problem connected to the applied potential dependence on pH, researchers have introduced a reversible hydrogen electrode (RHE) as reference [19] by taking into account the pH shift, and hence the theoretical potential required for OER is always 1.23 V vs RHE at all pHs. As shown in Eqs. (4.1) and (4.2), the production of each O_2 molecule requires a transfer of four electrons, and as multiple electron transfer in one step it is not kinetically favored, OER usually involves multiple steps with one electron transfer per step [16]. An accumulation of the energy barrier in each step leads to the slow kinetics of OER with large overpotential to overcome [20].

4.1.1 Catalytic activity and kinetic parameters for OER

To quantitatively compare the activity of catalysts and study structure/composition/activity relationships, common performance parameters are required. The

Tafel slope is often used to compare the catalytic activity for OER [21]. Its value (slope of the experimental linear dependence of E on $\log j$, where j is the current density) is particularly important from an applicative point of view and gives significant information about the reaction mechanism providing the current density changes with increasing overpotential. To evaluate the Tafel slopes, the measurements should be carried out at low scan rate (below 5 mV s^{-1}) so obtaining a quasi-stationary current/potential curves.

However, different kinetic parameters can be used in combination with the Tafel slope to better define the activity of catalysts for oxygen evolution.

In particular, it is evaluated as activity parameter the current density value at a certain potential, normalized to the catalyst mass. The potential at a steady-state current density (with geometric surface area normalization) cannot be used as an activity parameter because it does not take into account the catalyst loading.

In addition the turnover frequency (TOF) represents a good parameter providing the intrinsic catalytic activity. The TOF is defined as the number of times per second a single active site (which we assume to be a single metal cation) evolves an O_2 molecule (by accepting four electrons from solution). TOFs are typically potential dependent [22], so the overpotential at which the TOF is measured must be reported [23]. At present TOF represents the activity parameter less affected by experimental inaccuracies together with the Tafel slope.

4.1.2 Requirements for oxygen evolution catalysts

Besides a high catalytic activity, an optimal catalytic material must also address other requirements. A high surface area is generally required since it allows minimizing the amount of employed catalyst, and this aspect is particularly important when noble metal-based catalysts are used [24].

In order to achieve a high surface area, porous powders should be employed. Beside the specific surface area, a high electrical conductivity at high electrode potentials is also necessary to minimize the ohmic drop in the material [24]. Another fundamental aspect in the development of suitable catalytic materials for OER is the resistance to corrosion, since anodic currents at high potentials (*i.e.*, above 1.4 V vs RHE) can result even from the occurrence of the catalyst and/or support oxidation/corrosion [25].

It is possible to estimate the catalyst selectivity using the rotating ring-disk electrode (RRDE) technique. Oxygen evolved by the catalyst can in principle be reduced on the surrounding Pt-ring electrode when it is potentiostatically kept in a potential range where oxygen reduction is entirely under diffusion control; the optimal conditions to minimize the local oxygen saturation and bubbles formation at the disk electrode were suggested to be 1 mA cm^{-2} at a rotation speed of 1600 rpm in a N_2 saturated electrolyte solution [26].

Another topic concerning water splitting electrolysis is the wettability of the electrodes. Gas bubbles are formed on both electrodes during water electrolysis due to the development of molecular hydrogen and oxygen, but as long as the bubbles are not big enough, they will not separate from the electrode surface, leading to a high ohmic resistivity. If the surface is covered by gas bubbles, the electron transfer is momentarily prevented so the involved catalyst surface area cannot contribute to the electrocatalytic process. Due to this situation, a high local current density can flow through a fraction of the electrode area, affecting the catalyst stability. The removal of gas bubbles can be accelerated mechanically by a circulating electrolyte. This can be improved either by using additives in the electrolyte solution or by increasing the wettability of the material since a higher hydrophilicity allows for an easier removal of small gas bubbles [27].

Another approach consists in the development of a nanostructured material with suitable pore size in order to minimize the gas bubble growth and favour the detachment of small bubbles in order to improve catalyst activity and stability.

Stability to corrosion is also necessary for the realization of a catalytic material, since in an operative system the conditions are harsh and the anode side experiences severe oxidative conditions.

Further important requirements for the future employment of electrocatalysts are the health safety, availability and low cost of the raw materials to allow for an economical large-scale production.

In the following sections the most studied materials will be discussed.

4.1.3 Trend of the catalysts activity for OER

The difference in the free binding energy between O^* and OH^* have been introduced as a universal catalytic descriptor for the OER to construct volcano plots (Figure 4.2). According to the Sabatier principle, an optimal, moderate binding energy of the OER

intermediates assures the highest catalytic activity [28]. In the case of surfaces that bind oxygen too weakly, intermediates cannot easily react and the potential is limited by the oxidation of HO^* . In the case of strong oxygen bonding, the intermediate states and the adsorbed products are quite stable and the potential is limited by the formation of HOO^* species. The obtained theoretical activity trends are, in general, consistent with old experimental investigations, which showed that the activity toward the OER on rutile, spinels, or perovskites follows a volcano-type dependence on the enthalpy change of the transition from a lower to higher oxide or other similar activity descriptors. The optimum case (top of the volcano plots) is therefore a mean bonding strength, such as in the case of RuO_2 , Co_3O_4 , NiO , PtO_2 , SrCoO_3 , LaNiO_3 , SrCoO_3 and SrNiO_3 .

Despite a good correlation between the theoretical and the experimental overpotential toward the OER is generally observed [29], there could be a few discrepancies derived from the simplification and/or from the model surfaces chosen for computational predictions which do not completely capture all the characteristics of polycrystalline surfaces (defects and changes in the surface state occurring during the reaction).

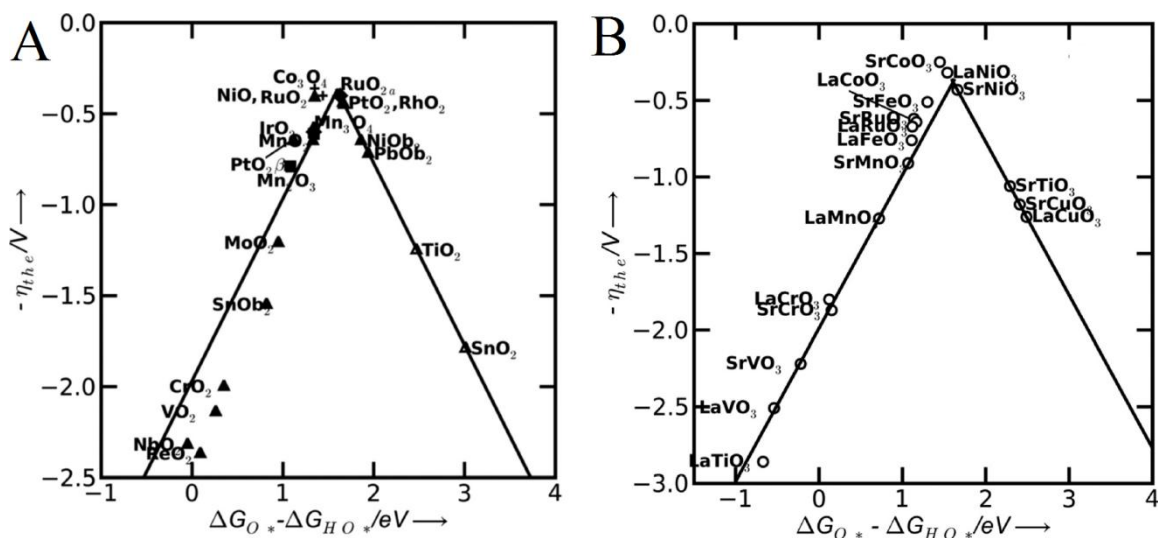


Figure 4.2 - Theoretical overpotential for oxygen evolution vs the difference between the standard free energy of two subsequent intermediates ($\Delta G_{O^*}^0 - \Delta G_{HO^*}^0$) for various binary oxides (A) and perovskite oxide (B) [29].

4.1.3.1 Noble metal oxides

Among noble metal oxides, as already seen, RuO_2 is the most active but is fairly expensive. The interest in RuO_2 electrodes started due to its reactivity at high current densities in alkaline cells. This compound has metallic-like conductivity in basic and

acidic media, but it is slowly attacked by alkaline electrolytes so losing its activity. Based on the experimentally observed OER kinetics, several mechanisms have been proposed, one involving the oxidation and reduction cyclic mechanism together with dissolution [30]. The dissolution of RuO₂ electrocatalysts has been extensively studied and was found to occur even if the electrocatalytic properties are good. One approach to improve RuO₂ stability and corrosion resistance, is to mix it with other metal oxides (TiO₂ [31], SnO₂ [32], ZrO₂ [33], etc) to form mixed oxides. For example, several studies have been conducted employing RuO₂ and IrO₂ mixed oxides as OER catalysts and it has been evidenced that mixed oxides containing RuO₂ and IrO₂ are able to enhance the catalyst stability [30,34]. Mamaca *et al.* [35] found that the presence of Ir contributed in the stability against Ru dissolution.

Catalysts based on pure IrO₂ [36] exhibit the lowest overpotential for OER in acid solutions, but have poor resistance to corrosion and display slightly lower activity than RuO₂. IrO₂ catalysts deactivation occurs under long-term polarization and is related to the increase of the valence value of the Ir cation [37].

4.1.3.2 Non-noble metals for alkaline water electrolysis

Taking into account the volcano plot, a wide range of catalytic materials can be investigated making it possible to replace noble metal catalysts with low-cost and abundant transition metals.

Regarding OER catalytic materials, the most promising transition cations can be found in the fourth row of the periodic table, especially Mn, Fe, Co and Ni [38,39]. Among them, the catalytic activity trend is reported as Ni > Co > Fe > Mn [40]. In particular, the most commonly employed materials are Ni-based hydroxides [41,42] and alloys, Co, Fe or Mn-based oxides [43] and also perovskites [44,45].

Recently, Co and Ni-based layered double hydroxides are attracting attention for this application and the literature has reported the development of LDHs and composite materials with carbon nanotubes or graphene as support for OER electrocatalysis. Furthermore, the presence of iron was discovered to have strong effects in catalyzing oxygen evolution reaction, however, the active site of Ni/Fe LDH remains unclear and further mechanistic studies could help to understand the structural relevance to OER electrocatalytic activity and to further improve Ni/Fe LDH-based electrocatalysts by constructing more advanced structures to tune the electronic properties.

4.2 Electrochemical capacitors

In recent years, electrochemical capacitors (ECs), also called supercapacitors, have attracted significant attention, essentially due to their characteristics to deliver high power density in short times and to display a long lifecycle. Furthermore, ECs represent a link between the traditional dielectric capacitors (which have high power output) and batteries/fuel cells (which have high energy storage) [46].

ECs could be employed in batteries or fuel cells to be used in a hybrid electric vehicle in order to provide the necessary power for acceleration, with the additional function of recuperating energy [47]. From other studies it has been found that ECs can play an important role in complementing lithium batteries or fuel cells in their energy storage functions since they are able to provide back-up power supplies to protect against power disruptions.

In the recent years, important progresses have been made in the research and development of ECs, as evinced by the large number of research papers [48-50]. At the same time, the disadvantages of ECs, including low energy density and high production cost, have been identified as the main challenges for the future of EC technologies [51]. To overcome this problem, one approach consists in the search of new materials for ECs electrodes. Concerning the material and thus the mechanism involved in energy storage, ECs can be divided into two categories, *i.e.*, the electrical double layer supercapacitors and the pseudocapacitors [52].

4.2.1 Electrical double layer supercapacitors and pseudocapacitors

Electrical double-layer supercapacitors (EDLS) have a limited specific capacitance (measured in Faradays per gram of the electrode material) and a low EC energy density [53]. Carbon materials are typically employed as EDLS materials, since they have high specific surface area for charge storage. Unfortunately, the charges physically stored on the carbon particles in porous electrodes are limited. Reaching the desired energy target implies further studies and the approach to increase the EC energy density consists in the development of composite materials containing electrochemically active molecules besides carbon-based materials or even in the replacement of the carbon materials with electrochemically active materials [54]. ECs with electrochemically active materials as

electrodes are called Faradaic supercapacitors (FS) or pseudocapacitors. The two EC mechanisms are depicted in Figure 4.3.

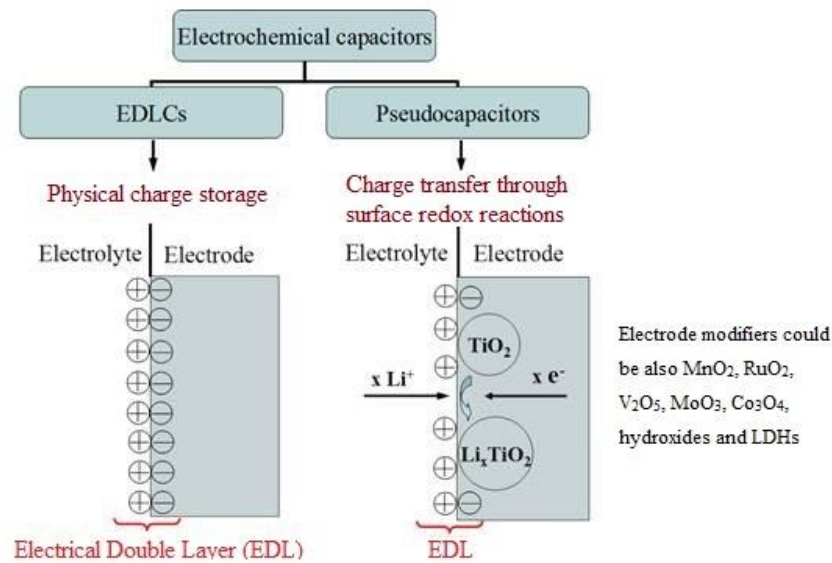


Figure 4.3 – Schematic image of an electrical double layer capacitor and a pseudocapacitor.

It has been demonstrated that pseudocapacitors can yield much higher specific capacitance and energy density than EDLS [55].

Concerning advanced EC materials, metal oxides and hydroxides are considered the most promising materials for the next ECs generation. In particular, high performances can be obtained employing materials as ruthenium and manganese oxides. In the next paragraph the attention will be focused on Faradaic capacitors and pseudocapacitor materials.

4.2.1.1 Faradaic supercapacitors

When a potential is applied to a pseudocapacitor, fast and reversible Faradaic reactions (redox reactions) take place on the electrode materials involving the passage of charge across the double layer, similarly to the charging and discharging processes that occur in batteries. Materials undergoing such redox reactions include conducting polymers and several metal oxides, such as RuO_2 , MnO_2 , and Co_3O_4 [56,57]. Three types of processes occurring at FS electrodes can take place: reversible adsorption, redox reactions of transition metal oxides, and reversible electrochemical doping–dedoping processes in conductive polymer based electrodes.

These Faradaic electrochemical processes extend the working voltage and increase the specific capacitance of the devices [58]. The electrochemical processes occur both on the surface and in the bulk near the surface of the electrode, so a supercapacitor exhibits larger energy density and 10–100 times higher capacitance than materials based on an electrical double layer mechanism [59]. However, the main problem connected to pseudocapacitors is the relatively lower power density than an EDLS and this is due to the Faradaic processes that are normally slower than non-Faradaic processes [60]. In addition, since redox reactions occur at the electrode, similarly to batteries a pseudocapacitor often lacks stability during the cycles.

To take advantage from both electrode materials and try to improve the cell voltage, energy, and power densities, ECs with an asymmetrical electrode configuration (*e.g.*, one electrode consisting of carbon material and the other consisting of Faradaic capacitance material) have been recently studied [61,62]. In this type of supercapacitor, both electrical double-layer capacitance and Faradaic capacitance phenomena occur simultaneously, but one of them plays a greater role. In both phenomena, large surface area, appropriate pore-size distribution, and high conductivity are essential properties of the electrode materials to achieve large capacitance.

- Electrode materials

The redox active materials, besides storing charges in the double layer region, undergo fast and reversible surface redox reactions. As a result, in the recent years the challenge is to develop electrode materials with high pseudocapacitance. The materials commonly employed are classified into two categories: conducting polymers and electroactive metal oxides.

Conducting polymers possess many advantages that make them suitable materials for ECs, such as low cost, low environmental impact, high conductivity in a doped state, high voltage window, high storage capacity, porosity, doping reversibility, and adjustable redox activity through chemical modification [63]. The capacitance behaviour arises from the redox processes: when oxidation takes place, ions are transferred to the polymer backbone, and when reduction occurs, the ions are released from this backbone into the electrolyte [64]. These redox reactions in the conducting polymer occur not just on the surface but involve the entire bulk. Because the charging and discharging reactions do not involve any structural alterations, the processes are highly reversible [65].

In those polymers the electronic conductivity can be induced by oxidation or reduction reactions (doping), which generate delocalized electrons on the polymer chains.

The most common polymers employed in supercapacitor applications are polyaniline (PANI) [66], polypyrrole (PPy), polythiophene (PTh) and their corresponding derivatives.

The conducting polymers are able to work within a strict potential window since they could be degraded at high positive potential, while when the potential is too cathodic, the polymer may be switched to an un-doped state. Unfortunately, ECs containing polymers suffer from poor performance during cycling, since swelling may occur during the intercalation/de-intercalation process leading to the degradation of the electrode. The disadvantage due to the low cycling stability can be mitigated using composite electrode materials with metal oxides/hydroxides or carbon-based materials (composite can improve the polymer chain structure, mechanical stability and processability) and controlling the morphology (for example nanofibers, nanowires, and nanotubes could reduce cycling degradation) [67].

Another class of compounds suitable for EC applications is represented by metal oxides/hydroxides that can provide higher energy density than conventional carbon materials and better electrochemical stability than polymer materials. They store energy like carbon materials do but also exhibit electrochemical Faradaic reactions within appropriate potential windows.

The oxide should be electronically conductive, the metal should exist in two or more oxidation states that coexist over a continuous range with no phase changes involving irreversible modifications of the structure, and the protons can freely intercalate into the oxide lattice on reduction and out of the lattice on oxidation. The best materials are represented by ruthenium oxide, manganese oxide, cobalt oxide, nickel oxide, and vanadium oxide [68,69].

RuO_2 has been the most extensively studied material due to its wide potential window, highly reversible redox reactions, three oxidation states accessible within a 1.2 V voltage window, high specific capacitance, good thermal stability, long cycle life and high conductivity [70,71]. The pseudocapacitive behaviour of ruthenium oxides in acidic or alkaline environments involves different reactions; anyway, the pseudocapacitance of RuO_x comes essentially from the surface reactions [72]. The higher the specific surface area, the more the metal centres will be capable of providing multiple redox reactions and the higher the specific capacitance will then be.

As cheaper and environmentally friendly alternative to RuO₂, other compounds were found to exhibit similar performances and electrochemical behaviour; among them MnO₂, NiO, Fe₃O₄, and V₂O₅. In particular Co/Ni composites should be promising materials in EC applications, in particular by choosing a proper composition of the binary oxides.

Manganese oxides present relatively low cost, low toxicity, and environmental safety, as well as high capacities [73]. The pseudocapacitance of manganese oxides is attributed to reversible redox transitions involving the exchange of protons and/or cations with the electrolyte, as well as the transitions between Mn(III)/Mn(II), Mn(IV)/Mn(III), and Mn(VI)/Mn(IV) within the electrode potential window of the electrolyte [74].

Despite the redox nature of the energy storage mechanism, MnO_x-based electrodes display also typical rectangular-shaped cyclic voltammetry curves, analogous to non-Faradaic energy storage mechanisms [75]. Both physical properties such as microstructure and surface morphology, and chemical factors affect the pseudocapacitive performance of Mn oxides so it is important to control the microstructure [76], while their specific capacitance is influenced by their chemically hydrous state.

Other interesting compounds are Co₃O₄ and Co(OH)₂ which seem to exhibit excellent reversible redox behaviour, large surface area, high conductivity, long-term performance, and good corrosion stability [77,78]. Nickel oxide is considered an alternative electrode material for EC in alkaline electrolytes due to its easy synthesis, relatively high specific capacitance and low cost [79]. It has been determined that Ni(OH)₂ and a Co(OH)₂–Ni(OH)₂ composite can yield much higher specific capacitances than NiO [80,81]. For further improvement, much better performance can be achieved if the micropore structure of this kind of materials is optimized.

Vanadium oxides have also been investigated for their potential use in EC due to their variable oxidation states, which can yield surface/bulk redox reactions [82] and also iron oxides, Fe₂O₃ and Fe₃O₄ are other candidates as EC electrode material, offering low cost and minimal environmental impact. The problem connected to these oxides is the poor electronic conductivity, but recently it was found that the incorporation of MWCNTs into α-Fe₂O₃ nanospheres seems to improve the conductivity of the material, leading to better ion diffusion [83].

In order to find new suitable materials the challenge is still going on and, recently, layered double hydroxides, a class of materials containing transition metals, are

becoming much and much interesting due to their peculiar properties such as fast ion exchange, redox activity and so on. [84,85].

4.2.2 Electrochemical studies of the EC materials

The electrochemical performances of the material coated on conductive supports can be evaluated by recording cyclic voltammetry in the chosen electrolyte. The specific capacitance too can be calculated from the CV curves but also from the charge-discharge galvanostatic curves recorded in a stable potential window, at different current densities. In addition to cyclic voltammetry, electrochemical impedance spectroscopy is a technique commonly employed in order to determine the capacitance of EC materials [86].

Generally EIS measurements are performed collecting the EC impedance data at the open-circuit potential by applying small amplitude of alternative interrupting potential over a wide range of frequency (*e.g.*, 1 mHz to 1 MHz). This provides the relationship between the imaginary part of impedance $Z(f)$ and the frequency, f . The capacitance can be calculated from the equation $C = 1/(2\pi f|Z|)$ using a linear portion of a $\log |Z|$ vs $\log f$ curve, which is called the Bode plot [87]. As shown by the Bode plot, the capacitance decreases with increasing frequency, and at the high frequency region the supercapacitors behave like a pure resistance, indicating that the electrolyte ions probably cannot penetrate into micropores, under these conditions. It is also possible to plot Nyquist diagrams, where the imaginary part of impedance, $Z(f)''$, is plotted against the real part of impedance, $Z(f)'$ [88]. From the Nyquist plot, considering the diameter of the semicircle, a charge transfer resistance can be obtained. At high frequency (more than 104 Hz), the impedance implies the conductivity of both active materials and electrolyte. The high-to-medium frequency region (from 104 to 1 Hz) shows pseudocharge transfer resistance, which is associated with the porous structure of the electrodes. At low frequency ranges (less than 1 Hz), the impedance plot has the characteristic feature of a pure capacitive behaviour. Theoretically, a pure capacitor should display a parallel line to the imaginary axis of the Nyquist plot. However, in normal cases, the plot shows a line with the inclined angle between 45° and 90° against the real axis, corresponding to the ion diffusion mechanism between Warburg diffusion and ideal capacitive ion diffusion (pseudocapacitance) [89]. This deviation from the parallel line may be attributed to two

reasons: one is the different penetration depth of the alternating current signal in virtue of pore size distribution at both electrodes, leading to abnormal capacitance, the other is the redox reaction at the electrode, giving rise to pseudocapacitance [90].

4.2.3 Properties and applications of EC

ECs have many advantages such as high power density, long-term stability, reversibility, high efficiency, wide range of operating temperatures, environmental friendliness, and safety if compared to other energy storage systems such as batteries and fuel cells [91,92].

In the case of EC the charging and discharging rates are much faster than the electrochemical redox reactions inside batteries [93], because the charge–discharge reaction is not necessarily limited by ionic conduction into the electrolyte bulk since an EC stores electrical charges both at the electrode surface and in the bulk near the surface of the electrode. These rapid rates lead to high power density in EC.

The storage of electrochemical energy in batteries is based on Faradaic reactions, involving irreversible interconversion of the chemical electrode reagents and irreversible phase changes. Differently from what happens in batteries, when energy is stored in an EC, no or negligibly small chemical charge transfer reactions and phase changes are involved during the charging and discharging, so an EC can have almost unlimited cyclability (up to one million cycles with only small changes in its characteristics). Even for pseudocapacitors, although fast redox reactions are involved during charging and recharging, their life expectancy is also much longer than that of batteries [58]. Furthermore ECs can operate at extremely high and low temperatures; the typical operating temperature ranges from 40 to 70 °C. This is advantageous for many applications.

Although ECs display many advantages, they suffer from limited energy density (about 3-4 Wh kg⁻¹) when compared to batteries (>50Wh kg⁻¹) and this is the major challenge for EC applications.

Moreover, the costs of raw materials and manufacturing should be further improved in order to favor EC large-scale commercialization. The major problem is represented by the high cost of the electrode materials. In fact carbon and noble metal oxide such as

RuO_2 , that are the most common electrode materials used in commercial ECs, are really expensive.

For the large-scale production it is also necessary to establish some general standards such as performance, electrode structure, electrode layer thickness, porosity and so on, but that is rather difficult due to the variety of applications.

4.3 Solar cells and organic solar cells

The solar cell is a device that converts the sun radiation to electrical energy. The sun supplies us a clean and unlimited resource of energy, helping us to relieve the energy crises and world pollution. The approach to efficiently utilize this precious source still represents a challenge. Photovoltaic cells have become extensively studied since the 1950s when the first crystalline silicon solar cell, which displayed an efficiency of 6%, was developed at Bell Laboratories [94].

In the last decade, the efficiency has reached about 24 % for crystalline Si solar cells, [95] thus the technology is about to reach the theoretical limit of 30 % [96].

Beside silicon, solar cells have been fabricated using many other semiconductor materials with a variety of device configurations such as single-crystal, polycrystalline, and amorphous thin-film structures [97].

The conventional inorganic solar cells [98] are constituted by a semiconductor that is doped to form a p-n junction across which the photovoltage is generated. The p side contains an excess of the positive charges (holes), and the n side contains an excess of the negative charges (electrons). In the region near the junction, an electric field is formed and the electrons and holes, which are generated by light absorption in the semiconductor bulk, diffuse to this junction where they are directed by the electric field towards the proper electrode.

Beside the most commonly employed inorganic semiconductors, in the last three decades there have been strong efforts to develop devices based on organic semiconductors for photovoltaic applications (OPVs) [99,100]. Organic semiconductors are conjugated solids where both optical absorption and charge transport are dominated by partly delocalized π and π^* orbitals [101]. Candidates for photovoltaic applications include crystalline or polycrystalline films of small molecules (low molecular weight), amorphous films of small molecules prepared by vacuum deposition or solution

processing [102], films of conjugated polymers or oligomers processed from solution, and combinations of any of these materials either with other organic solids or with inorganic materials. Organic semiconductors have become more and more interesting due to their attractive properties such as low cost, high optical absorption coefficients [103] and the possibility to easily coat any substrate, even flexible plastic. For these features organic materials offer the potential to develop a technology that is economically viable for large-scale power generation, based on the production of very thin photovoltaic cells and also thin flexible devices.

In 1959 the first study concerning OPV cell was carried out; the cell was based on anthracene single crystal and exhibited an extremely low efficiency that made it unsuitable for any practical application [104].

An important development in OPV cells came out in 1986 when Tang obtained an efficiency of about 1 % [105]. The result was achieved after the introduction of a new cell architecture, called heterojunction, consisting in the introduction of an electron donor (D) and an electron acceptor (A) in the cell. As it will be discussed in the following paragraph, optical absorption in organic materials does not directly lead to free electron and hole carriers. Thus, to generate an electrical current the hole-electron pair (exciton) must first dissociate; this is the reason why a critical step in the OPVs architecture is the design of the heterojunction between an electron-donor and an electron-acceptor material. Due to the different electron affinities and ionization potentials of the two materials, the resulting potentials at the interface are strong and may favour exciton dissociation: the electron will be accepted by the material with the larger electron affinity and the hole will be accepted by the material with the lower ionization potential, in the case that the difference in potential energy is larger than the exciton binding energy.

After this discover, many efforts have been made in order to achieve the best device configuration and to find the best donor and acceptor materials to improve the power efficiency conversion of the cells.

4.3.1 Organic cells mechanism

The physical process of converting light into electricity in an organic solar cell consists of three steps [106]: sunlight photons which are absorbed inside the device excite the donor (1), leading to the formation of an excited state, consisting of electron-hole pair

(exciton) in the conjugated polymer, the excitons start to diffuse within the donor domain (2) and if they encounter the interface with the acceptor, then a fast dissociation takes place (3) leading to charge separation.

In a conventional inorganic semiconductor, optical absorption results in the immediate creation of free charge carriers, on the contrary in an organic semiconductor it leads to the formation of an electron and hole with opposite spin, bound by their Coulombic attraction in a singlet exciton state, *i.e.*, a Frenkel-like localized exciton [107], which is electrically neutral. This mechanism is due to the low dielectric constant (typically 2–4) [108] of the organic materials compared to inorganic semiconductors. As a result, the bound electron–hole pair either recombines or dissociates into free charge carriers when the carriers are able to escape their mutual Coulombic attraction. In this case the thermal energy at room temperature is not sufficient to dissociate a photogenerated exciton (typical binding energy of 0.4 eV) into free charge carriers [109]. In Figure 4.4 the charge transport mechanism and energy level diagram of an organic solar cell are shown. The exciton diffusion length, which characterizes the effective width of the active area of the polymer film at the acceptor interface, has been reported to be 5–8 nm in conjugated polymers [110]. In the ideal case, the characteristic size of the polymer phase in the active layer of the cell grants that all excitons are formed within the diffusion distance from an electron acceptor interface.

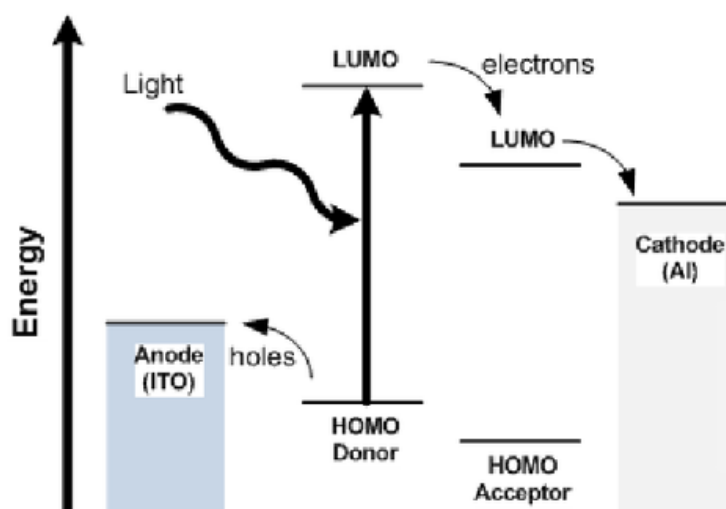


Figure 4.4 – Schematic image of the heterojunction organic solar cells.

As a result, the interpenetrating donor:acceptor network, typical of bulk heterojunction (BHJ) cells, allows for a photon absorption improvement by a simple increase of the

active-layer thickness, thereby maintaining an efficient dissociation of excitons. Exciton diffusion is, therefore, a beneficial process for polymer-based cells because it governs the transfer of the photoexcitation energy towards the electron donor/acceptor interface, where charge carriers are formed. Improvement of the exciton diffusion allows for bigger sized polymer domains leading to an enhanced absorption and solar cell performance [108].

It is possible to study the quenching of the photoluminescence from polymer/fullerene heterostructures [111]. In this approach, the change in the photoluminescence with varying polymer layer thickness in a heterostructure directly reflects the change in exciton population due to their diffusion and subsequent charge transfer at the interface.

4.3.2 Devices architecture

The first and simplest developed heterojunction cells architecture was the single layer, then in order to improve the devices performances, different and more efficient design were studied leading to the production of bilayer heterojunction and eventually bulk heterojunction. The latter are the most efficient and thus, most commonly employed architectures.

In the following paragraphs the main heterojunction cells structures, working principle and properties are briefly described.

4.3.2.1 Single layer heterojunction

Single layer OPV cells are the simplest form. These cells are made of a layer of organic electronic materials in between two metallic conductors [112].

The difference of work function between the two electrodes originates an electric field in the organic layer. When the organic layer absorbs light, forming excitons, the potential produced by the different work functions helps to separate the electron-hole pairs, pulling electrons to the cathode and holes to the anode. Since in organic semiconductors the electrical field developed by the asymmetric work functions of the electrodes does not provide the necessary driving force for charge separation, the principal weakness of single layer architectures is the high probability of charge recombination [113].

4.3.2.2 Bilayer heterojunction

Bilayer cells contain two layers in between the conductive electrodes. One layer is constituted of the electron-acceptor material and the other one of the donor, therefore, electrostatic forces are generated at the interface between the two layers [114]. In the bilayer devices, also called a planar donor-acceptor heterojunction, the organic D/A interface separates excitons much more efficiently than an organic/metal interface in the single layer device. In this device the excitons should be formed within the diffusion length of the interface, otherwise, the excitons will decay, yielding, *e.g.*, luminescence instead of a contribution to the photocurrent. Since the exciton diffusion lengths in organic materials are much shorter than the absorption depth of the film, this limits the width of effective light-harvesting layer.

4.3.2.3 Bulk heterojunction

In the 1990s the first bulk heterojunction cells were developed [115], where the donor and acceptor material are blended together (Figure 4.5); this architecture leads to an increase of the interfacial area between D and A. If the length scale of the blend is similar to the exciton diffusion length, the exciton decay process is considerably reduced since in the proximity of every generated exciton there is an interface with an acceptor where fast dissociation takes place. Hence, charge generation occurs everywhere in the active layer.

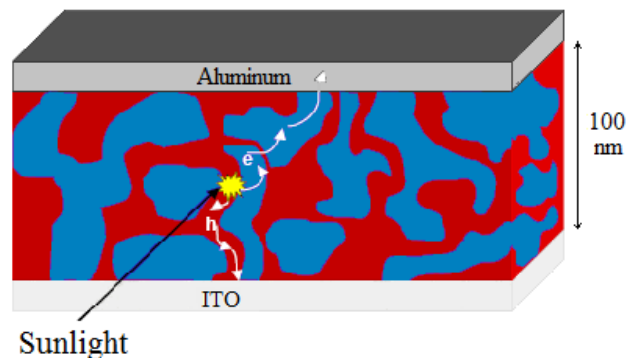


Figure 4.5 – Bulk heterojunction solar cell structure

Provided that continuous pathways exist in each material from the interface to the respective electrodes, the photon-to-electron conversion efficiency and, hence, the photosensitivity is dramatically increased [116].

4.3.3 Common OPV devices materials

As already mentioned, one class of organic materials used as donor in the photoactive layer in BHJ cells that have received considerable attention in the last few years are conducting polymers since they combine the optoelectronic properties of semiconductors with the excellent mechanical and processing properties of plastic materials [117]. Furthermore, it is possible to synthesize the polymer in different ways and to cast it on a support from a solution, using techniques such as spin-coating, ink-jet printing and screen printing. It is also possible to tune the polymer properties, such as band gap, molecular orbital energy level, structural properties, as well as doping.

The first electron-acceptor material employed in the BHJ cells was buckminsterfullerene (C₆₀), then also fullerene derivatives have been studied and among them [6,6]-Phenyl C₆₁ butyric acid methyl ester (PCBM) is currently the most commonly employed molecule.

The first BHJ OPVs, employed poly[2-methoxy,5-(20-ethyl-hexyloxy)-p-phenylene vinylene) (MEH-PPV):C₆₀ or the more easily processable components poly(2-methoxy-5-(30,70-dimethyloctyloxy)-1,4-phenylenevinylene) (MDMO-PPV):PCBM [118]. Recently, the attention has been shifted towards cells based on polythiophene derivatives such as poly(3-hexylthiophene) (P3HT) blended with PCBM. By optimizing the processing conditions, efficiencies of 4-5% have been reported for this materials system [119]. The relatively high efficiency of P3HT:PCBM devices has been partly attributed to the ability of P3HT to self-organize into a two-dimensional lamellar structure in a process mediated by the interpenetration of the side groups of adjacent polymer chains. This ordered structure leads to a very small (3.8 Å) [120] distance between the polymer chains and a high charge mobility for a conjugated polymer.

The molecular structure of the most employed donors and acceptors are shown in Figure 4.6.

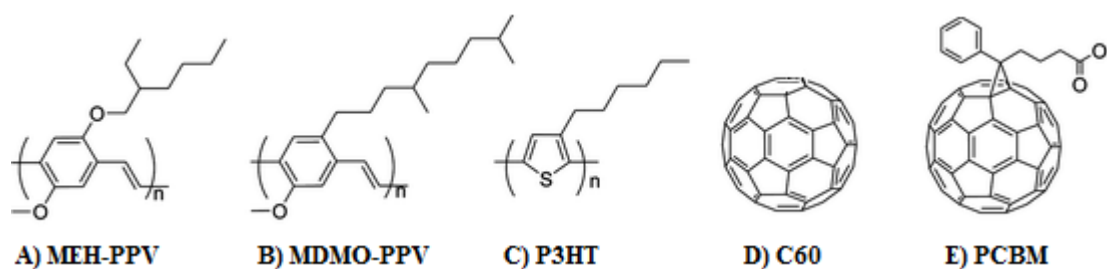


Figure 4.6 – Molecular structure of the main donor (A-C) and acceptor materials (D and E).

An efficient solar cell should have a wide absorption spectrum, so as to create as many excitons as possible. P3HT absorbs photons with wavelengths smaller than 675 nm (band gap energy $E_g \sim 1.85$ eV) [121] but the introduction of aromatic macrocyclic compounds inside the polymer could improve the blend absorption in the visible region spectrum. For this reason, recently, polythiophenes bearing porphyrin groups have been considered [122,123].

4.3.4 Structure of the OPV cells and role of the “hole extracting layer”

The BHJ cells are composed by an anode made of UV/Vis transparent material, which is generally represented by a glass coated with Indium Tin Oxide (ITO). The active layer is composed by the mix (blend) of the donor polymer (polythiophene or a derivative) and the acceptor (fullerene, or derivatives such as PCBM). The cathode of the cells generally consists in an Al film obtained by vacuum deposition of the metal.

In electroluminescence devices and solid-state solar cells it is important that the cell anode is put in contact to a thin film (~ 50 nm) of a buffer layer which favours the holes transport and extraction [124]. Poly(3,4-ethylenedioxythiophene):poly(4-styrenesulfonate) (PEDOT:SS), whose structure is shown in Figure 4.7, is commonly employed because of its suitable properties, such as high conductivity, stability, and transparence [125].

The higher work function of the PEDOT:PSS in comparison with that of ITO, moves the Fermi-level closer to the conjugated polymers HOMO [126]. For this reason the buffer layer improves electronic junction and enhances charge injection at the interface of the electrode, which plays an essential role in various electronic devices [127].

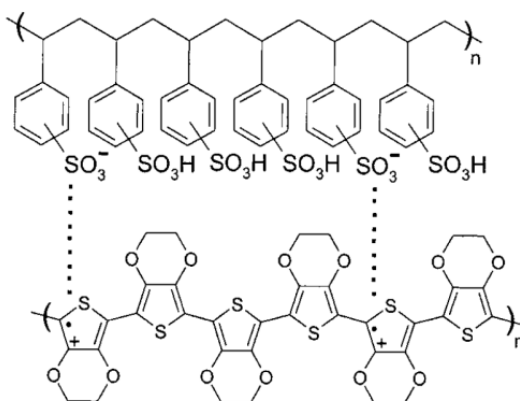


Figure 4.7 – PEDOT:PSS molecular structure.

The buffer layer could be further improved in order to obtain more homogeneous films with the suitable thickness and higher electrical conductivities. In fact, PEDOT:PSS displays a good electrical conductivity (ca. 10 S cm^{-1}) and, even if by virtue of its solubility, thin films can be easily prepared by many kinds of conventional techniques (solvent-casting, spin-casting and dip-coating methods), the surface morphology of the resultant film is not so good, because PEDOT:PSS is a colloidal dispersion in water as a result of the emulsifier effect of PSS.

In literature higher PEDOT conductivities are reported when LiClO_4^- is employed as dopant instead of PSS [128]. Furthermore, the buffer layer could be electrosynthesized directly on ITO electrodes, and even in this case, the best properties of PEDOT, as to its application in organic solar cells, are obtained in the presence of LiClO_4 as the supporting electrolyte [129].

4.3.4.1 Annealing treatments

To improve the cells efficiency, it is important to obtain a photoactive film with a high crystallinity phase, and this goal can be reached performing a thermal annealing after the blend deposition [130,131].

In the case of P3HT:PCBM blends, the annealing treatment leads to the formation of P3HT long fibrils and enhances the hole mobility by an order of magnitude [132] while micrometric PCBM aggregates are formed thanks to diffusion and crystallization of PCBM [119,133]. After a treatment at $150 \text{ }^\circ\text{C}$ for 30 minutes, the best performances in terms of cells efficiency have been reported in the literature [134].

A proper annealing treatment is necessary also for the PEDOT layer. In particular the best conditions in order to obtain the desired morphology and properties of PEDOT films consist of a thermal treatment at $120 \text{ }^\circ\text{C}$, under vacuum for 2 hours [135].

4.3.5 Parameters and performances

The typical current-voltage curves of a solar cell in the dark (A) and under illumination (B) are shown in Figure 4.8. In the dark, there is almost no current flowing, and the cell behaves as a diode. Under illumination the device generates power and the highest production of current (I_{mpp}) occurs at the maximum power point. In the same figure, I_{SC}

is the short-circuit current, *i.e.*, the current through the solar cell when the voltage (V_{OC}) across the solar cell is zero [136]. The short-circuit current is due to the generation and collection of light-generated carriers. For an ideal solar cell at the most moderate resistive loss mechanisms, the short-circuit current and the light-generated current are identical. Therefore, the short-circuit current is the largest current which may be drawn from the solar cell.

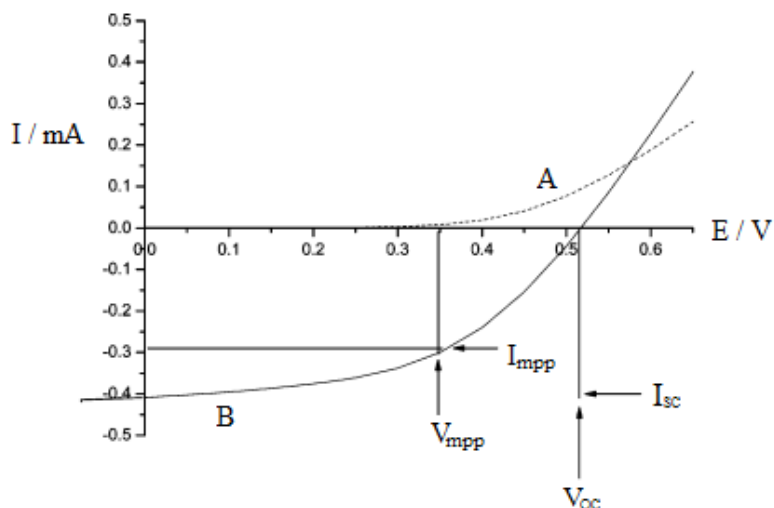


Figure 4.8 – Characteristic I/V curves relative to an organic solar cell in the dark (A) and under illumination (B).

The photovoltaic power conversion efficiency (PCE) of a solar cell is determined by the following formula [137]:

$$PCE = \frac{J_{sc} \cdot V_{oc} \cdot FF}{P_i} \quad (4.4)$$

where V_{OC} is the open circuit voltage, J_{SC} is the short circuit current divided by the cell active area, FF is the fill factor, and P_i is the incident light power density.

J_{SC} is determined by the efficiency of the charge generation, separation and collection. V_{OC} is related to the gap between LUMO of acceptor and HOMO of donor. The fill factor is defined as the ratio of the actual maximum obtainable power to the product of the open circuit voltage and short circuit current. Fill factor is governed primarily by cell resistances, *i.e.*, internal shunt (parallel) and series resistances. In an ideal cell, parallel resistances would be infinite and series resistances would be negligible. Such a cell would be an ideal diode, for which the J/V plot follows an exponential curve and has a

fill factor of 0.89 [138]. The overall solar energy conversion efficiency is the maximum extracted power compared to the incident solar power.

This light intensity is standardized at 1000 W m^{-2} with a spectral intensity distribution matching that of the sun on the earth's surface at an incident angle of 48.2° , which is called the Air Mass (AM) 1.5 spectrum [139].

REFERENCES

- [1] M.G. Walter, E.L. Warren, J.R. McKone, S.W. Boettcher, Q. Mi, E.A. Santori, N.S. Lewis. *Chem. Rev.* 110 (2010) 6446.
- [2] A. Kudo, Y. Miseki. *Chem. Soc. Rev.* 38 (2009) 253.
- [3] M. Winter, R.J. Brodd, *Chem. Rev.* 104 (2004) 4245.
- [4] H. Ibrahim, A. Ilinca, J. Perron, *Renew. Sust. Energ. Rev.* 12 (2008) 1221.
- [5] B. Dunn, H. Kamath, J.M. Tarascon. *Science* 334 (2011) 928.
- [6] I. Katsounaros, S. Cherevko, A.R. Zeradjanin, K.J.J. Mayrhofer. *Angew. Chem. Int. Ed.* 53 (2014) 102.
- [7] B.C.H. Steele, A. Heinzl, *Nature* 414 (2001) 345.
- [8] C.L. Choi, J. Feng, Y. Li, J. Wu, A. Zak, R. Tenne, H. Dai. *Nano Research* 6 (2013) 921.
- [9] G.W. Crabtree, M.S. Dresselhaus, M.V. Buchanan. *Phys. Today* 57 (2004) 39.
- [10] H.B. Gray. *Nat. Chem.* 1 (2009) 7.
- [11] M.W. Kanan, D.G. Nocera. *Science* 321 (2008) 1072.
- [12] S.I. Córdoba, R.E. Carbonio, M. López Teijelo, V.A. Macagno. *Electrochim. Acta* 32 (1987) 749.
- [13] C. Bocca, G. Cerisola, E. Magnone, A. Barbucci. *Int. J. Hydrogen Energ.* 24 (1999) 699.
- [14] M.T.M. Koper. *J. Electroanal. Chem.* 660 (2011) 254.
- [15] S. Floquet, M.E.G. Lyons. *Phys. Chem. Chem. Phys.* 13 (2011) 5314.
- [16] V.I. Birss, A. Damjanovic, P.G. Hudson. *J. Electrochem. Soc.* 133 (1986) 1621.
- [17] B.E. Conway, T.C. Liu. *Langmuir* 6 (1990) 268.
- [18] H. Lv, Y.V. Geletii, C. Zhao, J.W. Vickers, G. Zhu, Z. Luo, J. Song, T. Lian, D.G. Musaev, C.L. Hill, *Chem. Soc. Rev.* 41 (2012) 7572.
- [19] Y. Cai, A.B. Anderson. *J. Phys. Chem. B* 108 (2004) 9829.
- [20] M. Gong, W. Zhou, M.-C Tsai, J. Zhou, M. Guan, M.-C Lin, B. Zhang, Y. Hu, *et al.* *Nat. Commun.* 5 (2014) 4695.
- [21] E. Fabbri, A. Haberer, K. Waltar, R. Kötz, T. J. Schmidt. *Catal. Sci. Technol.* 4 (2014) 3800.
- [22] A.J. Bard, L.R. Faulkner, *Electrochemical Methods: Fundamentals and Applications*, 2001, Second ed., Wiley, New York.
- [23] I.J. Godwin, M.E.G. Lyons. *Electrochem. Commun.* 32 (2013) 39.

- [24] S. Trasatti. *Electrochim. Acta* 29 (1984) 1503.
- [25] A.R. Zeradjanin, N. Menzel, W. Schuhmann, P. Strasser, *Phys. Chem. Chem. Phys.* 16 (2014) 13741.
- [26] C.C.L. McCrory, S. Jung, J.C. Peters, T.F. Jaramillo. *J. Am. Chem. Soc.* 135 (2013) 16977.
- [27] K. Zeng, D. Zhang, *Prog. Energy Combust. Sci.* 36 (2010) 307.
- [28] H. Dau, C. Limberg, T. Reier, M. Risch, S. Roggan, P. Strasser. *Chem. Cat. Chem.* 2 (2010) 724.
- [29] I.C. Man, H.-Y. Su, F. Calle-Vallejo, H.A. Hansen, J.I. Martínez, N.G. Inoglu, J. Kitchin, T.F. Jaramillo, J.K. Nørskov, J. Rossmeisl, *Chem. Cat. Chem.* 3 (2011) 1159.
- [30] R. Kotz, H.J. Lewerenz, P. Bruesch, S. Stucki. *J. Electroanal. Chem.* 150 (1983) 209.
- [31] L.A. Da Silva, V.A. Alves, M.A.P. Da Silva, S. Trasatti, J.F.C. Boodts. *Electrochim. Acta* 42 (1997) 271.
- [32] E.N. Balko, P.H. Nguyen. *J. Appl. Electrochem.* 21 (1991) 678.
- [33] A. Benedetti, P. Riello, G. Battaglin, A. de Battisti, A. Barbieri. *J. Electroanal. Chem.* 376 (1994) 195.
- [34] T. Audichon, E. Mayousse, S. Morisset, C. Morais, C. Comminges, T.W. Napporn, K.B. Kokoh. *Int. J. Hydrogen Energy* 9 (2014) 16785.
- [35] N. Mamaca, E. Mayousse, S. Arrii-Clacens, T.W. Napporn, K. Servat, N. Guillet, *et al. Appl. Catal. B* 111-112 (2012) 376.
- [36] H.G. Sanchez Casalongue, M. Ling Ng, S. Kaya, D. Friebel, H. Ogasawara, A. Nilsson. *Angew. Chem. Int. Ed* 53 (2014) 1.
- [37] D.N. Buckley, L.D. Burke, J.K. Mulcahy. *J. Chem. Soc.* 72 (1976) 1896.
- [38] M. Hamdani, M.I.S. Pereira, J. Douch, A. Ait Addi, Y. Berghoute, M.H. Mendonça, *Electrochim. Acta* 49 (2004) 1555.
- [39] C. Yuan, H.B. Wu, Y. Xie, X.W. Lou. *Angew. Chem. Int. Ed.* 53 (2014) 1488.
- [40] R. Subbaraman, D. Tripkovic, K.-C. Chang, D. Strmcnik, A.P. Paulikas, P. Hirunsit, M. Chan, J. Greeley, V. Stamenkovic, N.M. Markovic, *Nat. Mater.* 11 (2012) 550.
- [41] X. Wang, H. Luo, H. Yang, P.J. Sebastian, S.A. Gamboa. *Int. J. Hydrogen Energy* 29 (2004) 967.
- [42] M.E.G. Lyons, M.P. Brandon. *Int. J. Electrochem. Sci.* 3 (2008) 1386.
- [43] L. Trotochaud, J.K. Ranney, K.N. Williams, S.W. Boettcher. *J. Am. Chem. Soc.* 134 (2012) 17253.

- [44] J. Suntivich, K.J. May, H.A. Gasteiger, J.B. Goodenough, Y. Shao-Horn. *Science* 334 (2011) 1383
- [45] K. Nishio, S. Molla, T. Okugaki, S. Nakanishi, I. Nitta, Y. Kotani. *J. Power Sources* 278 (2015) 645.
- [46] S. Kandalkar, D. Dhawale, C. Kim, C. Lokhande. *Synth. Met.* 160 (2010) 1299.
- [47] R. Kötz, S. Müller, M. Bäertschi, B. Schnyder. P. Dietrich, F.N. Büchi, A. Tsukada, G.G. Scherer, *et al. Electrochem. Soc. Proc.* 21 (2001) 564.
- [48] S. Peng, L. Li, C. Li, H. Tan, R. Cai, H. Yu, S. Mhaisalkar, M. Srinivasan, S. Ramakrishna, Q. Yan. *Chem. Commun.* 49 (2013) 10178.
- [49] V. Hoa Nguyena, C. Lamiela, J.-J. Shim, *Mater. Lett.* 170 (2016) 105.
- [50] R. Ramachandran, S.-M. Chen, G. Gnana Kumar. *Int. J. Electrochem. Sci.* 10 (2015) 10355.
- [51] A.S. Arico, P. Bruce, B. Scrosati, J.-M. Tarascon, W. Van Schalkwijk, *Nat. Mater.* 4 (2005) 366.
- [52] P. Simon and Y. Gogotsi, *Nat. Mater.* 7 (2008) 845.
- [53] J.R. Miller, P. Simon. *Science* 321 (2008) 651.
- [54] G. Yua, X. Xieb, L. Pand, Z. Baod, Y. Cui. *Nano Energy* 2 (2013) 213.
- [55] T. Stimpfling, F. Leroux. *Chem. Mater.* 22 (2010) 974.
- [56] X. Dong, W. Shen, J. Gu, L. Xiong, Y. Zhu, H. Li and J. Shi. *J. Phys. Chem. B* 110 (2006) 6015.
- [57] M.S. Wu and P.C. Chiang. *Electrochem. Solid-State Lett.* 7 (2004) A123.
- [58] Y. Zhang, H. Feng, X. Wu, L. Wang, A. Zhang, T. Xia, H. Dong, X. Li and L. Zhang. *Int. J. Hydrogen Energy* 34 (2009) 4889.
- [59] A. Burke. *J. Power Sources* 91 (2000) 37.
- [60] C. Ming Chuang, C.W. Huang, H. Teng, J.M. Ting. *Energy Fuels* 24 (2010) 6476.
- [61] J. Huang, P. Xu, D. Cao, X. Zhou, S. Yang, Y. Li, G. Wang. *J. Power Sources* 246 (2014) 371.
- [62] Y. Xiao, Y. Cao, Y. Gong, A. Zhang, J. Zhao, S. Fang, D. Jia, F. Li. *J. Power Sources* 246 (2014) 926.
- [63] V. Gupta, N. Miura. *Mater. Lett.* 60 (2006) 1466.
- [64] K. Naoi, M. Morita. *Electrochem. Soc. Interfaces* 17 (2008) 44.
- [65] L. Zhang, X.S. Zhao. *Chem. Soc. Rev.* 38 (2009) 2520.
- [66] L.Z. Fan, Y.S. Hu, J. Maier, P. Adelhelm, B. Smarsly, M. Antonietti, *Adv. Funct. Mater.* 17 (2007) 3083.

- [67] Y.G. Wang, H.Q. Li, Y.Y. Xia. *Adv. Mater.* 18 (2006) 2619.
- [68] D. Choi, G.E. Blomgren, P.N. Kumta, *Adv. Mater.* 18 (2006) 1178.
- [69] Y. Wei, G. Wang, J. Zhu. *ECS Trans.* 58 (2014) 61.
- [70] C.-C. Hu, K.-H. Chang, M.-C. Lin, Y.-T. Wu. *Nano Letters* 6 (2006) 2690.
- [71] X.Y. Lang, A. Hirata, T. Fujita, M.W. Chen. *Nat. Nanotechnol.* 6 (2011) 232.
- [72] T.-C. Wen, C.-C. Hu, *J. Electrochem. Soc.* 139 (1992) 2158.
- [73] G. Mo, Y. Zhang, W. Zhang, J. Ye. *Electrochim. Acta* 113 (2013) 373.
- [74] C.C. Hu, T.W. Tsou. *Electrochem. Commun.* 4 (2002) 105.
- [75] E. Macheaux, T. Brousse, D. Bélanger, D. Guyomard. *J. Power Sources* 165 (2007) 651.
- [76] M.T. Lee, J.K. Chang, W.T. Tsai. *J. Electrochem. Soc.* 154 (2007) A875.
- [77] Z.Y. Li, P.T.M. Bui, D.H. Kwak, M.S. Akhtar, O.B. Yang. *Ceram. Int.* 42 (2016) 1879.
- [78] A.S. Pillai, R. Rajagopalan, A. Amruthalakshmi, J. Joseph, A. Ajay, I. Shakir, S.V. Nair, A. Balakrishnan. *Colloids and Surfaces A: Physicochem. Eng. Aspects* 470 (2015) 280.
- [79] W. Sun, L. Chen, S. Meng, Y. Wang, H. Li, Y. Han, N. Wei. *Mater. Sci. Semicond. Process.* 17 (2014) 129.
- [80] L. Yang, S. Cheng, Y. Ding, X. Zhu, Z. L. Wang, M. Liu. *Nano Lett.* 12 (2012) 321.
- [81] C.-H. Wang, J.-L. Liu, H.-Y. Huang. *Electrochim. Acta* 182 (2015) 47.
- [82] T. Kudo, Y. Ikeda, T. Watanabe, M. Hibino, M. Miyayama, H. Abe and K. Kajita. *Solid State Ionics* 152 (2002) 833.
- [83] X. Zhao, C. Johnston, P.S. Grant. *J. Mater. Chem.* 19 (2009) 8755.
- [84] B. Wang, Q. Liu, Z. Qian, X. Zhang, J. Wang, Z. Li, H. Yan, Z. Gao, F. Zhao, L. Liu. *J. Power Sources* 246 (2014) 747.
- [85] H. Chen, L. Hu, M. Chen, Y. Yan, L. Wu. *Adv. Funct. Mater.* 24 (2014) 934.
- [86] A.A. Yadav, V.S. Kumbhar, S.J. Patil, N.R. Chodankar, C.D. Lokhande. *Ceram. Int.* 42 (2016) 2079.
- [87] G. Wang, L. Zhang, J. Zhang. *Chem. Soc. Rev.* 41 (2012) 797.
- [88] M. Inagaki, H. Konno, O. Tanaike. *J. Power Sources* 195 (2010) 7880.
- [89] W. Sun, R. Zheng, X. Chen. *J. Power Sources* 195 (2010) 7120.
- [90] H. Liu, P. He, Z. Li, Y. Liu, J. Li. *Electrochim. Acta* 51 (2006) 1925.
- [91] B. Babakhani and D. G. Ivey. *J. Power Sources* 195 (2010) 2110.
- [92] S. Sarangapani, B. V. Tilak and C. P. Chen. *J. Electrochem. Soc.* 143 (1996) 3791.

- [93] M. Uzunoglu, M.S. Alam, *IEEE Trans. Energy Convers.* 23 (2008) 263.
- [94] D.M. Chapin, C.S. Fuller, G.L. Pearson. *J. Appl. Phys.* 25 (1954) 676.
- [95] M.A. Green, K. Emery, D.L. King, S. Igari, W. Warta, *Prog. Photovoltaics* 13 (2005) 49.
- [96] M.A. Green, *Solar Cells: Operating Principles, Technology and System Applications*, 1982, Prentice-Hall, Englewood Cliffs, NJ.
- [97] A.M. Bagher, M.M. Abadi Vahid, M. Mohsen. *Am. J. Optics Photonics* 3 (2015) 94.
- [98] S.E. Gledhill, B. Scott, B.A. Gregg, *J. Mater. Res.* 20 (2005) 3167.
- [99] F. Qing, Y. Sun, X. Wang, N. Li, Y. Li, X. Li, H. Wang. *Polym. Chem.* 2 (2011) 2102.
- [100] M. Theander, O. Inganäs. *J. Phys. Chem. B* 103 (1999) 7771.
- [101] A. Mozer, N.S. Sariciftci. *C. R. Chimie* 9 (2006) 568.
- [102] H. Hoppe, N.S. Sariciftci, *J. Mater. Chem.* 19 (2004) 1924.
- [103] H. Hoppe, N.S. Sariciftci, D. Meissner, *Mol. Cryst. Liq. Cryst.* 385 (2002) 113.
- [104] H. Kallmann, M. Pope. *J. Chem. Phys.* 30 (1959) 585.
- [105] C. W. Tang. *Appl. Phys. Lett.* 48 (1986) 183.
- [106] D. Veldman, O. Ipek, S.C.J. Meskers, J. Sweelssen, M.M. Koetse, S.C. Veenstra, J.M. Kroon, S.S. van Bavel, J. Loos, R.A.J. Janssen. *J. Am. Chem. Soc.* 130 (2008) 7721.
- [107] J.-L. Brédas, J.E. Norton, J. Cornil, V. Coropceanu. *Acc. Chem. Res.* 42 (2009) 1691.
- [108] T.M. Clarke, J.R. Durrant. *Chem. Rev.* 110 (2010) 6736.
- [109] P.W.M. Blom, V.D. Mihailetschi, L.J.A. Koster, D.E. Markov. *Adv. Mater.* 19 (2007) 1551.
- [110] D.E. Markov, E. Amsterdam, P. W. M. Blom, A. B. Sieval, J. C. Hummelen. *J. Phys. Chem. A* 109 (2005) 5266.
- [111] M. Hallermann, S. Haneder, E. Da Como. *Appl. Phys. Lett.* 93 (2008) 053307.
- [112] D. Wöhrle, D. Meissner. *Adv. Mater.* 3 (1991) 129.
- [113] P.M. Beaujuge and J.M.J. Fréchet. *J. Am. Chem. Soc.* 133(50) (2011) 20009.
- [114] C. Winder, N.S. Sariciftci. *J. Mater. Chem.* 14 (2004) 1077.
- [115] G. Yu, J. Gao, J. C. Hummelen, F. Wudl, A. J. Heeger. *Science* 270 (1995) 1789.
- [116] M.C. Scharber, N.S. Sariciftci. *Progress in Polymer Science* 38 (2013) 1929.
- [117] I. Burguès-Ceballos, M. Stella, P. Lacharmoise, E. Martínez-Ferrero. *J. Mater. Chem. A* 2 (2014) 17711.

- [118] S.E. Shaheen, C.J. Brabec, N.S. Sariciftci, F. Padinger, T. Fromherz, J.C. Hummelen. *Appl. Phys. Lett.* 78 (2001) 841.
- [119] M. Reyes-Reyes, K. Kim, D. L. Carroll. *Appl. Phys. Lett.* 87 (2005) 083 506.
- [120] T.J. Prosa, M.J. Winokur, R.D. McCullough. *Macromolecules* 29 (1996) 3654.
- [121] G. Denzler, M.C. Scharber, C.J. Brabec. *Adv. Mater.* 21 (2009) 1323.
- [122] W.J. Belcher, K.I. Wagner, P.C. Dastoor. *Sol. Energ. Mat. Sol. C.* 91 (2007) 447.
- [123] K.B. Burke, W.J. Belcher, L. Thomsen, B. Watts, C.R. McNeill, H. Ade, P.C. Dastoor. *Macromolecules* 42 (2009) 3098.
- [124] D. Wakizaka, T. Fushimi, H. Ohkita, S. Ito. *Polymer* 45 (2004) 8561.
- [125] L. Groenendaal, F. Jonas, D. Freitag, H. Pielartzik, J.R. Reynolds. *Adv. Mater.* 12 (2000) 481.
- [126] A.J. Moulé, M.-C. Jung, C.W. Rochester, W. Tress, D. LaGrange, I.E. Jacobs, J. Li, S.A. Mauger, M.D. Rail, *et al.* *J. Mater. Chem. C* 3 (2015) 2664.
- [127] F.L. Zhang, M. Johansson, M.R. Andersson, J.C. Hummelen, O. Inganäs. *Adv. Mater.* 14 (2002) 662.
- [128] Z. Zhengyou, S. Haijun, X. Jingkun, L. Congcong, J. Qinglin, S. Hui. *J. Mater. Sci: Mater. Electron.* 26 (2015) 429.
- [129] A.I. Melato, M.H. Mendonça, L.M. Abrantes. *J. Solid State Electrochem.* 13 (2009) 417.
- [130] R. Cugola, U. Giovanella, P. Di Gianvincenzo, F. Bertini, M. Catellani, S. Luzzati. *Thin Solid Films* 511-512 (2006) 489.
- [131] N. Camaioni, G. Ridolfi, G. Casalbore-Miceli, G. Possamai, M. Maggini. *Adv. Mater* 14 (2002) 1735.
- [132] T. Erb, U. Zhokhavets, G. Gobsch, S. Raleva, B. Stuhn, P. Schilinsky, C. Waldauf, C.J. Brabec. *Adv. Funct. Mater.* 15(7) (2005) 1193.
- [133] H. Hoppe, M. Niggemann, C. Winder, J. Kraut, R. Hiesgen, A. Hirsch, D. Meissner, N.S. Sariciftci. *Adv. Funct. Mater.* 14 (2004) 1005.
- [134] L. Angiolini, V. Cocchi, M. Lanzi, E. Salatelli, D. Tonelli, Y. Vlamidis. *Mater. Chem. Phys.* 146 (2014) 464.
- [135] U. Zhokhavets, T. Erb, H. Hoppe, G. Gobsch, N.S. Sariciftci. *Thin Solid Films* 496 (2006) 679.
- [136] W. Ma, C. Yang, X. Gong, K. Lee, A.J. Heeger. *Adv. Funct. Mater.* 15 (2005) 1617.
- [137] S. Günes, H. Neugebauer, N.S. Sariciftci. *Chem. Rev.* 107 (2007) 1324.

[138] M.G. Walter, A.B. Rudine, C.C. Wamser. *J. Porphyrins Phthalocyanines* 14 (2010) 759.

[139] J. Rostalski, D. Meissner. *Sol. Energy Mater. Sol. Cells* 61 (2000) 87.

5. ELECTROCHEMICAL SENSORS

Amperometric sensors are advantageously applied in many important areas such as food authentication or processing, environmental monitoring, quality control in a number of productions, human health, and a wide number of industrial and natural sectors in which sensing brings added value with respect to laboratory analyses.

Electrochemical sensors have typically small dimension, so they can represent even portable devices, and in addition they allow performing measurements of short duration, they present meaningless deterioration of all components, especially of the sensitive element and require simple pre-treatment of the sample or none at all. Additionally, they are typically low-cost devices. All these characteristics make the sensing systems suitable to perform on-line or even in-line (*in situ*) measurements [1]. Sensors often allow for continuous monitoring of an evolving or flowing system.

In the last two decades a lot of CMEs have been proposed in the literature for the development of electrochemical sensors. Many materials are commonly employed as electrode modifiers. Among the electrode materials suitable for amperometric sensing the most common are polymers [2], organoclays [3], hexacyanometallates [4,5], carbon nanomaterials (carbon nanotubes [6], graphene oxide [7,8], etc), clays [9], metal nanoparticles [10,11], biological recognition elements in the case of biosensors [12,13], zeolites [14], hydrotalcite-like compounds [15] and so on.

The key properties that an amperometric sensor should display are: a low overpotential, high resolution of the individual responses, often gained by the activation of electrocatalytic processes, high sensitivity and very low limit of detection (LOD) in respect to the target analytes, rapid response time, response stability over time, long life time, no occurrence of fouling in order to obtain repeatability of the responses and good selectivity (thus the signals due to the interfering species should be minimized).

5.1 Electrocatalytic process at a CME

Electrochemically reactive molecules are the most interesting candidates to attach to a functionalized surface since they allow for studying the nature of charge transfer and

charge transport processes in thin films, and they can be also employed in electrocatalysis.

By applying a potential to the modified electrode immersed in an electrolytic solution, the redox active specie present in the modifier layer can undergo the same oxidation and reduction processes it would exhibit if dissolved in solution. Thus, sweeping the potential linearly, as in cyclic voltammetry, the reversible redox active specie becomes oxidized as evidenced by an anodic current peak and it is reduced in the reverse potential sweep, giving a cathodic current peak. In this application, the attached molecules act as fast electron transfer mediators for a substrate, dissolved in the solution, and only slowly reduced directly at the bare electrode [16].

In Figure 5.1 is shown a typical example of electrocatalytic process at a CME with decrease in overpotential (η). The terms P and Q correspond to reduced and oxidized states, respectively of the reversible mediator couple.

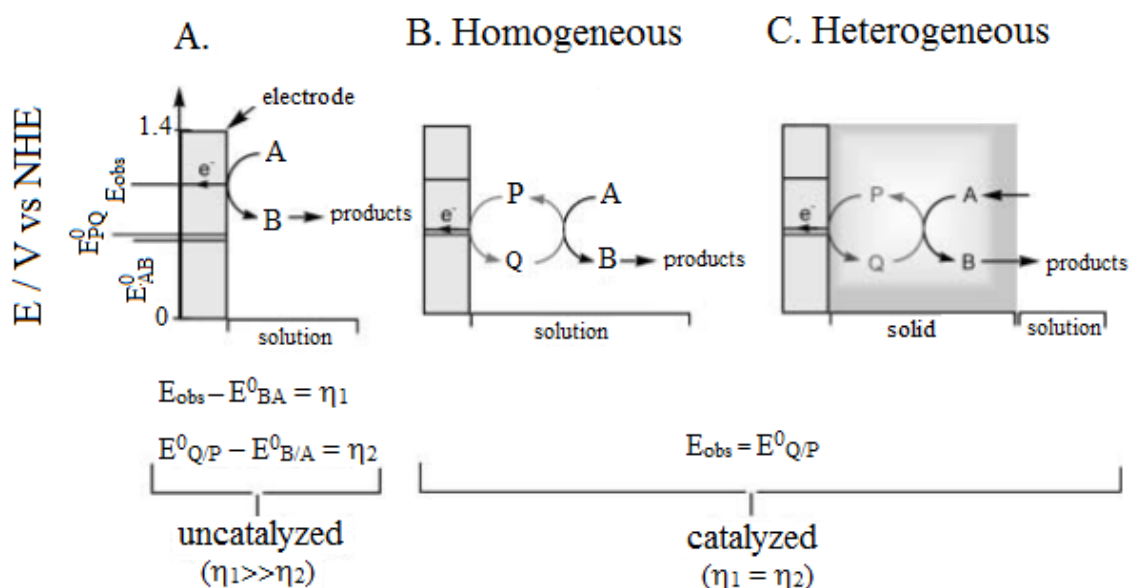


Figure 5.1 - Schematic representation for the oxidation reaction of $A \rightarrow B$ on bare electrode (A) and in the presence of a mediator (B and C). The E_{obs} , $E_{P/Q}^0$, $E_{A/B}^0$ and η correspond to the uncatalyzed process, P/Q mediated process, standard and overpotentials, respectively. In homogenous catalyzed reaction, the P/Q mediator and reactant are in solution phase, while for heterogeneous catalyzed reaction, the P/Q is bonded on the electrode surface [17].

The reversible redox mediator Q/P with a standard potential of $E_{Q/P}^0$ is bonded to a functionalized electrode to promote the irreversible oxidation reaction of $A \rightarrow B^+ + e^-$. A relatively high η is observed at a bare electrode while in the presence of Q/P the reaction

is promoted by redox mediation at $E_{P/Q}^0$ with a low η . This type of CME is not only selective and sensitive but also fast and reusable in analytical measurements.

Even if CMEs can operate both amperometrically and potentiometrically, they are generally used as amperometric sensors, so a Faradaic (charge transfer) reaction is the basis of the experimental measurement or study. In fact, amperometric sensors involve a heterogeneous electron transfer as a result of an oxidation/reduction of an electroactive species at a sensing electrode surface. A current is measured at a certain imposed voltage to the electrode with respect to the reference electrode. Analytical information is obtained from the current-concentration relationship at the chosen applied potential.

On the contrary, potentiometric sensors measure a potential under conditions of equilibrium (zero current) which logarithmically related to the concentration of the analyte in the gas or solution phase. For example, gas-sensing electrodes (*e.g.*, for CO₂ [18], NH₃ [19], NO_x [20]) are potentiometric sensors [21] with the exception of the detection of oxygen, which is generally performed using amperometric electrodes [22].

Also biosensors can operate both amperometrically and potentiometrically. In such sensors the electrode surface is modified by the attachment of a biological recognition element (*e.g.*, enzyme, antibody, DNA, *etc.*), and the electrodes detect the products of a reaction between the immobilized biochemical receptor and a substrate [23].

Another type of chemical sensors is represented by field-effect transistor. Chemically sensitive field effect transistors (CHEMFETs) are basically non-Faradaic electrode systems in which electric field variations in the semiconductor gate region control the magnitude of the source-drain current [24].

5.2 Carbohydrates electrochemical determination

Carbohydrates determination is fundamental in many practical applications such as quality control in food industry, since they are the main constituents of fruits, vegetables and other natural matrices and are involved in many food characteristics such as flavor, quality and storage conditions [25].

Furthermore, glucose has attracted continuous attention in clinical applications. An important issue is to determine directly the level of glucose in biological fluids since its concentration is a crucial indicator for many diseases, such as diabetes and endocrine metabolic disorders [26]. Thus, direct glucose sensing by portable electronic devices is

recognized to be an important power source for evidencing diseases in initial steps. The development of a reliable, accurate, sensitive, rapid, and low-cost glucose sensor is still now very significant.

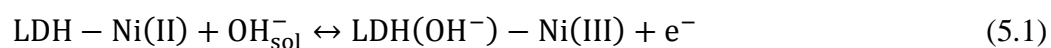
The direct electrochemical process of glucose oxidation at bare electrodes have been deeply studied [27] but most methods suffer from low sensitivity, poor electron transport reaction at the interface, small response stability in a wide range of solution compositions, and high applied potential at which electron transfer takes place [28].

Glucose sensors can be divided into two classes: enzyme-based and non-enzymatic sensors. Enzyme-based sensors have been widely employed as amperometric sensors [29,30] but they suffer from some disadvantages such as instability, high cost of enzymes, complicated immobilization procedures, and critical operating conditions restrict their use.

Among the non-enzymatic sensors LDHs based sensors, as said before, are suitable for glucose detection due to their noticeable electrocatalytic properties towards oxidizable substrates. In addition, they show interesting features, in terms of sensitivity and detection limit, because the catalytic properties are associated to the capability of preconcentrating the analyte, when it is an anion, inside the interlayers domain [31]. Studies are still going on in order to further enhance the sensitivity and the LOD of such sensors.

5.3 Mechanism involved in LDHs electrocatalysis

Ni/Al and Co/Al LDHs have been deeply investigated as electrodes modifiers for amperometric detection. The sensitivity of the measurements depends both on the number of oxidizable sites and on the steric hindrance of the analyte and, hence, on the interlayer spacing [32]. On the basis of all the results obtained on the charge transport and electrocatalytic activity of the Ni³⁺/Ni²⁺ redox couple, the mechanism which involves the Ni centres as redox mediators can be summarized as follows:



where the second reaction is slower than the first one since it has been demonstrated that the rate-limiting step for the oxidation of alcohols and sugars is the diffusion of the substrate towards the Ni centres of the LDH material.

The electrocatalytic properties of LDHs containing Co as the bivalent cation were also studied. The substitution of Ni with Co does not alter significantly the characteristics of CMEs, but Co^{2+} is oxidized at slightly lower potential than Ni^{2+} . This fact induces selectivity in the electro-oxidation of molecules containing hydroxyl groups. In particular, Co/Al- NO_3 -modified electrodes do not display electrocatalytic activity towards monohydric compounds and, consequently, only molecules containing more than one hydroxyl functional group (*e.g.* glycerol, monosaccharides and polysaccharides) can be oxidized at Co/Al LDH-modified electrodes.

In the case of Co/Al LDHs the sensor response is based on the analytes oxidation catalysed by the Co(IV) centres of the LDH layers [33].

REFERENCES

- [1] J.B. Callis, D.L. Illman, B.R. Kowalski. *Anal. Chem.* 59 (1987) 624A.
- [2] C. Zanardi, F. Terzi, R. Seeber. *Anal. Bioanal. Chem.* 405 (2013) 509.
- [3] I.K. Tonle, E. Ngameni, F.M.M. Tchieno, A. Walcarius. *J. Solid State Electrochem.* 19 (2015) 1949.
- [4] F. Ricci, G. Palleschi. *Biosens. Bioel.* 21 (2005) 389.
- [5] H. He, J. Du, Y. Hu, J. Ru, X. Lu. *Talanta* 115 (2013) 381.
- [6] Q. Zhao, Z. Gan, Q. Zhuang. *Electroanalysis* 14 (2002) 1609.
- [7] X. Gong, Y. Bi, Y. Zhao, G. Liub, W.Y. Teoh. *RSC Adv.* 4 (2014) 24653.
- [8] G.G. Wallace, J. Chen, D. Li, S.E. Moulton, J.M. Razal. *J. Mater. Chem.* 20 (2010) 3553.
- [9] D. Tonelli, E. Scavetta, M. Giorgetti. *Anal. Bioanal. Chem.* 405 (2012) 603.
- [10] K.E. Toghill, R.G. Compton. *Int. J. Electrochem. Sci.* 5 (2010) 1246.
- [11] W. Chen, S. Cai, Q.Q. Ren, W. Wen, Y.D. Zhao. *Analyst* 137 (2012) 49.
- [12] J.J. García-Guzmán, M.P. Hernández-Artiga, L. Palacios-Ponce de León, D. Bellido-Milla. *Food Chem.* 182 (2015) 47.
- [13] L. Kong, S. Huang, Z. Yue, B. Peng, M. Li, J. Zhang. *Microchim. Acta* 165 (2009) 203.
- [14] X. Xu, J. Wang, Y. Long. *Sensors* 6 (2006) 1751.
- [15] B. Ballarin, M. Morigi, E. Scavetta, R. Seeber, D. Tonelli. *J. Electroanal. Chem.* 492 (2000) 7.
- [16] P. Gründler, *Chemical Sensors*, 2007, Springer, New York.
- [17] J.-M. Zen, A.S. Kumar, D.-M. Tsai. *Electroanalysis* 15 (2003) 1073.
- [18] J. Maier, M. Holzinger, W. Sitte. *Solid State Ionics* 74 (1994) 5.
- [19] S.C. Hernandez, D. Chaudhuri, W. Chen, N.V. Myung, A. Mulchandani. *Electroanalysis* 19 (2007) 2125.
- [20] N. Miura, G. Lu, N. Yamazoe. *J. Electrochem. Soc.* 143 (1996) L33.
- [21] E.R. Macama, B.M. Whitea, B.M. Blackburnd, E. Di Bartolomeo, E. Traversa, E.D. Wachsmann. *Sensor. Actuat. B-Chem.* 160 (2011) 957.
- [22] R. Toniolo, N. Dossi, A. Pizzariello, A.P. Doherty, S. Susmel, G. Bontempelli. *J. Electroanal. Chem.* 670 (2012) 23.
- [23] F. Charmantray, N. Touisni, L. Hecquet, C. Mousty. *Electroanalysis* 25 (2013) 630.

- [24] J. Janata. *Chem. Rev.* 90 (1990) 691.
- [25] F. Jiménez-Márquez, J. Vázquez, J. Úbeda, J.L. Sánchez-Rojas. *Sens. Actuators B* 225 (2016) 121.
- [26] N. Akhtar, S.A. El-Safty, M.E. Abdelsalam, H. Kowarada. *Adv. Healthc. Mater.* 4 (2015) 2110.
- [27] B. Beden, F. Largeaud, K.B. Kokoh, C. Lamy. *Electrochim. Acta* 41 (1996) 701.
- [28] B. Haghighi, S. Varma, F.M. Alizadeh Sh, Y. Yizgaw, L. Gorton. *Talanta* 64 (2004) 3.
- [29] X. Zhang, Q. Liao, M. Chu, S. Liu, Y. Zhang. *Biosens. Bioelectron.* 52 (2014) 281.
- [30] M. Wooten, S. Karra, M. Zhang, W. Gorski. *Anal. Chem.* 86 (2014) 752.
- [31] C. Mousty. *Appl. Clay Sci.* 27 (2004) 159.
- [32] E. Scavetta, M. Berrettoni, M. Giorgetti, D. Tonelli. *Electrochim. Acta* 47 (2002) 2451.
- [33] I. Gualandi, A.G. Solito, E. Scavetta, D. Tonelli. *Electroanalysis* 24 (2012) 857.

6. EXPERIMENTAL SECTION

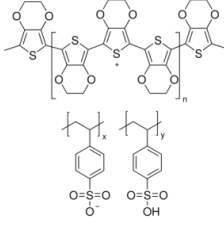
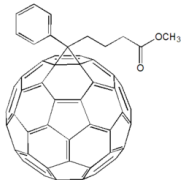
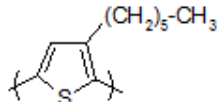
In this section the preparation of the modified electrodes, and the experimental setup for the measurements will be described.

6.1 Chemicals

Table 6.1 List of all the chemicals employed.

Reagent	Chemical formula	Assay	Brand / manufacturer
Cobalt(II) nitrate hexahydrate	$\text{Co}(\text{NO}_3)_2 \cdot 6\text{H}_2\text{O}$	98 % pure	Sigma-Aldrich
Nickel(II) nitrate hexahydrate	$\text{Ni}(\text{NO}_3)_2 \cdot 6\text{H}_2\text{O}$	99.999 % pure	Sigma-Aldrich
Aluminum nitrate nonahydrate	$\text{Al}(\text{NO}_3)_3 \cdot 9\text{H}_2\text{O}$	> 96 % pure	Sigma-Aldrich
Iron(III) nitrate nonahydrate	$\text{Fe}(\text{NO}_3)_3 \cdot 9\text{H}_2\text{O}$	99 % pure	Riedel-de Haenand
Sodium hydroxide	NaOH	98 % pure	Sigma-Aldrich
Sulfuric acid	H_2SO_4	95-98 % w/w	J. T. Backer
Ni/Al, Ni/Fe, Mg/Al and Mg/Fe layered double hydroxides	$[\text{M}(\text{II})_{x-1}\text{M}(\text{III})_x(\text{OH})_2]\text{Br}_{0.19}(\text{CO}_3)_{0.05} \cdot n\text{H}_2\text{O}$	Aqueous colloidal suspensions containing 3.5 mg/mL	Synthesized by Researchers from CNR-ISOF of Bologna and University of Perugia.
Hydrochloric acid	HCl	37 % (w/w)	Merck
Hydrogen peroxide	H_2O_2	35 % (w/w)	Aldrich
Ammonia	NH_3	28 % (w/w)	Normapur
Lithium perchlorate	LiClO_4	> 99 % pure	Fluka BioChemika
Chlorobenzene	$\text{C}_6\text{H}_5\text{Cl}$	99% pure	Carlo Erba
Acetonitrile	CH_3CN	99,8 % pure	JT Baker

EXPERIMENTAL SECTION

Acetone	CH_3COCH_3	$\geq 98.8\%$ pure	Nova Chimica
Isopropyl alcohol	$\text{C}_3\text{H}_7\text{OH}$	$\geq 99.7\%$ pure	Sigma-Aldrich
3,4-Ethylenedioxythiophene	EDOT $\text{C}_6\text{H}_6\text{O}_2\text{S}$	MW=142.15 g/mol $d = 1.334 \text{ g/cm}^3$	Aldrich
Tetrabutylammonium hexafluorophosphate	TBAPF6	$> 99.0\%$ pure	Fluka
Poly(3,4-ethylenedioxythiophene-poly(styrene sulfonate))	PEDOT:PSS 	(2.8 % w/w, dispersion in water, PEDOT content 0.14 %, PSS content 2.6 %, M.W. 1000-1500 g mol^{-1})	Aldrich
[6,6]-Phenyl C61 butyric acid methyl ester	PCBM 	99 % pure	SES Research Texas
Poly(3-hexylthiophene)	P3HT 		Synthesized by the Polymers Research Group at the Department of Industrial Chemistry, Bologna.
Poly[(3-(6-bromohexyl)thiophene)- <i>co</i> -(3-[5-(4-phenoxy)-10,15,20-triphenylporphyrinyl]hexylthiophene)]	rr-P(T6Br- <i>co</i> -P6TPP)		Synthesized by the Polymers Research Group at the Department of Industrial Chemistry, Bologna.

6.2 Chemical equipments

- Analytical balance (AT21 Comparator, Mettler Toledo, accuracy: ± 0.001 mg, capacity up to 22 g).
- Analytical balance (SCALTEC SPB32, error: ± 0.0001 g, capacity up to 120 g).
- Micropipettes 0.5-10, 10-100, 100-1000 μL (Pipetman Gilson).

- Laboratory glassware.

The electrochemical deposition and characterization were performed by using a PGSTAT 20 Autolab potentiostat (Ecochemie) controlled by a personal computer via GPES 4.9 software (Windows operating system) and by using a CH Instrument Mod. 660 C, controlled by a personal computer via CH Instrument software, connected to a PINE Research Instrumentation Modulated Speed Rotator (MSR).

All electrochemical experiments were carried out using a single compartment, three-electrode cell composed by the following electrodes:

- Working electrodes:
 - ❖ Pt or GC rotating disk electrode (0.5 mm diameter) for the applications of the LDH modified electrodes as OER catalysts and as pseudocapacitor materials;
 - ❖ Pt electrodes (BASi, 2 mm diameter) for the LDHs sensors applications;
 - ❖ ITO coated glass slides ($R_s = 4\text{--}8 \Omega \text{ cm}^{-1}$, size 2.5 cm \times 0.8 cm, thickness 1 mm), purchased from Delta Tech, for the fabrication of BHJ solar cells.
- Reference electrodes:
 - ❖ Hg/HgO electrode (Amel Instruments) to carry out the characterizations in alkaline solutions;
 - ❖ saturated calomel electrode (SCE, Amel Instruments), for the other measurements (electrosynthesis, electrodes pretreatments, etc).
- Counter-electrode: Pt wire (Sigma Aldrich).

6.3 Modification of the electrodes with LDHs

During the experimental work Pt and GC electrode supports were employed and different LDHs were electrosynthesized in order to study the performances of the modified electrodes as OER catalysts and pseudocapacitor materials. The electrochemical behaviour and the electrocatalysis performance of the LDHs containing Iron were deeply investigated and compared with those of the better known Al-based LDHs.

6.3.1 Electrodes modification procedures

6.3.1.1 Pt pre-treatment and electrode modification

Cleaning the electrode is a critical step to achieve a well adherent coating. A pre-treatment of Pt electrodes was performed following the procedure described below. It was demonstrated that the nitrate reduction needs a lower overvoltage for the Pt surfaces submitted to the electrochemical pretreatments, so it can be avoid the addition of KNO_3 as further nitrate sources [1]. The surface was polished to a mirror-like surface first by a mechanical cleaning, using SiC sand-paper and aqueous alumina ($0.05 \mu\text{m}$) slurry on a wet polishing cloth, and then the electrode was submitted to the following electrochemical treatment. First 250 cycles between -0.25 V and $+1.30 \text{ V}$ were performed in $0.1 \text{ M H}_2\text{SO}_4$ at the scan rate of 1 V s^{-1} . Afterwards the electrode was polarized at the potential of -0.90 V vs SCE for 300 s (under stirring in order to remove hydrogen bubbles) in $1.0 \text{ M H}_2\text{SO}_4$, followed by 3 CV cycles between -0.20 V and $+1.30 \text{ V}$ in $0.1 \text{ M H}_2\text{SO}_4$.

The LDH films were deposited on the electrode surface by cathodic reduction of a freshly prepared 0.03 M solution containing M(II) and M(III) at a molar ratio of 3:1 in doubly distilled water. The electrochemical reaction was carried out by applying a fixed potential (-0.90 V vs SCE) for 30 s. After performing the modification, the electrode was immediately rinsed with water. An image of the electrochemical cell (on the left) and a typical LDH film obtained by potentiostatic deposition on Pt (image on the right) are shown in Figure 6.1.



Figure 6.1 – Left: image of the electrochemical cell during the Ni/Fe LDH electrodeposition, right: Pt electrode coated with an electrochemically synthesized Ni/Fe LDH film.

6.3.1.2 GC pre-treatment and electrode modification

Even in the case of GC electrode, a mechanical treatment followed by an electrochemical cleaning was performed. The electrode surface was polished to a mirror-like surface first by a mechanical cleaning with SiC sand-paper and aqueous alumina (0.05 μm) slurry on a wet polishing cloth. Afterwards the electrode was cycled between -0.50 V and +0.50 V in 0.1 M H_2SO_4 at the scan rate of 0.1 V s^{-1} until the cycles were superimposable. For the GC electrode the LDHs films were obtained in the same conditions as those used for Pt with the only exception that the electrode was biased at -1.1 V *vs* SCE.

6.4 LDHs modified electrode characterizations

The electrosynthesized LDHs were characterized by several methods. The electrochemical behaviours were studied by cyclic voltammetry to understand if the presence of iron could affect the redox reactions occurring during the linear potential ramp application. Structural characterizations were performed in order to confirm the LDH phase and better understand the oxidation state of Iron and the possible interaction between M(II) and Fe centres next to each other. The morphology and the adhesion of the material were investigated by SEM.

6.4.1 Electrochemical characterization

The CVs were recorded in order to study the redox activity of the clays and determine the stability of the modified electrodes.

6.4.1.1 Cyclic Voltammetry

The electrochemical behaviour of the LDH modified electrodes (Pt and GC) was studied by cyclic voltammetry between 0 V and the solvent discharge potential at different scan rate (0.005, 0.01, 0.02, 0.04, 0.05, 0.06, 0.08 and 0.1 V s^{-1}), in 0.1 and 1.0 M NaOH. In each experiment CV curves were recorded until the cycles resulted superimposable.

EXPERIMENTAL SECTION

6.4.1.2 Electrodeposition monitored by Electrochemical Quartz Chrystal Microbalance

EQCM experiments were performed using a MAXTEK PM-710EQCM device, connected to the Autolab potentiostat. The probe was equipped with a 5 MHz AT-cut quartz crystal coated with sputtered Pt (surface area 1.37 cm²). Even in this case, before the electrodeposition the electrode was pre-treated as described in paragraph 6.3.1.1.

6.4.2 Structural characterization

6.4.2.1 X-ray diffraction

The XRD patterns of the chemical and electrosynthesized LDH films were recorded, after metallization with gold, using a Philips X'Pert Pro diffractometer with a Cu K α radiation ($\lambda = 0.15415$ nm) operating at 40 kV and 40 mA and using an X'Celerator detector. A step size of 0.0334 2 θ degree with a counting time per step of 650 s was used for the electrochemically deposited LDHs in order to increase the spectra resolution. The samples were analyzed directly introducing the Pt electrode plates (area =1 cm²) in the optical center of the diffractometer. In order to have films thickness suitable for this characterization the electrodeposition step (previously described in paragraph 6.3.1.1) was repeated 10 times at the same electrode (total deposition time of 300 s).

6.4.2.2 X-ray Photoelectron Spectroscopy

A PHI 5000 Versaprobe II Scanning X-ray Photoelectron Spectrometer, equipped with a monochromatic Al K-alpha X-ray source (1486.6 eV energy, 15 kV voltage and 1.0 mA anode current), was used to investigate surface chemical composition. A spot size of 100 μm^2 was used in order to collect the photoelectron signal for both the high resolution (HR) and the survey spectra. Different pass energy values were exploited: 187.85 eV for survey spectra and 23.5 eV for HR peaks. All the spectra were analysed by using the Casa XPS software. Peaks shifts were normalized with the C1s peak set at 284.5 eV and after calibration the background from each spectrum was subtracted using a Shirley-type background. The core level spectra were deconvoluted with a nonlinear iterative least

squares Gaussian fitting procedure. All survey scans were analysed to determine the composition of the analysed samples by applying the proper sensitivity factors.

The samples were prepared on Pt electrode plates (area =1 cm²), with the same procedure described for the XRD characterizations in the previous paragraph. Besides the films as such, also samples of the same LDHs were prepared and oxidized in potentiostatic conditions at the oxidation peak potential for 180 s.

6.4.2.3 X-ray Absorption Spectroscopy

XAS experiments were performed at ELETTRA Synchrotron Radiation Laboratory (Basovizza, Trieste), at the XAFS beam line 11.1. The data were recorded in fluorescence mode using a large area Si drift diode detector (KETEK).

Two samples were prepared, namely, Ni/Fe LDH pristine and oxidized. For these experiments the Ni/Fe LDHs samples were electrosynthesized on ITO electrodes ($R_s = 4\text{--}8 \Omega \text{ cm}^{-1}$, size 2.5 cm × 0.8 cm, thickness 1 mm), purchased from Delta Tech. Before the film deposition the electrodes were cleaned as follows; ITO-coated glasses were soaked in sequence in aqueous detergent solution, acetone and isopropyl alcohol for 15 min, under sonication, and then dried. A Bandelin Sonorex Super Sonicator (RK 510 H) was used for the cleaning of the ITO electrodes.

The electrodeposition of the LDHs was carried out performing two deposition steps of 30 seconds at the potential of -1.1 V vs SCE. One sample was then oxidized in potentiostatic conditions, applying the anodic peak potential for 120 seconds.

XAS spectra were recorded at the Ni and Fe K-edge (8333 eV and 7112 eV, respectively) using a Si(111) single crystal as monochromator. EXAFS and XANES curves were recorded at room temperature.

6.4.3 Morphological characterization

The composition of the electrosynthesized LDHs was investigated by SEM/EDX analysis, using an EVO 50 Series Instrument (LEO ZEISS) equipped with an INCA Energy 350 EDX microanalysis system and INCA SmartMap for imaging the spatial variation of the elements in a sample (Oxford Instruments Analytical). The accelerating voltage was 25 kV or 10 kV, the beam current 1.5 nA and the spectra collection time 100

s. FE-SEM images were acquired with a Zeiss Supra 55 FE-VP operating at 3 keV, after metallization with gold.

6.5 Evaluation of the performances of LDH modified electrodes

6.5.1 OER catalytic activity and modified electrode durability

The OER catalytic activity of the electrodes coated with the LDHs was investigated in alkaline solution (0.1 and 1.0 M NaOH) by linear sweep voltammetry, recording iR-corrected polarization curves at the scan rate of 0.005 V s⁻¹.

The durability of the LDHs was studied recording chronopotentiometric curves by applying for an hour three different current densities: 1.5, 2.0 and 2.5 mA cm⁻². During both the LSV and chronopotentiometric experiments, the working electrode was constantly rotated at 1600 rpm in order to remove the oxygen bubbles from the electrode surface.

The Tafel slopes were calculated between 0.63 and 0.71 V for the Al-based LDHs and between 0.61 and 0.65 for the Fe-based LDHs.

6.5.2 Pseudocapacitors performances

Electrochemical impedance spectroscopy was employed to study the capacitance behaviour of Ni/Al, Co/Al, Ni/Fe and Co/Fe LDHs. Impedance spectra were recorded for each LDH in the potential range of the anodic wave avoiding potential higher than that of the oxygen evolution reaction and were plotted in the Nyquist plot form.

The specific capacitances of the Co-based LDHs on Pt and GC were calculated by two different methods. One way to perform measurements on material capacitance is to coat an electrode surface with the chosen material, then to record cyclic voltammograms of the material, from which the capacitance can be calculated.

The specific capacitance of the electrodes coated with the LDHs was calculated also from the galvanostatic charge-discharge curves recorded at different current densities. The electrochemical measurements were conducted in alkaline solution (0.1 and 1.0 M NaOH).

The specific capacitance (F g⁻¹) was evaluated from the CV [2], since the charge accumulated inside the material is related to the area under the cyclic voltammogram in a

proper potential window. When the solution was 0.1 M NaOH, the values were calculated between 0.35 and 0.70 V in the case of Co/Al, between 0.50 and 0.75 V for the Co/Fe, between 0.63 and 0.73 V for the Ni/Al, and between 0.54 and 0.63 V for the Ni/Fe LDH. In 1.0 M NaOH C_s was calculated between 0.34 and 0.61 V for the Co/Al, between 0.17 and 0.55 V in the case of Co/Fe, between 0.55 and 0.66 V for the Ni/Al, and between 0.55 and 0.63 for the Ni/Fe LDH.

From the CVs the specific capacitance can be obtained by eqn (6.1) where I (A) is the current value, m (g) is the mass and v is the scan rate ($V s^{-1}$).

$$C_s = \frac{I^2}{v \cdot m} \quad (6.1)$$

The mass of the material deposited on Pt electrode during the electrosynthesis was determined from the EQCM response for each LDH.

The LDHs were tested by performing galvanostatic charge-discharge tests, in a stable potential window under the charging condition of constant current density (1.0, 2.0, 5.0 and 10.0 $A g^{-1}$). The discharge was performed with the same constant current density.

The specific capacitance was calculated by equation 6.2 [3]:

$$C_s = \frac{I \cdot \Delta t}{m \cdot \Delta V} \quad (6.2)$$

Where I (A) represents the discharge current, m (g) is the mass, Δt and ΔV are the total discharge time and the potential drop during discharge, respectively.

Long-term cycling stability was investigated carrying out 1000 cycles at a current density of 5.0 $A g^{-1}$.

6.6 Bulk heterojunction solar cells fabrication

6.6.1 Electrochemical measurements and characterizations

The redox behaviour of PEDOT:PSS and PEDOT:ClO₄ films on Pt electrodes was studied by cyclic voltammetry between -1.25 and +1.1 V vs SCE. Prior to the electrochemical measurements, the solution was purged by bubbling N₂ for 20 min and a nitrogen atmosphere was maintained over the solution during the experiments.

The redox behaviour of the OPV device components was studied by cyclic voltammetry. All the electrochemical measurements were performed using a single-compartment,

EXPERIMENTAL SECTION

three-electrode cell in acetonitrile solution with 0.1 M TBAPF₆ as supporting electrolyte. The electrochemical characterizations of the polymers and of the blend were performed using a Pt electrode coated with a thin film of polymer deposited by casting of a proper solution. The rr-P(T6Br-co-T6TPP) was investigated by CV between 0 and +1.3 V, PCBM between -2.1 and +1.2 V and the blend between -2.1 and +1.3 V. The CV of PCBM was recorded keeping the compound in an acetonitrile/dichlorobenzene solution. Generally, the CVs were recorded at different potential scan rates, from 0.1 to 0.5 V s⁻¹ and five voltammograms were sequentially recorded.

UV-Vis-NIR spectra of casted thin films of PEDOT:PSS, PEDOT:ClO₄, rr-P(T6Br-co-T6TPP) copolymer, rr-P(T6Br-co-T6TPP):PCBM blend (1:1 w/w) and PCBM on ITO were recorded by an HP 8453 diode array spectrophotometer (Agilent) at room temperature, using quartz cuvettes.

The emission spectra of the photoactive layer components casted on quartz support were obtained using an Edinburgh FLS920 spectrometer equipped with a Peltier-cooled Hamamatsu R928 photomultiplier tube (185-850 nm). An Edinburgh Xe900 450 W xenon arc lamp was used as the excitation light source.

Morphological studies were performed by atomic force microscope using a Solver Pro P47-H and an Axiolab A optical microscope (Zeiss). AFM characterizations were performed in standard semi-contact mode acquiring simultaneously both height and phase signal.

The photovoltaic properties of the fabricated devices were measured by recording the J/V characteristics using a Keithley Instruments 2400 SourceMeter, under 1000 W m⁻² white light illumination from a standard AM 1.5 Solar Simulator lamp (Abet Technologies LS 150-Xe). J/V curves were recorded to test the devices operability as diodes and as solar cells, measuring current with a potential sweep from -3 to +3 V and from -0.1 to +0.6 V, respectively. To evaluate the reproducibility of cells fabrication, three independent devices were prepared for each experiment.

The power conversion efficiency was calculated by the following equation [4]:

$$\text{PCE} = \frac{J_{\text{sc}} \cdot V_{\text{oc}} \cdot \text{FF}}{P_{\text{i}}} \quad (6.3)$$

where V_{oc} is the open circuit voltage, J_{sc} is the short circuit current divided by the cell active area, FF is the fill factor, and P_{i} is the incident light power density.

6.6.2 ITO electrode preparation

To remove the ITO film from the edge of the electrodes in order fix to the area (0.25 cm^2 , as shown in Figure 6.2) and to avoid a short circuit, a chemical etching was done using a 10% (w/w) HCl solution, at $60 \text{ }^\circ\text{C}$.

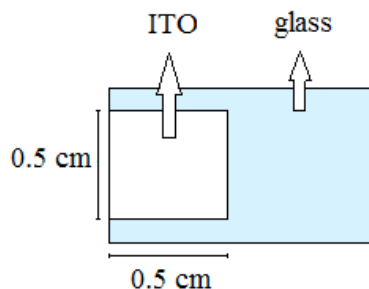


Figure 6.2 – Schematic illustration of an ITO after the etching.

Then ITO-coated glasses were soaked in sequence in aqueous detergent solution, acetone and isopropyl alcohol for 15 min, under sonication, and then dried. A Bandelin Sonorex Super Sonicator (RK 510 H) was used for the cleaning of the ITO electrodes. The substrates as such were employed for the PEDOT electrodeposition, whereas a further cleaning procedure was applied in order to activate the hydroxyl groups of the electrode surface before PEDOT:PSS casting. The glasses were immersed in a solution consisting of 20 mL of distilled water and 1 mL of 33% (w/w) aqueous NH_3 which was heated to $60 \text{ }^\circ\text{C}$, then 4 mL of 35 % (w/w) H_2O_2 were added and the solution was kept at the mentioned temperature for 20 min (RCA cleaning procedure [5]).

6.6.3 Fabrication of the OPV devices

The ITO anode was coated with the hole transporting layer PEDOT, either by casting (PEDOT:PSS) or by electrochemical synthesis (PEDOT: ClO_4). PEDOT:PSS was diluted 1:1 in isopropyl alcohol before the deposition. Doctor Blade equipment (Sheen Instruments Model S265674) was used as film applicator to coat ITO with PEDOT:PSS in order to obtain the desired layer thickness ($\sim 50 \text{ nm}$). The polymeric film was dried under nitrogen gas stream. Then, the PEDOT-modified electrodes were annealed at $120 \text{ }^\circ\text{C}$ under vacuum for 2 h, using a Büchi B-580 evaporator and stored under vacuum.

The photoactive layer, *i.e.*, the blend constituted of the copolymer (rr-P(T6Br-co-T6TPP)) or P3HT:PCBM was deposited, after filtration on a Teflon septum ($0.2 \text{ }\mu\text{m}$ pore

EXPERIMENTAL SECTION

size), by casting onto the ITO/PEDOT electrode (thickness ~ 150 nm). P3HT was synthesized by us using the McCullough procedure [6] (98 % HT dyads content, $51.000 \text{ g mol}^{-1}$). Poly [(3-(6-bromohexyl)thiophene)-*co*-(3-[5-(4-phenoxy)-10,15,20-triphenylporphyrinyl] hexylthiophene) (rr-P(T6Br-*co*-T6TPP)) was synthesized by the polymer research group (Department of Industrial Chemistry, Bologna) [7]. The chemical structure of the rr-P(T6Br-*co*-T6TPP) copolymer is shown in Figure 6.3.

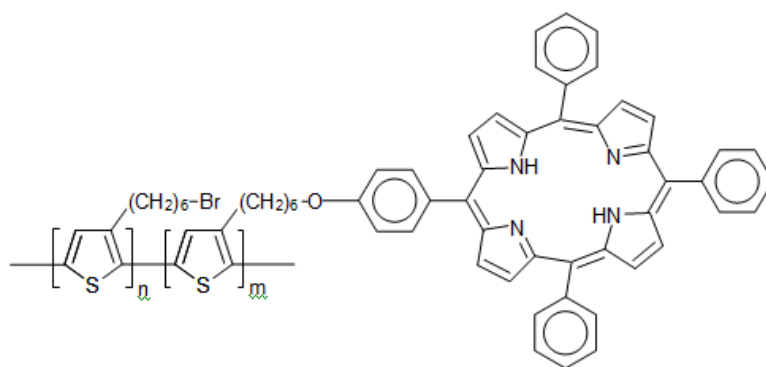


Figure 6.3 - Chemical structure of rr-P(T6Br-*co*-T6TPP) copolymer

The blend was prepared by dissolving 20 mg of rr-P(T6Br-*co*-T6TPP) or P3HT and 20 mg of PCBM in 1 mL of chlorobenzene. The film was dried under nitrogen gas stream and stored in vacuum. After the blend deposition, the cells were annealed at $150 \text{ }^\circ\text{C}$ for 30 min.

Finally, an aluminum cathode (150–200 nm thick) was deposited onto the composite film by vapor deposition under vacuum (pressure of about 1×10^{-4} Pa) using an Edwards coating system E306A. The active area of the cell was fixed to be 0.25 cm^2 by an aluminum mask. The cells structure is schematically shown in Figure 6.4.

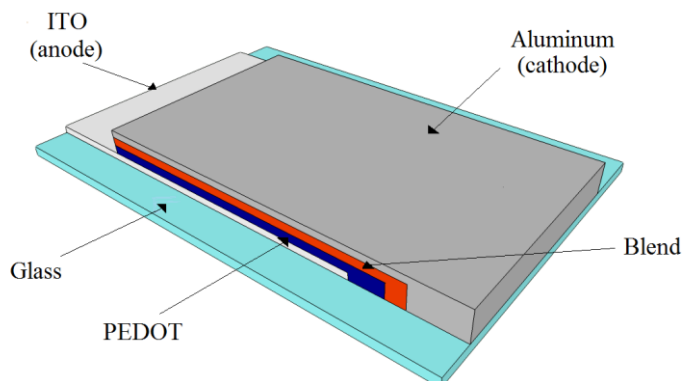


Figure 6.4 - Schematic structure of the fabricated bulk heterojunction solar cells.

6.6.4 *Synthesis of PEDOT:ClO₄*

The PEDOT layer was polymerized from $5.0 \cdot 10^{-3}$ M EDOT aqueous solution in the presence of 0.1 M LiClO₄ as supporting electrolyte. The oxidative polymerization was carried out applying a constant potential of +1.05 V vs SCE for 10 s. The obtained film was thinned applying 25 potential cycles at 0.05 V s^{-1} from 0 to +1.3 V in the solution containing only the supporting electrolyte in order to obtain a film thickness of about 50 nm, which is the ideal value required for traditional cells. The films thickness was checked before and after the application of potential cycles by AFM. Finally, PEDOT-modified ITO electrodes were washed in distilled water and dried in nitrogen gas stream.

6.7 Amperometric sensors based on LDH modified electrodes

6.7.1 *Sensors based on chemically and electrochemically synthesized Ni-based LDH for the detection of glucose*

6.7.1.1 Equipments

Metal analyses of the LDHs obtained by chemical synthesis were performed by Varian 700-ES series Inductively Coupled Plasma–Optical Emission Spectrometer (ICP–OES) using solutions prepared by dissolving the samples in concentrated HNO₃ and then properly diluted.

Coupled thermogravimetric (TGA) and differential thermal (DTA) analyses were performed with a Netzsch STA 449C apparatus, in air flow and heating rate of $10 \text{ }^\circ\text{C min}^{-1}$.

The XRD patterns of the chemical and electrosynthesized LDH films were recorded, after metallization with gold, using a Philips X'Pert Pro diffractometer with a Cu K α radiation ($\lambda = 0.15415 \text{ nm}$) operating at 40 kV and 40 mA equipped with an X'Celerator detector. A step size $0.0170 \text{ } 2\theta$ degree with 20 s step scan was used for chemically prepared LDHs. The samples were analyzed directly introducing the Pt electrode plates (area = 1 cm^2) in the optical center of the diffractometer.

Atomic force microscopy (Solver-Pro, NT-MDT) was also used to provide information on particle size and shape. The samples of the chemically and electrochemically

EXPERIMENTAL SECTION

synthesized LDHs were deposited on Pt plates (area = 1 cm²). Atomic force microscope topographical images were collected using an NT-MDT solver scanning probe microscope in tapping mode.

6.7.1.2 Pt surface modification

The LDHs obtained by chemical route were synthesized by Researchers from National Research Council (CNR-ISOF) of Bologna and from the University of Perugia, according to the following method (all chemicals were of reagent grade purity, purchased by Sigma-Aldrich and used as received). Colloidal aqueous dispersions of Mg/Al, Mg/Fe, Ni/Al and Ni/Fe LDHs were prepared by the double-microemulsion method [8]. Briefly, two microemulsions designated A and B were prepared by dispersing 6.25 g of Cetyltrimethylammonium bromide, 18.1 mL of n-butanol, 7.75 mL of isooctane, and 6.75 mL of aqueous phase. The aqueous phase A consisted of 0.4 M M(NO₃)₂ (where M can be Mg or Ni) and 0.125 M M(NO₃)₃ (where M can be Al or Fe). The aqueous phase B was a NH₃ solution (5.0 M for the Mg/Al and Mg/Fe LDH samples and 1.25 M for the Ni/Al and Ni/Fe LDH samples).

Equal volumes of the two microemulsions were mixed to obtain the precipitation of LDH nanoparticles (NPs) in the reverse micelles. The resulting system was aged at 70 °C for 16 h. Afterward, the particles were recovered by centrifugation (12,000 rpm, 10 min). The precipitate was washed with an ethanol–chloroform mixture (1:1 v/v) (3 x 30 mL) and then with water (3 x 30 mL). Finally, the precipitate was reconstituted in water (40 mL) to give a colloidal dispersion which was characterized in term of NPs amount by a gravimetric method ([NPs] = 3.5 mg/mL).

After 15 minutes of sonication, 1 µL of a NPs colloidal aqueous dispersion, thus corresponding to a deposited mass of 3.5 µg, was deposited by drop-casting on pretreated Pt electrodes. Finally, the electrode was stored at r.t. for 24 h up to complete dryness.

The electrochemically synthesized LDHs were obtained as described in Par. 6.3.1.1.

6.7.1.3 CV characterizations and amperometric detection of glucose

After the preparation of the electrodes described in the previous paragraph, both the chemically and electrochemically prepared LDHs were stabilized in 0.1 M NaOH, performing 20 CV cycles between +0.3 and +0.7 V in the case of the electrochemical

Ni/Al and the chemical Ni/Fe LDH, between +0.3 and +0.6 V for the electrochemical Ni/Fe LDH and between +0.3 and +0.75 V for the chemical Ni/Al LDH. The stabilization is carried out in order to activate the Ni redox system; between the very first cycles and the last ones, when the cycles become superimposable, the current slowly increases.

Mg/Fe and Mg/Al LDHs were characterized also by CV, performing 20 cycles in the same electrolytic solution between -0.8 and +0.75 V.

The analytical performances of the chemically and electrochemically synthesized Ni/Al and Ni/Fe LDHs were studied in 0.1 M NaOH; the electrode responses were evaluated recording CV curves at different scan rates (0.05 and 0.01 V s⁻¹) for increasing glucose additions (0.1 mmol L⁻¹) to define the working potential. After each addition the solution was stirred for a few minutes and then 3 CV cycles were recorded.

For the best materials in terms of sensitivity, also chronoamperometric curves were recorded for subsequent glucose additions, keeping the solution under stirring. From these curves the calibration graphs (current vs concentration) were obtained. The chosen potential for the measurements were +0.58 V for the electrochemical Ni/Fe and +0.65 V for the electrochemical Ni/Al LDH.

Nyquist plots were obtained recording impedance spectra for each coated electrode, at the peak potential (0.56 and 0.62 V for the electrochemically synthesized Ni/Fe and Ni/Al LDHs, respectively, and 0.61 and 0.66 V for the chemically synthesized Ni/Fe and Ni/Al LDHs).

The catalytic constants were calculated in the following way, according to the literature [9]. Equation 6.4 allows the determination of the rate constant of the reaction between an oxidizable substrate and the oxidized Ni centres in the LDH material:

$$\frac{I_{cat}}{I_L} = \gamma^{0.5} \left[\pi^{0.5} \operatorname{erf}(\gamma^{0.5}) + \frac{e^{-\gamma}}{\gamma^{0.5}} \right] \quad (6.4)$$

where I_{cat} is the catalytic current recorded at the Ni coated electrode in the presence of the substrate, I_L is the limiting current recorded in the same conditions in the absence of an oxidizable substrate, and γ is defined as:

$$\gamma = kc_0t \quad (6.5)$$

EXPERIMENTAL SECTION

where k is the reaction kinetic constant, t is time and c_0 is the substrate bulk concentration. When γ exceeds 1.5, the second factor of Eq. (6.4) is almost equal to $\pi^{0.5}$ and the equation can be reduced to:

$$\frac{I_{cat}}{I_L} = \gamma^{0.5} \pi^{0.5} = \pi^{0.5} (k c_0 t)^{0.5} \quad (6.6)$$

Accordingly, the slope of the plot I_{cat}/I_L as a function of $c_0^{0.5} t^{0.5}$ is equal to $(k \cdot \pi)^{0.5}$.

For each electrode the I_{cat}/I_L versus $c_0^{0.5} t^{0.5}$ plot is linear when the value of $c_0^{0.5} t^{0.5}$ is between $5 \cdot 10^{-3}$ and $2 \cdot 10^{-2} M^{0.5} \cdot s^{0.5}$, and this indicates a good adherence to the model.

The chronoamperometric curves for those calculations were performed by recording the response of the modified electrode in absence of glucose and after several additions of analyte (each one corresponding to 0.05 mM) in the linear range. A pretreatment potential was firstly applied for 30 s, corresponding to a potential at which the Ni centres starts to be oxidized; the pretreatment was then followed by the application of the potential at which the electrocatalysis occurs, for 10 s. The potentials chosen were $E_{pre} = 0.61$ V, $E = 0.65$ V for the electrochemical Ni/Al, $E_{pre} = 0.56$ V, $E = 0.58$ V for the electrochemical Ni/Fe, $E_{pre} = 0.55$ V, $E = 0.63$ V for the chemical Ni/Al LDH. The catalytic constant was not calculated for the chemical Ni/Fe LDH since the electrocatalysis occurs at potentials very close to the solvent discharge.

6.7.2 Co/Al LDH coated Pt for in flow amperometric detection of sugars

The apparatus for the flow injection analysis (FIA) consisted of a HPLC pump (LabFlow 1000), a six-way injection valve equipped with a 50 μ L loop, an electrochemical detector (Metrohm, VA 641 Model) interfaced with a personal computer. The electrochemical detector was constituted of 1 μ L wall-jet cell (Metrohm, 656 Model) in the three-electrode configuration (Ag/AgCl/ KCl 3.0 M as the reference, 2 mm diameter Au as the counter, and the working electrode) and a potentiostat for the amperometric measurements. In the HPLC configuration, the METROSEPCARB1 column (Metrohm) was inserted between the injection system and the detector. The eluent was a 0.1 M NaOH solution prepared starting from a 50 % (w/w) solution, previously-decarbonated, and, DD water. The flow rate was set at 1 mL min⁻¹.

6.7.2.1 Pt surface modification

The electrodeposition was carried out on pretreated Pt electrodes, using the chosen condition for the potentiostatic synthesis described in section 6.3.1.1, for different times, namely 10, 20, 30 and 60 s. The modified electrodes were washed with DD water before performing the characterizations in CV. The electrocatalytic tests were performed for the LDHs electrosynthesized for 20 and 60 s.

6.8 Data elaboration

All the graphs were elaborated using the software Origin 9.0 and Microsoft Office Excel 2007. EIS data were fitted using Z-view software (Scribner Associates, USA).

REFERENCES

- [1] I. Gualandi, A.G. Solito, E. Scavetta, D. Tonelli. *Electroanalysis* 24(4) (2012) 857.
- [2] T. Stimpfling, F. Leroux. *Chem. Mater.* 22 (2010) 974.
- [3] Q. Wang, L. Jiao, H. Du, Y. Wang, H. Yuan. *J. Power Sources* 245 (2014) 101.
- [4] S. Günes, H. Neugebauer, N.S. Sariciftci. *Chem. Rev.* 107 (2007) 1324.
- [5] B. Gunduz, I.S. Yahia, F. Yakuphanoglu. *Microelectron. Eng.* 98 (2012) 41.
- [6] R.S. Lowe, P.C. Ewbank, J. Liu, L. Zhai, R.D. McCullough. *Macromolecules* 34 (2001) 4324.
- [7] K.B. Burke, W.J. Belcher, L. Thomsen, B. Watts, C.R. McNeill, H. Ade, P.C. Dastoor. *Macromolecules* 42 (2009) 3098.
- [8] F. Bellezza, M. Nocchetti, T. Posati, S. Giovagnoli, A. Cipiciani. *J. Colloid Interface Sci.* 376 (2012) 20.
- [9] M.H. Pournaghi-Azar, H. Razmi-Nerbin. *J. Electroanal. Chem.* 488 (2000) 17.

RESULTS AND DISCUSSION

7. LDHs AND CONDUCTING POLYMERS AS ELECTRODES MODIFIERS: ENERGY APPLICATIONS

7.1 LDHs characterizations and performances

In this section the electrochemical and structural characterizations of the LDH modified electrodes will be reported and the performances obtained employing the modified electrodes as OER catalysts and pseudocapacitor materials will be discussed.

7.1.1 LDHs electrochemical characterizations

The electrochemical characterizations of the LDHs were performed by cyclic voltammetry in alkaline medium (0.1 and 1.0 M NaOH). A preliminary check of the film stability was performed by recording several CV curves for each Pt or GC electrode coated by the electrosynthesized LDH. The signals resulted superimposable for hundreds of cycles for both supports, and this suggested a good adhesion of the clays on both supports. Therefore, the mechanical and electrochemical stability can be considered very good. In the next paragraphs representative CV curves and the description of the involved mechanism will be reported.

7.1.1.1 Ni/Al-LDH

The electrochemical behaviour of electrodes modified with Ni based LDHs has been deeply investigated in our laboratory by voltammetric techniques.

The electrochemical response of Ni/Al LDH recorded in cyclic voltammetry, at a scan rate of 0.05 V s^{-1} in 0.1 M NaOH is shown in Figure 7.1 A. A progressive increase of the current peak occurs upon cycling, reaching a maximum value after about 50 cycles, after that the cycles become superimposable. The stabilization in CV is carried out in order to activate the Ni redox system. In Figure 7.1 B the characterization CV curves recorded in 0.1 NaOH at different scan rates are shown.

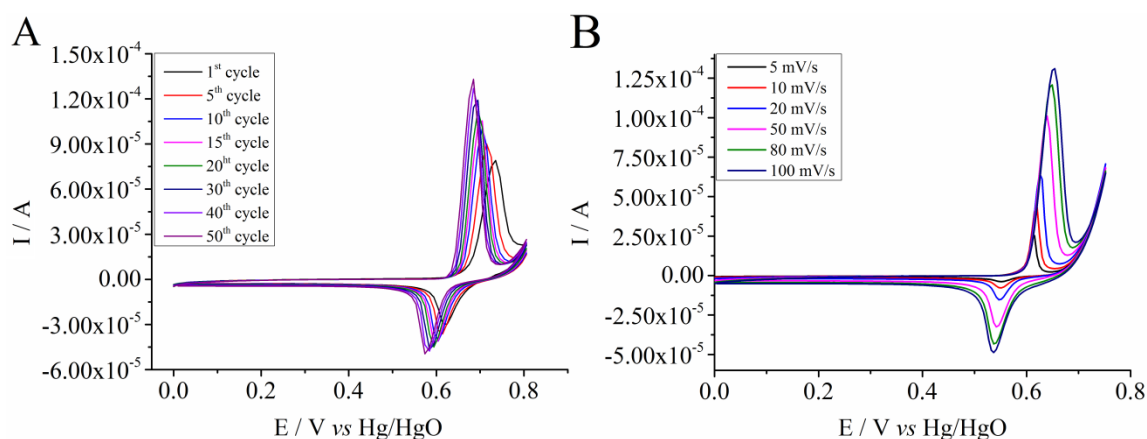


Figure 7.1 – CV curves recorded for a Ni/Al LDH coated electrode in 0.1 M NaOH at 0.05 V s^{-1} (A) and at different scan rates (B).

A noticeable change of color, from light blue to black, on the electrode surface indicates that the oxidation process starts from the edge of the coating and propagates to the center of the LDH thin film. The typical peaks, observed in the potential window between +0.51 and +0.75 V ($E_{pc} = 0.57 \text{ V}$ and $E_{pa} = 0.68 \text{ V}$) are related to the not completely reversible redox couple Ni(III)/Ni(II) [1]. This partial irreversibility might be explained by a chemical/structural instability of the oxidized LDH, due to the presence of Ni(III) which is characterized by a cooperative Jahn-Teller effect [2]. This can cause a structural instability with consequent disgregation of the material. Nevertheless, it is possible to use the electrodes in repeatable and reproducible manner for a long time, since the dissolution of the electrode takes place very slowly.

In the potential range at which Ni centres can be involved in a redox process the material displays good conductivity which is due both to an electronic and ionic transport. The signals relevant to the couple Ni(III)/Ni(II) can be described by the following reaction [3]:



where the OH^- diffusion–migration from the solution into the LDH interlayer, when an anodic potential is applied, ensures the electroneutrality.

The conduction mechanisms of the electrodes modified with Ni or Co-based LDHs have been intensively investigated even by electrochemical impedance spectroscopy and from those experiments [4] it was proved that the electronic conductivity of the LDH materials is strongly dependent on the potential, while the resistance related to the ionic charge transfer mechanism, being related only to the desolvation and adsorption of OH^- onto the

electrode surface, is almost potential independent. Moreover, from the calculation of the activation energies of the two conduction processes the kinetic limiting step of the overall redox process was found to be the electron hopping between localized redox centres (metal cations) in the bulk of material [5].

Two regions can be distinguished in these materials, the external LDH coating/electrolyte solution interface and the internal LDH coating/electrode interface located inside the pores, channels, and interlayer domains, the latter being less accessible for OH⁻ ions. It was demonstrated that due to that structure, the electrochemical reaction is governed by a diffusion process [6].

The main difference between Ni and Co based LDHs is the better electrical conductivity displayed by the material containing nickel as bivalent metal.

7.1.1.2 Co/Al LDH

Co/Al LDH coatings on Pt were characterized by carrying out 20 voltammetric cycles, at different scan rates, in the potential range between 0 and 0.80 V, starting with the segment in the positive direction. In Figure 7.2 the fifth cycle for each scan rate is shown. The successive CV traces become superimposable and do not change after several hundreds of cycles, indicating the good stability of the film modifying the electrode, as stated before.

The current signals observed from the second cycle correspond to the reactions (7.2) and (7.3) regarding the oxidation of Co(II) cations to Co(III) and Co(IV).



The broad feature (C/C') displayed by the LDH coating is due to the closeness of the formal potentials related to the reactions (7.2) and (7.3) which does not allow the resolution of the two voltammetric peaks. Anyway, the behaviour of the two redox couples can be considered reversible since the ratio of the anodic to the cathodic charge of the feature (C/C') is close to 1.

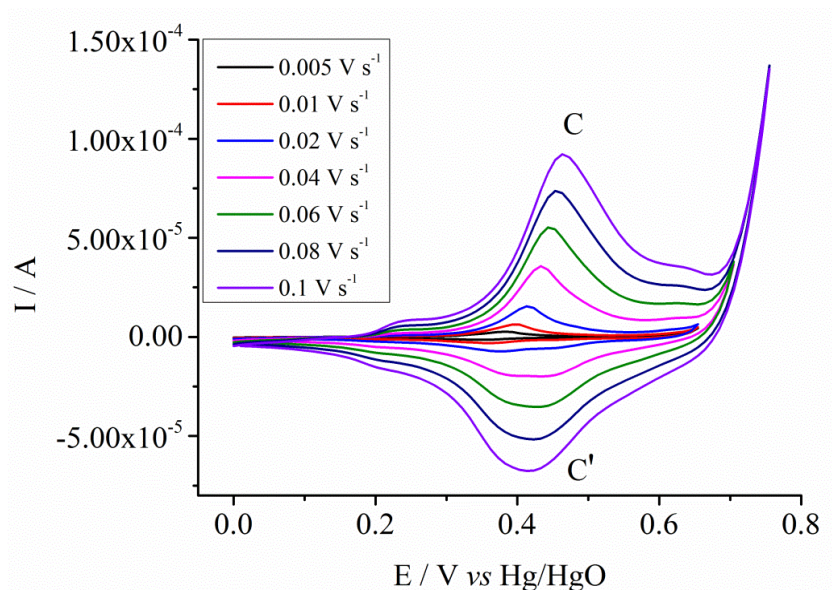


Figure 7.2 - Cyclic voltammograms (the fifth scan is shown) recorded for a Co/Al LDH coated electrode in 0.1 M NaOH, at different scan rates.

In Figure 7.3 are shown the first three cycles and the tenth scan of the CVs recorded in 0.1 M NaOH. In the first cycle it is observed an irreversible oxidation peak. The first forward scan is characterized by a small peak at about 0.35 V (A) and a large one at ~0.7 V (B), whereas the response does not change any more since the first inversion of the potential direction. In fact, during the cathodic sweep only one very broad feature (C') in the range 0.35-0.65 V is present to which a broad peak centred at ~0.55 V (C) is associated since the second anodic potential sweep.

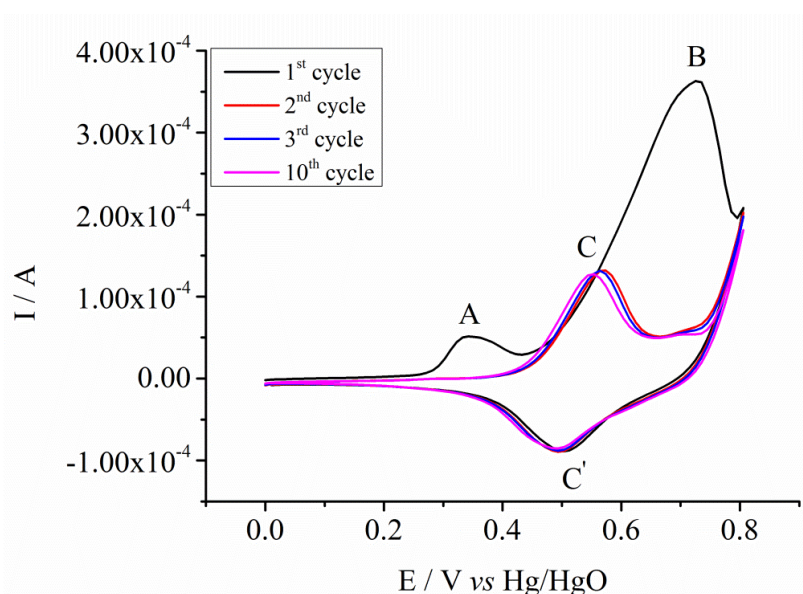


Figure 7.3 - Cyclic voltammograms (1st, 2nd, 3rd and 10th scans) recorded for a Co/Al LDH coated electrode in 0.1 M NaOH, $v = 0.05 \text{ V s}^{-1}$.

The freshly prepared film appeared weakly pink in agreement with the expected color of the Co/Al layered double hydroxide phase. After the first cycle, the film irreversibly changed its color becoming dark brownish, suggesting the oxidation of most Co(II) sites [7]. These observation led to suppose that an irreversible oxidation of some Co(II) sites could take place during the first CV cycle. The color change has been already observed by many researchers when Co/Al LDHs were submitted to thermal ageing treatments and it is ascribable to a partial oxidation of the divalent cobalt to the trivalent state, probably due to the easy formation of cobalt spinel Co₃O₄ [8]. Furthermore, in previous studies the Co(III) moles, produced in the first segment of the first scan, were calculated by integration of the anodic current and resulted to be about 20% of the total Co moles in the film, thus confirming the hypothesis [9]. It was supposed that the oxidation of Co(II) gave rise to a new hydrotalcite-like structure, Co(II)/Co(III)/Al(III), which is stabilized by the concomitant intercalation of OH⁻ anions from the solution in the interlayer spacing (a Co_{1-x}Al_xOOH like phase) [10].

The oxidation process induces structural changes in the solid, and part of the trivalent aluminium migrates to the interlayer region [11]. Such an oxidation is not surprising since it is well known that Co(II) ions are easily oxidised in alkaline solution due to the low value of the standard potential ($E^{\circ} = +0.17$ V) of the reaction:



The big charge related to the C peak during the first anodic scan could be due only to the oxidation of Co(II), or it could involve also the irreversible oxidation of other species produced during the electrochemical reductions of nitrates, occurring during the synthesis. Nitrite is one of possible products of such reactions which could be both adsorbed on the LDH surface and inserted in the interlayer domain due to its anionic nature. The adsorbed nitrite should oxidise irreversibly at potentials less anodic than the intercalated one. The nitrite oxidation on Pt needs a high overpotential but it should occur at lower potentials at the Co/Al LDH modified electrode because of the high affinity of nitrite towards Co ions, especially Co(III) [12]. To verify this hypothesis several experiments were carried out.

In one case the just prepared modified electrode was kept in contact with a solution of 0.1 M sodium carbonate and in the other with a solution of 0.1 M sodium nitrite. Later the LDH coatings were characterized by CV (Figure 7.4 A and B). After the interaction

of LDH with carbonate, which is known to be easily exchanged with any other ion present in the interlamellar space, due to its strong affinity towards such compounds [13], the less anodic feature (peak A in Figure 7.4 B) is fully disappeared. On the contrary, after being in contact with nitrite this feature is more evident. These results confirm that A peak in Figure 7.3 and in Figure 7.4 B is due to the oxidation of the adsorbed nitrite ions.

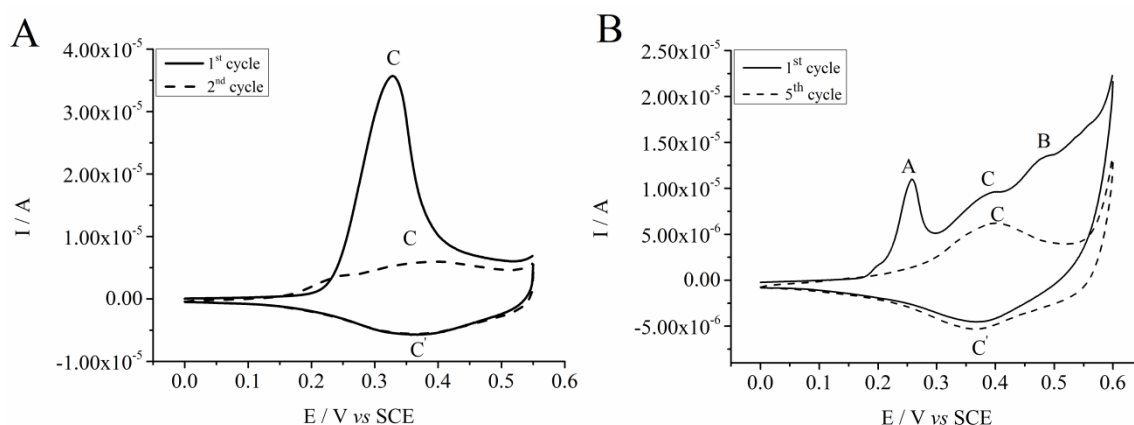


Figure 7.4 - Cyclic voltammograms recorded for a Co/Al LDH coated electrode in 0.1 M NaOH, after keeping in contact for an hour in 0.1 M sodium carbonate solution (A) and in 0.1 M sodium nitrite solution (B). Scan rate: 0.01 V s⁻¹, the first and the second scan are shown.

Furthermore, after the contact of the Co/Al LDH with carbonate the characterization CV does not display the B broad system but another peak (C) which is anticipated at about 0.3 V. The anodic charge exchanged for the corresponding redox processes is much lower and can be ascribed only to the Co centres irreversibly oxidised and to the ones involved in reactions (7.2) and (7.3). The CV recorded after contact with the nitrite confirms this statement since two well resolved redox systems are evident, the most anodic (B peak, centred at ~0.46 V) being due to the irreversible oxidation of the intercalated nitrite to nitrate.

7.1.1.3 Ni/Fe LDH

Figure 7.5 shows the characterization of a Ni/Fe LDH coating on Pt recorded at different scan rates in 0.1 M NaOH. In this case the oxidation of Ni occurs at a potential very close to the solvent discharge, while for Ni/Al LDH the redox peak system is well separated from the process related to the evolution of oxygen.

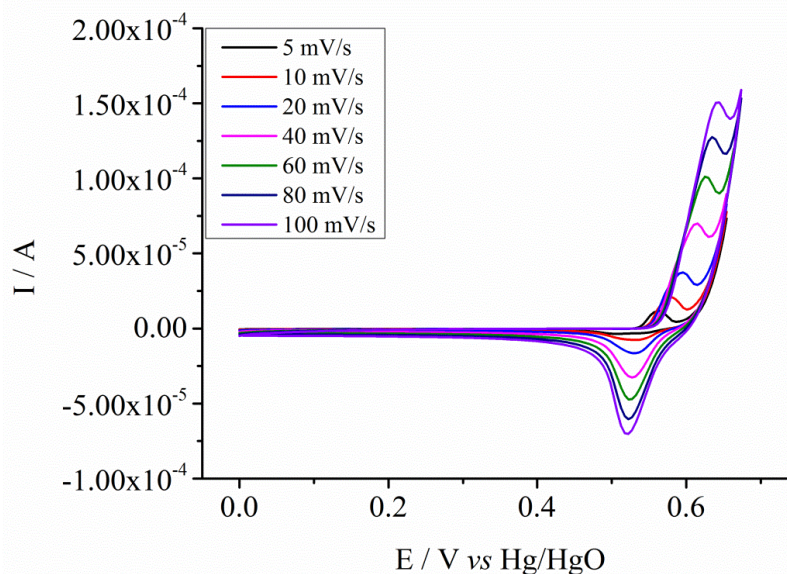


Figure 7.5 – CV curves recorded for a Ni/Fe LDH in 0.1 M NaOH at different scan rates.

From the comparison between the CV curves relevant to Ni/Al and Ni/Fe, shown in Figure 7.6 A, it is evident that the presence of iron affects the electrochemical behaviour of the clay since such LDHs show a CV response different from the LDHs containing Al as trivalent metal.

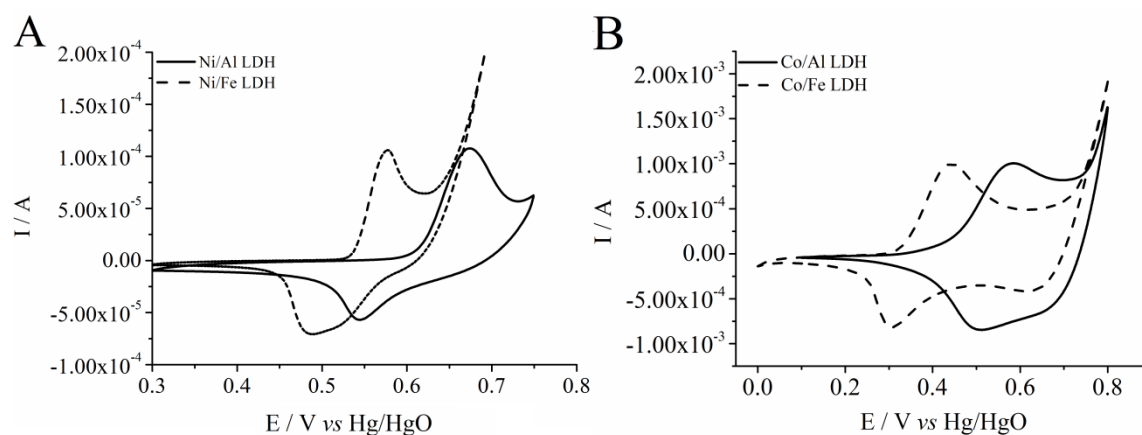


Figure 7.6 - CV curves of the four LDHs electro synthesized on Pt, recorded in 0.1 M NaOH at a potential scan rate of 0.05 V s^{-1} . The fifth scan is shown.

7.1.1.4 Co/Fe LDH

The representative CV characterization curves of Co/Fe LDH recorded at different scan rate in 0.1 M NaOH are shown in Figure 7.7.

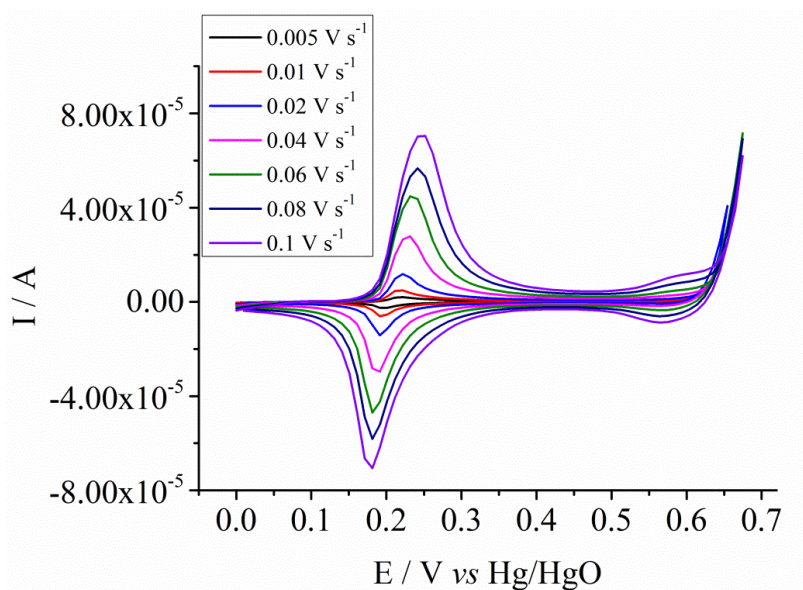


Figure 7.7 - CV curves recorded for a Pt electrode coated with Co/Fe LDH in 0.1 M NaOH at different scan rates.

The CVs evidence a broad feature which even in this case is ascribable to the two redox systems corresponding to the oxidation of Co(II) to Co(III) and Co(III) to Co(IV), respectively.

If compared to Co/Al LDH (see Figure 7.6 B), the feature occurs at lower potentials (about 0.2 V), so even though Fe is not electroactive, it seems to influence the electrochemical behaviour of the divalent cation.

7.1.1.5 Electrode support and pH influence

The characterization CVs of the four LDH coatings were recorded also on another conductive support, namely glassy carbon, since the LDHs performances as OER catalysts and as pseudocapacitor materials were investigated even using this conductive material. In Figure 7.8 the relative CV curves, recorded in 0.1 M NaOH, are reported.

When GC is used as support, the Ni redox peak system seems to be more irreversible since the charge associated to Ni reduction peak is lower than the one relevant to the oxidation process.

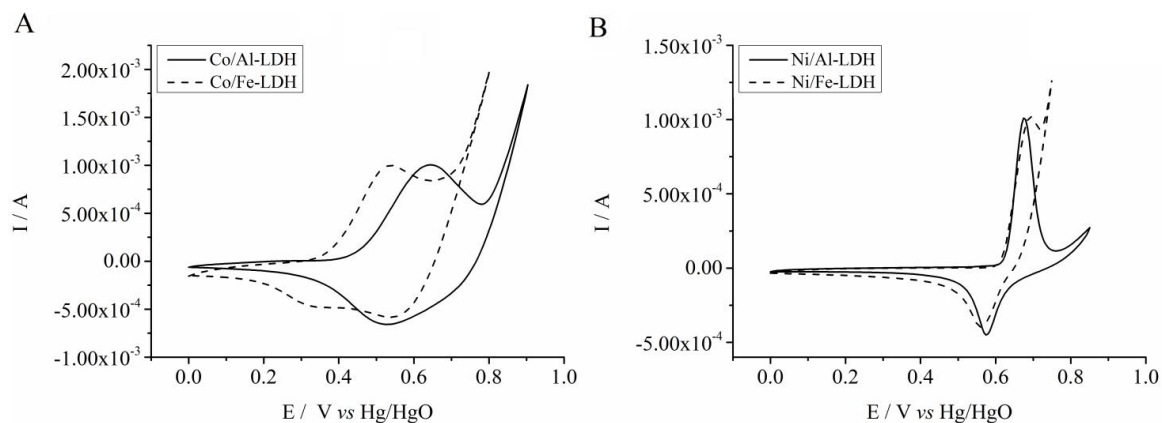


Figure 7.8 - CV curves of the four LDHs electrosynthesized on GC, recorded in 0.1 M NaOH at a potential scan rate of 0.05 V s⁻¹. The fifth scan is shown.

Peak position and intensity depend on the pH. Similar results were obtained when the LDHs were characterized in more alkaline solutions (1.0 M NaOH) with the only difference of a shift toward less anodic potentials of the Co and Ni redox systems, as expected [5]. Representative CVs recorded in 1.0 M NaOH are reported in Figure 7.9 and Figure 7.10 for Pt and GC coated electrodes, respectively.

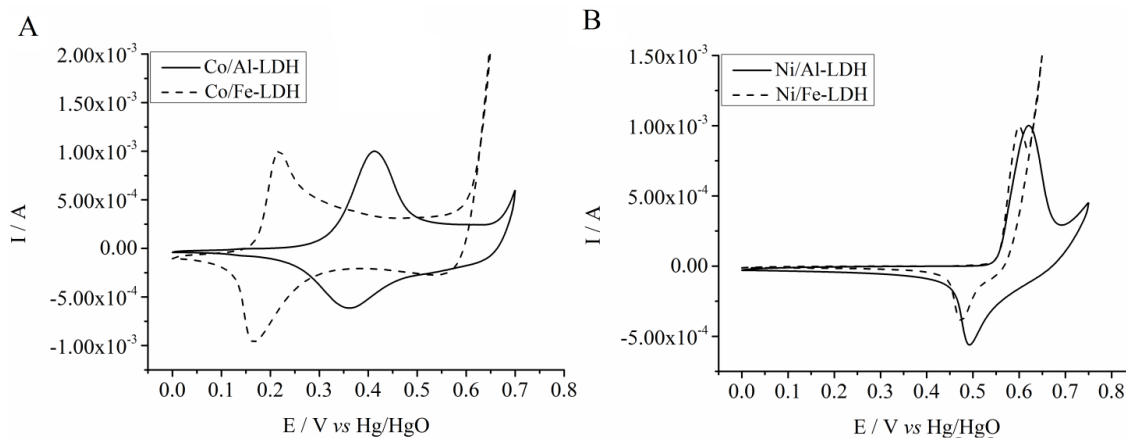


Figure 7.9 - CV curves of the LDHs containing Co (A) and Ni (B) deposited on Pt, recorded in 1.0 M NaOH at a potential scan rate of 0.05 V s⁻¹. The third scan is shown.

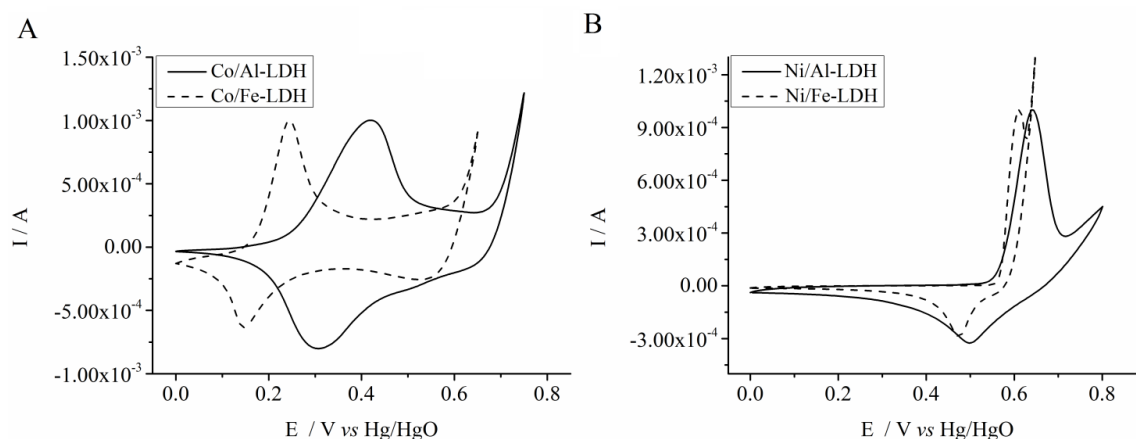


Figure 7.10 - CV curves of the LDHs containing Co (A) and Ni (B) deposited on GC, recorded in 1.0 M NaOH at a potential scan rate of 0.05 V s^{-1} . The third scan is shown.

EQCM experiments were performed in order to determine the mass deposited during the electrosynthesis, working with a Pt electrode. Figure 7.11 shows the massograms recorded throughout the potential pulse for the four LDHs. In the case of Co/Al LDH, the mass grows very quickly during the first 10 s of the application of the cathodic potential necessary to reduce nitrates. Co/Fe LDH shows a similar trend, growing during the first 15 seconds, whereas during the remaining time the LDH deposition still occurs but the process is slow due to the presence of the inorganic material coating the Pt surface which hinders the diffusion/migration of nitrate ions to the underlying electrode.

A different trend of mass growth is shown by the LDHs containing Ni since in that case the mass continues to increase during the whole deposition time. After 30 seconds, a lower mass is recorded for the Ni/Fe in respect to the Ni/Al LDH.

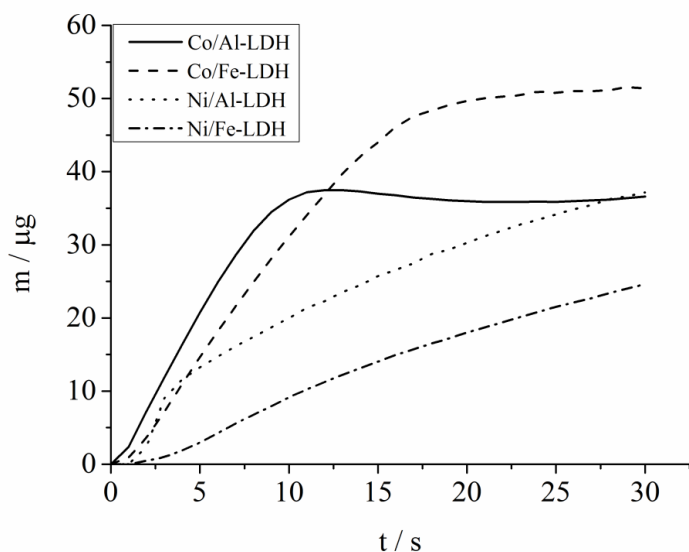


Figure 7.11 – Left: mass vs time plots recorded during the electrosynthesis of the four LDHs on Pt, carried out at -0.90 V vs SCE . Right: Pt metalized quartz crystal electrode coated with a film of oxidized Co/Al LDH.

7.1.2 Structural characterization

The electrochemically synthesized LDHs structure was confirmed by recording XRD spectra. Furthermore X-ray spectroscopy experiments were performed in order to study the local structural environment of the M(II) sites and the influence of Fe presence on the divalent cation in the compounds. XPS and XAS spectra were recorded for the pristine and oxidized LDHs. XPS experiments were performed in order to investigate the oxidation states of the metal cations in the four LDHs before and after the oxidation. XAS experiments were carried out to evidence structural changes in the local environment of the metal sites taking into account Ni/Fe LDH.

7.1.2.1 X-ray diffraction

With the aim to verify the structure of the LDHs, X-ray diffraction analysis has been carried out on Pt-electrodes. The patterns of the four samples, reported in Figure 7.12, show the main diffraction maximum typical of a LDH phase, indexed as 003 reflection. In three samples also the 006 peak is detectable [14]. The maxima of Co containing samples are slightly shifted to lower angles if compared to those containing Ni, suggesting a slightly contraction of the interlayer distances in Ni containing LDHs, as expected on the basis of the smaller ionic radius. The c-axis can be calculated from the position of 003 reflection as 2.6 nm, 2.5 nm, 2.4 nm, and 2.4 nm for Co/Al, Co/Fe, Ni/Al and Ni/Fe LDHs, respectively. As the Co/Al sample shows narrow reflections, its crystal domains are bigger and better formed in respect to the others and can be determined by Scherrer equation [15] from the width of the 003 reflection. A rough estimation of coherently scattering domain (*i.e.* crystal size) is 5 nm in the interlayer direction for the Co/Al sample and 20% less (4 nm) for the other samples.

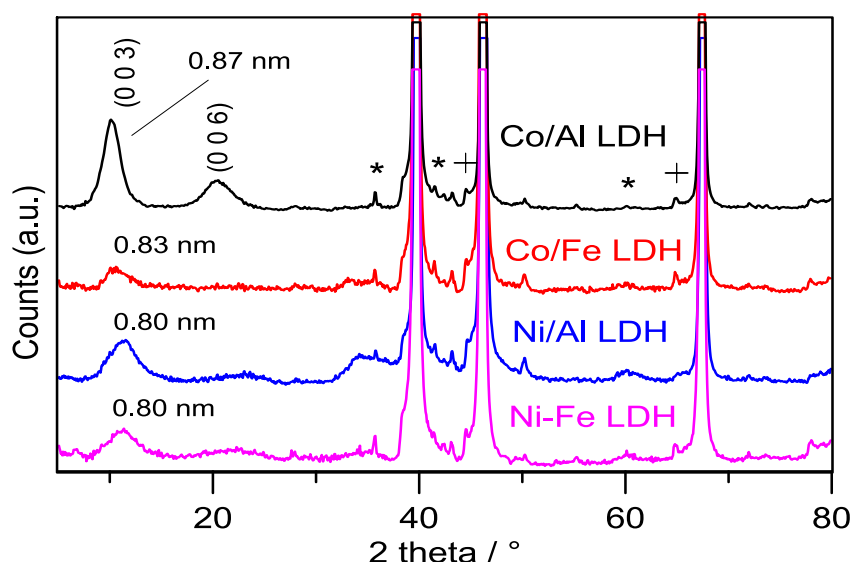


Figure 7.12 - XRD patterns, instrumental background subtracted, of the LDHs electro synthesized on Pt. The asterisks and the cross mark peaks due respectively to $\text{CuK}\beta$ and WLa contamination radiation detected because the very high intensity of Pt peaks.

7.1.2.2 X-ray photoelectron spectroscopy

XPS experiments were performed in order to study the oxidation states of the metal cations in the four LDHs.

The deconvoluted XPS spectrum of Ni $2p_{3/2}$, reported in Figure 7.13 A, shows different components: the contributions at ~ 855.9 , 857.8 , and 861.5 eV are associated in the literature to Ni^{2+} in nickel hydroxide phase, whereas the band at around 856.7 eV is most likely due to the presence of a limited amount Ni^{3+} [16]. Figure 7.13 B is related to the deconvoluted Ni spectrum obtained after cycling in alkaline solution: no substantial differences in the observed contributions are evidenced, except for the presence of a signal at around 858.1 eV which is associated in the literature to the presence of a oxyhydroxide phase ($\gamma\text{-NiOOH}$) [17].

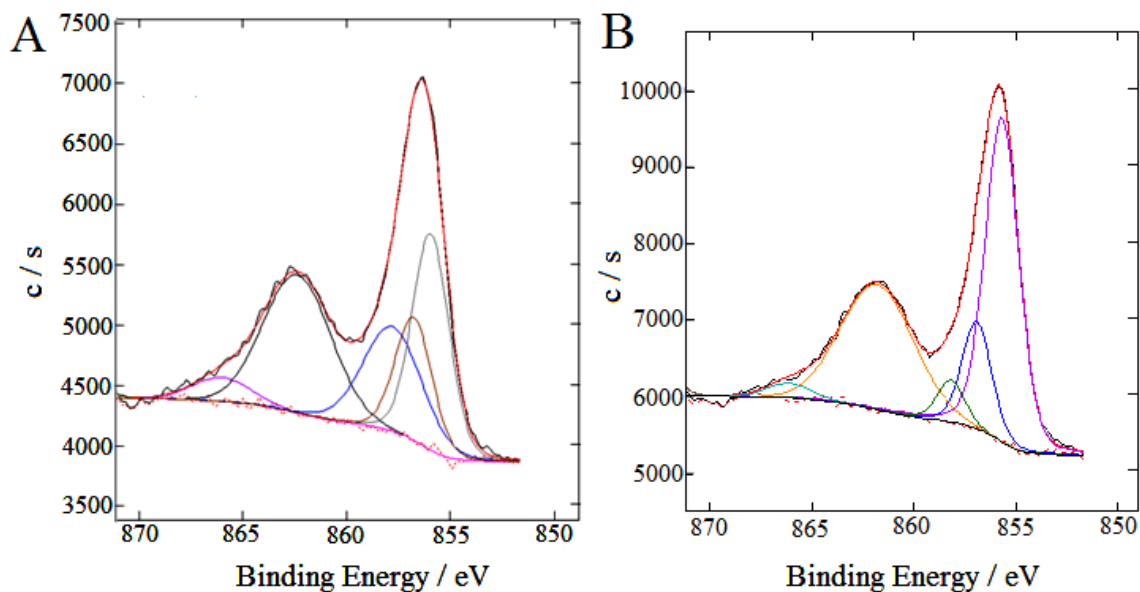


Figure 7.13 - Deconvoluted Ni spectrum of Ni/Al LDH before cycling (A) and after cycling (B).

Deconvoluted spectrum of Ni in Ni/Fe LDH before cycling is reported in Figure 7.14 A: the most important contribution is centred at around 856.5, which is the signal associated to the presence of Ni^{3+} in oxyhydroxide phases. The other observed contributions are ascribed to Ni in +2 oxidation state.

After cycling the main difference in the deconvoluted spectrum of Ni (Figure 7.14 B) is the increase in intensity of the contribution observed at ~ 856.5 eV ascribed to Ni in +3 oxidation state [16].

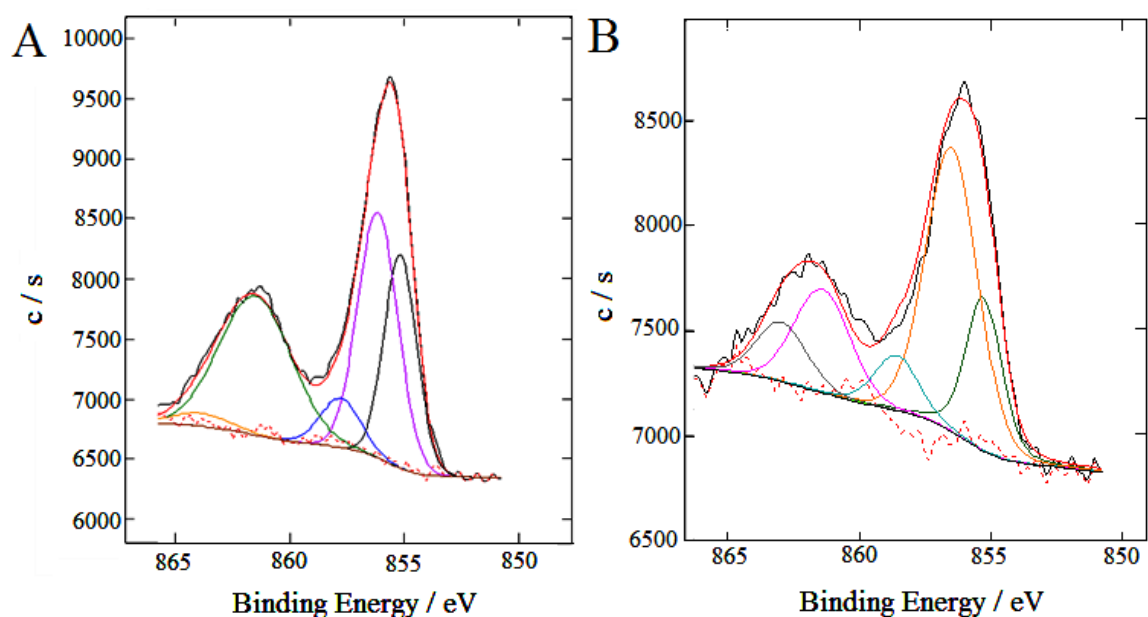


Figure 7.14 - Ni $2p_{3/2}$ spectrum of Ni/Fe LDH before cycling (A) and after cycling (B).

The spectrum of Fe before and after oxidation (Figure 7.15) is basically the same, suggesting that no substantial change of iron chemical environment occurs.

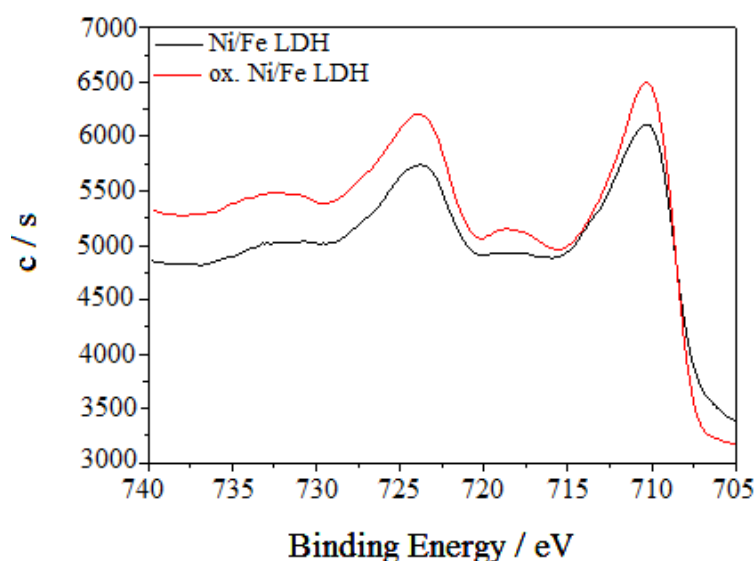


Figure 7.15 - XPS Fe spectrum of Ni/Fe LDH pre and post cycling.

Deconvoluted spectrum of Co is reported in Figure 7.16 A: the signals centred at 780.1 eV, 782.5 eV, and 786.2 eV are attributed to the multiplet of Co^{2+} in a $\text{Co}(\text{OH})_2$ phase, a small contribution at 779.7 eV is ascribable to Co^{3+} . After cycling (Figure 7.16 B) the main component is observed at ~ 779.7 eV, suggesting a significant increase of the amount of surface Co^{3+} . The component at higher binding energy (786.2 eV) has been depleted after cycling, suggesting a transition to a CoOOH phase.

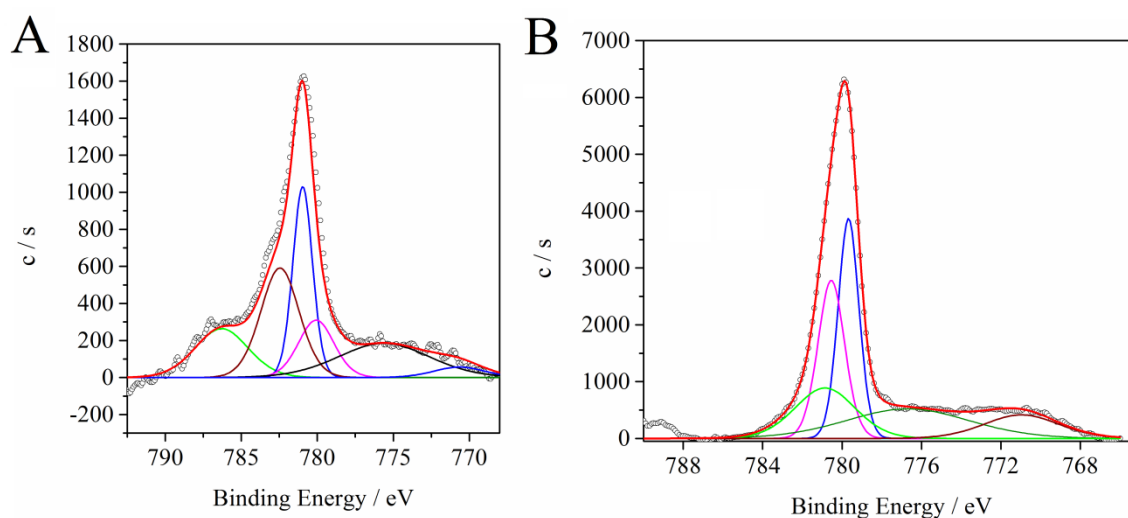


Figure 7.16 - Deconvoluted Co spectrum of Co/Al LDH before cycling (A) and after cycling (B).

Deconvoluted spectrum of Co in Co/Fe LDH is reported in Figure 7.17 A and shows the multiplet related to Co^{2+} in $\text{Co}(\text{OH})_2$ phase, without any significant contribution of Co^{3+} . After cycling (Figure 7.17 B) the main component is shown at 779.7 eV, typical of $\text{Co}(\text{III})$, suggesting a significant surface enrichment of this species. Signals due to Co^{2+} are, as expected, still found.

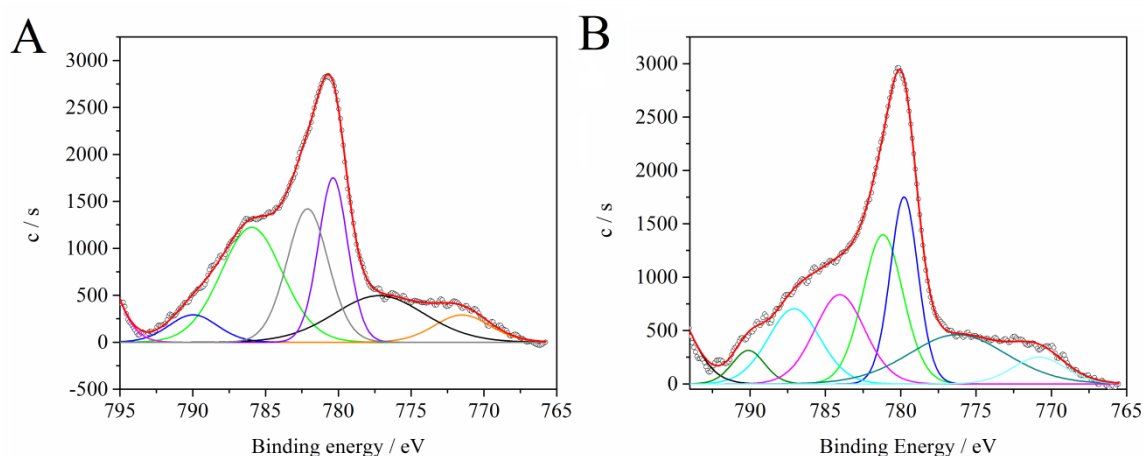


Figure 7.17 - Deconvoluted Co spectrum of Co/Fe LDH before cycling (A) and after cycling (B).

7.1.2.3 X-ray absorption spectroscopy

XAS structural studies are commonly employed for several materials including LDHS [18]. In this research X-ray absorption spectroscopy was applied to pristine and oxidized Ni/Fe LDH obtained by electrochemical synthesis in order to gain information about the structural and electronic changes in the local environment around the selected metallic sites. For this class of compounds, the most frequently investigated site is Ni [19,20], but the presence of another metal cation, Fe, allows for probing its local structural environment too.

Figure 7.18 shows the comparison between the XANES spectra of the pristine and the oxidized Ni/Fe LDHs at the Ni K-edge (8333 eV).

XANES spectra displayed in the figure are almost superimposable, thus indicating that the local structure around Ni does not change in the investigated samples. The nickel site in the LDH structure is octahedrally coordinated by six oxygen atoms, two in apical position and four in equatorial position, at the same distance [21]. The experiments suggested that the coordination geometry remains unchanged during the oxidation.

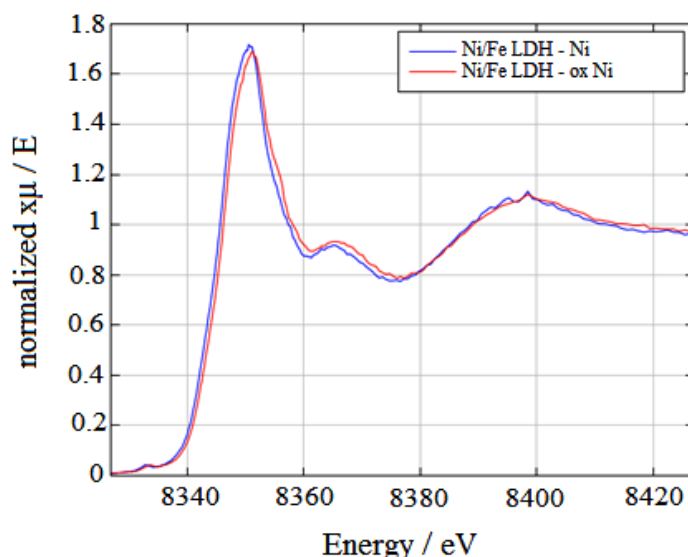


Figure 7.18 – Comparison of the XANES spectra of both the pristine and the oxidized Ni/Fe LDHs at the Ni K-edge (8333 eV).

The Fourier transforms curves related to EXAFS signals (shown in Figure 7.19) confirms this hypothesis since they do not evidence changes in the peaks position, a part from a very slight difference of the second one, due to the second atomic shell around Ni, which is probably ascribable to a structural disorder.

On the contrary, concerning the edge energy in the XANES spectra (Figure 7.18), it is evident a K-edge shifts toward higher energy, consistent with the LDH oxidation. Therefore, the experiment confirms the electroactivity of Ni^{2+} , which is oxidized (probably) to Ni^{4+} .

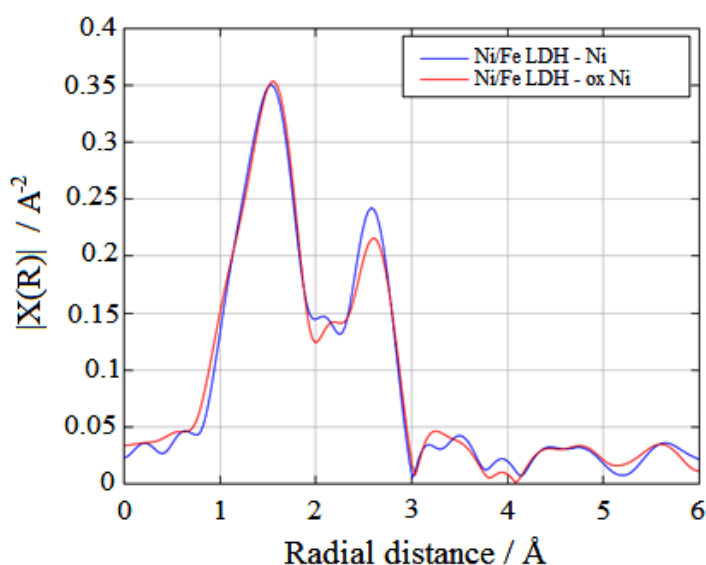


Figure 7.19 - Fourier transforms relative to the XANES spectra of both the pristine and the oxidized Ni/Fe LDHs at the Ni K-edge.

Figure 7.20 displays the XANES spectra at the Fe K-edge (7112 eV) of both the pristine and oxidized LDHs. The spectra appear nearly superimposable and only little differences are evidenced. Firstly, it is noticeable a slight energy shift, consistent with Fe(III) oxidation. In addition, the spectra appear different after the pre-edge peak (see Figure 7.21). In fact, while the pre-edge peak (at ~7114-7115 eV) remains unchanged, the following resonance, at ~7120-7121 eV, displays a bump in the case of the oxidized LDH. Such a feature in the edge zone could be due to a different long range order of Fe, possibly ascribable to structural defects such as hexacyanoferrate ion vacancies.

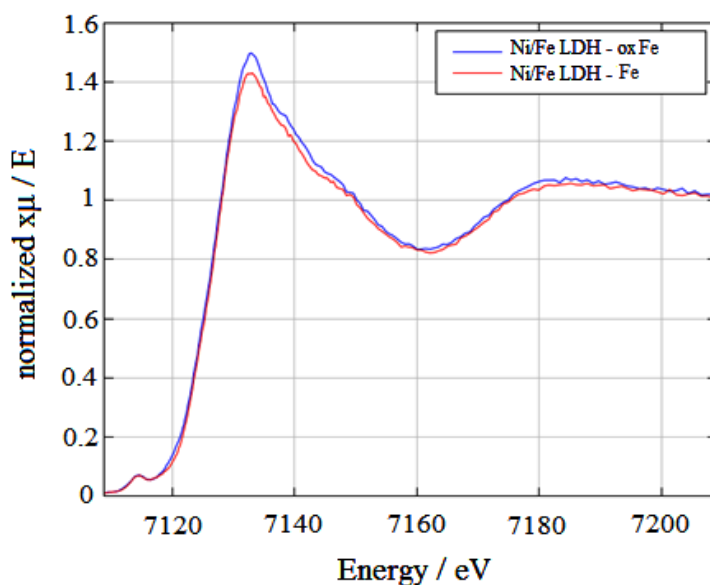


Figure 7.20 - XANES spectra at the Fe K-edge (7112 eV) of both the pristine and oxidized LDHs.

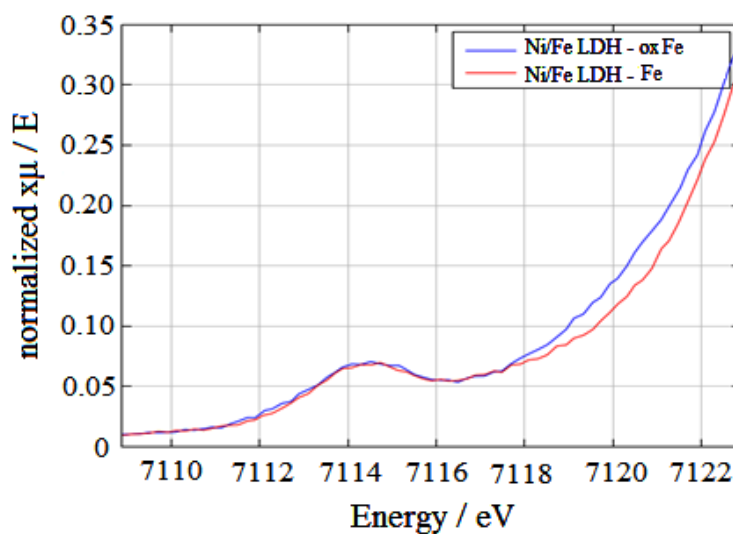


Figure 7.21 – Magnification of the pre-edge peak zone of the XANES spectra at the Fe K-edge of the pristine and oxidized LDHs.

The study of the absorption spectra at the K-edge of the pristine and oxidized Ni/Fe LDHs confirmed the presence of the electroactive couple $\text{Ni}^{2+}/\text{Ni}^{4+}$, besides little differences in the charge associated to Fe (after the oxidation). The observed charge transfer resulted associated to minor changes (local structural arrangements) of the Ni and Fe sites structure.

7.1.3 Morphological characterizations

The morphological characterization of the four LDHs electrosynthesized on GC and Pt (Figure 7.22 and 7.23) was performed using FE-SEM. Both supports seemed homogeneously covered. Investigating some areas of the LDH films, a different compactness of the coatings was pointed out in dependence on the support.

When GC was used for the electrodeposition all the LDHs coatings appeared very compact and consisted of round particles with an uniform size distribution. In particular, the smallest particles (10-20 nm) were observed for the Ni/Al LDH (Figure 7.22 A), whereas for the other three LDHs the average size was about 40-50 nm.

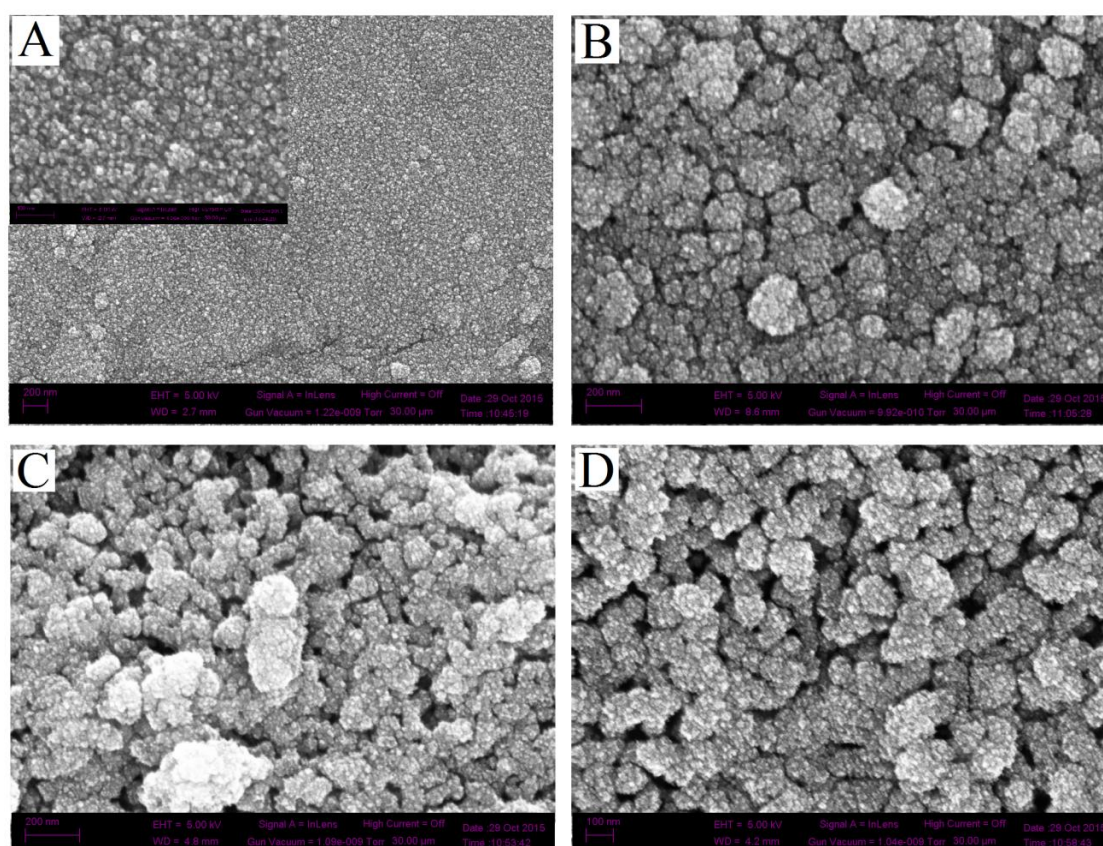


Figure 7.22 - FE-SEM images of Ni/Al (A), Ni/Fe (B), Co/Al (C) and Co/Fe (D) LDHs on GC electrodes. The inset in Figure A shows a different magnification of the Ni/Al LDH.

In case of Pt the morphology of the four LDH coatings displays some small differences (Figure 7.23). Concerning the Ni/Al LDH the nanoparticles appear spherical and display the largest size in comparison to those relevant to the other LDHs. Furthermore, the film is particularly compact and the particles appears almost fused each others. In case of the Ni/Fe LDH the morphology consists of well defined spherical particles which are smaller (about 20-40 nm) and in close contact so that the film surface is compact enough and smooth. As to the Co/Fe LDH the morphology is similar to the one showed when GC is used as the support but the film presents a relief structure which leads to a minor compactness.

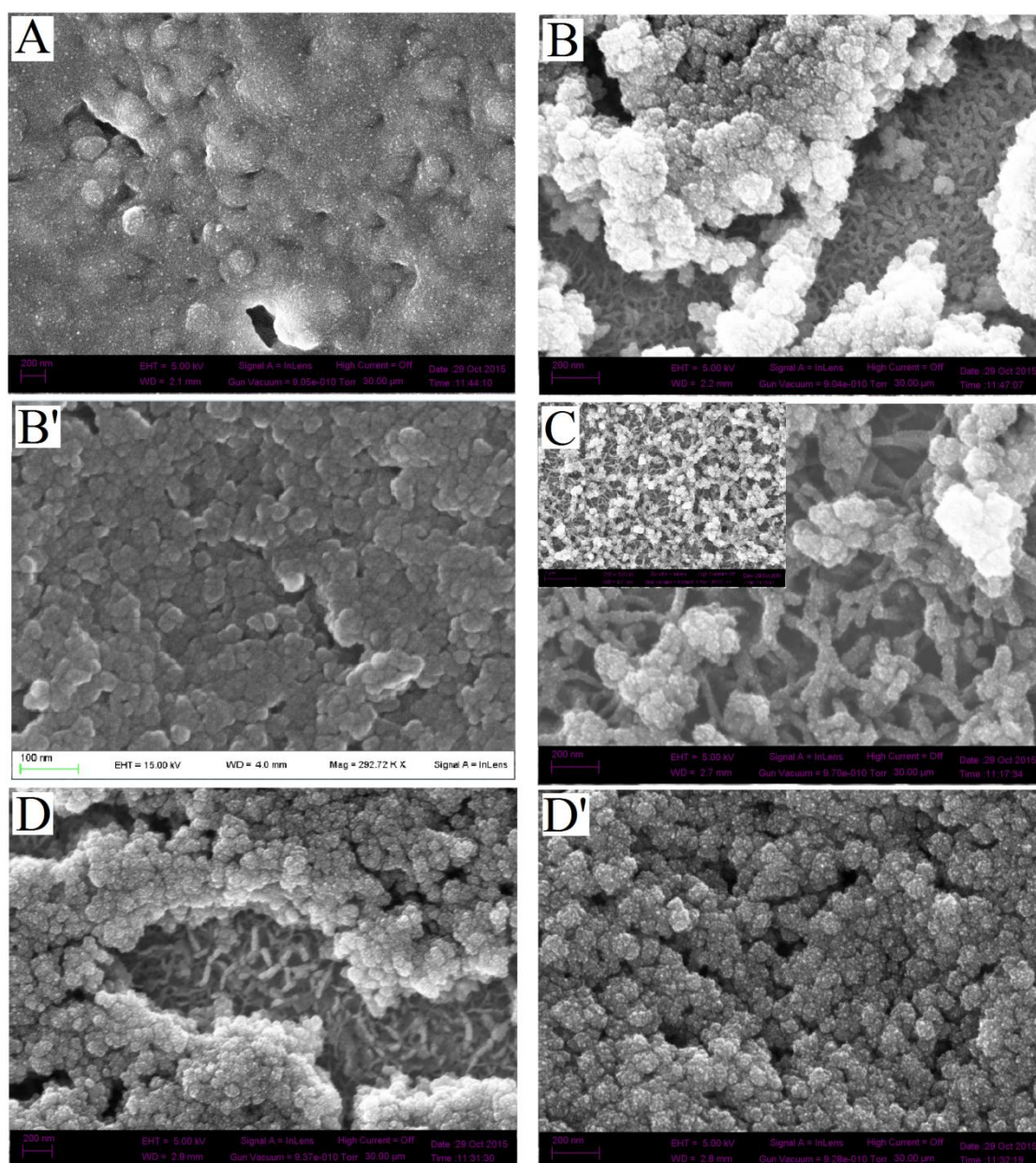


Figure 7.23 - FE-SEM images of Ni/Al (A), Ni/Fe (B and B'), Co/Al (C) and Co/Fe (D and D') LDHs on Pt electrodes. The inset in Figure C shows a different magnification of the Co/Al LDH.

Eventually, the Co/Al LDH shows a more complex morphology consisting of highly interconnected tubular structures (whose wideness is about 10 nm) on which flower-like architectures are grown so inducing the formation of 3D hierarchical nanostructures. The film is uniform but displays a loose packing structure.

The LDH films were also characterized by semi-quantitative SEM/EDX analysis to determine the M(II)/M(III) atomic ratio. All the values resulted about 2.5, rather similar to the molar ratio of the salts present in the electrolytic solutions used for the synthesis. These values are compatible with a LDH stoichiometry.

7.1.4 OER catalytic activity and modified electrode durability

In this paragraph the studies carried out employing the four LDHs as OER catalysts are reported. The parameters most commonly used to evaluate the performances of the materials, *i.e.*, the onset potential (which is the potential at which the oxygen evolution starts), the current density for a fixed overpotential, and the turnover frequency which is defined as the number of molecules reacting for a given reaction per unit time per active center. Furthermore, the durability and the mechanism of OER were deeply investigated taking into account Tafel plots.

7.1.4.1 OER onset potential determined by linear sweep voltammetry

LSV curves at the LDH coated electrodes were recorded at a slow scan rate (0.005 V s^{-1}) in 0.1 and 1.0 M NaOH. For the LDHs containing Co, it is clearly evident the peak which can be ascribed to Co centres oxidation, whereas for the Ni based LDHs the oxidation peak occurs at a higher potential and appears less visible due to the overlapping with the solvent discharge.

From the direct comparison of the LSV curves of the four LDHs it is evident that electrodes modified with Fe-based materials display a considerable reduction of the OER onset potential if compared to the value exhibited by both the bare electrode and the support modified with the LDHs containing Al. In Figure 7.24 the *iR*-corrected polarization curves of the four LDHs deposited on Pt and GC, recorded in 1.0 M NaOH, are shown. In particular, Ni/Fe and Co/Fe LDHs exhibit values of onset potential which

are averagely of +0.58 V, on both substrates. These low overpotentials demonstrate the effect of iron which lowers the activation barrier for the OER.

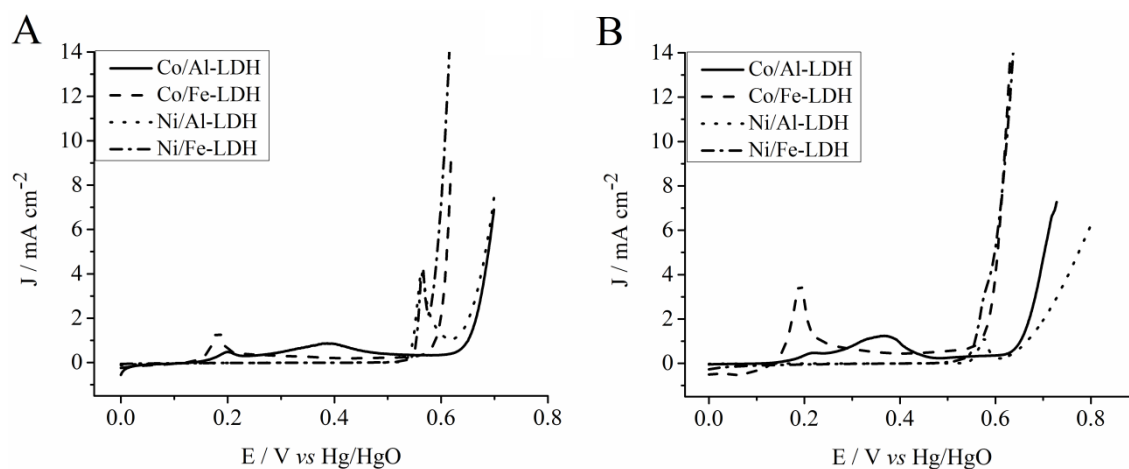


Figure 7.24 - *iR*-corrected polarization curves of the four LDHs electrosynthesized on Pt electrode (A) and GC (B) recorded in 1.0 M NaOH at the scan rate of 0.005 V s⁻¹.

The OER onset potentials in 0.1 and 1.0 NaOH for the four LDHs synthesized on Pt or GC are reported in Table 7.1. As can be seen, no substantial differences are observed for both supports even if the onset potentials are generally lower when the catalyst is deposited on GC, especially working in less alkaline conditions. Therefore, the two supports seem almost comparable.

From Figure 7.24 it is evident that the current densities increase very steeply, with the only exception represented by the Ni/Al sample on GC. Faour *et al.* found out a complex correlation between the structure/microstructure and the electrochemical performance of the Ni/Al–CO₃ LDHs, deposited as thin films on Pt electrodes, taking into account the effect of particles size, morphology and structural defects [22]. Even in our case the electrocatalytic performances of the LDHs towards the oxygen evolution could be related in some way to the morphological characterization of the films by SEM as shown in Figure 7.22 and Figure 7.23. The observation that the current density does not increase very steeply for the Ni/Al LDH electrodeposited on GC could be the result of the very small particles (10-20 nm) which generate a film (Figure 7.22 A) so compact that the OH⁻ ions diffusion/migration is strongly hindered. This hypothesis is supported by the observation that the Ni oxidation peak, in the linear sweep trace recorded at low scan rate (Figure 7.24 B), is much smaller than the one recorded for the LDH containing Fe.

The current densities recorded at the arbitrary overpotential of 0.61 V for the Fe-based LDHs and of 0.68 V for the Al-based LDHs are shown in Table 7.2 from which it is evident that highest values are exhibited by the Fe based LDHs on both supports, so confirming the positive role played by iron. As expected from the extent of the film compactness, the system displaying the worst performance is the Ni/Al LDH deposited on GC.

The fact that the current densities for the iron based LDHs on GC are almost the same could be related to the similar morphologies and particles size as shown in Figure 7.22. This is not true for the Fe based LDHs coating the Pt support. In fact, the Ni/Fe LDH shows a current density much higher than that displayed by the clay containing Co which is rather similar to the one obtained on GC.

As evident from Figure 7.23 B, the Ni/Fe LDH morphology consists of well defined spherical particles (average size 20-40 nm), close each others, which confer to the film a good ionic permeability so that both the electron hopping and the hydroxide ions diffusion occur efficiently. As to the Co/Fe LDH the morphology is similar to the one displayed when the electrode is GC. This observation could again support a possible relation between the film morphology and the electrocatalytic efficiency (EE) of the clay.

Table 7.1 OER onset potential of the four LDHs coatings on Pt and GC electrodes, in 0.1 and 1.0 M NaOH.

LDH	$E_{\text{onset}} / \text{V}$			
	Pt electrode		GC electrode	
	0.1 M NaOH	1.0 M NaOH	0.1 M NaOH	1.0 M NaOH
Ni/Al	0.75	0.63	0.73	0.61
Ni/Fe	0.65	0.58	0.62	0.59
Co/Al	0.76	0.63	0.73	0.62
Co/Fe	0.68	0.57	0.62	0.57

The turnover frequency for the oxygen evolution was calculated by the following equation [23]:

$$\text{TOF} = \frac{i \cdot N_{\text{A}}}{4 \cdot F \cdot N_{\text{atoms}}} = \frac{J}{4 \cdot Q} \quad (7.5)$$

where i is current, N_{atoms} is the number of active sites, J is the current density (A cm^{-2}), Q is the charge storage capacity of the main Ni(II/III) or Co(II/III) oxidation peak, F is the Faraday constant and N_A is the Avogadro constant. The formula assumes that all the Co and Ni centres are catalytically active in the OER reaction.

The turnover frequencies are reported in Table 7.2; the best coating material was found to be again Ni/Fe-LDH, which achieved a TOF of 1.55 s^{-1} in 1.0 M NaOH when GC was employed as support. A lower value of about 50% was estimated when the Ni/Fe-LDH was electrodeposited on Pt. At the same potential of 0.61 V, Co/Fe LDH displayed a lightly worse TOF, which was almost equal for Pt and GC supports (0.40 and 0.48 s^{-1} , respectively). Also for the second indicator, GC electrode seems to favor the kinetics of the oxygen evolution, particularly for the Ni/Fe LDH which is the clay with the best catalytic activity.

Table 7.2 Turnover frequencies, current densities^a and Tafel slopes relevant to Pt and GC coated with the four LDHs, in 1.0 M NaOH.

LDH	TOF / s^{-1}		J / mA cm^{-2}		Tafel slope / mV dec^{-1}	
	Pt	GC	Pt	GC	Pt	GC
Ni/Al	0.2	0.54	4.62	1.35	40	29
Ni/Fe	1.02	1.55	9.98	6.98	35	25
Co/Al	0.15	0.26	3.70	2.74	39	30
Co/Fe	0.40	0.48	5.37	6.46	45	29

^a The values were determined at $E = 0.61 \text{ V}$ in the case of Fe-based LDHs and at $E = 0.68 \text{ V}$ for the LDHs containing Al.

Although it is difficult to make a comparison with the values reported by the literature, the TOFs exhibited by Ni and Co/Fe LDHs electrosynthesized on both GC and Pt can be considered very satisfactory. They result similar to the TOFs observed by Yeo and Bell for very thin films of Ni(OH)_2 or Co(OH)_2 deposited on gold [24,25]. We have to remark that those values were evaluated at an overpotential 90 mV higher (0.70 V vs Hg/HgO) than the one considered in our work. Furthermore, the TOFs calculated for Ni/Fe LDH on both GC and Pt compare favorably with the value reported by Gong *et al.* [26] who

employed an ultrathin layer of LDH nanoplates on mildly oxidized multiwalled carbon nanotubes.

7.1.4.2 Durability tests

Besides high OER activity, another important criterion for a good electrocatalyst is the high durability. The stability of the LDHs modified electrodes was studied by recording chronopotentiometric curves, applying three current densities of 1.5, 2.0 and 2.5 mA cm⁻² for an hour. The four LDHs coatings on both Pt and GC exhibited good durability in alkaline solutions, as it can be seen from Figure 7.25, where we report the chronopotentiometry responses obtained at 2.5 mA cm⁻² in 1.0 M NaOH. It resulted that all the materials showed a nearly constant operating potential; the lowest value was again obtained for the Ni/Fe LDH on both Pt (~0.567 V) and GC (~0.550 V). What is outstanding is that, when biased galvanostatically on GC, the Co/Fe LDH shows a working potential that is only 7-8 mV higher than Ni/Fe LDH, the Co/Al LDH a value which is about 20 mV higher, whereas the Ni/Al LDH shows an increase in overpotential by ~60 mV in comparison with Ni/Fe LDH. This order of operating potential reflects the trend observed for the current density reported in Table 7.2. The behaviour of the LDHs on Pt is slightly different. Firstly, the working potentials are comprised within a narrow range (25 mV) secondly, their values increase in the order: Ni/Al, Co/Fe, and Co/Al LDH. Again, we can observe that this is almost the same order displayed by the current density when Pt is used as electrode material.

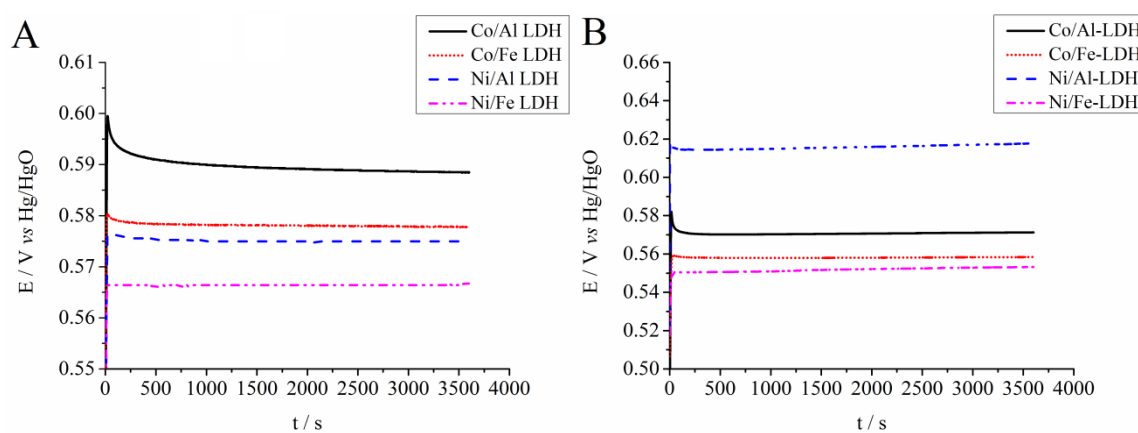


Figure 7.25 - Chronopotentiometry curves of the four LDHs on Pt electrode (A) and GC (B), recorded in 1.0 M NaOH at a constant current density of 2.5 mA cm⁻².

7.1.4.3 Tafel slopes and OER proposed mechanism

Fe plays a critical, but not yet understood, role in enhancing the activity for oxygen evolution reaction of Ni-based electrocatalysts. Trotochaud *et al.* demonstrated that pure NiOOH is a poor catalyst for OER whereas if Fe is present, even at trace level, the OER activity greatly increases [27]. Ni_{1-x}Fe_x(OOH) oxyhydroxide electrocatalysts have resulted the most active catalysts in basic media and this is consistent with the hypothesis that Fe enhances the activity of NiOOH through a Ni-Fe partial charge-transfer activation process occurring throughout the film, similar to that observed by Yeo and Bell for noble-metal electrode surfaces [24]. Those authors compared the OER activity of NiOOH films with varying thicknesses and demonstrated that the TOF increased for films with less than a few monolayers in thickness. The effect was most pronounced on Au, which is the more-electronegative substrate, and was attributed to partial electron transfer from the NiOOH to Au with a consequent modification of the electronic properties of the Ni- based catalyst. In Ni_{1-x}Fe_x(OOH) catalysts iron should exert a similar electron-withdrawing effect on Ni as the Au substrate does. Under OER conditions, Pourbaix diagrams predict both Fe³⁺ and Fe⁴⁺ [28]. Corrigan *et al.* evidenced from in situ Mössbauer spectroscopy a partial electron transfer away from Fe³⁺ accompanying the reduction of Ni³⁺ [29]. This strong electronic coupling between Fe and Ni is supported by the result that the potential of the Ni^{2+/3+} couple in Ni_{1-x}Fe_xOOH depends on the Fe content [27].

More recently, analogous results have been obtained for CoOOH since Fe incorporation increases the intrinsic OER activity by about 100-fold, with peak activity at 40–60% (m/m) Fe content. Also in this case, the voltammetry of Co_{1-x}Fe_x(OOH) showed a strong dependence of the Co^{2+/3+} potential on the Fe content, indicating strong electronic interactions between Fe and Co [30]. The reported results support a hypothesis where CoOOH provides a conductive, chemically stable, and porous host for Fe, which substitutes Co and serves as the (most) active site for OER catalysis.

Our results confirm the key role of iron in LDHs containing Ni and Co since when aluminum is present as M(III) in substitution of iron the three parameters utilized by us to evaluate the catalytic activity toward OER are much worse. The only exception is the TOF for Ni/Al LDH electrosynthesized on GC which is comparable with the values calculated for Co/Fe LDH, even if we have to point out that for the Al-based LDHs the

determinations were carried out at a potential 70 mV more anodic, since they exhibit a higher OER onset potential.

Eventually, an important consideration is related to the fact that the two electrode supports we have utilized for the LDHs electrodepositions have resulted comparable in terms of performances displayed by the catalysts towards the oxygen evolution reaction, particularly when Fe-based LDHs are taken into account, even if the clays exhibit the best performances when GC is used as support.

Tafel slope is another important parameter that is typically exploited to characterize the electrode performance, because it is related to the mechanism at different overpotentials.

One commonly accepted reaction pathway for oxygen evolution in alkaline solutions, the Krasil'shcikov path [31], is shown in Eq. 7.6 to 7.9:



$$b = 2.3 (2\text{RT}/\text{F}) \cong 120 \text{ mV dec}^{-1}$$



$$b = 2.3 (\text{RT}/\text{F}) \cong 60 \text{ mV dec}^{-1}$$



$$b = 2.3 (2\text{RT}/3\text{F}) \cong 40 \text{ mV dec}^{-1}$$



$$b = 2.3 (\text{RT}/4\text{F}) \cong 15 \text{ mV dec}^{-1}$$

where Me is an active site of the catalyst, and b represents the Tafel slope. As previously indicated in the literature for these types of deposits, it is probable that tetravalent oxidation states of Co and/or Ni metal ions, are involved as intermediate states [32]. Therefore, surface oxidation, previous to the OER, gives rise to Co(IV) and Ni(IV) catalytic centres. Then, the primary discharge of OH⁻ ions, reaction 7.6, occurs which is considered rate limiting for catalysts exhibiting Tafel slopes near 100 mV dec⁻¹. Equation 7.7 represents an acid-base reaction, favored by the strongly alkaline environment. Finally, after another oxidation reaction, the recombination of the surface oxygen species generates oxygen and the Me catalytic centres.

When Tafel slopes decrease to less than 50 mV dec⁻¹, reaction 7.8 and/or 7.9 become the rate-limiting step. The Tafel plots obtained from polarization curves in 1.0 M NaOH for the four LDHs on Pt and on GC were fashioned and the slope values are reported in

Table 7.2. As an example, in Figure 7.26 we report the Tafel plots related to the four LDHs on GC. The resulting slopes were ~ 29 , 25, 30, and 29 mV dec^{-1} current density for Ni/Al, Ni/Fe, Co/Al and Co/Fe LDH, respectively. All the values are slightly lower than those found out for Pt, and suggest a similar OER mechanism for all the materials independently of the electrode support. In fact, a significant change in the Tafel slope is usually interpreted as a change in the rate-limiting step. Significantly, Tafel slopes of about 30 mV dec^{-1} as displayed by our Fe based LDH films electrodeposited on GC, were reported in the literature for Ni/Fe chemically synthesized [33,34].

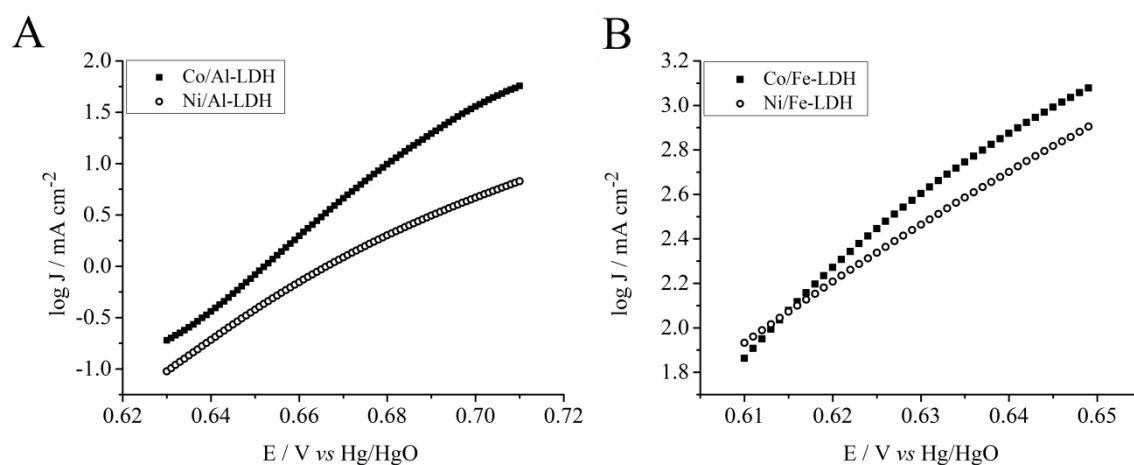


Figure 7.26 - Tafel plots of the Al-based LDHs (A) and the Fe-based LDHs (B) electrosynthesized on GC recorded in 1.0 M NaOH.

7.1.5 Pseudocapacitors performances

7.1.5.1 Performances of the LDHs coatings on Pt

Impedance spectra were recorded for each LDH in the potential range of the anodic wave avoiding potential higher than that of oxygen evolution reaction and were plotted in the Nyquist plot form. The shape of the Nyquist plot, shown in Figure 7.27, and the equivalent circuits (Figure 7.28) employed to fit the EIS spectra depend on the nature of the bivalent metal.

For Ni based LDHs the anodic wave relative to Ni(II) oxidation occurs in a narrow range and thus only two EIS spectra were recorded, one at the half peak potential and the other at a potential 50 mV higher.

The spectra of the two LDHs are similar, showing a main common and well evident feature, *i.e.*, a great semicircular arc which covers all the frequency range, whose diameter decreases as the potential is increased. On the basis of our previous works and other authors' studies relative to nickel based LDHs, we can state this arc describes the electronic transport inside the LDH structure, due to an electron hopping mechanism between adjacent nickel centres, which is more and more efficient as the potential is increased since an increasing number of Ni(II) sites start to be involved in the oxidation process leading to an increase of the electronic conductivity.

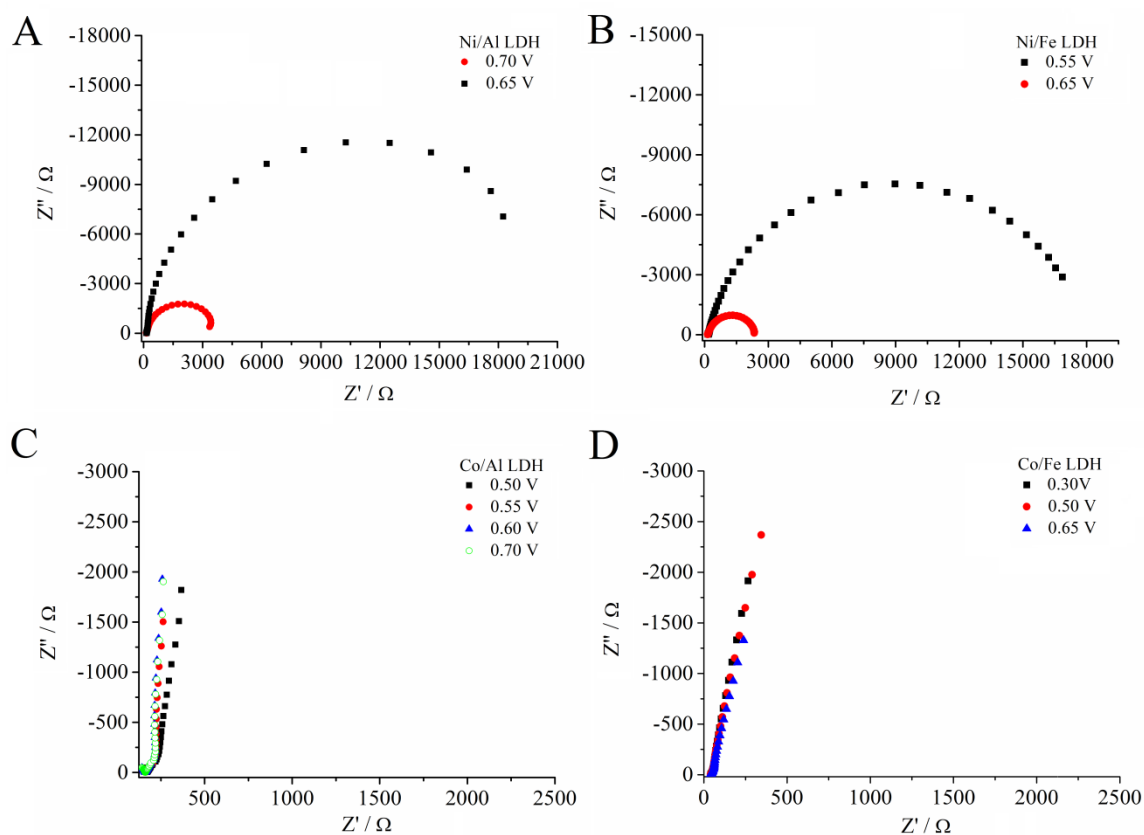


Figure 7.27 - Nyquist plots obtained in 0.1 M NaOH at the potentials indicated in the legends for Pt electrodes coated with A) Ni/Al LDH, B) Ni/Fe LDH, C) Co/Al LDH and D) Co/Fe LDH.

We simulated the experimental data with the equivalent circuits shown in Figure 7.28 which had already provided a good fitting of the EIS data in our previous studies. R_s represents the resistance of the solution and has always a value around 150 Ω . On the contrary, R_e value depends on the LDH type and is strongly influenced by the potential, decreasing as the potential is increased, because the number of nickel sites involved in the electrochemical process increases and the material becomes more conductive.

For Ni/Al LDH R_e ranges from a value of 19520 Ω at the peak potential to 3050 Ω for a potential 50 mV higher, whereas for Ni/Fe LDH R_e decreases from 16800 Ω to 2310 Ω in the same measuring conditions. This means that iron plays an important role in affecting the material conductivity: it does not participate directly to the electronic process but Ni/Fe LDH is more conductive than Ni/Al LDH.

Actually, in view of a supercapacitor development it is important to look at the capacitance values: for both the LDHs the capacitances are independent from the applied potential, C_{dl} having a mean value of $8 \cdot 10^{-8}$ F whereas C_e resulting $1.5 \cdot 10^{-4}$ F for Ni/Al LDH and $2.3 \cdot 10^{-4}$ F for Ni/Fe LDH, and thus not sufficiently high to enable the use of these materials as supercapacitors.

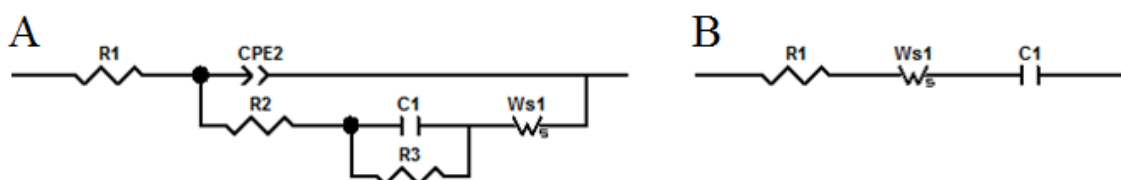


Figure 7.28 - Equivalent circuits employed to fit the Nyquist plots relative to Ni-based (A) and Co-based LDHs (B).

A completely different behaviour is observable when the bivalent metal is Co. In this case the main feature of the spectra is a quasi-straight line almost parallel to the y axis in the low frequency region, which displays a typical capacitive behaviour. The data, plotted in the Nyquist plot form are shown in Figures 7.27 C and D, for Co/Al and Co/Fe LDHs, respectively. The equivalent circuit used to fit the spectra is shown in Figure 7.28 B and is similar to that proposed by P. Vialat [35].

R_1 which represents the electrolyte resistance always displays a constant value around 150 Ω for Co/Al LDH, and 50 Ω for Co/Fe LDH. C_1 represents the capacitance linked to the electronic transfer among cobalt centres and is characterized by an almost $\pi/2$ angle toward Z' axis, like an ideal capacitor. A change in slope is observed in the lower frequency region and thus a Warburg element was introduced which takes into account the OH^- diffusion inside the LDH layer to balance the excess of positive charge generated after cobalt oxidation.

For Co/Fe LDH the capacitance goes from $5.78 \cdot 10^{-3}$ F at 0.35 V to $1.4 \cdot 10^{-3}$ F at 0.65 V, whereas for Co/Al LDH the capacitance values range from $4.53 \cdot 10^{-3}$ F at 0.50 V to $3.80 \cdot 10^{-4}$ F at 0.70 V.

This preliminary electrochemical characterization leads us to conclude that cobalt LDHs are more suitable to be used as materials for the development of supercapacitors than the Ni-based LDHs. Anyway, the evaluation of the specific capacitance was performed for the four investigated LDHs with the aim to elucidate the role of iron in affecting their performances as pseudocapacitors. Tests were made both in 0.1 and 1.0 M NaOH.

7.1.5.2 Specific capacitance and cycling life-time

The specific capacitances (C_s), as a function of the applied potential, were calculated by data deriving from the CV curves and the EIS measurements. Moreover C_s values were also obtained by the charge-discharge curves recorded at different current densities.

The specific capacitance ($F\ g^{-1}$) was evaluated from the CV responses as those displayed in Figure 7.29, since the charge accumulated inside the material is related to the area under the voltammogram in a proper potential window. When the solution is 0.1 M NaOH, the values were calculated between 0.35 and 0.70 V in the case of Co/Al, between 0.50 and 0.75 V for the Co/Fe, between 0.63 and 0.73 for the Ni/Al and between 0.54 and 0.63 for the Ni/Fe LDH. C_s can be obtained by eqn (7.10) where I (A) is the current value, m (g) is the mass and v is the scan rate ($V\ s^{-1}$) [27].

$$C_s = \frac{I \cdot 2}{v \cdot m} \quad (7.10)$$

In 0.1 M NaOH the average specific capacitance values resulted respectively 702 and 810 $F\ g^{-1}$ for Co/Al and Co/Fe LDHs, respectively, whereas when the solution was 1.0 M NaOH the values resulted 881 and 971 $F\ g^{-1}$. Also the specific capacitances of Ni-based LDHs were calculated and the values were lower than the ones related to Co-based LDHs; Ni/Al and Ni/Fe LDHs showed C_s values of 619 and 723 $F\ g^{-1}$, respectively, in 1.0 M NaOH. In 0.1 M NaOH the values were 537 and 654 $F\ g^{-1}$ for Ni/Al and Ni/Fe LDHs, respectively.

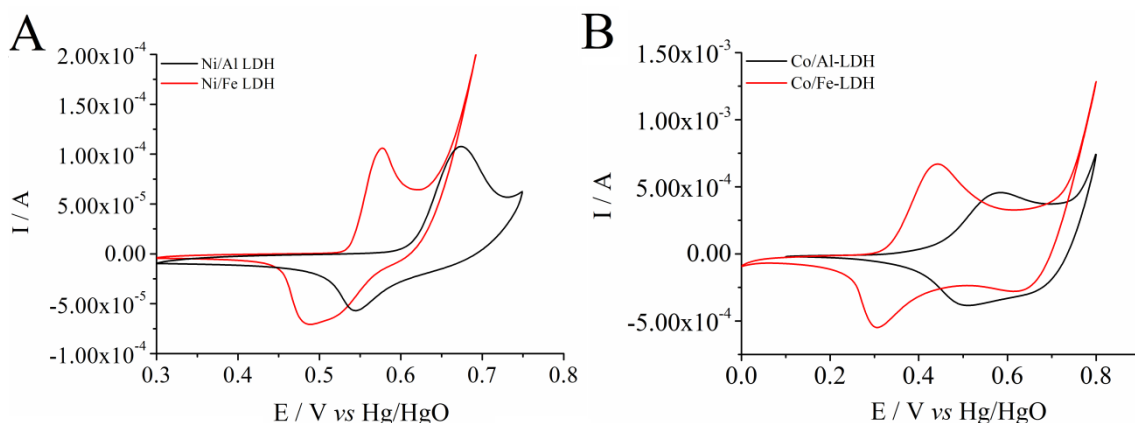


Figure 7.29 - CV curves of the four LDHs electro synthesized on Pt, recorded in 0.1 M NaOH at a potential scan rate of 0.05 V s^{-1} . A) Ni/Al and Ni/Fe LDH, B) Co/Al and Co/Fe LDH. The fifth scan is shown.

For the Co-based LDHs the specific capacitance was also calculated from the EIS measurements. In Figure 7.30 the C_s values resulting from EIS measurements at different potential values are reported. Even if the data are only five, it can be noticed that they follow well enough the curve obtained from the CVs data.

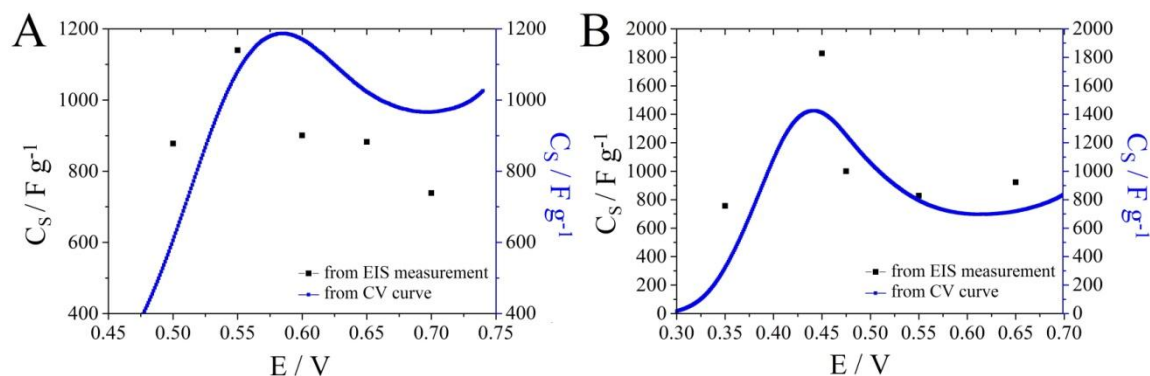


Figure 7.30 – C_s vs E plots obtained from the CV curves and from the EIS measurements, recorded in 0.1 M NaOH for Pt electrodes coated with Co/Al LDH (a) and Co/Fe LDH (b).

The LDHs were also tested by performing galvanostatic charge-discharge tests, in a stable potential window ($0 \div 0.58 \text{ V}$ and $0 \div 0.65 \text{ V}$ for Co/Al and Co/Fe LDH, respectively) under the charging condition of constant current density ($1.0, 2.5, 5.0$ and 10.0 A g^{-1}) in 0.1 and 1.0 M NaOH. The discharge was carried out at the same constant current density. In Figure 7.31 the chronopotentiometric curves for Co/Al and Co/Fe LDHs deposited on Pt, recorded in 0.1 M NaOH are shown. The curves display typical pseudocapacitive behaviours; when the trivalent metal is Al, it can be seen that the galvanostatic charge/discharge curves are not symmetrical triangles like in the case of the electric double layer capacitors. In the first part, from 0 to the potential where the redox

reaction starts to occur, both of them appears as vertical curves, which indicates electric double layer capacitance.

In fact, since the redox reaction still does not occur, the only phenomenon which takes place is the charge adsorption at the interface. For the Co/Fe LDH, it can be observed the typical isosceles triangle-shaped galvanostatic charge/discharge curves, with the discharge curve nearly symmetrical to its corresponding charging counterpart. This result demonstrates the excellent electrochemical reversibility and good coulombic efficiency of the process when Fe is present in the brucite layers. The galvanostatic curves at higher voltage exhibit a smaller slope than the lower voltage section for Co/Al LDH, *i.e.*, in the potential range where the main process is Faradaic. For Co/Fe LDH the slope of the curve in the high voltage region is higher indicating an efficient capacitive behaviour.

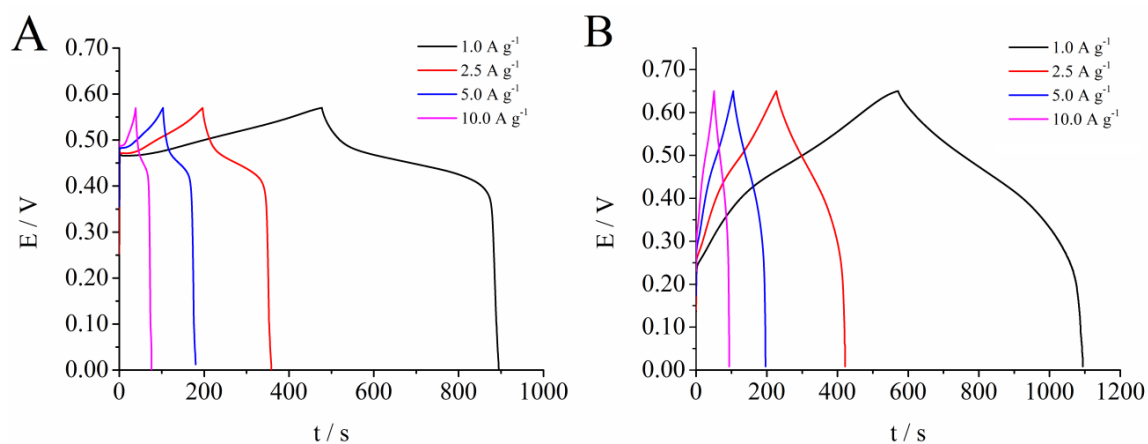


Figure 7.31 - Charge-discharge curves of Co/Al (A) and Co/Fe (B) LDHs electro synthesized on Pt electrode recorded in 0.1 M NaOH at different current densities.

In Figure 7.32 are reported the specific capacitances calculated from the corresponding charge-discharge curves at various current densities, in 0.1 and 1.0 M NaOH. The values were calculated using equation 7.11 [36]:

$$C_s = \frac{I \cdot \Delta t}{m \cdot \Delta V} \quad (7.11)$$

Where I (A) represents the discharge current, m (g) is the mass, Δt (s) and ΔV (V) are the total discharge time and the potential drop during discharge, respectively.

The specific capacitances decrease gradually, as the current density increases since diffusion limits the movement of electrolyte ions at high current densities. This is mainly caused by the increase of the voltage drop of the electrode materials. Nevertheless, the

materials retain a good rate in their performances which means that the Faradaic reaction is still reversible at higher current densities. Co/Fe LDH showed the highest C_s values, 810, 750, 723, and 705 $F\ g^{-1}$ at current densities of 1.0, 2.5, 5.0 and 10.0 $A\ g^{-1}$, respectively in 0.1 M NaOH. Slightly higher values were obtained in 1.0 M NaOH, indeed the C_s values reach up to 854 and 869 $F\ g^{-1}$ at 1.0 $A\ g^{-1}$ for Co/Al and Co/Fe LDHs, respectively.

These results are comparable with those previously reported in literature for similar compounds; Gupta *et al.* [37] calculated a specific capacitance of 706 $F\ g^{-1}$ at current density of 1.0 $A\ g^{-1}$ in 1.0 M KOH for a Co/Al LDH prepared by a potentiostatic electrodeposition on stainless steel electrodes.

As expected, even in this case Ni-based LDHs showed lower C_s values than the ones obtained for Co-based LDHs. Ni/Fe LDH displayed a slightly higher C_s than Ni/Al LDH and the best results were obtained in 1.0 M NaOH (674 $F\ g^{-1}$ at 1.0 $A\ g^{-1}$).

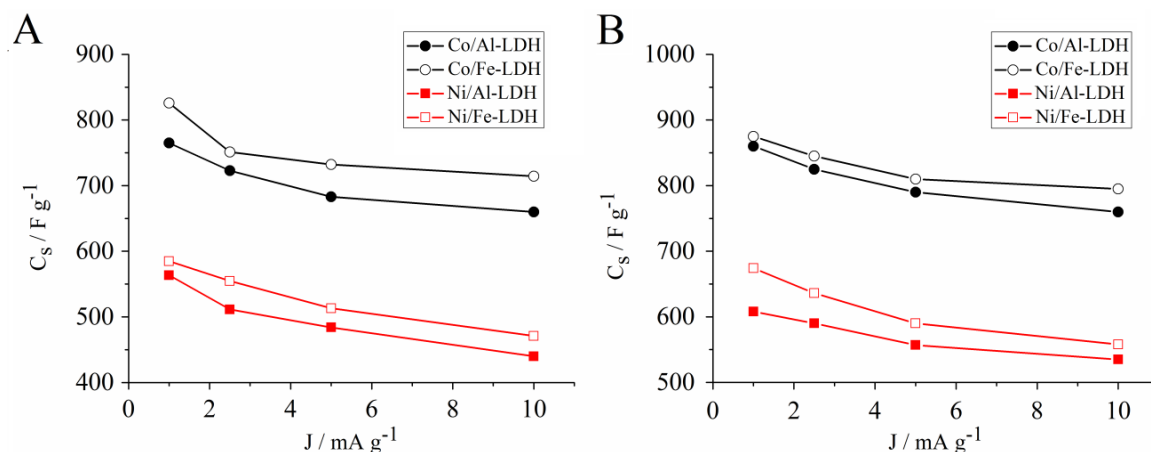


Figure 7.32 - Specific capacitances calculated from the charge-discharge curves of the four LDH coatings on Pt, at different current densities. The values shown were obtained in 0.1 (A) and in 1.0 M (B) NaOH.

Cycling performance is a key factor for the pseudocapacitors for many practical applications. The cycling tests for the Co-based LDHs were carried out applying a constant current density of 5.0 $A\ g^{-1}$. As shown in Figure 7.33, after 1000 charge-discharge cycles, the specific capacitances of Co/Al and Co/Fe LDHs exhibited a high long-term stability since those materials can retain 81 and 82 %, respectively, of their original specific capacitance.

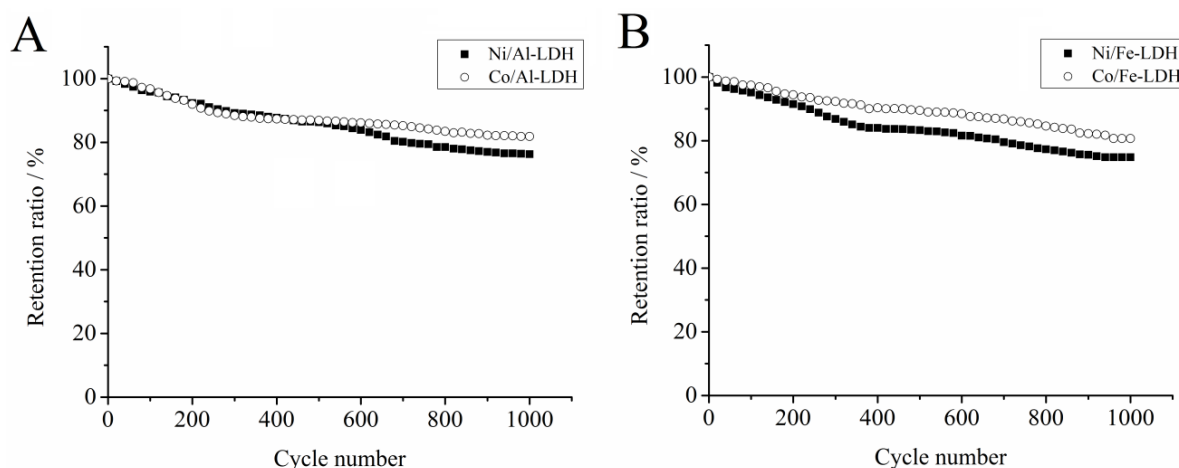


Figure 7.33 - Retention of the specific capacitances of the Ni-based (A) and the Co-based LDHs on Pt in 1.0 M NaOH, at 5 A g⁻¹.

Guoxiang *et al.* reported a Co/Al LDH nanoflake arrays synthesized by a hydrothermal synthesis method on nickel foam. The Co/Al LDH showed a specific capacitance of 930 F g⁻¹ at 2.0 A g⁻¹ and after 2000 cycles, the specific capacitance still maintained 88.9 % of the maximum value. They suggest that the high cycling performance is due to the presence of Al³⁺ in the LDH structure which prevents the occurrence of the commonly observed conversion from α to β phase for the pure cobalt hydroxide, during the charging/discharging process [38].

7.1.5.3 Performances of the LDHs on GC

The same studies carried out using Pt as support were conducted for LDHs coated GC electrodes. The mass of each LDH was calculated by extrapolating the values from the EQCM responses.

In Table 7.3 are reported the C_s values obtained for the LDHs coating on GC in 0.1 and 1.0 M NaOH. The values calculated from the CVs are slightly lower to the ones obtained for the Pt coated with the LDHs.

Even in this case the specific capacitance of the four LDHs was also calculated at different current densities of 1.0, 2.0, 5.0 and 10.0 A g⁻¹ in 0.1 and 1.0 M NaOH.

Table 7.3 Specific Capacitance calculated from the CV curves of the four LDHs coated on GC, in 0.1 and 1.0 M NaOH.

LDHs	$C_s / F g^{-1}$	
	0.1 M NaOH	1.0 M NaOH
Ni/Al	508.8	615.9
Ni/Fe	644.4	746.1
Co/Al	685.6	834.7
Co/Fe	706.1	844.8

The LDHs were also tested by performing galvanostatic charge-discharge tests, in a stable potential window under the charging condition of constant current density. The discharge was performed with the same current density. The specific capacitances vs the current densities are reported in Figure 7.34.

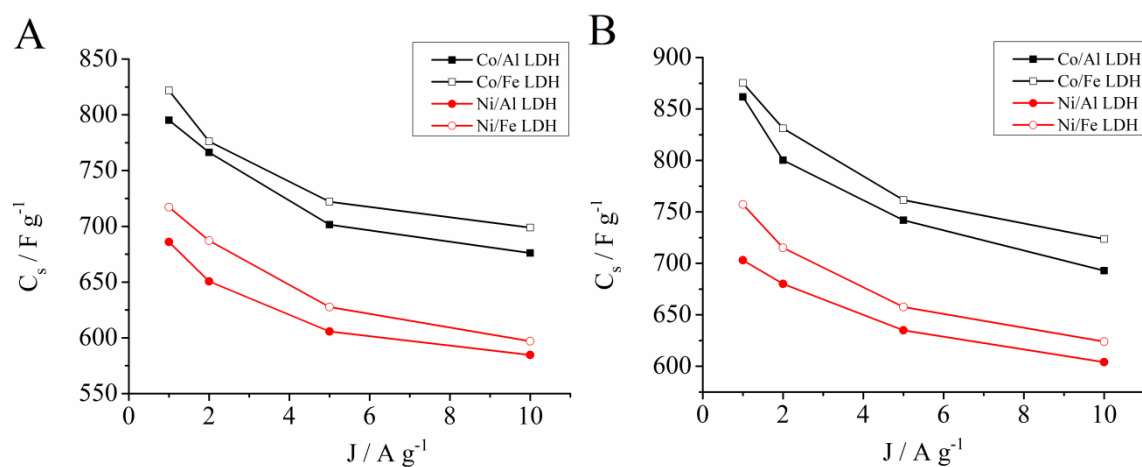


Figure 7.34 - Specific capacitances calculated from the charge-discharge curves of the four LDH coatings on GC, at various current densities. The values shown were obtained in 0.1 (A) and in 1.0 M (B) NaOH.

The values obtained were slightly lower than the ones calculated for the same LDHs coated on Pt, but the trend was almost the same. The higher specific capacitance was again displayed by Co/Fe LDH and the lower values were obtained for the Ni-based LDHs. Even in this case the presence of Fe slightly enhances the performances.

7.2 Conducting polymers electrodeposition: bulk heterojunction solar cells

Bulk heterojunction solar cells were fabricated employing different PEDOT buffers: one deposited by electrochemical potentiostatic synthesis (perchlorate as counterion) and the other by casting a commercial polymer (polystyrene sulfonate, PSS, as counterion) on ITO electrodes. To exploit the potentialities of the electrochemical approach we carried out a detailed study to find the best experimental conditions for PEDOT:ClO₄ electrosynthesis in order to construct BHJ solar cells.

The electrochemical synthetic approach allows for the rapid obtainment of PEDOT films directly on the electrode surface, with tunable electroactivity and thickness. Besides, very low amounts of monomer are consumed and it is also possible the introduction of different counterions to compensate the polymer positive charge in dependence on the used electrolyte. In literature, it was reported that the best properties of PEDOT, as to its application in organic solar cells, were obtained in the presence of LiClO₄ as the supporting electrolyte since this salt leads to a higher electropolymerization efficiency and to an increase of electroactivity and crystallinity of the resulting polymers [39]. For this reason, the research work was aimed to fabricate BHJ cells containing electrosynthesized PEDOT:ClO₄ as buffer layer and to compare their performances with the ones displayed by cells where the hole extracting layer was constituted of the commercially available PEDOT:PSS.

The photoactive layer was composed by PCBM as electron acceptor in the blend, and the most commonly employed regioregular P3HT or a polythiophene copolymer, functionalized with a porphyrin derivative, as electron donor. In particular, the latter was the regioregular thiophenic copolymer (poly [3 - (6 – bromohexyl) thiophene –*co*- (3 - [5-(4–phenoxy)-10,15,20-triphenylporphyrinyl] hexylthiophene)] (rr-P(T6Br-*co*-T6TPP)), which had been synthesized by the polymer group of the Department of Industrial Chemistry “Toso Montanari” (University of Bologna), in order to improve the absorption in the UV/Vis region in terms of both wideness and intensity [40,41].

In the following paragraphs the morphologies of the PEDOT and the photoactive layers, investigated by atomic force microscopy, will be shown in order to correlate the particles size and compactness of the layers with the cells performances.

7.2.1 Electrochemical synthesis of PEDOT:ClO₄

To fabricate the electrochemical cells different approaches were tried in order to obtain the desired characteristics for PEDOT:ClO₄ film. Many experiments were done to find the best conditions to deposit the PEDOT layer on ITO; the applied techniques were chronoamperometry (potentiostatic route) and cyclic voltammetry (potentiodynamic route). The PEDOT film synthesized by chronoamperometry (CA, Figure 7.35) resulted more stable and more homogeneous, as inspected by optical microscopy; so, this technique was chosen for the electrodeposition. The lowest concentration of EDOT to obtain a homogeneous film was found to be $5.0 \cdot 10^{-3}$ M.

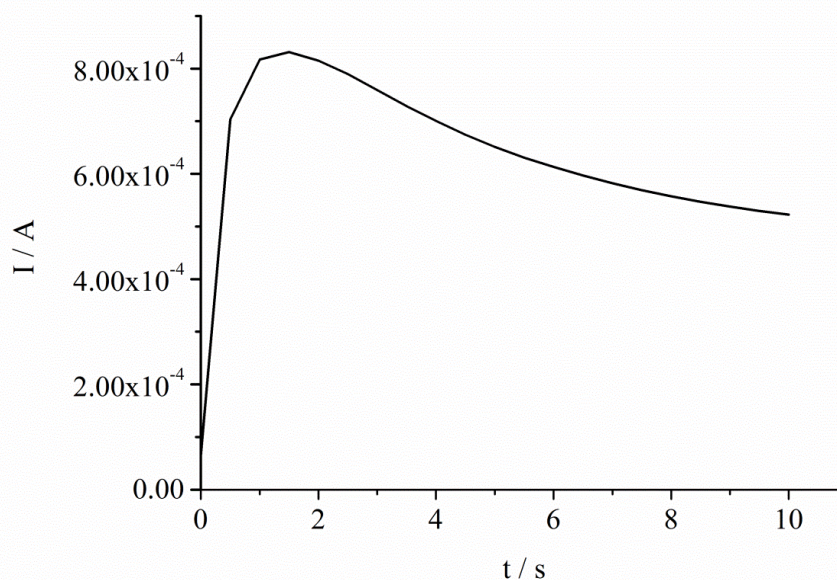


Figure 7.35 – Potentiostatic deposition (at +1.05 V vs SCE) of PEDOT:ClO₄ on ITO from a solution containing $5.0 \cdot 10^{-3}$ M EDOT and 0.1 M LiClO₄.

However, the thickness of the obtained film was too high (~200 nm) to be used for the fabrication of the BHJ cells. Therefore, a thinning procedure consisting of 25 CV cycles in distilled water, containing only the supporting electrolyte, was applied to ITO glasses after the electrodeposition. This treatment guaranteed a uniform degradation of the layer, down to ~50 nm, without creating uncovered zones.

7.2.2 Annealing treatments

The relatively high efficiency of P3HT:PCBM devices has been partly attributed to the ability of P3HT to self-organize into a two-dimensional lamellar structure in a process mediated by the interpenetration of the side groups of adjacent polymer chains. This ordered structure leads to a very small (3.8 Å) [42,43] distance among the polymer chains and a high charge mobility for a conjugated polymer. Furthermore, a higher crystallinity of P3HT:PCBM films is observed upon annealing, which leads to the formation of P3HT long fibrils and enhances the hole mobility by an order of magnitude [44,45] whilst micrometric PCBM aggregates can form thanks to diffusion and crystallization of PCBM [46]. All the BHJ cells investigated in this work were fabricated submitting both the PEDOT layer and the blend film to a proper annealing treatment. In particular, PEDOT films were annealed at 120 °C under vacuum for 2 h, and after the blend deposition, the cells were again annealed at 150 °C for 30 min. These conditions were chosen on the basis of both the literature data [47] and the expertise acquired by our group in the fabrication of devices constituted of commercial PEDOT:PSS and P3HT:PCBM blend.

7.2.3 Electrochemical characterization of the polymeric films and the blend

BHJ solar cells are fabricated using ITO as transparent electrode (cell anode) which is generally coated, by casting, with two layers: the lower consisting of the hole transporting material PEDOT:PSS and the upper of the blend obtained by mixing PCBM with the electron donor copolymer.

We decided to electrochemically characterize the components of the fabricated BHJ solar cells and of the composite PEDOT:PSS/blend by cyclic voltammetry using Pt as electrode support instead of ITO, which has worse conductivity, in order to record better electrochemical responses.

7.2.3.1 Electrochemical characterization of PEDOT:PSS and PEDOT:ClO₄ films

The commercial PEDOT:PSS and the electrosynthesized PEDOT:ClO₄ were electrochemically characterized by CV. The relevant curves (Figure 7.36) were recorded

in acetonitrile containing TBAPF6 as supporting electrolyte, using a Pt electrode coated either with PEDOT:PSS or PEDOT:ClO₄.

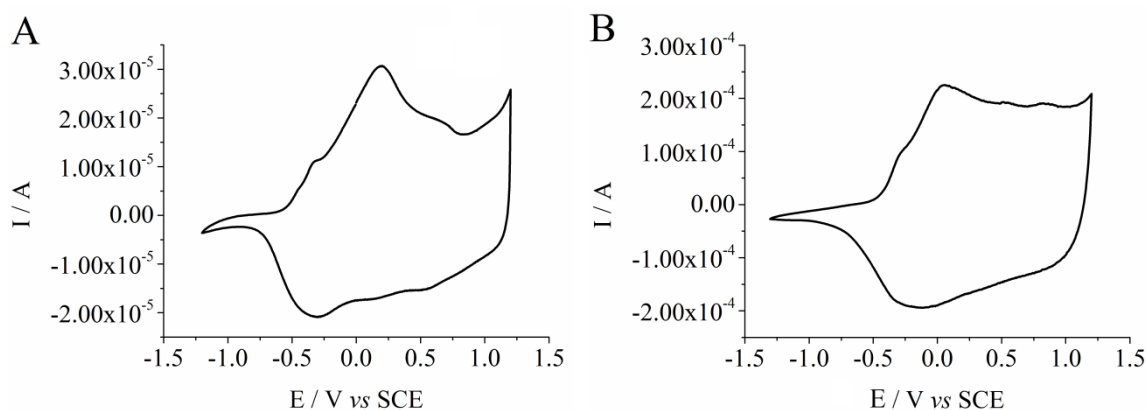


Figure 7.36 - CV curves (fifth cycle) recorded in 0.1 M TBAPF6 acetonitrile solution at the scan rate of 0.5 V s⁻¹ for a Pt electrode coated with a thin film of PEDOT:ClO₄ (A) and PEDOT:PSS (B).

It can be seen that the electrochemical behaviour is similar for both polymers since they acquire conductive character at very low potential (about -0.5 V), even if for PEDOT:ClO₄ (Figure 7.36 A) the oxidative doping process starts at ~0.05 V less anodic potential. Furthermore, the electrochemical characterization of PEDOT:PSS (Figure 7.36 B) displays a more capacitive behaviour. Obviously, the recorded currents are not comparable since the procedure to coat the Pt surface with PEDOT:PSS involves a higher amount of material. For both polymers, the CV responses evidence two oxidation steps which correspond to the formation of polarons and bipolarons, typical of the conductive mechanism of this kind of polymers [48].

7.2.3.2 Electrochemical characterization of rr-P(T6Br-co-T6TTP), PCBM and blend

In Figure 7.37 A are shown the CVs relevant to the Pt electrode coated with the regioregular copolymer rr-P(T6Br-co-T6TTP) copolymer, recorded in acetonitrile containing TBAPF6 as supporting electrolyte.

It can be observed that the rr-P(T6Br-co-T6TTP) copolymer film displays an onset of the p-doping process at about +0.8 V. The good conductivity displayed by the copolymer confirms that it can be successfully employed as electron donor.

The HOMO level of rr-P(T6Br-co-T6TTP) was calculated from CV data, while the LUMO energy was calculated indirectly, taking into account that it corresponds to the HOMO energy plus the optical energy gap (E_{opt}). E_{opt} (1.80 eV) corresponds to the

energy of the long wavelength edge of the exciton absorption band [49] and was estimated from the UV/Vis spectrum of the copolymer (see below in Figure 7.39, paragraph 7.2.4.1). The onset point of the p-doping process of rr-P(T6Br-co-T6TTP) is +0.8 V, which leads to HOMO level energy of -5.20 eV, considering that the SCE reference electrode has a potential of +4.40 eV relative to vacuum [50].

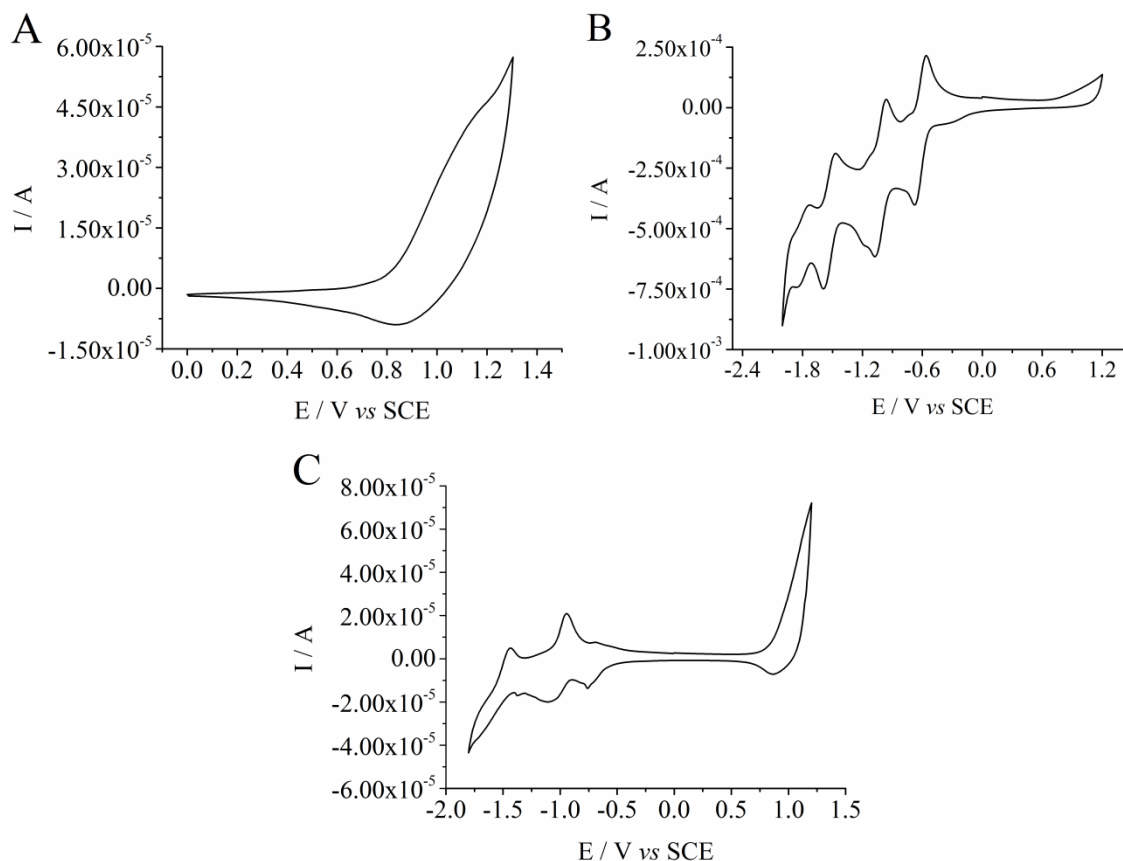


Figure 7.37 - CV curves recorded in 0.1 M TBAPF₆ acetonitrile solution at 0.02 V s^{-1} for a Pt electrode coated with (A) a thin film of the rr-P(T6Br-co-T6TTP), (B) CV recorded with the Pt electrode soaked in a solution of acetonitrile/o-dichlorobenzene (1:1 V/V) containing 0.075 mM PCBM, and (C) a thin film of the blend composed of rr-P(T6Br-co-T6TTP)/PCBM. The fifth scan is shown, scan rate: 0.1 V s^{-1} for B and C.

The energy of the LUMO level is then -3.40 eV. Thus, rr-P(T6Br-co-T6TTP) displays a lower band gap, +1.8 eV, than the usually reported polyalkylthiophenes, having E_g values around 2.0 eV [51], which can be attributed to its broad absorption in the visible range. Due to its low band gap the porphyrin containing conjugated copolymer appears, therefore, a suitable material for applications in polymeric solar cells.

The displayed CV of PCBM (Figure 7.37 B) was recorded when the electron acceptor of the BHJ cell was present in solution and not as thin film on the Pt surface. This choice permitted to better point out all the reversible reductions ascribable to the four one-electron processes characteristic of this fullerene derivative in the potential range

between -0.3 and -1.9 V vs SCE [52]. In fact, in the case of the thin film, the four peaks system was not evident at all. The CV displayed by the Pt electrode coated only with the blend (Figure 7.37 C) can be considered as due to the single contributions of the two components (see Figure 7.37 A and B). In particular, it can be seen that the copolymer is conductive for anodic potentials higher than 0.8 V, whereas the presence of the fullerene derivative in the blend is evidenced by the complex feature in the cathodic range of the potential which comes from a sort of convolution of the four redox processes, above cited. The electrochemical behaviour of the blend well explains why the copolymer works as the electron donor and the PCBM as the electron acceptor in the BHJ cell.

7.2.4 Optical properties of the OPV cells components

The spectroscopic properties of the cells layers and components were fully investigated recording UV-Vis absorption and photoluminescence (PL) emission spectra. The absorption spectra were useful to study the PEDOT oxidation degree and, thus, the doping level, beside, of course, the wideness of the solar light absorption of the device. Photoluminescence measurements were fundamental to study the charge transfer in the blended film of the copolymer bearing porphyrin groups with PCBM.

7.2.4.1 Cells components absorption spectra

Figure 7.38 shows the absorption spectra recorded for both PEDOT polymers using ITO as a support. Again, the absorption values are different due to the different deposited amounts. Nevertheless, it is possible to examine the shape of the spectra in order to obtain some information about the oxidation degree of the material in the pristine state. In the range between 300 and 600 nm, the two spectra display the same trend, whereas the shapes are different in the range 600 – 800 nm. This spectral zone corresponds to the absorption of polarons and bipolarons which displays a maximum at about 900 nm and a plateau between 750 and 900 nm, respectively [53]. Unfortunately, we were not able to record the absorbance over 800 nm due to a high noise. Hence, our results suggest that PEDOT:ClO₄ displays an oxidation degree higher than the pristine PEDOT:PSS due the presence of a plateau in its spectrum that is consistent with the formation of bipolarons, maybe ascribable to the potentiostatic electropolymerization.

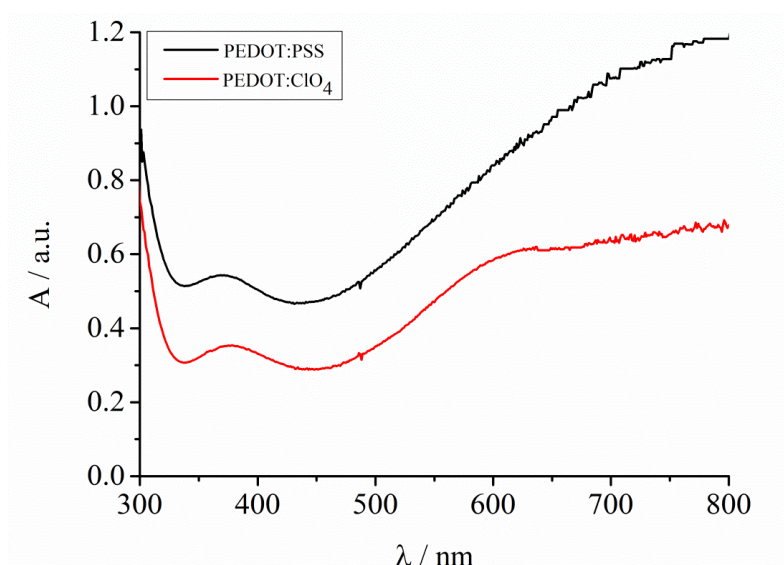


Figure 7.38 - Absorption spectra of PEDOT:PSS (black line) and PEDOT:ClO₄ (red line) coated ITO.

The UV-Vis absorption spectra of the rr-P(T6Br-co-T6TPP), PCBM and blend (1:1 w/w) as thin films on ITO are shown in Figure 7.39. The absorption of rr-P(T6Br-co-T6TPP) shows the porphyrins typical features [54], *i.e.*, the Soret band at about 420 nm, and the four Q-bands at 522, 555, 595, 647 nm, while the absorption between 455 and 500 nm, partially overlapped to the porphyrin bands, corresponds to the thiophene moiety of the copolymer. The PCBM absorption spectrum exhibits a well-defined band centered at 340 nm. All the features of the blended film absorption can be reproduced by a linear combination of rr-P(T6Br-co-T6TPP) and PCBM absorptions in agreement with the composition of the film.

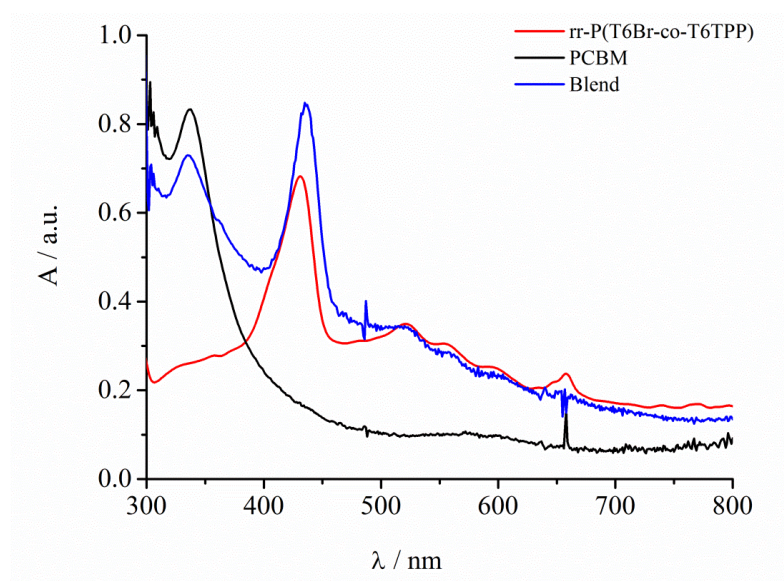


Figure 7.39 - UV/Vis spectra of thin films of rr-P(T6Br-co-T6TPP), PCBM and rr-P(T6Br-co-T6TPP)/PCBM (1:1, w/w) blend on ITO.

7.2.4.2 Emission spectra of the photoactive layer components

To confirm the possibility of charge transfer between the donor and the acceptor molecules in the blended film, a photoluminescence study of the rr-P(T6Br-co-T6TPP) 85/15, PCBM neat thin films and of the blend (1:1 w/w) was performed. The photoluminescence measurements were carried out by photoexcitation of the components at the maximum absorption and the PL spectra are shown in Figure 7.40. The neat copolymer rr-P(T6Br-co-T6TPP) shows two PL emission peaks at 657 and 725 nm, under excitation at 430 e 480 nm, respectively, corresponding to the absorption wavelength of the porphyrin Soret band, and of the thiophene component, respectively. The PCBM PL emission spectrum shows a large feature in the wavelength range from 700 to 850 nm, under excitation at 370 nm. Concerning the blend spectrum of rr-P(T6Br-co-T6TPP) with PCBM, a large emission peak is observed from 750 nm onward, with a maximum at about 814 nm. The shape of the peak strongly resembles the pristine PCBM emission slightly red-shifted, whereas a very small emission band is observed at about 655 nm, due to the copolymer. The emission of the copolymer in the blend is, therefore, quenched, suggesting the occurrence of the electron transfer from the copolymer to PCBM and means that the energy transfer between the components is faster than the singlet exciton decay in the copolymer and PCBM [55,56].

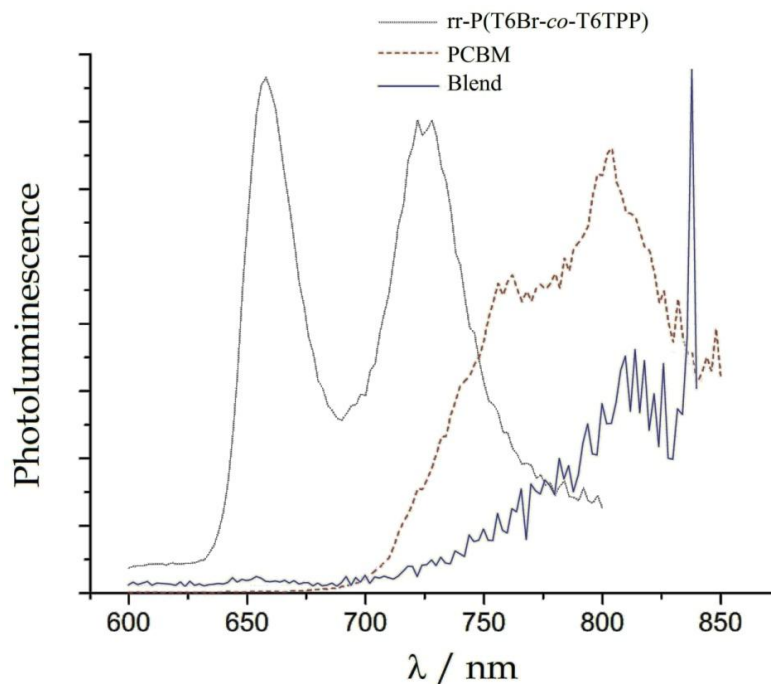


Figure 7.40 - Photoluminescence spectra of thin films of rr-P(T6Br-co-T6TPP), PCBM and rr-P(T6Br-co-T6TPP)/PCBM (1:1 w/w) blend.

7.2.5 Photovoltaic performances of the BHJ cells

The most commonly used parameters to test the performances of the OPV devices were measured, *i.e.*, the short circuit current density J_{SC} , the open circuit voltage V_{OC} and the fill factor. The overall solar energy conversion efficiency is the maximum extracted power compared to the incident solar power.

The different cells configurations fabricated (an example is shown in Figure 7.41) were tested under standard conditions of illumination.



Figure 7.41 – BHJ solar cell composed of an anode of ITO, PEDOT:ClO₄ as buffer layer, P3HT:PCBM as blend and Al as cathode.

All the cells were not optimized for their photovoltaic performances (as evidenced by the obtained low values of J_{SC} and FF) since the measurements aimed to compare the photoelectric effects in identical conditions so favoring the data reproducibility rather than the overall efficiency.

The fabrication reproducibility of the BHJ cells was verified preparing three identical cells for each of the four devices, *i.e.* those based on PEDOT:PSS and P3HT or rr-P(T6Br-co-T6TPP), as electron donor in the photoactive layer, or those based on PEDOT:ClO₄ and the same donors. An example of the I/V characteristic curves of the cells fabricated with the two blends and PEDOT:PSS and PEDOT:ClO₄, obtained under illumination are reported in Figure 7.42 and 7.43.

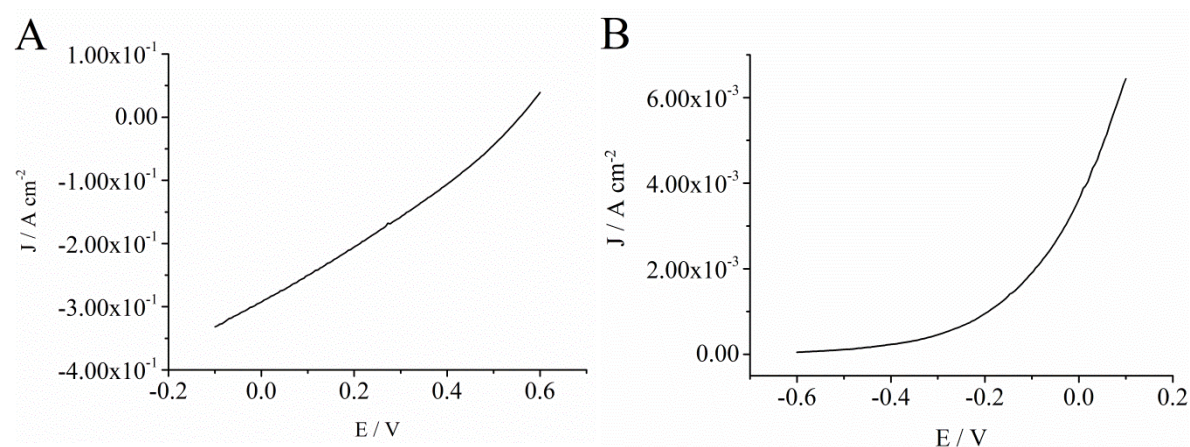


Figure 7.42 – I/V curves recorded under AM 1.5 illumination of a OPVs realized using as photoactive layer the blend rr-P(T6Br-co-T6TPP):PCBM annealed at 150 °C for 30 min and as buffer layer PEDOT:PSS (A) and PEDOT:ClO₄ (B).

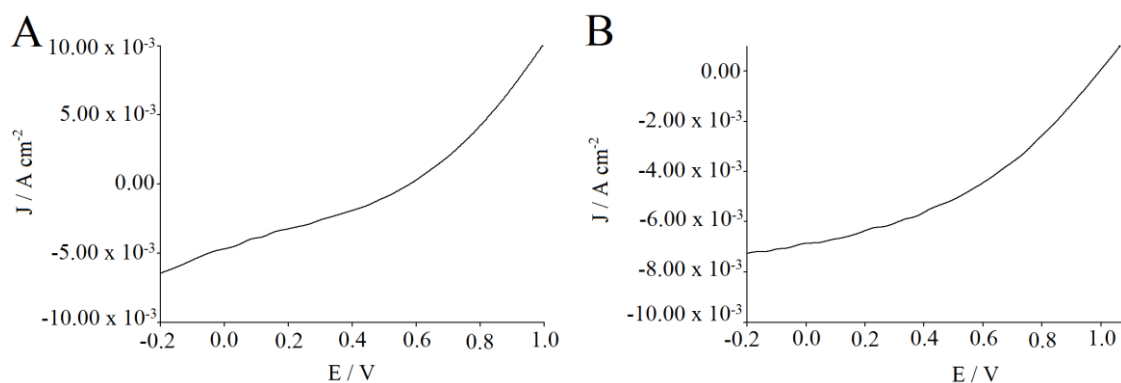


Figure 7.43 – I/V curves recorded under AM 1.5 illumination of a OPVs realized using as photoactive layer the blend P3HT:PCBM annealed at 150 °C for 30 min and as buffer layer PEDOT:PSS (A) and PEDOT:ClO₄ (B).

The efficiencies and the main characteristic parameters of all the tested cells are shown in Tables 7.4 and 7.5. Looking at the individual efficiencies, we can say that the reproducibility of the cells construction was very good (percentage standard deviation ~2). The average efficiency of the cells prepared using PEDOT:PSS as buffer layer was 0.20 and 0.86 % when the photoactive polymer was rr-P(T6Br-co-T6TPP) or P3HT, respectively. When PEDOT:PSS was substituted by PEDOT:ClO₄, the power conversion efficiency (PCE) of the cells made with the copolymer lowered to 0.15 % whilst those made with P3HT reached a mean efficiency of 1.06 %.

Table 7.4 Characteristic parameters of the tested solar cells fabricated with PEDOT:PSS and the two different blends.

Blend	J_{sc} / $10^{-3} \text{ A cm}^{-2}$	V_{oc} / V	FF %	PCE %
rr-P(T6Br-co-P6TPP):PCBM	1.24 ± 0.07	0.55 ± 0.01	29.08 ± 0.02	0.201 ± 0.005
P3HT:PCBM	4.80 ± 0.05	0.57 ± 0.01	31.00 ± 0.05	0.86 ± 0.01

Table 7.5 Characteristic parameters of the tested solar cells fabricated with PEDOT:ClO₄ and the two different blends.

Blend	J_{sc} / $10^{-3} \text{ A cm}^{-2}$	V_{oc} / V	FF %	PCE %
rr-P(T6Br-co-6TPP):PCBM	1.01 ± 0.02	0.52 ± 0.01	28.91 ± 0.06	0.150 ± 0.002
P3HT:PCBM	5.90 ± 0.01	0.60 ± 0.01	30.00 ± 0.04	1.06 ± 0.01

Using the regioregular copolymer P(T6Br-co-T6TPP):PCBM blend instead of the commonly employed P3HT:PCBM system, the lower efficiency can be attributed to a loss of the lamellar stacking in the solid state packing due to the steric hindrance of the porphyrin moiety. Therefore, even if more excitons can be produced by inserting thiophene units bearing a chromophore which widens the absorption spectrum, steric factors significantly affect the arrangement of the polymer chains in the donor domains, maybe preventing the interpenetration of the side groups of adjacent polymer chains. The decrease of organization in donor domains results in a worse charge transport (as evidenced by the low measured J_{SC} values) which overcomes the expected improvement of cell performance related to the optical absorption characteristics of the polymer.

Comparing the efficiencies obtained for the BHJ cells fabricated either with PEDOT:PSS or PEDOT:ClO₄, we can state that the values are almost the same even if higher PCEs result when the donor is the P3HT using PEDOT:ClO₄ (~20 %) whereas when the donor is the copolymer, higher PCEs are obtained using PEDOT:PSS (~25 %). These differences are hardly explainable but support the point of view that PEDOT electrochemical synthesis can be used as a valid alternative to PEDOT:PSS coating.

7.2.6 AFM morphological characterizations

Figure 7.44 shows atomic force microscopy surface topographies of PEDOT:PSS, PEDOT:ClO₄ and photoactive layers. The PEDOT:PSS layer displays a root mean square (RMS) roughness of 3.92 nm and the morphology of the domains is cauliflower-like. In the height-modulated image, the boundaries between the different particles are not well defined because PEDOT:PSS is a gel where the external polymeric chains interact, so leading to grains merging.

The phase modulated image highlights better the particles of PEDOT:PSS that are constituted of two different parts. The inner ones are black and are composed of PEDOT:PSS. The outer parts are grey and consist essentially of PSS that is added to the commercial formulation in excess to generate a negative charge on the particles in order to increase their stability [57]. The separation between the two polymer materials is not very sharp probably because PEDOT concentration decreases at the particles boundaries.

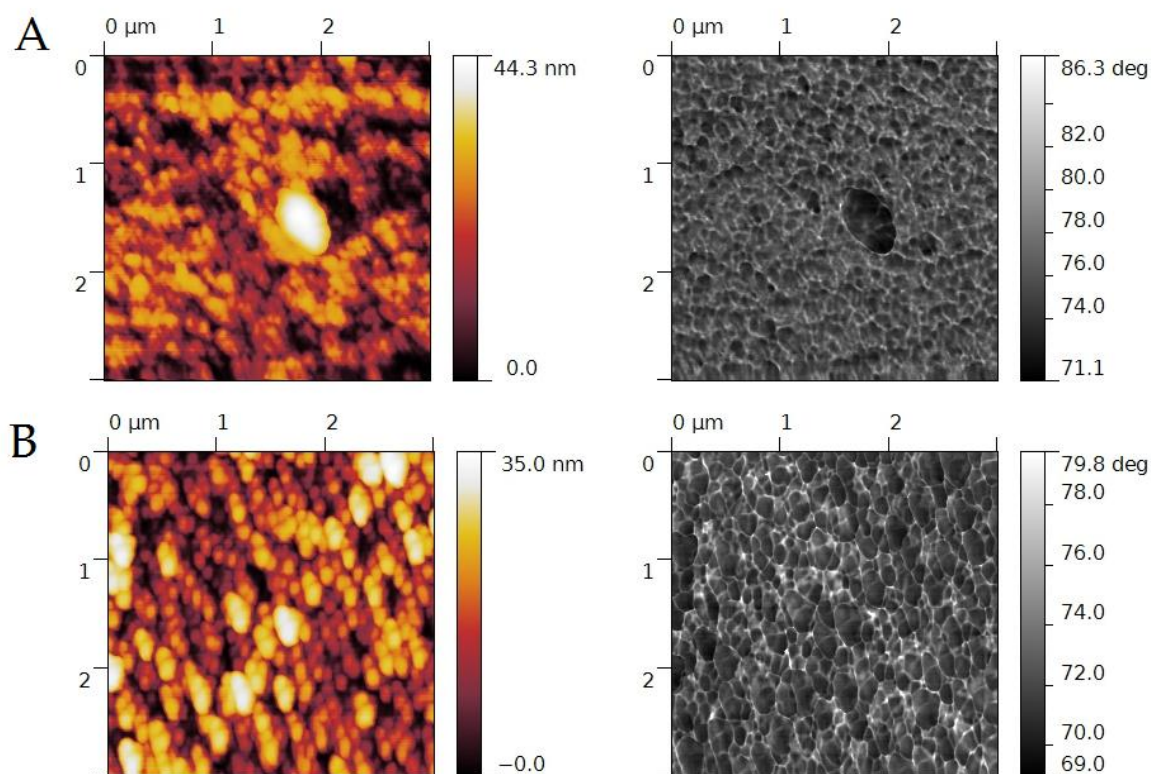


Figure 7.44 – AFM images of PEDOT:PSS (A) and PEDOT:ClO₄ (B) (left: height-modulated images; right: phase-modulated images).

The PEDOT:ClO₄ shows a RMS roughness of 4.53 nm with an ellipsoidal morphology of the particles. In Table 7.6 are reported the RMS roughness of the photoactive films beside the average diameter size of the grains.

The shape of the domains is very well defined both in the height- and in the phase-modulated images. Probably, in this material, the formation of crystalline domains is preferred, due to the smaller size of ClO₄⁻ anions, and so the boundaries of the different grains appear very clear-cut. The preferential formation of crystalline domains has been already reported for PEDOT:Tos (tosylate) [58].

Table 7.6 RMS roughness and average diameter size of the grains of the photoactive films.

Blend	PEDOT:PSS		PEDOT:ClO ₄	
	RMS / nm	Diameter / nm	RMS / nm	Diameter / nm
rr-P(T6Br-co-P6TPP):PCBM	8.90	17	9.15	17
P3HT:PCBM	9.68	18	5.08	12

From Figure 7.45 it can be seen that the blends deposited on the commercial PEDOT:PSS layer show a less homogeneous morphology, with a coarse structure and with aggregates having a larger average domain size. This is particularly true for rr-P(T6Br-co-T6TPP):PCBM sample, in which the cauliflower like domains, typical of PEDOT:PSS chains, are still visible, even if surrounded by the copolymer chains. P3HT also shows an irregular surface, with a lot of dots ascribable to the nanoaggregates of PCBM. Passing from commercial to electrosynthesized PEDOT, we can observe small differences in the copolymer based sample, but a very different behaviour in the presence of the conventionally adopted P3HT. In fact, this time, the photoactive blend shows very small aggregates with the lowest roughness, as evidenced by the RMS value.

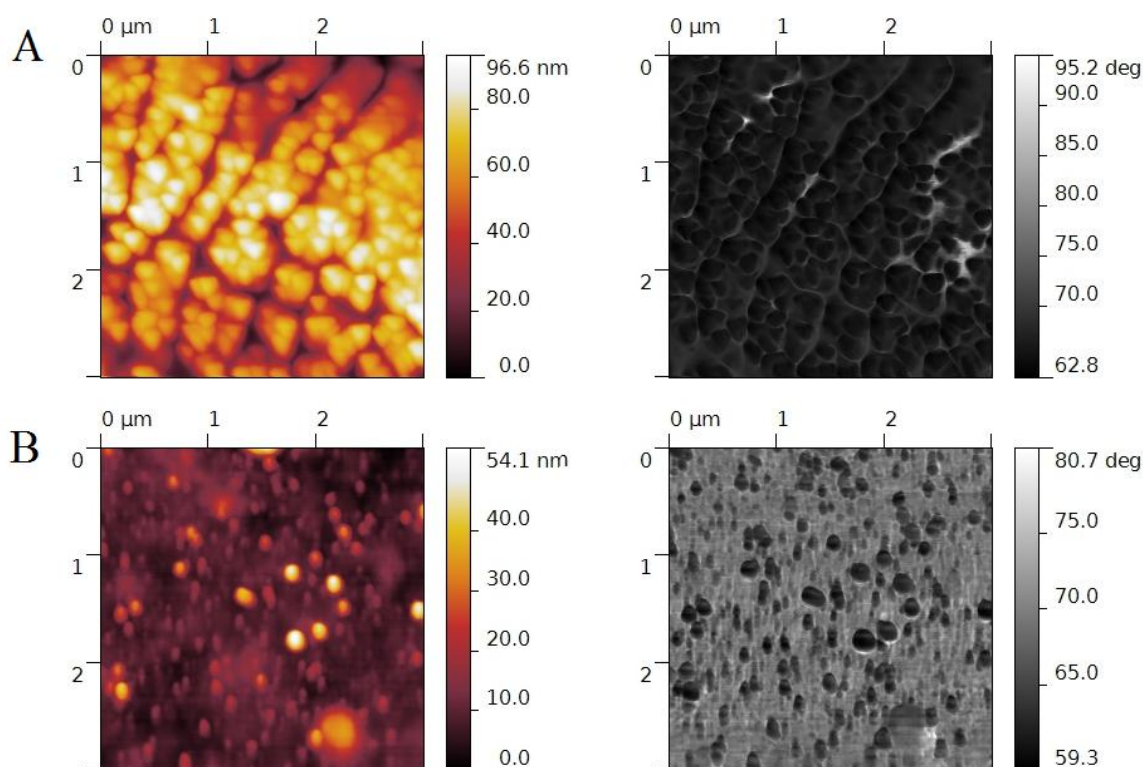


Figure 7.45 - AFM images of the prepared blends (left: height-modulated images; right: phase-modulated images): rr-P(T6Br-co-T6TPP):PCBM with PEDOT:PSS (A) and P3HT:PCBM with PEDOT:PSS (B).

Using LiClO₄ (Figure 7.46) it is possible to obtain a compact structure with clusters of small dimension due to the easy insertion of Li⁺ inside the polymer matrix during the electrosynthesis, which can occupy all the empty spaces in the polymer chains [59]. The high interfacial area of the electron acceptor domains in the electron donor matrix as well as their uniform distribution can effectively lead to a better control of the separation of

the components in the photoactive blend, giving a positive effect on the conversion efficiency.

After these considerations it can be said that the PEDOT layer does not act only a “buffer layer” but is also able to drive the morphology of further layers thanks to its morphological characteristics. Thus, electrochemically deposited PEDOT has beneficial effects on the morphology of the P3HT sample only, since the lower solubility and higher tendency to self-aggregate of rr-P(T6Br-co-T6TPP) polymer probably prevent a uniform separation of the active blend components to be achieved on a nanoscale domain. This behaviour still remains unclear since the final morphology of the active layer is influenced by many factors acting simultaneously, such as the solubility of the components in the filming solvent, the affinity between the filming solvent and the underlying PEDOT layer and the affinity among the electron acceptor molecules, the electron donor polymer and the buffer layer components.

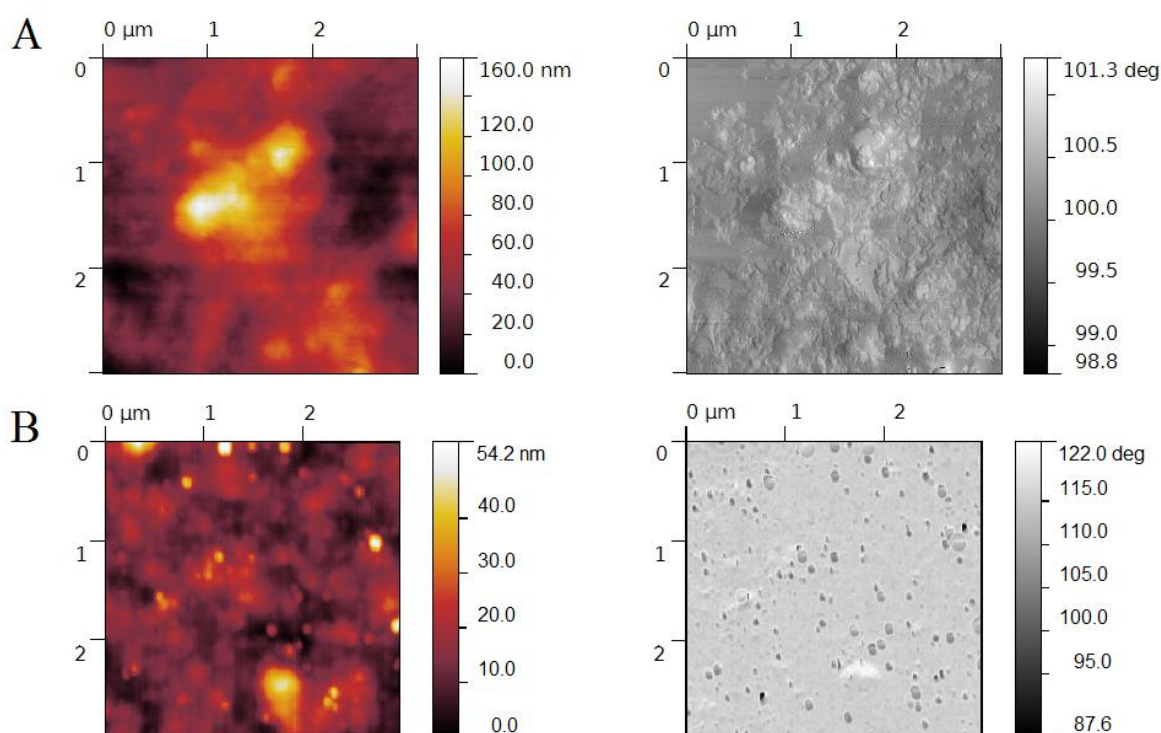


Figure 7.46 – AFM images of the prepared blends (left: height-modulated images; right: phase-modulated images): rr-P(T6Br-co-T6TPP):PCBM with PEDOT:ClO₄ (A) and P3HT:PCBM with PEDOT:ClO₄ (B).

REFERENCES

- [1] E. Scavetta, A. Casagrande, I. Gualandi, D. Tonelli. *J. Electroanal. Chem.* 722-723 (2014) 15.
- [2] F. Cavani, F. Trifirò, A. Vaccari. *Catal. Today* 11 (1991) 173.
- [3] E. Scavetta, M. Berrettoni, M. Giorgetti, D. Tonelli. *Electrochim. Acta* 47 (2002) 2451.
- [4] E. Scavetta, M. Berrettoni, F. Nobili, D. Tonelli, *Electrochim. Acta* 50 (2005) 3305.
- [5] E. Scavetta, B. Ballarin, M. Berrettoni, I. Carpani, M. Giorgetti, D. Tonelli. *Electrochim. Acta* 51 (2006) 2129.
- [6] A. Faour, C. Mousty, V. Prevot, B. Devouard, A. De Roy, P. Bordet, E. Elkaim, C. Taviot-Gueho. *J. Phys. Chem. C* 116 (2012) 15646.
- [7] M.A. Ulibarri, J.M. Fernández, F.M. Labajos, V. Rives. *Chem. Mater.* 3 (1991) 626.
- [8] M. Herrero, P. Benito, F.M. Labajos, V. Rives. *J. Solid State Chem.* 180 (2007) 873.
- [9] E. Scavetta, B. Ballarin, M. Gazzano, D. Tonelli. *Electrochim. Acta* 54 (2009) 1027.
- [10] E. Scavetta, B. Ballarin, C. Corticelli, I. Gualandi, D. Tonelli, V. Prevot, C. Forano, C. Mousty. *J. Power Sources* 201 (2012) 360.
- [11] C. Barbero, G.A. Planes, M.C. Miras. *Electrochem. Commun.* 3 (2001) 113.
- [12] A. Araneo, *Chimica Analitica Qualitativa*, 1990, Ambrosiana, Milan.
- [13] S. Miyata. *Clays Clay Miner.* 31 (1983) 305.
- [14] PDF database, file n. 89-0460. *International Centre for Diffraction Data*, Newtown Square, PA, U.S.A.
- [15] H.P. Klug, L.E. Alexander, *X-ray Diffraction Procedures for Polycrystalline and Amorphous Materials*, 1974, Wiley-Interscience, New York.
- [16] A. Grosvenor, M.C. Biesinger, R.St.C. Smart, N.S. McIntyre. *Surf. Sci.* 600 (2006) 1771.
- [17] M.C. Biesinger, B.P. Payne, A.P. Grosvenor, L.W.M. Lau, A.R. Gerson, R.St.C. Smart. *App. Surf. Sci.* 257 (2011) 2717.
- [18] M. Giorgetti. *Hindawi Publishing Corporation ISRN Materials Science*, Volume 2013, Article ID 938625.
- [19] I. Carpani, M. Berrettoni, M. Giorgetti, D. Tonelli. *J. Phys. Chem. B* 110 (2006) 7265.
- [20] A. Mignani, B. Ballarin, M. Giorgetti, E. Scavetta, D. Tonelli, V. Prevot, C. Mousty, A. Iadecola. *J. Phys. Chem. C* 117 (2013) 16221.

- [21] U. Costantino, F. Marmottini, M. Rocchetti, R. Vivani, *Eur. J. Inorg. Chem.* 10 (1998) 1439.
- [22] A. Faour, C. Mousty, V. Prevot, B. Devouard, A. De Roy, P. Bordet, E. Elkaim, C. Taviot-Gueho. *J. Phys. Chem. C* 116 (2012) 15646.
- [23] I.J. Godwin, M.E.G. Lyons. *Electrochem. Commun.* 32 (2011) 39.
- [24] B.S. Yeo, A.T. Bell. *J. Phys. Chem. C* 116 (2012) 8394.
- [25] B.S. Yeo, A.T. Bell. *J. Am. Chem. Soc.* 133 (2011) 5587.
- [26] M. Gong, Y. Li, H. Wang, Y. Liang, J.Z. Wu, J. Zhou, J. Wang, T. Regier, F. Wei, H. Dai. *J. Am. Chem. Soc.* 135 (2013) 8452.
- [27] L. Trotochaud, S.L. Young, J.K. Ranney, S.W. Boettcher. *J. Am. Chem. Soc.* 136 (2014) 6744.
- [28] G.K. Schweitzer, L.L. Pesterfield, *The Aqueous Chemistry of The Elements*, 2010, Oxford University Press, Oxford.
- [29] D.A. Corrigan, R.S. Conell, C.A. Fierro, D.A. Scherson, In-situ Mössbauer study of redox processes in a composite hydroxide of iron and nickel. *J. Phys. Chem.* 91 (1987) 5009.
- [30] M.S. Burke, M.G. Kast, L. Trotochaud, A.M. Smith, S.W. Boettcher. *J. Am. Chem. Soc.* 137 (2015) 3638.
- [31] E.L. Miller, R.E. Rocheleau. *J. Electrochem. Soc.* 144 (1997) 3072.
- [32] E. Castro, C. Gervasi. *Int. J. Hydrogen. Energ.* 25 (2000) 1163.
- [33] Y. Xu, Y. Hao, G. Zhang, Z. Lu, S. Han, Y. Li, X. Sun. *RSC Adv.* 5 (2015) 55131.
- [34] M.A. Oliver-Tolentino, J. Vázquez-Samperio, A. Manzo-Robledo, R. de Guadalupe González-Huerta, J.L. Flores-Moreno, D. Ramírez-Rosales, A. Guzmán-Vargas. *J. Phys. Chem. C* 118 (2014) 22432.
- [35] P. Vialat, P. Rabu, C. Mousty, F. Leroux. *Power Sources* 293 (2015) 1.
- [36] Q. Wang, L. Jiao, H. Du, Y. Wang, H. Yuan. *J. Power Sources* 245 (2014) 101-106.
- [37] V. Gupta, S. Gupta, N. Miura. *J. Power Sources* 177 (2008) 685.
- [38] P. Guoxiang, X. Xinhui, L. Jingshanb, C. Feng, Y. Zhihong, F. Hongjin. *Appl. Clay Sci.* 102 (2014) 28.
- [39] A.I. Melato, M.H. Mendonça, L.M. Abrantes. *J. Solid State Electrochem.* 13 (2009) 417.
- [40] W.J. Belcher, K.I. Wagner, P.C. Dastoor. *Sol. Energ. Mat. Sol. Cells* 91 (2007) 447.
- [41] M.G. Waltera, A.B. Rudine, C.C. Wamser. *J. Porphyrins Phthalocyanines* 14 (2010) 759.

- [42] T.A. Chen, X. Wu, R.D. Rieke, *J. Am. Chem. Soc.* 117 (1995) 233.
- [43] T.J. Prosa, M.J. Winokur, R.D. McCullough. *Macromolecule* 29 (1996) 3654.
- [44] T. Erb, U. Zhokhavets, G. Gobsch, S. Raleva, B. Stuhn, P. Schilinsky, C. Waldauf, C.J. Brabec. *Adv. Funct. Mater.* 15(7) (2005) 1193.
- [45] N. Camaioni, G. Ridolfi, G. Casalbore-Miceli, G. Possamai, M. Maggini. *Adv. Mater.* 14(10) (2002) 1735.
- [46] H. Hoppe, M. Niggemann, C. Winder, J. Kraut, R. Heisgen, A. Hinsch, D. Meissner, N.S. Sariciftci. *Adv. Funct. Mater.* 14 (2004) 1005.
- [47] U. Zhokhavets, T. Erb, H. Hoppe, G. Gobsch, N.S. Sariciftci. *Thin Solid Films* 496 (2006) 679.
- [48] H. Randriamahazaka, V. Noël, C. Chevrot, *J. Electroanal. Chem.* 472 (1999) 103.
- [49] J. Hou, H.Y. Chen, S. Zhang, G. Li, Y. Yang. *J. Am. Chem. Soc.* 130 (2008) 16144.
- [50] J. Pommerehne, H. Westweber, W. Guss, R.F. Mahrt, H. Bassler, M. Porsch. *J. Daub. Adv. Mater.* 7 (1995) 551.
- [51] B. Carsten, F. He, H.J. Son, T. Xu, L. Yu. *Chem. Rev.* 111 (2011) 1493.
- [52] D. Dubois, K. M. Kadish, S. Flanagan, R. E. Haufler, L. P. F. Chibante, L. J. Wilson. *J. Am. Chem. Soc.* 113 (1991) 4364.
- [53] N. Massonnet, A. Carella, O. Jaudouin, P. Rannou, G. Laval, C. Celle, J.P. Simonato. *J. Mater. Chem. C* 2 (2014) 1278.
- [54] M. Gouterman. *J. Mol. Spectroscopy* 6 (1961) 138.
- [55] M. Lanzi, L. Paganin, F. Errani. *Polymer* 53 (2012) 2134.
- [56] Y.-B. Wang, Z. Lin. *J. Am. Chem. Soc.* 125 (2003) 6072.
- [57] G. Zotti, S. Zecchin, G. Schiavon, F. Louwet, L. Groenendaal, X. Crispin, W. Osikowicz, W. Salaneck, M. Fahlma. *Macromolecules* 36(9) (2003) 3337.
- [58] K.E. Aasmundtveit, E.J. Samuelsen, L.A.A. Pettersson, O. Inganäs, T. Johansson, R. Feidenhan. *Synth. Met.* 101 (1999) 561.
- [59] M.C. Pham, J. Moslih. *J. Electroanal. Chem.* 316 (1991) 143.

8. AMPEROMETRIC SENSORS BASED ON LDH MODIFIED ELECTRODES

8.1 Sensors based on chemically and electrochemically synthesized Ni-based LDH for glucose detection

In this paragraph the electrocatalytic performances of Ni/Al and Ni/Fe LDH synthesized by electrochemical route are compared to the ones obtained using Pt electrodes coated with LDHs synthesized according to the microemulsion method [1]. In order to verify a possible electroactivity of Fe, also chemically synthesized Mg/Al and Mg/Fe LDHs were prepared and characterized.

In this paragraph the electrochemically and the chemically synthesized LDHs will be referred to as (electrochem) and (chem), respectively.

8.1.1 LDHs composition

The chemical composition of the LDHs was assigned with a combination of thermogravimetry, used to estimate the amount of adsorbed and intercalated water, and inductively coupled plasma analysis for the chemically prepared LDHs, and EDX analysis for the electrochemically synthesized ones. The resulting compositions are reported in Table 8.1.

Table 8.1 Chemical composition of the studied LDH samples.

LDH samples	Chemical composition
Mg/Al (chem)	$[\text{Mg}_{0.71}\text{Al}_{0.29}(\text{OH})_2]\text{Br}_{0.19}(\text{CO}_3)_{0.05} \cdot 0.69\text{H}_2\text{O}$
Mg/Fe (chem)	$[\text{Mg}_{0.76}\text{Fe}_{0.24}(\text{OH})_2]\text{Br}_{0.12}(\text{CO}_3)_{0.06} \cdot 0.65 \text{H}_2\text{O}$
Ni/Al (chem)	$[\text{Ni}_{0.77}\text{Al}_{0.23}(\text{OH})_2]\text{Br}_{0.15}(\text{CO}_3)_{0.04} \cdot 0.81 \text{H}_2\text{O}$
Ni/Fe (chem)	$[\text{Ni}_{0.75}\text{Fe}_{0.25}(\text{OH})_2]\text{Br}_{0.17}(\text{CO}_3)_{0.04} \cdot 0.91 \text{H}_2\text{O}$
Ni/Al (electrochem)	$[\text{Ni}_{0.71}\text{Al}_{0.29}(\text{OH})_2](\text{NO}_3)_{0.29} \cdot 0.60 \text{H}_2\text{O}$
Ni/Fe (electrochem)	$[\text{Ni}_{0.71}\text{Fe}_{0.29}(\text{OH})_2](\text{NO}_3)_{0.29} \cdot 0.80 \text{H}_2\text{O}$

8.1.2 Structural characterizations

Figure 8.1 shows the XRD patterns of the samples listed in Table 8.1. All samples exhibit the typical reflections of the LDH structure and the full width at half maximum (FWHM) of the reflections gives an idea about the nanoscale dimension of the particles. Chemically prepared LDHs were characterized by an identical interlayer distance (~ 8.06 Å), which is compatible with the presence of bromide anions in the interlayer region [2,3]. The electrochemically synthesized LDHs, as said before, show broader reflections than those relative to the chemically prepared LDHs resulting in a more amorphous material due to the short times of deposition.

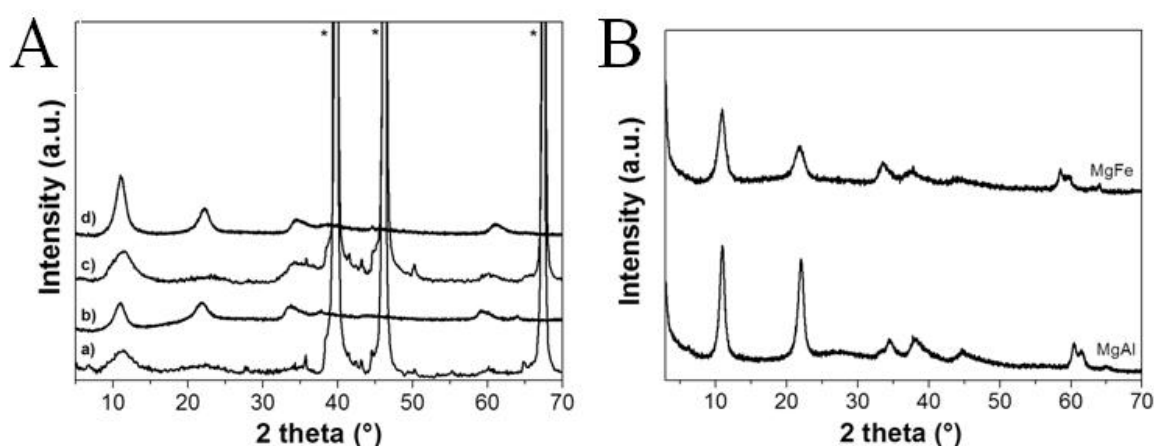


Figure 8.1 – A) Comparison between XRD patterns of the electrochem Ni/Fe (a), chem Ni/Fe (b), electrochem Ni/Al (c) and chem Ni/Al (d) LDHs. (*) Reflections due to the Pt electrode. B) XRPD patterns of the chemically prepared Mg/Al and Mg/Fe LDHs.

The diameters of the LDHs electrochemically synthesized were calculated applying the Debye-Scherrer equation on the (003) Bragg reflection and were compared with those of the corresponding LDH chemically synthesized (Table 8.2) [4]. The electrochemical synthesis gives smaller particles with diameters of about 3 nm.

Table 8.2 Average diameter of the LDHs calculated by the Debye-Scherrer equation $D = 0.9 \cdot \lambda / (\delta \cdot \cos\theta)$ (λ = incident ray wavelength: 1.54050 Å; δ = FWHM; θ = diffraction angle).

LDH	$2\theta / ^\circ$	FWHM / $^\circ$	Average diameter / nm
Ni/Al (chem) [1]	11.05	1.53	5.2
	22.07	1.72	4.7
Ni/Al (electrochem)	11.462	2.83	2.9
Ni/Fe (chem) [1]	11.06	1.68	4.8
	22.17	2.11	3.8
Ni/Fe (electrochem)	11.26	2.86	2.8

8.1.3 Electrochemical characterizations

Figure 8.2 A shows the comparison of the CV curves relative to the different Ni-based LDH coatings on Pt, recorded in 0.1 M NaOH, obtained both by chemical precipitation or electrochemical deposition and Figure 8.2 B shows the CV curves recorded at a bare Pt and Pt electrodes coated with a thin film of Mg/Al or Mg/Fe LDH. The Mg-based LDHs were chemically synthesized in order to evaluate a possible electroactivity of Fe.

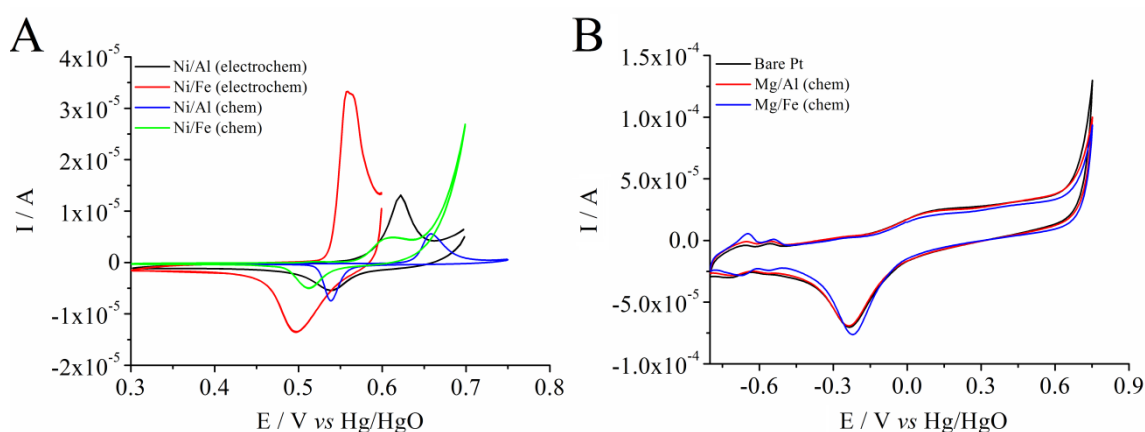


Figure 8.2 - CV curves recorded, in 0.1 M NaOH, at Pt electrodes coated with all the synthesized LDHs. Potential scan rate: 0.01 V s⁻¹.

It is well evident that the CV curves of Mg/Al and Mg/Fe overlap to that of the bare Pt electrode; that means that the Mg/Al and Mg/Fe LDHs are not electroactive. This

behaviour was expected for Mg/Al LDH since it does not contain any oxidizable or reducible metal, but the fact that the same CV response is also recorded at the Mg/Fe LDH demonstrates that Fe centres are not redox active. The only peak evident in the CV curves of the Mg LDHs coated electrodes is the cathodic peak, at $E = -0.25$ V which is also evident in the CV curve of the bare Pt electrode and is due to the PtO reduction.

In Figure 8.3 the CVs of the chemically synthesized Ni/Al and Ni/Fe LDHs, recorded at different scan rates are shown. Similarly to what observed for the electrochemically synthesized Ni-based LDHs, the (chem) Ni/Al and Ni/Fe LDHs show a quasi-reversible peak system relative to the redox couple Ni(II)/Ni(III), as described by Eq. 7.1 (paragraph 7.1.1.1), whose current intensity and position depend on the trivalent metal and on the way of the electrode preparation. In fact, even in this case, when Fe is present the oxygen evolution takes place at less anodic potential if compared to the Ni/Al LDH and the oxidation of Ni occurs at a potential very close to the solvent discharge.

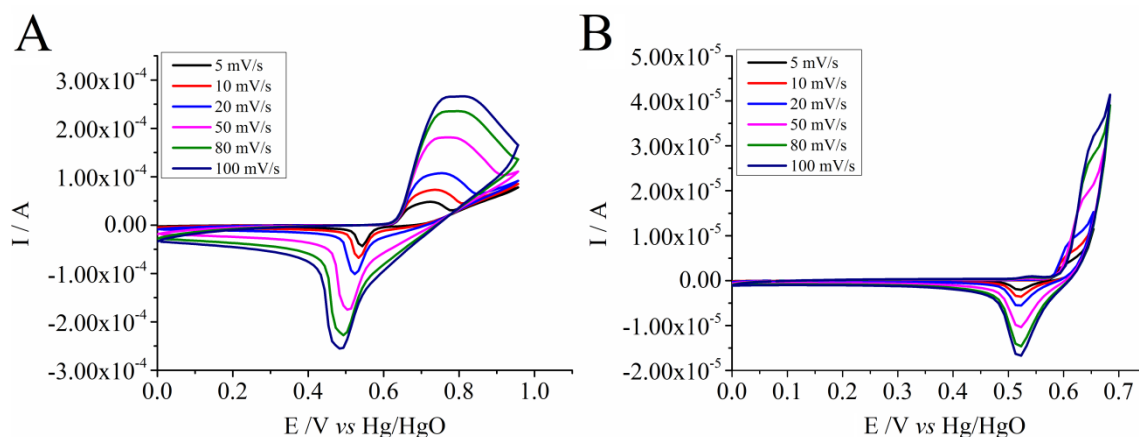


Figure 8.3 – CV curves relative to the (chem) Ni/Al (A) and Ni/Fe LDH (B), recorded in 0.1 NaOH at different scan rates.

For each electrode the Ni electroactive centres were calculated by integrating the anodic peak at slow scan rate (0.005 V s^{-1}). The total moles of Ni sites were calculated by means of the formulae reported in Table 8.3. The relevant masses were the amounts casted on the electrode, and those resulting from EQCM experiments, for the (chem) and (electrochem) LDHs, respectively. Table 8.3 shows the characteristic parameters of each coated electrode.

When the LDHs are electrochemically synthesized the Ni peak couple occurs at less anodic potential and has a current intensity higher than the one of the corresponding chemically prepared LDH. For all the electrodes only a limited amount of Ni sites is

electroactive: the percentage is higher for electrosynthesized materials and increases when the trivalent metal is iron.

Table 8.3 Characteristic parameters of the Ni-based LDHs obtained by CV.

LDH	E_{pa}/V	E_{pc}/V	Ni electroactive sites / moles	Ni sites on the electrode / moles	% electroactive Ni centres
Ni/Al (chem)	0.659	0.540	$1.52 \cdot 10^{-10}$	$2.35 \cdot 10^{-8}$	0.65
Ni/Fe (chem)	0.610	0.512	$2.58 \cdot 10^{-10}$	$2.00 \cdot 10^{-8}$	1.29
Ni/Al (electrochem)	0.622	0.540	$6.81 \cdot 10^{-10}$	$5.50 \cdot 10^{-9}$	12.4
Ni/Fe (electrochem)	0.559	0.498	$1.26 \cdot 10^{-9}$	$5.60 \cdot 10^{-9}$	22.5

To get a better insight of the electrochemical behaviour of the LDHs coated electrodes, impedance spectra were recorded, for each electrode, at the peak potential and were plotted in the form of Nyquist plots (Figure 8.4).

All the spectra show a main common and well evident feature: a great semicircular arc in the low-middle frequency region which, on the basis of our previous works and on similar studies by other authors relative to nickel based LDHs, can be related to the electronic transport inside the LDH structure, due to an electron hopping mechanism between adjacent nickel centres [5].

The experimental data were interpolated using the Z-view software with the equivalent circuit shown in the inset of Figure 8.4 that was able to fit all the spectra, giving χ^2 values in the range 10^{-4} – 10^{-3} . This circuit is similar to that proposed in one of our previous studies aimed to investigate the electrochemical behaviour of the Ni/Al LDH obtained by coprecipitation [5].

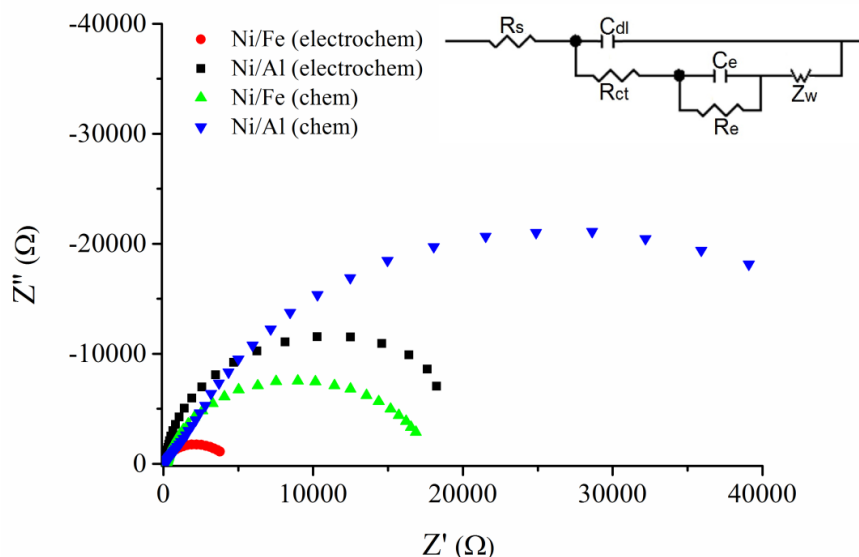


Figure 8.4 - Nyquist plots obtained for the nickel based LDHs at the peak potential in 0.1 M NaOH. In the inset the equivalent circuit used to fit the data is shown.

Figure 8.5 shows a comparison between experimental and calculated data for the electrochemically synthesized LDHs, from which it is evident the good fitting. Analogous results have been obtained for the spectra relative to the chemically synthesized LDHs.

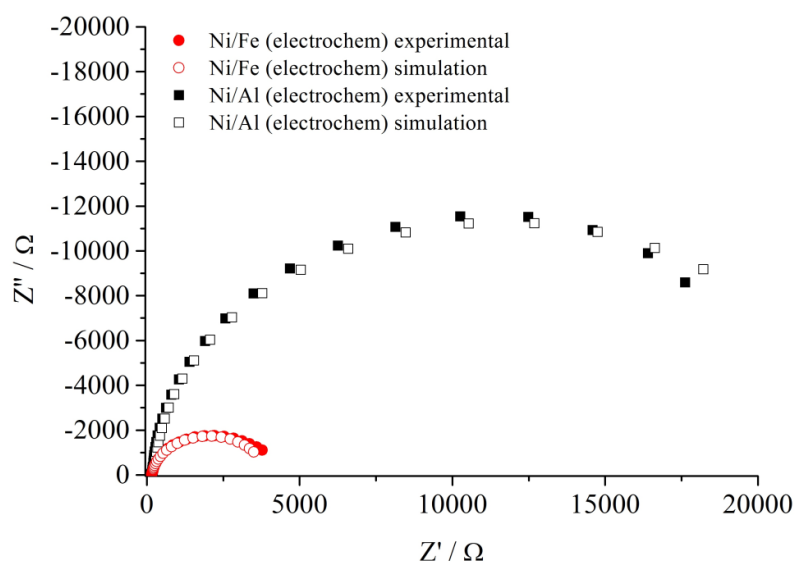


Figure 8.5 - Nyquist plots obtained for electrochemically synthesized LDHs at the peak potential recorded by CV in 0.1 M NaOH. Comparison between the experimental and the simulated data.

Concerning the circuit, R_s represents the resistance of the solution and has always a value around 60 Ω ; R_{ct} and C_{dl} describe, respectively, the charge-transfer resistance and the

associated capacitance at the interface electrode/solution; The ($C_e R_e$) parallel element is the most important in describing the LDH features, since it represents the electronic transfer resistance inside the material and the related capacitance, probably due to a nanosize accumulation of charges inside the active grains of the material [3]; finally, the Z_w element represents a Warburg impedance associated with diffusion. All the C elements were substituted with constant phase element (CPE) [6] with n close to 1, to take into account local non homogeneous nature of the electrode.

Impedance spectroscopy confirms the results obtained by CV, *i.e.*, the chemically synthesized LDHs possess a higher electronic transfer resistance than the analogous electrosynthesized materials. In particular, the R_e values are 4.8 and $2.3 \cdot 10^4 \Omega$ for the Ni/Al LDHs chemically and electrochemically synthesized, respectively, while for the Ni/Fe LDHs they result $1.5 \cdot 10^4$ and $4.3 \cdot 10^3 \Omega$. From these results it is evident that R_e values are lower for the Fe-based LDHs in respect to those containing Al. Also this datum confirms that iron is responsible of an increase in the LDH apparent electronic conductivity (calculated as the reciprocal of the related resistance), even if it does not participate directly to the redox process. This result is in agreement with the values of the percentages of the electroactive Ni sites (Table 8.3) as the material is more conductive when more Ni centres are involved in the electron hopping process.

All these evidences point out that Fe has a key role in promoting Ni reaction, as already suggested by the recent literature. In fact, our data confirm that Fe does not undergo a redox reaction in the range of applied potential, as proven by Friebel [7] but leads to a decrease of the resistance to the electronic transport, in agreement to what hypothesized by Trotochaud [8]. Furthermore, our results demonstrate also that the order degree of the LDH structure plays an important role in affecting the conductivity of the material, being the R_e value of the electrochemically synthesized LDH systematically lower than those of the chemically prepared LDHs, especially when Fe is present as the trivalent metal in the brucite-like layers.

8.1.4 Morphological characterization of the chemical Ni-based LDHs

The morphologies relative to the electrochemically synthesized LDHs were previously shown and described. With regards to the LDH films obtained by chemical synthesis, the morphologies are shown in Figure 8.6. As it can be seen, the films appear homogeneous

and well packed confirming that aqueous dispersions of LDHs having nanometric dimension possess a very high tendency to spontaneously form films because the uniform and small crystal sizes of the LDH favor the face-to-face and edge-to-edge interactions among the particles [4,9].

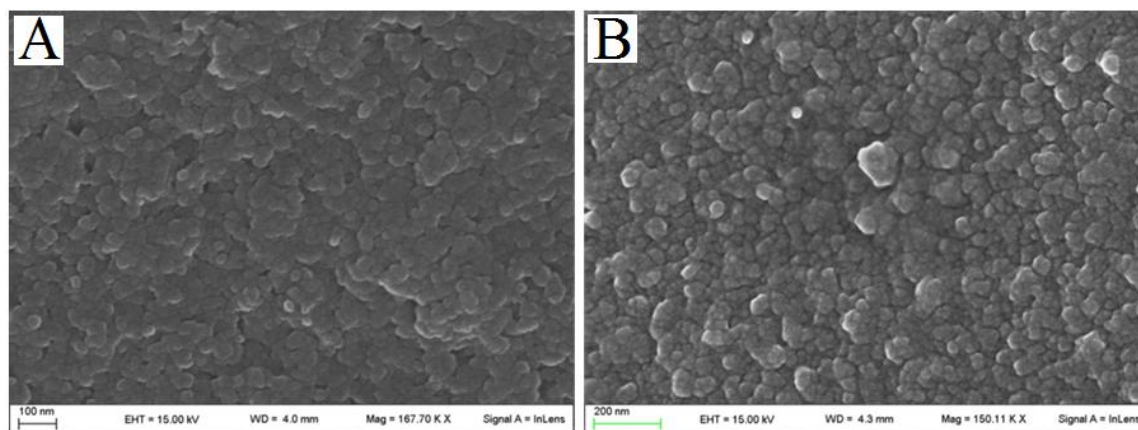


Figure 8.6 – SEM images of the chemically synthesized Ni/Fe (A) and Ni/Al (B) LDHs.

The morphology of the four LDH films was investigated also by AFM analyses (Figure 8.7). AFM is a powerful tool to obtain direct information about the surface topography of a film with a nanometer spatial resolution.

The films obtained for (electrochem) Ni/Fe LDH (Figure 8.7 A), (chem.) Ni/Fe, and Ni/Al LDH (Figure 8.7 B and D) display a similar grainy morphology with average roughness of about 39 nm, 27 nm and 26 nm, respectively. However, in the chemically prepared Ni/Al LDH, the single nanoparticles are more evident (Figure 8.7 D). Differently, the Ni/Al LDH obtained by electrochemical deposition (Figure 8.7 C), generates films with an average roughness of about 36 nm in which small aggregates are noticeable. In particular, AFM image reveals that these aggregates are actually formed by smaller particles. Collectively, these results indicate that despite the similar morphology, the electrochemically prepared LDH appear slightly rougher than chemically synthesized ones.

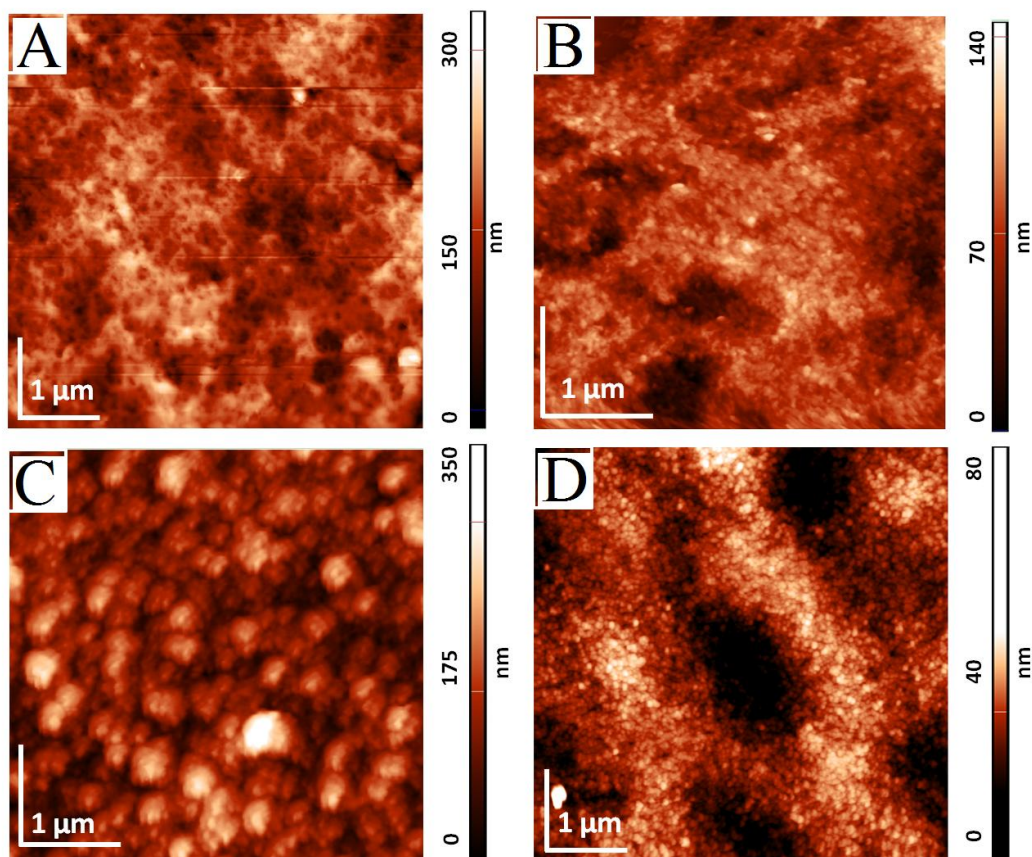


Figure 8.7 - AFM images of (electrochem) Ni/Fe and Ni/Al (A) and (C), and (chem) Ni/Fe and Ni/Al (B) and (D) LDH samples.

8.1.5 Glucose detection

The electrocatalytic mechanism responsible of the sensor response can be represented by the following reactions, where Ni centres inside the LDH layers act as redox mediators:



The electrocatalytic behaviour of the four different coated electrodes was assessed considering glucose as the analyte. In Figure 8.8 are shown the CVs recorded by adding increasing amounts of glucose in the range of concentration 0.1-1.0 mM, for all the investigated LDHs in 0.1 NaOH (scan rate: 0.05 V s⁻¹).

It is evident that the Ni anodic peak increases proportionally with increasing glucose concentration, so confirming the electrocatalytic mechanism of glucose oxidation. The peak potential moves to more anodic values in order to sustain the catalytic reaction due to the greater ratio Ni(II)/Ni(III) [10].

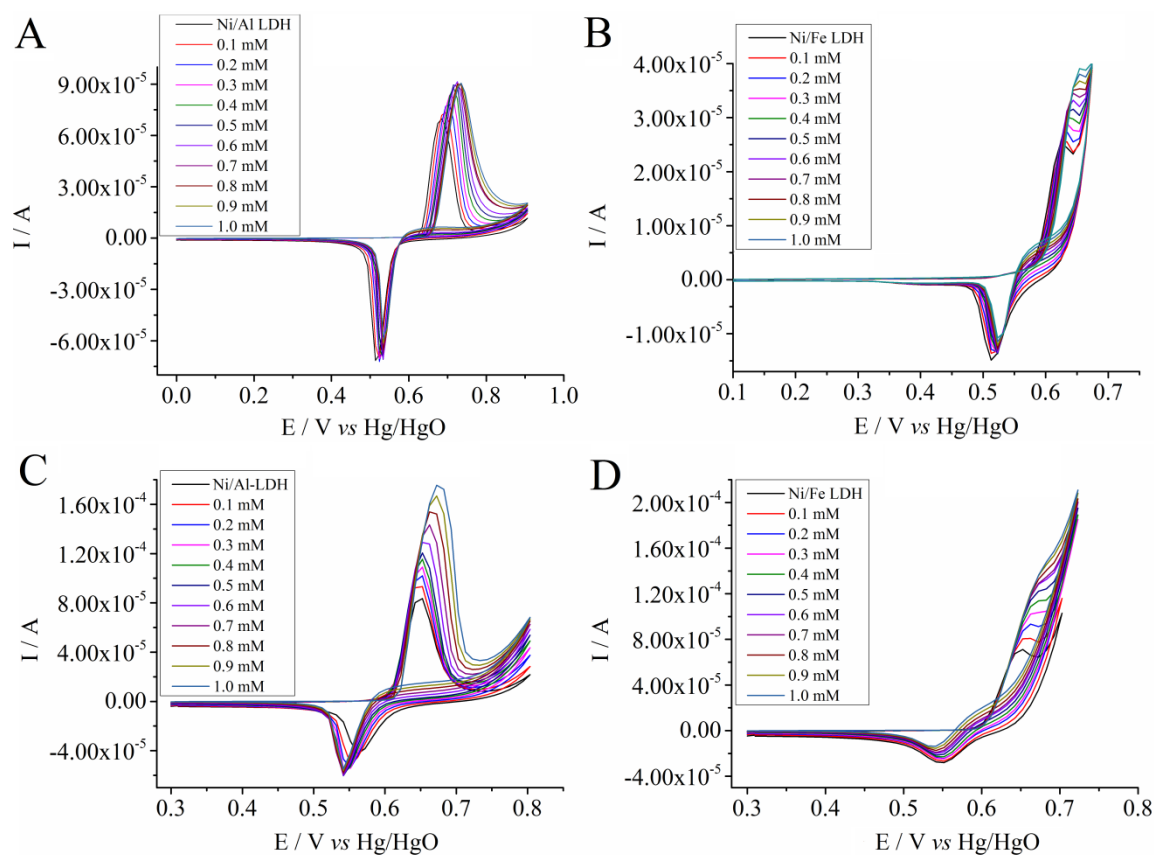


Figure 8.8 – CVs recorded for the four LDHs in the presence of glucose at the concentrations shown in the insets. A) Chemical Ni/Al, B) chemical Ni/Fe, C) electrosynthesized Ni/Al and D) electrosynthesized Ni/Fe LDH. Scan rate 0.05 V s^{-1} .

Figure 8.9 shows the CV curves, normalized with respect to the peak anodic current, recorded at 0.05 and 0.01 V s^{-1} in the absence and in the presence of glucose.

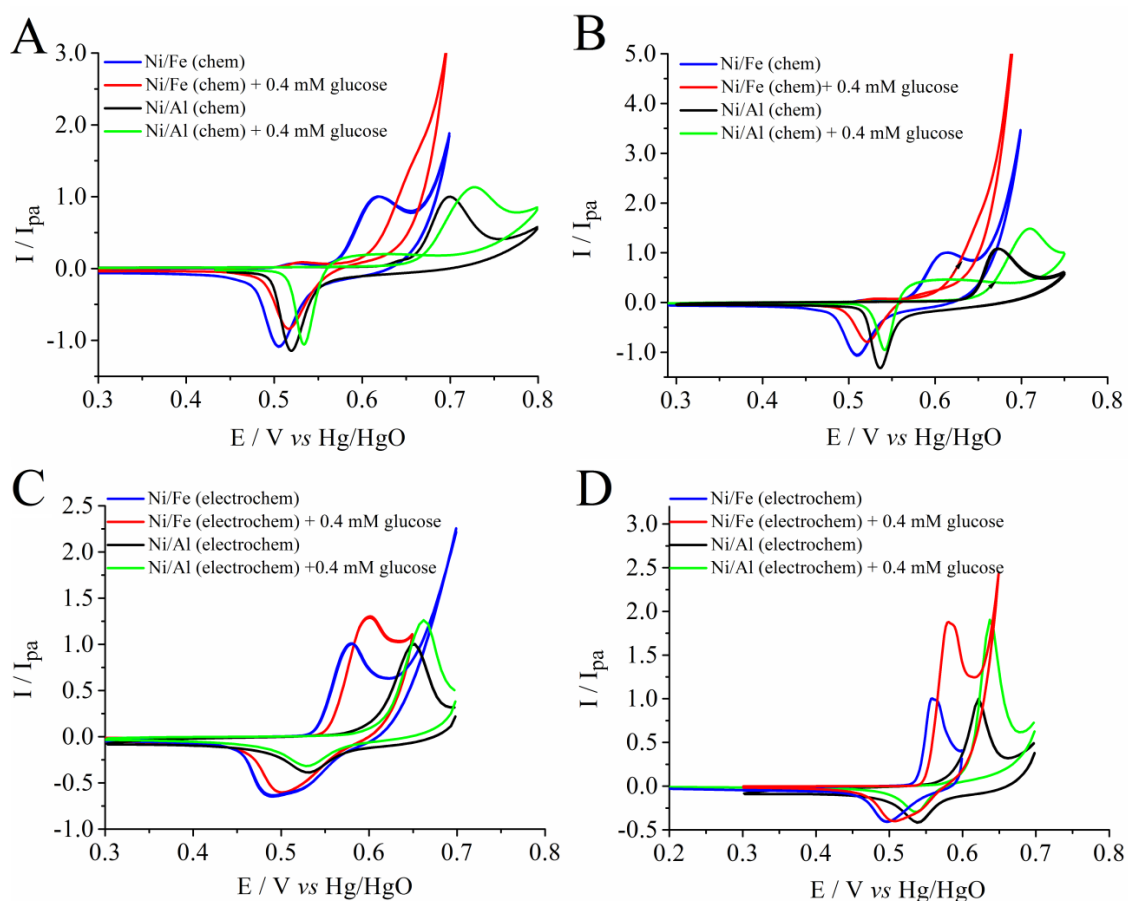


Figure 8.9 - CV curves recorded in 0.1 M NaOH in the absence and in the presence of glucose at a Pt electrode coated with the chemically synthesized Ni-based LDHs (A and B) and electrochemically synthesized (C and D); Scan rate = 0.05 V s⁻¹ for A and C, and 0.01 V s⁻¹ for B and D.

The sensitivities of the analytical determination (slopes of calibration plots) obtained at the two scan rates, the upper limit of linearity (LOL) and the LOD are reported in Table 8.4.

Table 8.4 Characteristic parameters of the calibration plots for glucose, obtained by CV, relevant to the Ni-based LDHs.

	Mean sensitivity* / mM ⁻¹ at 0.01 V s ⁻¹	Mean sensitivity* / mM ⁻¹ at 0.05 V s ⁻¹	LOL / mM	LOD / mM
Ni/Al (chem)	0.9 ± 0.1	0.30 ± 0.02	1.0	0.02
Ni/Fe (chem)	1.2 ± 0.1	0.6 ± 0.1	0.2	0.02
Ni/Al (electrochem)	2.2 ± 0.2	0.6 ± 0.1	1.0	0.01
Ni/Fe (electrochem)	2.2 ± 0.1	0.7 ± 0.2	1.0	0.01

*mean value ± SD from 5 determinations.

For the chemical Ni/Fe LDH the upper linearity limit is lower than that achievable with the other LDHs because in this case the onset potential for the oxygen evolution reaction is very close to the Ni peak potential. Since Ni peak moves toward more anodic values when glucose concentration increases, the two features merge into each other so that the catalytic current is no more measurable.

Independently from the electrode used, the electrocatalytic efficiency, defined as the ratio of the anodic catalytic current for a 0.4 mM glucose addition to the anodic peak current relative to the 'blank' signal, increases as the scan rate is decreased, indicating that the diffusion of the substrate to reach a close contact with the nickel centres in the LDH is a rate determining step [11].

The data show that the catalytic efficiency depends on the synthesis way of the LDH and on its nature. Also the shape of the electrocatalytic response, and in particular the presence of the hysteresis, depends on the electrode type. For the chemically synthesized Ni/Al LDH it is well evident the presence of a hysteresis, which is a feature typical of electrocatalytic processes in which the rate of the chemical reaction between the redox mediator and the analyte (Eq. 8.2) is lower than that of reaction (8.1) [11]. This behaviour was already studied by us and it was demonstrated that at longer times, corresponding to the appearance of the hysteresis, also the inner layers of the LDH are involved in the catalytic process, the main limitation being the diffusion of the substrate inside the layer structure, to react with Ni sites.

The hysteresis is completely absent for the electrochemically prepared LDHs and for the chemical Ni/Fe LDH, suggesting that for such LDHs the diffusion of glucose toward the inner Ni sites is favored, probably due to a lower crystallinity of the material which helps the analyte to come in contact even with the inner Ni sites. Our results confirm that the crystallinity of a particular LDH strongly affects its electrochemical behaviour and it is preferable a low crystallinity to enhance its performance for applications as electrochemical sensors.

As expected, the highest electrocatalytic efficiency is obtained for the electrodes coated with the electrochemically synthesized LDHs, independently of their composition. The EE reported in Table 8.5 show almost equal values for the electrochemically synthesized Ni/Al and Ni/Fe LDHs despite the catalytic rate constants would predict a higher efficiency for glucose oxidation at the Pt modified with Ni/Fe LDH. This behaviour could be again explained taking into account that it is the substrate diffusion inside the LDH layers the limiting factor of the electrocatalytic process. This means that the

number of electroactive Ni(III) centres, in both LDHs is always in excess with respect to the analyte.

The curves relevant to the catalytic current recorded for the electrochemically synthesized LDHs in the presence of the glucose (limiting current), recorded in the same conditions as in the absence of analyte are shown in Figure 8.10.

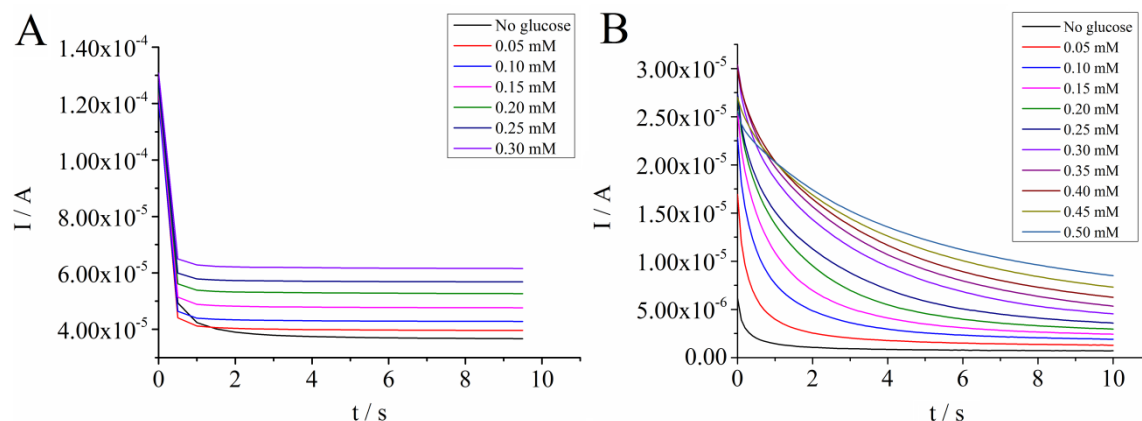


Figure 8.10 – Chronoamperometric curves recorded in 0.1 M NaOH for increasing amounts of glucose. A) electrochem Ni/Al (E = 0.65 V), B) electrochem Ni/Fe (E = 0.58 V).

For each electrode the I_{cat}/I_L versus $c_0^{0.5}t^{0.5}$ plot is linear when the value of $c_0^{0.5}t^{0.5}$ is between $5 \cdot 10^{-3}$ and $2 \cdot 10^{-2} M^{0.5} \cdot s^{0.5}$, and this is indicative of a good adherence to the model. The catalytic constant values are dependent on the nature and way of preparation of the LDH material and are reported in Table 8.5. In particular, when the trivalent metal is Fe the k values are systematically higher than the analogous materials containing Al, indicating a more efficient reaction between Ni catalytic centres and glucose. Moreover, k is higher when the LDHs are electrosynthesized.

Table 8.5 Kinetic constants of the electrocatalytic reaction obtained by CA.

	EE at 0.01 V s ⁻¹	EE at 0.05 V s ⁻¹	Catalytic rate constant / M ⁻¹ s ⁻¹
Ni/Al (chem)	1.4 ± 0.1	1.1 ± 0.1	3.4 · 10 ³
Ni/Fe (chem)	n.e.	n.e.	1.2 · 10 ⁴
Ni/Al (electrochem)	1.9 ± 0.2	1.2 ± 0.1	2.5 · 10 ⁴
Ni/Fe (electrochem)	1.9 ± 0.1	1.3 ± 0.2	6.4 · 10 ⁴

n.e. = not estimable.

For the electrochemically synthesized LDHs, which displayed the best electrocatalytic performances when studied in CV, chronoamperometric curves were also recorded (Figure 8.11). From the CA graphics recorded by adding different amounts of glucose to a 0.1 M NaOH, it is well evident the increase of the anodic current as the analyte concentration becomes higher.

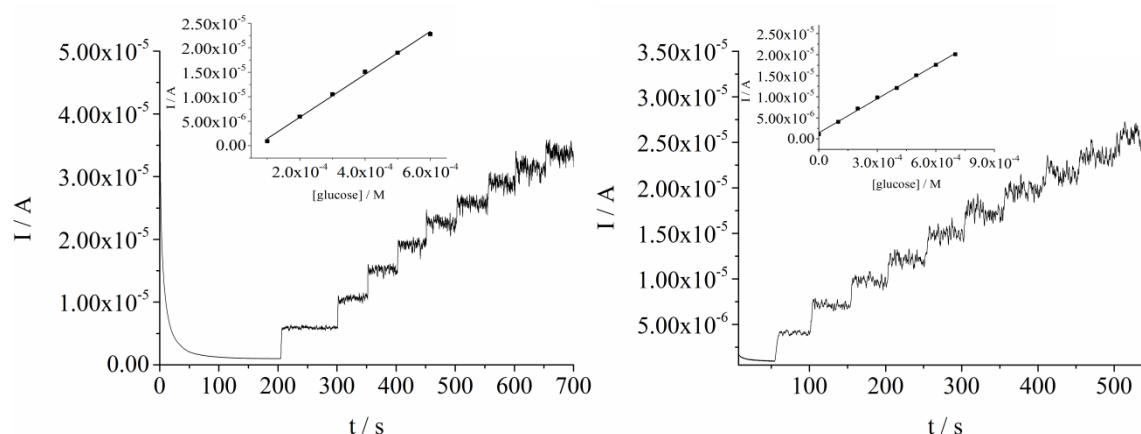


Figure 8.11 – Chronoamperometric curves relative to the electrochem Ni/Al (A) and Ni/Fe (B) LDH. Each glucose addition corresponds to a concentration of 0.1 mM. In the inset the calibration curves are reported.

The analytical performances relevant to the calibration curves, *i.e.*, the limit of detection and the sensitivity were obtained by plotting the limiting current as a function of glucose concentration. The values obtained are reported in Table 8.6. The highest sensitivity and lowest LOD were obtained for the Ni/Al LDH. In any case the sensitivity obtained by CA is higher than the one observed when using CV due to the highest sensibility of the technique.

Table 8.6 Sensitivity and LOD values relative to the calibrations of glucose by CA for Pt modified with the electrosynthesized Ni/Al and Ni/Fe LDHs.

LDH	Applied potential	Sensitivity / A M ⁻¹	LOD / M
Ni/Al	E = 0.65 V	$4.02 \cdot 10^{-2}$	$6.71 \cdot 10^{-5}$
Ni/Fe	E = 0.58 V	$2.50 \cdot 10^{-2}$	$8.51 \cdot 10^{-5}$

8.2 Co/Al LDH coated Pt for in flow amperometric detection of sugars

This section concerns the research carried out in order to prepare and optimize a sensor based on Co/Al LDH coated Pt electrode for sugars amperometric detection. Its response is based on the analytes oxidation catalysed by the Co(IV) centres of the LDH layers [12]. The LDH deposition time has been investigated in order to obtain a film with suitable mechanical properties and to get high sensitivities for sugar determination. Some of the most important mono- and di-saccharides were taken into account and separated by high performance anionic chromatography. The best operative conditions which allow for the highest detection sensitivity and stability have been established using standard mixtures of glucose, fructose and sucrose. Finally, real samples analysis was carried out using the Co/Al LDH modified electrode as amperometric detector.

8.1.1 Co/Al LDH morphology and effect of deposition time

Varying the deposition time it is possible to control the LDH coating thickness, in fact for longer time of applied potential the film becomes thicker. In order to determine the best time of deposition to obtain films with satisfactory mechanical characteristics, Co/Al LDHs were electrosynthesized on Pt applying the cathodic potential for different times, namely 10, 20, 30 and 60 s. As shown in Figure 8.12, the surface results compact and smooth in any case and the Pt support is homogeneously covered.

For the longest deposition time, 60 s, the outer surface part of the LDH coating shows spherical nanoparticles aggregated in bigger spherically shaped nodules, ranging from 150 to 600 nm, with the typical cauliflower structure (Figure 8.12 D). This deposition morphology, together with the higher size, confers more elevated porosity and a loose packing structure of the outermost surface coating.

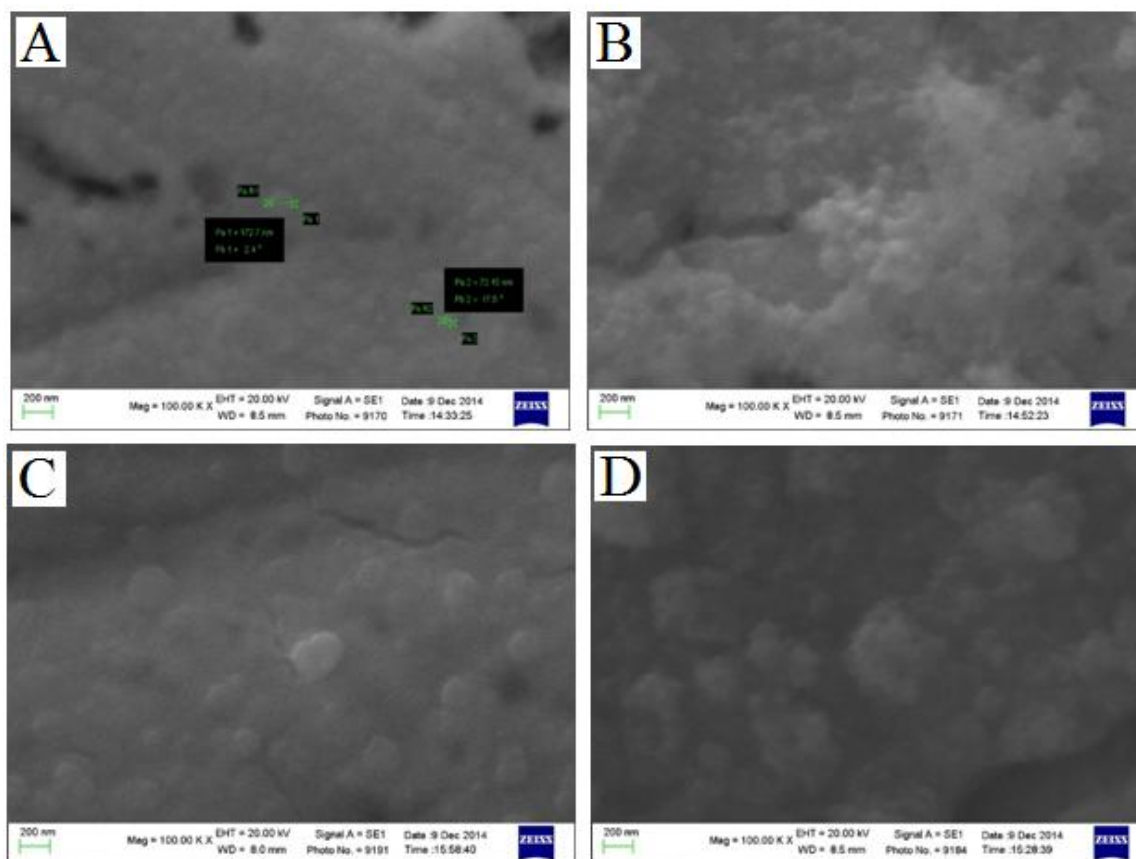


Figure 8.12 - High-magnification SEM images of LDH coatings electrodeposited for different times: 10, 20, 30, and 60 s from A to D.

8.1.2 Amperometric sensors performances

A preliminary study was carried out by CV in order to select the optimal working conditions for the amperometric determination of sugars, in terms of applied potential and electrolytic solution. CV curves were recorded in basic solutions at pH 10 and 11 (0.1 M buffer borate), 12 (0.01 M NaOH + 0.1 M KNO₃) and 12.8 (0.1 M NaOH). The electrochemical response related to the Co(II)/Co(III) and Co(III)/Co(IV) couples shifts toward more anodic potentials as the pH of the solution decreases.

To verify the electrocatalytic response of the Co/Al LDH coated electrode (60 s electrodeposition), glucose was first investigated. As an example, Figure 8.13 A shows the CV traces recorded by adding different amounts of glucose to a 0.1 M NaOH from which it is well evident the increase of the anodic current as the analyte concentration becomes higher. In such conditions the chronoamperometric responses were obtained by setting the potential of the CME at 0.40 V (Figure 8.13 B). Analogous experiments were

carried out for the other basic solutions which were taken into account to perform electrocatalysis.

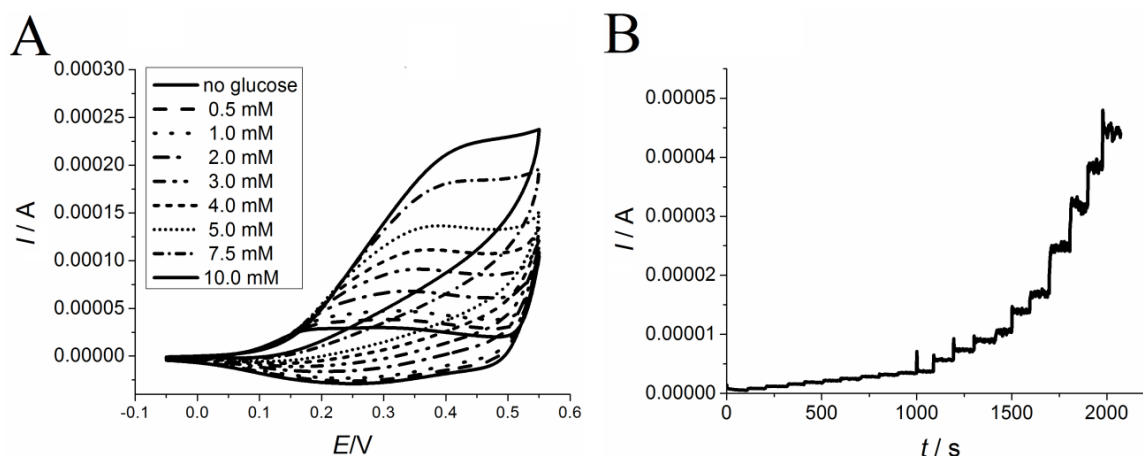
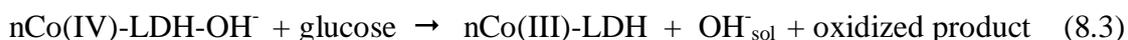


Figure 8.13 - CVs recorded for a Co/Al LDH coated electrode (deposition time 60 s) in 0.1 M NaOH, containing glucose at different concentrations, $\nu = 10 \text{ mV s}^{-1}$ (A); Chronoamperometric curves recorded at the same electrode poised at +0.40V in 0.1 M NaOH for different glucose additions (concentrations after each addition: 0.01, 0.02, 0.03, 0.04, 0.05, 0.06, 0.08, 0.09, 0.10, 0.15, 0.20, 0.25, 0.30, 0.40, 0.50, 0.75, 1.00, 1.25, 1.50 mM) (B).

The calibration graphs were constructed by plotting the anodic peak currents of the CV response and the limiting current in the case of CA, as a function of glucose concentration: the sensitivity, expressed as the slope of the resulting line and the LOD values, obtained at the different pHs, are reported in Table 8.7.

The highest sensitivity and the lowest LOD were obtained when the most basic solution was employed, due to the highest efficiency of the reaction involving the Co (IV) centres [13] according to:



In all cases, the sensitivity achievable by CA was higher than the one observed when using CV, independently of the solution pH.

Table 8.7 Sensitivity and LOD values relative to the calibrations of glucose by CV and CA in solutions at different pHs.

Solution	Technique	Sensitivity / A M ⁻¹	LOD / M
0.1 M NaOH	CA at E=0.40 V	$3.28 \cdot 10^{-2}$	$9 \cdot 10^{-6}$
	CV	$1.98 \cdot 10^{-2}$	$7 \cdot 10^{-4}$
0.01 M NaOH	CA at E=0.45 V	$3.96 \cdot 10^{-2}$	$2 \cdot 10^{-5}$
	CV	$7.98 \cdot 10^{-3}$	$3 \cdot 10^{-4}$
0.1 M borate buffer (pH 11)	CA at E=0.65 V	$2.08 \cdot 10^{-3}$	$2 \cdot 10^{-5}$
	CV	$1.09 \cdot 10^{-3}$	$5 \cdot 10^{-5}$
0.1 M borate buffer (pH 10)	CA at E=0.70 V	$1.76 \cdot 10^{-3}$	$2 \cdot 10^{-5}$
	CV	$3.97 \cdot 10^{-4}$	$2 \cdot 10^{-3}$

The same tests were also performed using the Pt surface modified with the LDH coating related to the 20 s electrodeposition. In Figure 8.14 the CV and CA curves recorded for increasing glucose concentrations are shown. In such a case the sensitivity of glucose determination by chronoamperometry was slightly superior ($6.73 \cdot 10^{-2}$ vs $3.28 \cdot 10^{-2}$ A M⁻¹ working in 0.1 M NaOH) but the LOD was much higher ($1 \cdot 10^{-4}$ vs $9 \cdot 10^{-6}$ M).

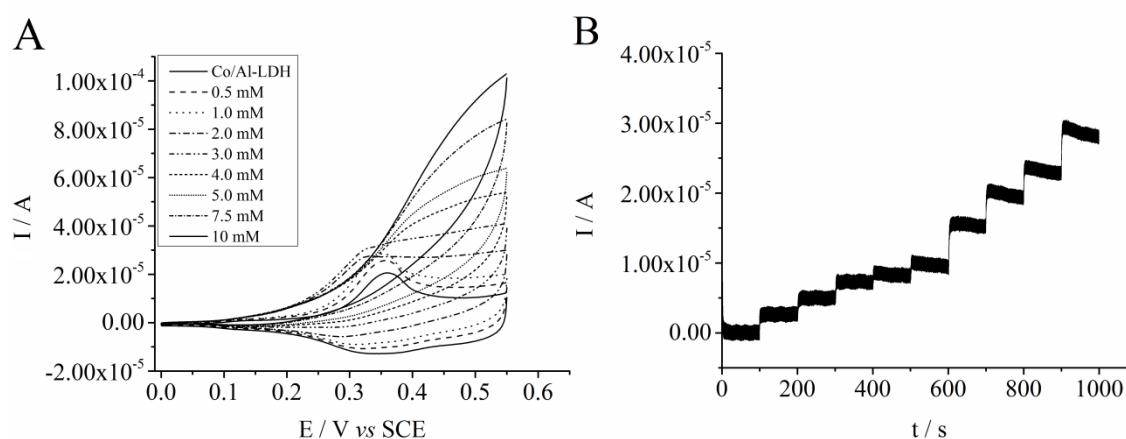


Figure 8.14 - CVs recorded at a Co/Al LDH coated electrode (deposition time 20 s) in 0.1 M NaOH, containing glucose at different concentrations, $v = 10 \text{ mV s}^{-1}$ (A); CA curves recorded at the same electrode poised at +0.40V in 0.1 M NaOH for different glucose additions (concentrations after each addition: 0.01, 0.02, 0.03, 0.04, 0.05, 0.1, 0.15, 0.20, 0.30 mM) (B).

Furthermore, using the CME with the thinner coating the LOL of the calibration graph was only 0.2 mM, whereas concentration range was expanded up to 2.0 mM at least for

the CME obtained after 60 s electrodeposition. These results are explainable with the absolute higher number of Co catalytic centres and the higher porosity exhibited by the thicker coating which allows an easier accessibility to the analyte molecules. For this reasons we decided to work with the coating obtained after 60 s electrodeposition for all the further investigations.

8.1.3 Mechanical stability of the Co/Al LDH coating

The detection of sugars in flow systems requires high mechanical and operational stability. To study this aspect, SEM was employed to observe the LDH coatings after performing qualitative bending tests in order to evaluate the adhesion of the material on Pt support.

As shown in Figure 8.15 A, the coating formed on platinum after 60 s of pulse application was found to be cracked by the bending test but no areas in which peeling had taken place were present. This image is indicative of the fact that the coating has a significant adhesion to the metal surface which is easily identifiable by the plastic deformation lines coming from mechanical cleaning of Pt surface. Also the average thickness of the coating was obtained by SEM image in transversal section (Figure 8.15 B) and resulted approximately 0.7 μm .

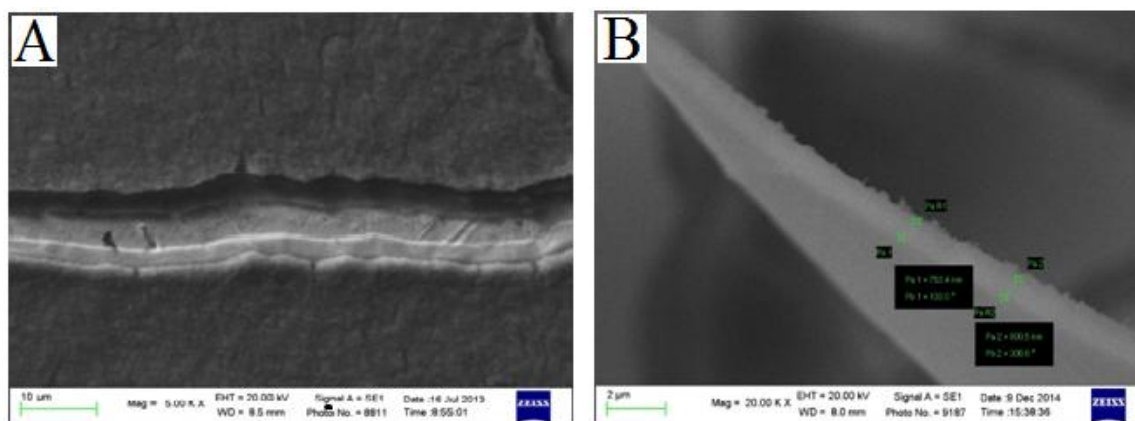


Figure 8.15 - SEM image of the LDH coating (60 s deposition time) after performing the bending test (A) and cross-sectional image of the same coating (B).

As far as the operational stability is concerned, the following experiment was carried out. The CME was soaked into a 0.1 M NaOH solution and was biased at 0.40 V vs SCE. After the stabilization of the “blank” current, glucose was added at a 0.75 mM

concentration and the current was recorded for 1000 s. The signal was very stable during the pulse application. Then the potential was switch off for 1000 s, afterwards the electrode was biased again at 0.40 V for 1000 s. These cycles of applied and not applied potential were repeated from the morning to the evening. The result was that the current response to glucose was practically unchanged each time it was recorded, so confirming the good stability of the sensor.

8.1.4 Flow injection analysis (FIA) of sugars

First the optimal operative conditions for the determination of sugars in flow conditions were searched. All the solutions at different pHs, above described, were tested as eluents changing the potential applied to the working electrode until the maximum current was recorded. The best signals were obtained with 0.1 M NaOH and 0.1 KNO₃ solution containing 0.01 M NaOH, whereas, when 0.1 M borate buffers were used, the typical FIA response was not recorded. In fact, after the injection the current did not display a trend with sharp peaks, probably because, in less basic solutions, the response time was not short enough to detect the concentration gradient which rapidly takes place in the detector microcell.

On the basis of the preliminary tests, 0.1 M KNO₃ containing 0.01 M NaOH was chosen as the optimal eluent for the successive analyses in order to avoid keeping the equipment in a strongly alkaline solution for a long time. Flow rate was also investigated and the best performance, in terms of repeatability of the measures, was obtained for a value equal to 1 mL min⁻¹.

Several carbohydrates were analyzed and Figure 8.16 shows a typical response obtained for injections of fructose solutions at increasing concentrations, working at a potential of +0.50 vs Ag/AgCl.

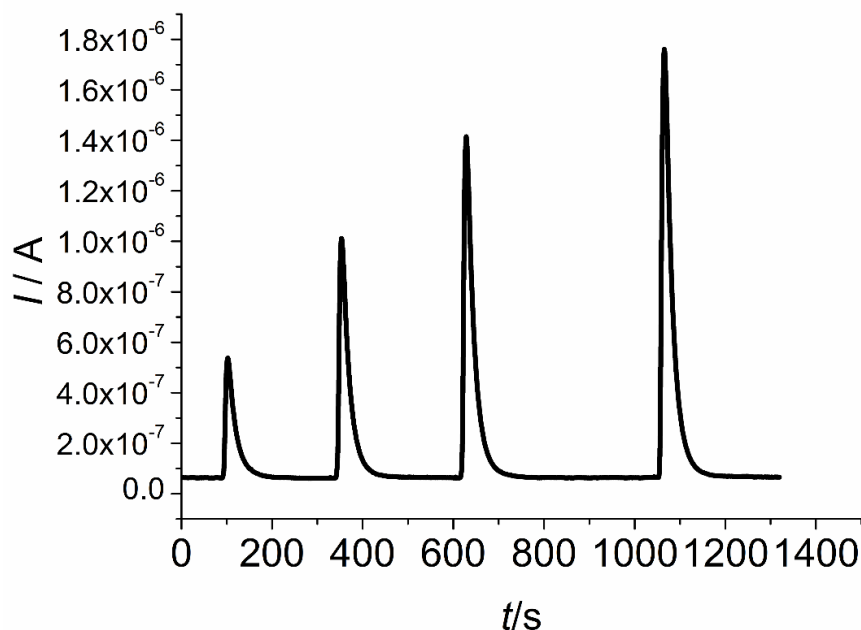


Figure 8.16 - I vs t curve obtained in FIA by injecting fructose solutions at different concentrations ($1.0 \cdot 10^{-4}$, $2.0 \cdot 10^{-4}$, $3.0 \cdot 10^{-4}$ and $4.0 \cdot 10^{-4}$ M).

Calibration graphs were constructed plotting the peak area as a function of the analyte concentration; the characteristic parameters of the plots are quoted in Table 8.8. Mono-saccharides displayed sensitivities higher than the di-saccharides and, within a class, the sensitivity is almost the same for all the sugars apart from sucrose, which responds less than maltose and lactose perhaps due to the absence of the hemiacetal group. The lower slope values of the calibration lines for di-saccharides, in comparison to mono-saccharides, let us think that, besides the total number of the oxidizable groups, the orientation of the molecule approaching the Co(IV) centres can also play a key role. Since a small molecule can come efficaciously in contact with the electrocatalytic centres in any direction, it is not surprising that di-saccharides respond less than mono-saccharides due to their greater steric hindrance.

The durability of the developed device was assessed operating it for 4-5 hours per day, five days a week, for several subsequent weeks. Day after day, the response of the Co/Al LDH coated Pt toward sugars maintained stable until the film detachment occurred, which generally took place after more than five weeks.

Table 8.8 Sensitivity and LOD values relative to the calibrations of sugars analyzed by FIA.

Analyte	Sensitivity /	LOD / M
---------	---------------	---------

	$\mu\text{C}\cdot\text{M}^{-1}$ NaOH	
	0.01 M	
Glucose	$1.65 \pm 0.05 \cdot 10^5$	$4 \cdot 10^{-5}$
Fructose	$1.10 \pm 0.02 \cdot 10^5$	$1 \cdot 10^{-5}$
Galactose	$1.3 \pm 0.1 \cdot 10^5$	$5 \cdot 10^{-5}$
Xylose	$1.13 \pm 0.03 \cdot 10^5$	$2 \cdot 10^{-5}$
Ribose	$1.25 \pm 0.04 \cdot 10^8$	$1 \cdot 10^{-4}$
Sucrose	$4.5 \pm 0.4 \cdot 10^4$	$5 \cdot 10^{-5}$
Maltose	$8.8 \pm 0.3 \cdot 10^4$	$2 \cdot 10^{-5}$
Lactose	$7.6 \pm 0.1 \cdot 10^4$	$5 \cdot 10^{-5}$

8.1.5 HPLC determination of sugars

In order to assess the efficiency of the overall separation process, mixtures of glucose, fructose and sucrose, which are the most widespread saccharides, were injected, testing different mobile phases (0.1 M NaOH, and 0.01 M NaOH) and flow rates (0.5, 1.0 and 1.2 mL min⁻¹): the only mobile phase which guaranteed a separation of the three analytes was 0.1 M NaOH operating at a flow rate of 1 mL min⁻¹. Figure 8.17 shows a typical chromatogram recorded in the optimized conditions for a mixture of the three sugars at a concentration of $1.5 \cdot 10^{-4}$ M, the order of elution being glucose, fructose and sucrose. Calibration curves were constructed injecting standard solutions of the three analytes and were linear within the investigated concentration range ($1 \cdot 10^{-5} \div 5 \cdot 10^{-3}$ M). The relevant slopes resulted $2.25 \cdot 10^5$ ($R^2=0.9941$), $2.16 \cdot 10^5$ ($R^2=0.9992$), and $1.41 \cdot 10^5$ ($R^2=0.9983$) $\mu\text{C M}^{-1}$ for glucose, fructose and sucrose, respectively.

Real samples of cereals and tea drink, containing glucose, fructose and sucrose were analyzed and the sugars content, calculated from the experimental data, was compared with the values declared on the label.

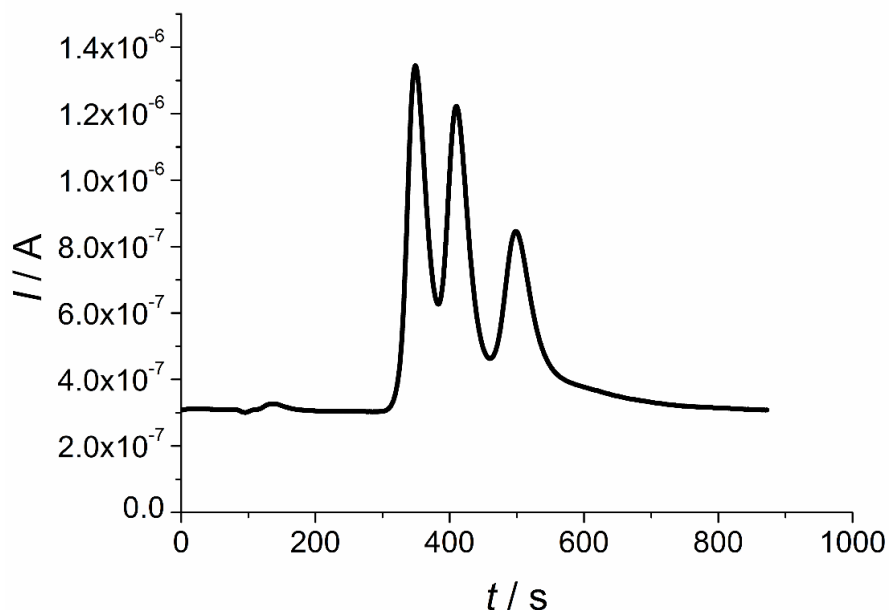


Figure 8.17 - Chromatogram obtained injecting a solution containing glucose, fructose, and sucrose (each one $1.5 \cdot 10^{-4}$ M).

In order to extract sugars, cereals samples (about 3 g) were grounded in a mortar until a fine powder was obtained, then a fixed amount of water (20 mL) was added and the suspension was kept under stirring for 1 hour. After filtration the aqueous extract was, diluted 100 times in 0.1 M NaOH and injected. The sample of tea did not require any specific pre-treatment, it was only diluted 1000 times and injected. The extraction was repeated three times and each extract was injected three times in order to evaluate the reproducibility of the analytical determination. The resulting % standard deviation was less than 3 % (Table 8.9).

Figure 8.18 shows the chromatograms recorded for cereals (A) and tea (B) samples demonstrating that glucose, fructose, and sucrose can be efficiently separated and quantified. For both samples the total sugar content we found was in agreement with the value declared on the label, as reported in Table 8.9.

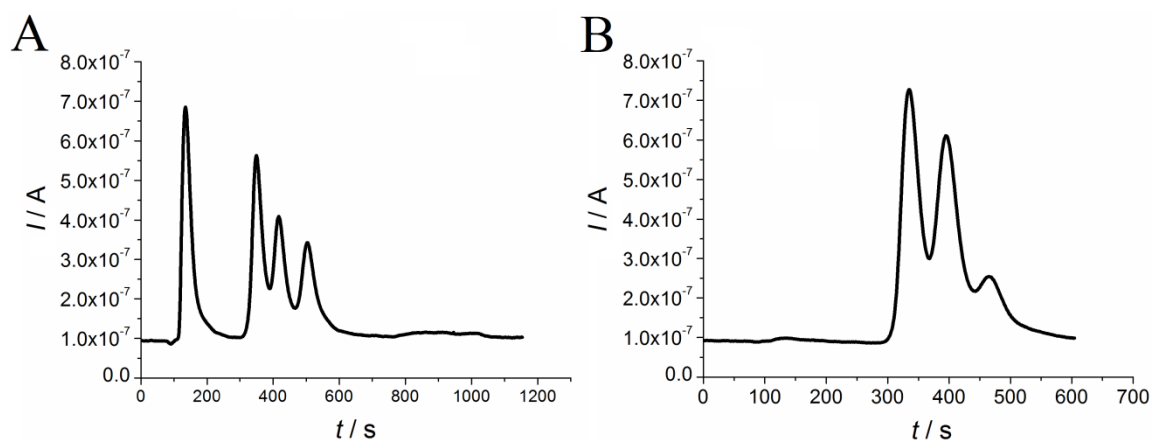


Figure 8.18. Chromatograms recorded injecting the aqueous extract obtained from the cereals sample (A) and the diluted tea sample (B).

Table 8.9 Mean content of sugars (\pm SD) as obtained by HPLC.

Analyte	Cereals		Tea	
	g/100g		g/100mL	
	Experimental	Declared	Experimental	Declared
Glucose	1.20 (\pm 0.04)		2.92 (\pm 0.06)	
Fructose	1.16 (\pm 0.04)		3.11 (\pm 0.07)	
Sucrose	4.1 (\pm 0.1)		3.47 (\pm 0.06)	
Total	6.5 (\pm 0.1)	6.5	9.4 (\pm 0.1)	8.2

REFERENCES

- [1] F. Bellezza, A. Cipiciani, U. Costantino, M. Nocchetti, T. Posati. *Eur. J. Inorg. Chem.* 18 (2009) 2603.
- [2] E. Scavetta, B. Ballarin, M. Gazzano, D. Tonelli. *Electrochim. Acta* 54 (2009) 1027.
- [3] C.G. Granqvist. *Appl. Phys. A* 57 (1993) 3.
- [4] F. Bellezza, M. Nocchetti, T. Posati, S. Giovagnoli, A. Cipiciani. *J. Colloid Interface Sci.* 376 (2012) 20.
- [5] E. Scavetta, D. Tonelli, M. Giorgetti, F. Nobili, R. Marassi, M. Berrettoni. *Electrochim. Acta* 48 (2003) 1347.
- [6] J.R. Macdonalds, *Impedance Spectroscopy. Emphasizing Solid Materials and Systems*, 1987, Wiley/Interscience, New York.
- [7] D. Friebe, M.W. Louie, M. Bajdich, K.E. Sanwald, Y. Cai, A.M. Wise, M. Cheng, D. Sokaras, *et al. J. Am. Chem. Soc.* 137 (2015) 1305.
- [8] L. Trotochaud, S.L. Young, J.K. Ranney, S.W. Boettcher. *J. Am. Chem. Soc.* 136 (2014) 6744.
- [9] L. Wang, C. Li, M. Liu, D.G. Evans, X. Duan. *Chem. Commun.* (2007) 123.
- [10] E. Scavetta, M. Berrettoni, M. Giorgetti, D. Tonelli. *Electrochim. Acta* 47 (2002) 2451.
- [11] B. Ballarin, R. Seeber, D. Tonelli, C. Zanardi. *Electroanalysis* 12 (2000) 434.
- [12] I. Gualandi, A.G. Solito, E. Scavetta, D. Tonelli. *Electroanalysis* 24 (2012) 857.
- [13] M.A. Ulibarri, J.M. Fernández, F.M. Labajos, V. Rives. *Chem. Mater.* 3 (1991) 626.

9. CONCLUSIONS

In this work layered double hydroxides and conducting polymers were studied as electrode modifiers for different applications.

The first part regarded the energy applications of modified electrodes, in particular LDHs performances as catalysts for oxygen evolution reaction and as pseudocapacitor materials were investigated, and the conditions for the electrosynthesis of a conducting polymeric film on ITO, having the desired characteristics, were studied in order to enhance the efficiency of organic solar cells.

- The electrosynthesis of four LDHs containing two different divalent (Ni or Co) and trivalent metals (Al or Fe) was described. The materials morphology and structure were characterized, respectively by SEM, XRD, XPS, XAS, and their electrochemical behaviour was deeply investigated by CV.

The XRD spectra confirmed the LDH phase and revealed a low crystallinity of the compounds. XPS analysis suggested the presence of M^{+2} and a small contribution of M^{3+} in the pristine Al-based LDHs and a significant increase of the amount of surface M^{3+} after their oxidation. In the case of LDH containing Fe the spectra of non oxidized materials revealed the presence of M^{2+} as prevalent species, whereas after oxidation the LDHs revealed a significant enrichment of M^{3+} .

XAS experiments, conducted on pristine and oxidized Ni/Fe LDHs, at the K-edge of Ni and Fe sites, confirmed the presence of the electroactive couple Ni^{2+}/Ni^{4+} , and evidenced also little differences in the charge associated to Fe (after the oxidation). The observed charge transfer resulted associated to minor changes (local structural arrangements) of the Ni and Fe sites structure.

- Concerning the energy applications, the catalytic properties towards the OER of the LDHs synthesized on Pt and GC electrodes were investigated in alkaline solutions recording LSV and chronopotentiometric curves.

The best performances in terms of onset potential, current density at a fixed potential and TOF were obtained for iron-based LDHs. Therefore, the presence of iron is crucial to significantly enhance the efficiency of a layered double hydroxide for OER. Only slight differences have been evidenced when GC was employed as

CONCLUSIONS

support instead of Pt, in particular, the parameters used to test OER activity resulted better if the LDHs were electrosynthesized on GC. This result can be considered very positive in view of the development of anodes for energy conversion technologies, due to the low cost of carbon based materials and the rapidity by which films of Ni and Co/Fe LDHs with good mechanical and electrochemical stability can be obtained on the conductive support.

- Concerning the energy storage applications, the pseudocapacitive properties of the four LDHs were investigated at first by EIS. The specific capacitance was then calculated following two methods, *i.e.*, from the CVs and by recording charge-discharge galvanostatic curves at several current densities. The cycling stability was tested calculating the C_s before and after performing 1000 charge-discharge cycles at 5.0 A g^{-1} . The Co-based LDHs showed a typical capacitive behaviour and satisfactory performances in terms of specific capacitance and long-term stability were obtained for those materials. Furthermore, when Fe was present, the LDH retained a pseudocapacitive behaviour in a higher potential range than the ones containing Al. Therefore even in this case the presence of iron displayed a positive effect on the performances of the LDH coated electrodes.

Co/Fe LDHs modified electrodes exhibited good charge storage characteristics and a high specific capacitance of 868.7 F g^{-1} at a current density of 1 A g^{-1} and cycling stability with only 18 % loss after 1000 cycles, in 1.0 M NaOH. The high capacitance came also from the porous structure of the materials and these results are promising since they indicate that those materials are suitable for interesting applications in supercapacitor devices.

- As regards the energy application of electrodes modified with conducting polymers, organic solar cells were fabricated employing different PEDOT buffers: one deposited by electrochemical synthesis (PEDOT:ClO₄) and the other by casting a commercial polymer (PEDOT:PSS). The electrochemical deposition was tested since it may offer some advantages like the use of low monomer concentrations, short times for the synthesis and good control of the film thickness. Two different donor materials were studied, *i.e.*, P3HT and a copolymer containing a porphyrin moiety on a thiophene monomer, synthesized to widen the absorption visible spectrum.

The HOMO and LUMO energy level of rr-P(T6Br-co-T6TTP) were calculated from CV data and taking into account the optical energy gap estimated from the UV/Vis spectra. Emission spectra of the photoactive layer containing rr-P(T6Br-co-T6TTP)

and PCBM suggested the occurrence of the electron transfer from the copolymer to PCBM, thus confirming a faster energy transfer between the components than singlet exciton decay in the copolymer and PCBM.

The cells composed by PEDOT:PSS and rr-P(T6Br-co-T6TPP):PCBM showed a power conversion efficiency of ~0.20% while the devices composed by PEDOT:ClO₄ and the same blend showed an efficiency of about 0.15%. The low efficiencies are due to the hindrance related to the porphyrin presence which does not allow for the formation of crystalline nanodomains, thus preventing the solid state chains packing. The efficiencies of the devices fabricated with PEDOT:ClO₄ instead of PEDOT:PSS resulted enhanced when P3HT was employed as blend donor material. Therefore, the electrochemically synthesized PEDOT can be considered a valid alternative to PEDOT:PSS taking into account that its properties could be further improved by acting on the synthesis parameters. Furthermore, the electrochemical approach could be applied to the photoactive layer as well by choosing properly the monomers and optimizing the electrochemical co-deposition parameters.

LDHs modified electrodes performances as amperometric sensors towards oxidizable substrates were studied. The electrocatalytic behaviour towards glucose oxidation of LDHs based on Ni as M(II) and Al or Fe as the trivalent metal was investigated with the aim of checking if the presence of Fe could improve the performance of the LDH coated electrodes. Another study regarded the evaluation of the performances of a Co/Al LDH on Pt for in flow detection of sugars, to be applied to real samples.

- Two different synthesis routes for Ni/Al and Ni/Fe LDHs, were carried out leading to different particles dimension and crystallinity degree. The chemical approach led to thin films well packed and uniform, constituted of particles having a mean size of about 5-15 nm. The direct electrodeposition on Pt, driven by the cathodic reduction of nitrates, was very rapid and again produced quite homogeneous and well packed LDH films where the mean particle diameter size was about 3 nm. XRD patterns revealed that the chemically synthesized LDHs displayed a higher crystallinity than those obtained by electrodeposition. The different order degree and the presence of iron inside the brucitic layers of the LDHs resulted key factors in determining the electrochemical behaviour of the materials. EIS and CV characterizations demonstrated that the electrodeposited LDHs have a higher conductivity than the chemically synthesized ones Moreover, in the presence of iron the conductivity of the

CONCLUSIONS

electrosynthesized LDHs was further increased since higher percentage of the nickel sites was involved in the electron hopping process.

The electrocatalytic behaviour of the Ni LDH coated electrodes was assessed by chronoamperometry and cyclic voltammetry, studying glucose as the analyte. The calculated catalytic rate constants were higher for the electrosynthesized LDH and for the LDHs containing iron. The diffusion of the substrate into the LDH structure was proved to be the rate determining step, thus limiting the electrocatalytic process and it was particularly evident for the chemically synthesized Ni/Al LDH. The highest electrocatalytic efficiency for glucose detection was obtained for the electrochemically synthesized LDHs and this result is due to the low crystallinity of the clays which makes easier for glucose to come in contact with the catalytic sites. The presence of Fe does not further improve the EE but allows to work at a potential value lower than the one required in the case of Ni/Al LDH.

- A Co/Al LDH electrosynthesized on Pt was employed in a wall jet cell for the amperometric detection of sugars, in flow systems. The modified electrode has been applied to determine some of the most common sugars by FIA and HPLC. The best operative conditions in terms of the eluent, pH, flow rate and anodic potential have been established in order to obtain a high sensitivity and a satisfactory durability of the sensor. The LDH film which displayed the highest sensitivity and a rather low LOD was that deriving from a deposition time of 20 s. The best performances of the electrochemical detector was achieved working at $E = 0.4 \text{ V}$ in 0.1 M NaOH due to the highest efficiency of the reaction involving the Co(IV) centres (sensitivity = $3.28 \cdot 10^{-2} \text{ A M}^{-1}$). Moreover, the sensor showed a quite wide linearity besides a good reproducibility and stability.

SCIENTIFIC PUBLICATIONS

1. L. Angiolini, E. Salatelli, M. Lanzi, V. Cocchi, D. Tonelli, Y. Vlamidis, Novel regioregular polythiophenes containing side-chain porphyrin groups for polymeric photovoltaic cells, *Materials Chemistry and Physics* 146 (2014) 464-471.
2. Y. Vlamidis, M. Lanzi, E. Salatelli, I. Gualandi, B. Fraboni, L. Setti, D. Tonelli, Electrodeposition of PEDOT perchlorate as an alternative route to PEDOT:PSS for the development of bulk heterojunction solar cells, *Journal of Solid State Electrochemistry* 19 (2015) 1685-1693.
3. I. Gualandi, E. Scavetta, Y. Vlamidis, A. Casagrande, D. Tonelli, Co/Al layered double hydroxide coated electrode for the amperometric detection of sugars, *Electrochimica Acta* 173 (2015) 67-75.
4. Y. Vlamidis, E. Scavetta, M. Gazzano, D. Tonelli, Iron vs aluminum based Layer Double Hydroxides as water splitting catalysts, *Electrochimica Acta* 188 (2016) 653-660.
5. E. Scavetta, Y. Vlamidis, D. Tonelli, T. Posati, M. Nocchetti, Glucose detection at Ni/Al and Ni/Fe layered double hydroxides Pt coated electrodes, revised version submitted to *Analytical and Bioanalytical Chemistry* .
6. Y. Vlamidis, E. Scavetta, N. Sangiorgi, D. Tonelli, Co and Ni based layered double hydroxides as pseudocapacitor materials, under review (submitted to *Journal of Power Sources*).

ACKNOWLEDGEMENTS

Ringrazio di cuore la prof.ssa Domenica Tonelli per la professionalità, la competenza e la disponibilità sempre mostrata e per avermi accolta presso il proprio laboratorio dandomi la possibilità di crescere professionalmente grazie questa importante esperienza.

Ringrazio molto la prof.ssa Erika Scavetta, il prof. Marco Giorgetti, il prof. Sergio Zappoli per l'aiuto e per i preziosi consigli, e tutte le persone che hanno contribuito alla realizzazione delle ricerche condotte nei tre anni, tra le quali la prof.ssa Elisabetta Salatelli, il prof. Massimiliano Lanzi, la prof.ssa Beatrice Fraboni (Dipartimento di Fisica e Astronomia), il prof. Massimo Gazzano (ISOF-CNR), la dott.ssa Tamara Posati (ISMN-CNR) e la prof.ssa Sonia Fiorilli (Politecnico di Torino).

Dedico in oltre un grande ringraziamento a tutti i tecnici del Dipartimento, Sandra, Stefano, Alberto, Biccio, Vincenzo, Ciro e Luigi, sempre competenti, disponibilissimi e a Fabrizio Tarterini per tutto l'aiuto e per l'infinita pazienza.

Grazie ai ragazzi del laboratorio, in particolare Isacco, Adriana, Marco e Tommaso per i bei momenti condivisi.

Un immenso grazie va agli amici e soprattutto alla mia famiglia che è stata costantemente il mio punto di riferimento.